Acoustical Physics, Vol. 51, No. 4, 2005, pp. 367–375. Translated from Akusticheskiĭ Zhurnal, Vol. 51, No. 4, 2005, pp. 437–446.

Solution of the Three-Dimensional Inverse Acoustic Scattering Problem on the Basis of the Novikov–Henkin Algorithm

N. V. Alekseenko, V. A. Burov, and O. D. Rumyantseva

Moscow State University, Vorob'evy gory, Moscow, 119992 Russia

e-mail: burov@phys.msu.ru

Received May 5, 2004

Abstract—A theoretical study of the practical abilities of the Novikov–Henkin algorithm, which is one of the most promising algorithms for solving three-dimensional inverse monochromatic scattering problems by functional analysis methods, is carried out. Numerical simulations are performed for model scatterers of different strengths in an approximation simplifying the reconstruction process. The resulting estimates obtained with the approximate algorithm prove to be acceptable for middle-strength scatterers. For stronger scatterers, an adequate reconstruction is possible on the basis of a rigorous solution. *© 2005 Pleiades Publishing, Inc.*

METHODS FOR SOLVING INVERSE SCATTERING PROBLEMS

The inverse scattering problem consists in the determination of the characteristics of a scatterer located in a spatial domain $\Re$ and described by a function $V(\mathbf{r})$, where $\mathbf{r} \in \Re$, from the measured scattered field. In the case of an infinite domain $\Re$, the function $V(\mathbf{r})$ is assumed to be rapidly decreasing at infinity. Below, scatterers concentrated in a finite domain $\Re$ are considered. The inverse problem is reduced to estimating $V(\mathbf{r})$ in the Schrödinger equation or the Helmholtz equation $\Delta u + k_0^2 u = V(\mathbf{r})u$, which coincides with the Schrödinger equation in the monochromatic case, for the total wave field u. Here, k_0 is the wave number in the homogeneous nonabsorbing background medium. For acoustic problems, in the case of a constant density of the medium, the function $V(\mathbf{r})$ characterizes the deviation of the phase velocity of sound $c(\mathbf{r})$ in the scattering region $\Re$ from its background value c_0: $V(\mathbf{r}) \equiv \omega^2[c_0^{-2} - c^{-2}(\mathbf{r})]$. If the scatterer possesses absorbing properties, $c(\mathbf{r})$ can be formally considered as a complex quantity. Two classes of approaches to solving the inverse scattering problem can be distinguished: one of them is based on iteration methods [1–3], and the other, on functional analysis methods [4, 5]; a review of the latter can be found in [6]. The advantage of the iteration methods is that they can proceed from fragmentary data obtained with different geometries of the experiment and at different frequencies. These methods impose no strict requirements on the completeness of the experimental scattering data and can use any *a priori* and *a posteriori* information. The main advantages of the functional approach are the possibility to obtain a rigorous solution and (in some cases) the use of a smaller number of computing operations than in the iteration methods.

The functional analytical methods for solving one-dimensional inverse scattering problems appeared as early as in the 1950s (Gel'fand, Levitan, Marchenko, and others). The first comprehensive studies of the multidimensional inverse scattering problem were carried out by Berezanskii in the 1950s and by Faddeev and Newton in the 1960–1970s. A systematic investigation of this problem in application to quantum mechanics can be found in [7]. In the 1980s, the ideas put forward by Faddeev were developed by Nachman and Ablowitz, who proposed a functional approach called the $\bar{\partial}$ method (here, the symbol $\bar{\partial}$ means differentiation with respect to the variable that is the complex conjugate of the main argument). Henkin and Novikov continued developing this approach by applying it to multidimensional inverse scattering problems with monochromatic data [6]. In such a problem, a plane monochromatic incident wave is characterized by the wave vector $\mathbf{k} \in \mathbb{R}^n$, while the scattered wave in the far-field zone is characterized by the wave vector $\boldsymbol{l} \in \mathbb{R}^n$, where $\mathbf{k}^2 = \boldsymbol{l}^2 = k_0^2$ and n is the space dimension. The experimental data are represented by the scattering amplitude $f(\mathbf{k}, \boldsymbol{l})$ related to the asymptotics of the scattered field in the far-field zone according to the formula

$$u(\mathbf{r}, \mathbf{k}) = \exp(i\mathbf{k}\mathbf{r}) + A_n \frac{\exp(ik_0|\mathbf{r}|)}{\sqrt{|\mathbf{r}|^{n-1}}} f\left(\mathbf{k}, \boldsymbol{l} = k_0 \frac{\mathbf{r}}{|\mathbf{r}|}\right) + \bar{\bar{o}}\left(\frac{1}{\sqrt{|\mathbf{r}|^{n-1}}}\right),$$

where $A_{n=2} = -(1+i)\pi\sqrt{\pi}/\sqrt{k_0}$ and $A_{n=3} = -2\pi^2$. The reconstruction of $V(\mathbf{r})$ is based on the following generalizations, which were first introduced by Faddeev [8].

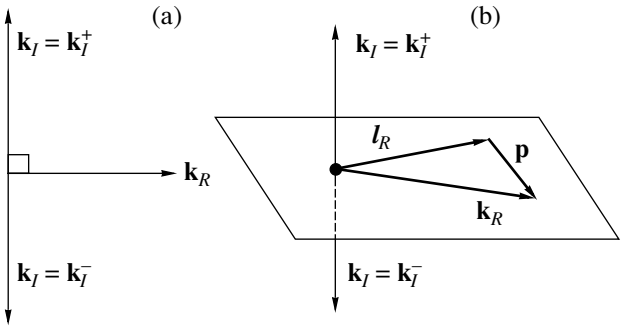

Fig. 1. Orientation of mutually orthogonal real and imaginary components of wave vectors in the (a) two-dimensional and (b) three-dimensional cases.

To solve the problem under consideration, it is proposed to formally extend the wave vectors to the complex domain $\mathbf{k}, \boldsymbol{l} \in \mathbb{C}^n$ by assuming that $\mathbf{k} = \mathbf{k}_R + i\mathbf{k}_I$ and $\boldsymbol{l} = \boldsymbol{l}_R + i\boldsymbol{l}_I$, where $\mathbf{k}_R \equiv \mathrm{Re}\,\mathbf{k}$, $\mathbf{k}_I \equiv \mathrm{Im}\,\mathbf{k}$, $\boldsymbol{l}_R \equiv \mathrm{Re}\,\boldsymbol{l}$, and $\boldsymbol{l}_I \equiv \mathrm{Im}\,\boldsymbol{l}$. This passage from real values to complex ones should be performed without leaving the k_0^2 constant-energy surface, which is expressed as

$$\mathbf{k}^2 = \boldsymbol{l}^2 = k_0^2; \quad \mathbf{k}, \boldsymbol{l} \in \mathbb{C}^n. \tag{1}$$

Requirement (1) means that the following conditions should be simultaneously satisfied:

$$\mathbf{k}_I \perp \mathbf{k}_R, \quad \mathbf{k}_R^2 - \mathbf{k}_I^2 = k_0^2; \quad \boldsymbol{l}_I \perp \boldsymbol{l}_R, \quad \boldsymbol{l}_R^2 - \boldsymbol{l}_I^2 = k_0^2. \tag{2}$$

Here, the value of $|\mathbf{k}|^2 = \mathbf{k}_R^2 + \mathbf{k}_I^2$ can be as large as one likes; however, when $|\mathbf{k}_R|$ increases, $|\mathbf{k}_I|$ should also increase, so that, according to conditions (2), the difference in their squares should always be equal to the "energy" of the incident wave k_0^2. The above passage is accompanied by the generalization of the classical wave fields and Green functions to the case of complex wave vectors [6, 9]. In particular, the classical scattering amplitude $f(\mathbf{k}, \boldsymbol{l})$ ($\mathbf{k}, \boldsymbol{l} \in \mathbb{R}^n$) passes into a generalized scattering amplitude (generalized scattering data) $h(\mathbf{k}, \boldsymbol{l})$, where $\mathbf{k}, \boldsymbol{l} \in \mathbb{C}^n$.

The imaginary part of the wave vector can be represented as $\mathbf{k}_I \equiv |\mathbf{k}_I|\boldsymbol{\gamma}$, where the vector $\boldsymbol{\gamma} \in \mathbb{R}^n$ ($|\boldsymbol{\gamma}| = 1$) characterizes the direction of the vector $\mathbf{k}_I$. When $|\mathbf{k}_I| \longrightarrow 0$, the limiting values of the generalized functions depend on the direction $\boldsymbol{\gamma}$ of the infinitesimal but oriented imaginary part $\mathbf{k}_I$. The limiting values of the function $h(\mathbf{k}, \boldsymbol{l})$ are $h_\gamma(\mathbf{k}_R, \boldsymbol{l}_R) \equiv \lim\limits_{|\mathbf{k}_I| \to 0} h(\mathbf{k}_R + i|\mathbf{k}_I|\boldsymbol{\gamma}, \boldsymbol{l}_R)$, where $|\boldsymbol{l}_R| = |\mathbf{k}_R| = k_0$ in the limit. The quantities $h_\gamma(\mathbf{k}_R, \boldsymbol{l}_R) \equiv \mathbf{h}_\gamma(\mathbf{k}, \boldsymbol{l})$, where $\mathbf{k}, \boldsymbol{l} \in \mathbb{R}^n$, are in one-to-one correspondence with $f(\mathbf{k}, \boldsymbol{l})$ according to the formula [4]

$$h_\gamma(\mathbf{k}, \boldsymbol{l}) = f(\mathbf{k}, \boldsymbol{l}) + 2\pi i \int\limits_{\mathbf{m} \in \mathbb{R}^n} h_\gamma(\mathbf{k}, \mathbf{m}) \times \theta[(\mathbf{m} - \mathbf{k}, \boldsymbol{\gamma})]\delta(\mathbf{m}^2 - \mathbf{k}^2) f(\mathbf{m}, \boldsymbol{l}) d\mathbf{m}; \quad \mathbf{k}, \boldsymbol{l} \in \mathbb{R}^n; \tag{3}$$

here, $\theta[(\mathbf{m} - \mathbf{k}, \boldsymbol{\gamma})]$ is the Heaviside function, whose argument is the scalar product of the vectors $\mathbf{m} - \mathbf{k}$ and $\boldsymbol{\gamma}$.

From condition (1), which is equivalent to conditions (2), it follows that, in the two-dimensional case, only two orientations are possible for the vector $\mathbf{k}_I = \mathbf{k}_I^\pm$ being orthogonal to a fixed vector $\mathbf{k}_R$ (Fig. 1a). The mutual orientation of the vectors $\boldsymbol{l}_R$ and $\boldsymbol{l}_I$ is similar. In addition, it is assumed that

$$|\boldsymbol{l}_R| = |\mathbf{k}_R| \text{ and, hence, } |\boldsymbol{l}_I| = |\mathbf{k}_I|. \tag{4}$$

The limiting values of $h_\gamma(\mathbf{k}, \boldsymbol{l})$ that correspond to these two orientations are denoted as $h^+(\mathbf{k}, \boldsymbol{l})$ and $h^-(\mathbf{k}, \boldsymbol{l})$, respectively. In the three-dimensional case, the vector $\mathbf{k}_I$ ($\mathbf{k}_I \perp \mathbf{k}_R$) can have any direction in the plane perpendicular to the fixed vector $\mathbf{k}_R$. At the same time, when solving a three-dimensional problem, an additional requirement should be introduced:

$$\mathbf{k}_I = \boldsymbol{l}_I. \tag{5}$$

From conditions (2) and (5), it follows that

$$\mathbf{k}_I \perp \mathbf{k}_R, \quad \mathbf{k}_I \perp \boldsymbol{l}_R, \quad |\boldsymbol{l}_R| = |\mathbf{k}_R|. \tag{6}$$

Therefore, $\mathbf{k}_I$ is orthogonal to the plane containing the two vectors $\mathbf{k}_R$ and $\boldsymbol{l}_R$ and, hence, the vector $\mathbf{p} \equiv \mathbf{k} - \boldsymbol{l} = \mathbf{k}_R - \boldsymbol{l}_R$. Then, the number of possible orientations of the vector $\mathbf{k}_I$ with respect to this plane becomes equal to two (Fig. 1b), as in the two-dimensional space. (The degenerate case of $\mathbf{k}_R \parallel \boldsymbol{l}_R$ is considered as the limiting situation for the case of noncollinear $\mathbf{k}_R$ and $\boldsymbol{l}_R$.)

NOVIKOV–HENKIN THREE-DIMENSIONAL ALGORITHMS FOR SOLVING THE INVERSE SCATTERING PROBLEM

A functional algorithm for solving the two-dimensional monochromatic inverse scattering problem with relatively strong scatterers was proposed by Novikov in [10] and by Grinevich and Manakov in [11]. Later, this algorithm was studied in application to acoustic tomography [9] and was also implemented in a computer program [12, 13]. In the framework of the two-dimensional problem, a scatterer $v(\mathbf{r})$ that causes no backscattering can be rigorously and stably reconstructed by a simplified scheme with allowance for multiple scattering processes on the basis of the known classical scattering amplitude and the two limiting functions $h^\pm(\mathbf{k}, \boldsymbol{l})$ (where $\mathbf{k}, \boldsymbol{l} \in \mathbb{R}^2$) obtained from it. From the absence of backscattering, it follows that the high-frequency components of the spatial spectrum of the scat-

terer $\tilde{v}(\boldsymbol{\xi}) \equiv \frac{1}{(2\pi)^n}\int v(\mathbf{r})\exp(-i\boldsymbol{\xi}\mathbf{r})d\mathbf{r}$, where $n = 2$, are negligibly small. For weak (Born) scatterers, these are the components with $|\boldsymbol{\xi}| \geq 2k_0$. As the scatterer strength increases, the corresponding threshold value for $|\boldsymbol{\xi}|$ becomes smaller than $2k_0$. However, if the spectrum $\tilde{v}(\boldsymbol{\xi})$ does contain high-frequency spatial components causing considerable backscattering, a rigorous reconstruction of $v(\mathbf{r})$ requires knowledge of not only the functions $h^{\pm}(\mathbf{k}, \boldsymbol{l})$ but also the generalized backscattering amplitude $h(\mathbf{k}, \boldsymbol{l} = -\bar{\mathbf{k}})$ for $\mathbf{k} \in \mathbb{C}^2$ [11, 14] (here, the overbar denotes complex conjugation: $\bar{\mathbf{k}}$). In this case, the rigorous algorithm allows one to reconstruct middle-strength scatterers with an arbitrary spatial spectrum. However, it proves to be fairly unstable under the effect of noise, which makes it less valuable from a practical point of view [15]. The instability that is caused by the presence of backscattering is typical of the two-dimensional inverse monochromatic scattering problem irrespective of the specific method of its solution. This is related to the dimensional nonredundancy of the two-dimensional monochromatic problem (a two-dimensional parametrized space of scattering data and also a two-dimensional domain of definition of the desired function $v(\mathbf{r})$), which was first mentioned by A.J. Devaney and also discussed in [16].

Experience in the computer realization of the algorithms developed for solving the aforementioned two-dimensional problems on the basis of functional analysis methods and the general understanding achieved with this experience have made it possible to proceed to solving three-dimensional problems, which are of most practical interest. The possibilities to obtain new results in this area are determined by the rapidly progressing abilities of modern computers. By now, Novikov and Henkin developed theoretically two monochromatic functional algorithms for reconstructing three-dimensional scatterers. In both algorithms, for reconstructing the scatterer spectrum $\tilde{v}(\boldsymbol{\xi})$ at a spatial frequency $\boldsymbol{\xi} = -\mathbf{p} = \boldsymbol{l} - \mathbf{k}$, it is necessary to consider the set M of all vectors $\mathbf{k} \in \mathbb{C}^3$ that simultaneously satisfy the following two conditions at any fixed vector $\mathbf{p} \in \mathbb{R}^3$:

$$\mathbf{k}^2 = k_0^2, \quad 2\mathbf{k}\mathbf{p} = \mathbf{p}^2. \tag{7}$$

Conditions (7) are equivalent to conditions (1) (or (2)) and (5) represented in terms of the vectors $\mathbf{k} \in \mathbb{C}^3$ and $\mathbf{p} = \mathbf{k}_R - \boldsymbol{l}_R$. Indeed, the substitution of $\boldsymbol{l} = \mathbf{k} - \mathbf{p}$ into the relationship $\boldsymbol{l}^2 = k_0^2$ yields $(\mathbf{k} - \mathbf{p})^2 = k_0^2$, which, with allowance for the requirement $\mathbf{k}^2 = k_0^2$, leads to conditions (7). The physical meaning of conditions (7) was already explained by Fig. 1b. Namely, at a fixed $\mathbf{p}$, the vector $\mathbf{k}_I$ is orthogonal to the plane containing the vectors $\mathbf{k}_R$ and $\mathbf{p}$, while the vector $\mathbf{k}_R$ satisfies the equation of this plane:

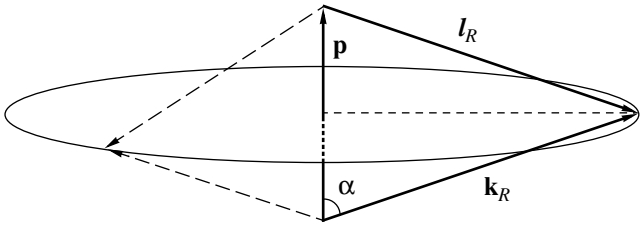

Fig. 2. Geometrical redundancy of the vector pairs $(\mathbf{k}_R, \boldsymbol{l}_R)$ generating the same vector $\mathbf{p} = \mathbf{k}_R - \boldsymbol{l}_R$ in three-dimensional space.

$$2\mathbf{k}_R\mathbf{p} = \mathbf{p}^2. \tag{8}$$

From Eq. (8), it follows that the projection of vector $\mathbf{k}_R$ on the direction of vector $\mathbf{p}$ always satisfies the condition $|\mathbf{k}_R|\cos\alpha = |\mathbf{p}|/2$ (where α is the angle between $\mathbf{k}_R$ and $\mathbf{p}$), which is equivalent to the condition $|\boldsymbol{l}_R| = |\mathbf{k}_R|$ (see Eq. (6)). In an exhaustive search through all possible directions of vectors $\mathbf{k} \in M$ corresponding to the fixed $\mathbf{p}$, the end of the vector $\mathbf{k}_R$ of a fixed length describes a circle of radius $|\mathbf{k}_R|\sin\alpha$ in the plane perpendicular to the vector $\mathbf{p}$. Simultaneously, the vector $\mathbf{k}_R$ describes a conic surface (Fig. 2).

The reconstruction of the scatterer with the first of the algorithms discussed in this paper is performed on the basis of the asymptotic relation [6, 17]

$$\tilde{v}(-\mathbf{p}) = \lim_{|\mathbf{k}| \to \infty,\, \mathbf{k} \in M} H(\mathbf{k}, \mathbf{p}), \tag{9}$$

where $H(\mathbf{k}, \mathbf{p}) \equiv h(\mathbf{k}, \boldsymbol{l} = \mathbf{k} - \mathbf{p})$; $\mathbf{k}, \boldsymbol{l} \in \mathbb{C}^3$.

This method is based on the decrease in the multiple scattering effects with increasing $|\mathbf{k}|$ at a fixed value of $\mathbf{k}^2 = k_0^2$ ($\mathbf{k} \in \mathbb{C}^3$). The minimal value $|\mathbf{k}| = |\mathbf{k}^{\min}|$ that should be reached to neglect the multiple scattering effects, i.e., to obtain a quasi-Born scattering, depends on the wave size of the scatterer and on the relative contrast of sound velocity $|\Delta c|/c_0$ in it. For a scatterer with a linear size L, which, in the first case, is represented by a single inhomogeneity with a fixed sign of the contrast $|\Delta c|/c_0$ and, in the second case, by an inhomogeneity with an alternating contrast fluctuating on a characteristic linear scale ΔL, the following conditions should, respectively, be satisfied [18]:

$$\frac{k_0}{|\mathbf{k}^{\min}|}\frac{|\Delta c|}{c_0}\frac{L}{\lambda_0} \ll 1, \quad \frac{k_0}{|\mathbf{k}^{\min}|}\frac{|\Delta c|}{c_0}\frac{\Delta L}{\lambda_0}\sqrt{\frac{L}{\Delta L}} \ll 1, \tag{10}$$

where λ_0 is the wavelength in the background medium. For weak, i.e., Born, scatterers, relation (9) is valid starting from $\mathbf{k}_I = 0$. As the scatterer strength increases, it becomes necessary to take into account the multiple scattering effects, and the stronger the scatterer, the greater the value of $|\mathbf{k}_I^{\min}|$ corresponding to $|\mathbf{k}^{\min}|$. How-

ever, the procedure proposed in [6, 17] for determining $H(\mathbf{k}, \mathbf{p})$ or $h(\mathbf{k}, \boldsymbol{l})$, where $\mathbf{k}, \boldsymbol{l} \in \mathbb{C}^n$, from $f(\mathbf{k}, \boldsymbol{l})$, where $\mathbf{k}, \boldsymbol{l} \in \mathbb{R}^n$, provides an acceptable noise robustness in the monochromatic regime only for $|\mathbf{k}_l|L \le 1$, i.e., for scatterers of a small wave size with insignificant deviations of wave parameters, when the minimal necessary imaginary component of vector $\mathbf{k}$ satisfies the condition $|\mathbf{k}_I^{\min}|L \le 1$ [19]. For more complex and stronger scatterers, the effect of noise and measurement errors grows as $\sim\exp(|\mathbf{k}_l|L)$ beyond an acceptable level, and even the dimensional redundancy of data in the three-dimensional problem does not noticeably improve the situation.

The second three-dimensional monochromatic algorithm for solving the inverse scattering problem, which was also proposed in [6], relates the spatial spectrum of the scatterer, $\tilde{v}(-\mathbf{p})$, to the generalized scattering data $H(\mathbf{k}, \mathbf{p})$ in the following manner:

$$\tilde{v}(-\mathbf{p}) = H(\mathbf{k}_*, \mathbf{p}) + Z_1[H(\mathbf{k}, \mathbf{p})|_{\mathbf{k}_I \neq 0}, \mathbf{k}_*] + Z_2[H(\mathbf{k}, \mathbf{p})|_{\mathbf{k}_I \to 0}, \mathbf{k}_*], \tag{11}$$

where

$$Z_1[H(\mathbf{k}, \mathbf{p})|_{\mathbf{k}_I \neq 0}, \mathbf{k}_*] \equiv \int\limits_{\mathbf{k}' \in M} \bar{\partial} H(\mathbf{k}', \mathbf{p}) \wedge K_{\mathbf{p}}(\mathbf{k}', \mathbf{k}_*);$$

$$Z_2[H(\mathbf{k}, \mathbf{p})|_{\mathbf{k}_I \to 0}, \mathbf{k}_*] \equiv \int\limits_{\mathbf{k}' \in \partial M} \{H^+(\mathbf{k}', \mathbf{p}) - H^-(\mathbf{k}', \mathbf{p})\} K_{\mathbf{p}}(\mathbf{k}', \mathbf{k}_*).$$

Here, $\mathbf{k}_* \in M$ is an arbitrary fixed vector from the given set. The integral kernel $K_{\mathbf{p}}(\mathbf{k}', \mathbf{k}_*)$ and the $\bar{\partial}$ derivative $\bar{\partial} H(\mathbf{k}', \mathbf{p})$ of the function $H(\mathbf{k}', \mathbf{p})$ are differential forms (as above, the overbar means complex conjugation):

$$K_{\mathbf{p}}(\mathbf{k}', \mathbf{k}_*) \equiv \frac{\det(\mathbf{p}, \mathbf{k}' + \mathbf{k}_*, \bar{\mathbf{k}}' - \bar{\mathbf{k}}_*)}{2\pi i |\mathbf{k}' - \mathbf{k}_*|^2} \times \left[\frac{dk'_x}{p_y k'_z - p_z k'_y} + \frac{dk'_y}{p_z k'_x - p_x k'_z} + \frac{dk'_z}{p_x k'_y - p_y k'_x}\right]$$
$$\equiv B_x(\mathbf{p}, \mathbf{k}', \mathbf{k}_*) dk'_x + B_y(\mathbf{p}, \mathbf{k}', \mathbf{k}_*) dk'_y + B_z(\mathbf{p}, \mathbf{k}', \mathbf{k}_*) dk'_z \equiv \sum_{n=1}^{3} B_n(\mathbf{p}, \mathbf{k}', \mathbf{k}_*) dk'_n, \tag{12}$$

$$\bar{\partial} H(\mathbf{k}', \mathbf{p}) \equiv \frac{\partial H(\mathbf{k}', \mathbf{p})}{\partial \bar{k}'_x} d\bar{k}'_x + \frac{\partial H(\mathbf{k}', \mathbf{p})}{\partial \bar{k}'_y} d\bar{k}'_y + \frac{\partial H(\mathbf{k}', \mathbf{p})}{\partial \bar{k}'_z} d\bar{k}'_z \equiv \sum_{m=1}^{3} \frac{\partial H(\mathbf{k}', \mathbf{p})}{\partial \bar{k}'_m} d\bar{k}'_m,$$

where $\dfrac{\partial}{\partial \bar{k}'_m} \equiv \dfrac{1}{2}\left[\dfrac{\partial}{\partial(\mathrm{Re}\, k'_m)} + i\dfrac{\partial}{\partial(\mathrm{Im}\, k'_m)}\right]$ and $\bar{\partial} H$ obeys the $\bar{\partial}$ equation [6]

$$\bar{\partial} H(\mathbf{k}', \mathbf{p}) = -2\pi \int\limits_{\zeta \in \mathbb{R}^3} (\zeta_x d\bar{k}'_x + \zeta_y d\bar{k}'_y + \zeta_z d\bar{k}'_z) \times H(\mathbf{k}', -\boldsymbol{\zeta}) H(\mathbf{k}' + \boldsymbol{\zeta}, \mathbf{p} + \boldsymbol{\zeta}) \delta(\boldsymbol{\zeta}^2 + 2\mathbf{k}'\boldsymbol{\zeta}) d\boldsymbol{\zeta}. \tag{13}$$

The subscripts $n, m = 1, 2, 3$ refer to the x, y, and z components of the vector $\mathbf{k}'$ (subscript n) and the complex conjugate vector $\bar{\mathbf{k}}'$ (subscript m). The symbol $\wedge$ (used in the complex analysis) appearing in the integrand in the formula for the functional term Z_1 denotes the "exterior product"

$$\bar{\partial} H(\mathbf{k}', \mathbf{p}) \wedge K_{\mathbf{p}}(\mathbf{k}', \mathbf{k}_*) \equiv \sum_{m=1}^{3} \sum_{n=1}^{3} \frac{\partial H(\mathbf{k}', \mathbf{p})}{\partial \bar{k}'_m} B_n(\mathbf{p}, \mathbf{k}', \mathbf{k}_*) d\bar{k}'_m \wedge dk'_n,$$

$$d\bar{k}'_m \wedge dk'_m = 2id(\mathrm{Re}\, k'_m) d(\mathrm{Im}\, k'_m),$$

$$d\bar{k}'_m \wedge dk'_n = \mu[d(\mathrm{Re}\, k'_m) d(\mathrm{Re}\, k'_n) + d(\mathrm{Im}\, k'_m) d(\mathrm{Im}\, k'_n)] + i[d(\mathrm{Re}\, k'_m) d(\mathrm{Im}\, k'_n) - d(\mathrm{Im}\, k'_m) d(\mathrm{Re}\, k'_n)],$$

where

$$\mu = \begin{cases} 1 \text{ for the pairs } \{m = x, n = y\}, \\ \{m = y, n = z\}, \{m = z, n = x\}; \\ -1 \text{ for the pairs } \{m = y, n = x\}, \\ \{m = z, n = y\}, \{m = x, n = z\}. \end{cases}$$

In the functional term Z_2, the boundary ∂M of the set M corresponds to the real vectors $\mathbf{k}' \in \mathbb{R}^3$ that satisfy conditions (7). The vectors $\mathbf{p}$, $\mathbf{k}_R \equiv \mathbf{k}'$, and the infinitesimal imaginary part $\mathbf{k}_I \equiv \pm 0([\mathbf{p} \times \mathbf{k}'])$, which determine the functions $H^{\pm}(\mathbf{k}', \mathbf{p}) \equiv H(\mathbf{k}' \pm i0([\mathbf{p} \times \mathbf{k}']), \mathbf{p})$, form the right-handed and left-handed coordinate systems, respectively (Fig. 1b). With $|k_*| \longrightarrow \infty$, algorithm (11) transforms into asymptotic algorithm (9) because Z_1, $Z_2 \longrightarrow 0$. It should be noted that relations close to algorithm (11) were later considered by Nachman [20], however, only for the limiting case of zero energy (frequency).

Thus, algorithms (9) and (11) refer to multidimensional inverse problems of mathematical physics. Previously, they were only considered from the viewpoint of obtaining mathematically rigorous solutions. However, their practical realization is difficult and, in addition, the stability of their solutions has not been theoretically analyzed. As a result, until the present time, no studies were performed with the aim of putting into practice mathematically rigorous methods for solving multidimensional inverse wave scattering problems and

to realize them in the form of efficient numerical algorithms. For practical implementation, it is important to estimate the physical contribution made by each of the functional terms of algorithm (11) to the estimate of $\tilde{v}(-\mathbf{p})$, as was briefly mentioned in [18]. The first term $H(\mathbf{k}_*, \mathbf{p})$ represents the generalized scattering data themselves. Since, with the multiple scattering processes taken into account, the function $H(\mathbf{k}_*, \mathbf{p})$ depends on $f(\mathbf{k}, \boldsymbol{l})$ ($\mathbf{k}, \boldsymbol{l} \in \mathbb{R}^3$) in a nonlinear manner, the function $H(\mathbf{k}_*, \mathbf{p})$ is not a purely Born-type estimate of the spectrum $\tilde{v}(-\mathbf{p})$ but additionally includes some non-Born information on the scatterer. For every fixed $\mathbf{p}$, it is possible to chose some $\mathbf{k}_* \in M$ (complex-valued in the general case) whose component $\mathrm{Re}\mathbf{k}_*$ in the direction of vector $\mathbf{p}$ is equal to $\mathbf{p}/2$; i.e., $|\mathbf{p}| = 2|\mathrm{Re}\mathbf{k}_*|\cos\alpha_*$, where α_* is the angle between $\mathbf{k}_*$ and $\mathbf{p}$. At the same time, all possible orientations of the vector $\mathrm{Re}\mathbf{k}_*$, with its length $|\mathrm{Re}\mathbf{k}_*|$ being fixed, allow one to obtain the vector $\mathbf{p}$ inside the sphere of radius $2|\mathrm{Re}\mathbf{k}_*|$; i.e., they lead to the values $|\mathbf{p}| \le 2|\mathrm{Re}\mathbf{k}_*|$. Since, for a complex $\mathbf{k}_*$, the value of $|\mathrm{Re}\mathbf{k}_*|$ can be chosen to be as large as one likes, the algorithm does not impose any strict limitations on the range of values of $|\mathbf{p}|$. However, the choice of $\mathrm{Im}\mathbf{k}_* \longrightarrow 0$ is most appropriate for the practical implementation of the algorithm under consideration, because, in this case, the function $H(\mathbf{k}_*, \mathbf{p})$ is directly calculated from Eq. (3). In this case, the spatial spectrum of the scatterer $\tilde{v}(-\mathbf{p})$ is only estimated in the region $|\mathbf{p}| \le 2k_0$. In addition, the term Z_1 is more stable for $\mathrm{Im}\mathbf{k}_* \longrightarrow 0$ than for $\mathrm{Im}\mathbf{k}_* \neq 0$.

The term Z_2, in which the limiting values of $H^{\pm}(\mathbf{k}', \mathbf{p})$ are also directly calculated from Eq. (3), is the result of the weighted integration of the difference between these values over the set of real vectors $\mathbf{k}' \in \partial M$ with a fixed length $|\mathbf{k}'| = k_0$. In this respect, algorithm (11) is similar to the two-dimensional algorithm mentioned above. When $|\mathbf{p}| < 2k_0$, the set ∂M represents a circumference that is determined by all of the vectors $\mathbf{k}'$ forming the given $\mathbf{p}$ (Fig. 2); this set degenerates into a point at $|\mathbf{p}| = 2k_0$. Thus, in the case of $|\mathbf{p}| < 2k_0$, the corresponding contribution to the estimate of $\tilde{v}(-\mathbf{p})$ is formed by the redundant scattering data. In the case of $|\mathbf{p}| > 2k_0$, the term Z_2 does not participate in the formation of the components of $\tilde{v}(-\mathbf{p})$, because conditions (7) cannot be satisfied due to $|\mathbf{k}'| = k_0$.

The term Z_1 is most difficult to calculate. It requires integration of the nonlinear combination $\bar{\partial}H(\mathbf{k}', \mathbf{p})$ of the functions $H(\mathbf{k}', \mathbf{p})$ over the surface of all the complex vectors $\mathbf{k}' \in M$ for a given $\mathbf{p}$ and, in addition, requires knowledge of $H(\mathbf{k}', \mathbf{p})$ for $\mathbf{k}' \in \mathbb{C}^3$. Therefore, in making a numerical estimate of $\tilde{v}(-\mathbf{p})$, it is desirable to ignore the surface integral Z_1 because of the cumbersome calculations and the instability of the procedure used for determining $H(\mathbf{k}', \mathbf{p})$ (which was mentioned in discussing asymptotic algorithm (9)). For these reasons, we tried to reconstruct the scatterer from only $H(\mathbf{k}_*, \mathbf{p})$ and the jump $H^+(\mathbf{k}', \mathbf{p}) - H^-(\mathbf{k}', \mathbf{p})$ that appears in the contour integral Z_2, by analogy with the aforementioned simplified algorithm in the two-dimensional case [10, 14]. However, the term Z_1 completely determines the estimate of the components of $\tilde{v}(-\mathbf{p})$ for $|\mathbf{p}| > 2k_0$ (together with the term $H(\mathbf{k}_*, \mathbf{p})$ in the case of $\mathrm{Im}\mathbf{k}_* \neq 0$). Moreover, when $|\mathbf{p}| \le 2k_0$ (even if the scatterer is such that $\tilde{v}(-\mathbf{p}) \equiv 0$ for $|\mathbf{p}| > 2k_0$), Z_1 makes a contribution to $\tilde{v}(-\mathbf{p})$ that is comparable to the contribution from the contour integral Z_2. Therefore, neglect of the term Z_1 always leads to some distortion of the scatterer estimate. Nevertheless, in some cases, this distortion proves to be relatively small, as is illustrated below by numerical simulation.

Thus, in the three-dimensional problem, unlike in the two-dimensional one, knowledge of only the limiting values of $H^{\pm}(\mathbf{k}', \mathbf{p})$, where $\mathbf{k}' \in \mathbb{R}^3$, does not allow one to obtain a rigorous reconstruction of a scatterer producing a multiple scattering of waves. However, the instability in calculating $H(\mathbf{k}, \mathbf{p})$ for $\mathbf{k} \in \mathbb{C}^3$ is likely to be a particular drawback of the specific procedure rather than a general feature of the three-dimensional inverse scattering problem.

RESULTS OF NUMERICAL SIMULATION

The direct scattering problem (simulation of scattering data) has a rigorous analytical solution for a very small number of scatterers. They include homogeneous scatterers in the form of a sphere, an ellipsoid, and a rectangular parallelepiped. At the same time, the numerical solution of the direct problem for three-dimensional scatterers of arbitrary shape and not overly small wave size involves such difficulties as either the inversion of large-dimension matrices or the provision for the convergence of the iterative solution. These problems are complicated and require special consideration. Therefore, at the very first step, we tested the efficiency of algorithm (11) in application to the reconstruction of a spherically symmetric scatterer in the form of a homogeneous sphere of radius a with a sound velocity c in it; c was assumed to be different from the background sound velocity c_0. In this case, the scattering amplitude $f(\mathbf{k}, \boldsymbol{l})$ can be calculated analytically (see [21], Vol. II, pp. 452–455), which considerably simplifies the numerical simulation of the algorithm. In addition, from Eq. (3) it follows that, for a three-dimensional spherically symmetric scatterer, $h^+(\mathbf{k}, \boldsymbol{l}) \equiv h^-(\mathbf{k}, \boldsymbol{l})$, i.e., $H^+(\mathbf{k}, \mathbf{p}) \equiv H^-(\mathbf{k}, \mathbf{p})$, and, hence, $Z_2 \equiv 0$. We considered refractive scatterers of different strengths determined by the wave size of the scatterer $2a/\lambda_0$ and by the relative contrast $\Delta c/c_0$ of the velocity inhomogeneity,

where $\Delta c \equiv c - c_0$. The additional phase shift of the wave due to its propagation along the diameter of the scatterer is $\Delta\psi \cong |k - k_0|2a = 2k_0 a \dfrac{\Delta c}{c_0}\dfrac{1}{1 + \Delta c/c_0}$, where $k_0 = \omega/c_0$ and $k = \omega/c$.

At the stage of computer simulation, the term Z_1 (the surface integral) was not considered, which simplified the numerical realization of the algorithm and simultaneously provided for the robustness of the solution. However, in this approximation, the multiple scattering processes are not completely taken into account in the reconstruction; as a result, the solution, i.e., the estimate of the spatial spectrum $\hat{\tilde{v}}(-\mathbf{p})$ and the corresponding scatterer function $\hat{v}(\mathbf{r})$, ceases to be rigorous. We assumed that $\mathrm{Im}\,\mathbf{k}_* \longrightarrow 0$, and, hence, in the approximate version of the algorithm that was realized, the spectrum $\tilde{v}(-\mathbf{p})$ was estimated on the basis of the limiting values $H^{\pm}$ of the generalized scattering amplitude for only the spatial components with $|\mathbf{p}| \le 2k_0$:

$$\hat{\tilde{v}}(-\mathbf{p}) \approx H^{\pm}(\mathbf{k}_*, \mathbf{p}). \qquad (14)$$

Therefore, the result of the reconstruction of $\hat{v}(\mathbf{r})$ was compared with the function $v_{\mathrm{cut}}(\mathbf{r})$, whose spatial spectrum coincided with the spectrum of the true scatterer $v(\mathbf{r})$ inside the sphere of radius $2k_0$ and was equal to zero outside this sphere. Relation (14) is similar to relation (9) for the asymptotic algorithm with $\mathbf{k}_I \longrightarrow 0$, i.e., without passing to the limit $|\mathbf{k}| \longrightarrow \infty$.

In the numerical simulation, we used the values $c_0 = 1500$ m/s and $\lambda_0 = 3 \times 10^{-3}$ m, which correspond to a typical situation of medical diagnosis. Because the nonlinear relation between the generalized scattering amplitude and the classical one takes into account multiple scattering, the resulting estimate $\hat{v}(\mathbf{r})$ proves to be more accurate than the estimate $\hat{v}_{\mathrm{Born}}(r)$ in the first Born approximation, in which $\hat{\tilde{v}}_{\mathrm{Born}}(-\mathbf{p} = \boldsymbol{l} - \mathbf{k}) = f(\mathbf{k}, \boldsymbol{l})$, where $\mathbf{k}, \boldsymbol{l} \in \mathbb{R}^3$. This can be clearly illustrated by the situation with purely refractive scatterers described by a real function $v(\mathbf{r})$. In the case of weak (Born) scatterers, for which the multiple scattering processes are insignificant, the generalized scattering amplitude coincides with the classical one and the two estimates coincide: $\hat{v}(\mathbf{r}) = \hat{v}_{\mathrm{Born}}(\mathbf{r})$. They differ from the true function $v(\mathbf{r})$ only because of the high-frequency components of $\tilde{v}(-\mathbf{p})$, which were taken to be equal to zero for $|\mathbf{p}| > 2k_0$ in the reconstruction process. As soon as the scatterer ceases to be weak, a false imaginary part $\mathrm{Im}\,\hat{v}_{\mathrm{born}}(\mathbf{r})$ appears in the Born estimate, and this part increases with growing scatterer strength. When the phase shift reaches $\Delta\psi \approx \pi/4$, the amplitudes of the functions $\mathrm{Re}\,\hat{v}_{\mathrm{born}}(\mathbf{r})$ and $\mathrm{Im}\,\hat{v}_{\mathrm{born}}(\mathbf{r})$ become equal in magnitude (Fig. 3a: $a = 1.2\lambda_0$ and $\Delta c/c_0 \approx -0.050$). At the same time, a similar false imaginary part $\mathrm{Im}\,\hat{v}(\mathbf{r})$ caused by the neglect of the term Z_1 in Eq. (11) becomes only slightly more noticeable, and then only for the scatterers that cause additional phase shifts greater than $\Delta\psi \approx 3\pi/4$, i.e., that are close to strong scatterers. For $\Delta\psi \le \pi/2$, the estimate of the spectrum $\hat{\tilde{v}}(-\mathbf{p})$ and the corresponding estimate of the scatterer $\hat{v}(\mathbf{r})$ provide a better reconstruction of the function $v_{\mathrm{cut}}(\mathbf{r})$ than that given by the estimates $\hat{\tilde{v}}_{\mathrm{Born}}(-\mathbf{p})$ and $\hat{v}_{\mathrm{Born}}(\mathbf{r})$ (Figs. 3a and 3b, for which $a = 1.2\lambda_0$, $\Delta c/c_0 \approx -0.085$, and $\Delta\psi \approx 3\pi/8$). However, when $\Delta\psi$ is about $\pi/2$ or greater, the distortions introduced into the estimate of the spatial spectrum $\hat{\tilde{v}}$ and, hence, into the estimate $\hat{v}(\mathbf{r})$ become more considerable and manifest themselves as an increase in the relative oscillation amplitude (Fig. 3c: $a = 1.2\lambda_0$, $\Delta c/c_0 \approx -0.116$, and $\Delta\psi \approx \pi/2$), thus testifying to the growing influence of the neglected term Z_1.

It should be noted that the character of the oscillations exhibited by the function $v_{\mathrm{cut}}(\mathbf{r})$ and the estimate $\hat{v}(\mathbf{r})$ because of the limitation of their spatial spectrum by components $|\mathbf{p}| \le 2k_0$ depends on the specific values of the parameters a and $\Delta c/c_0$. For example, Figs. 3a and 4 represent the results for different scatterers that cause the same phase shift $\Delta\psi \approx \pi/4$. The fluctuation of the function $\hat{v}(\mathbf{r})$ in comparison with the true scatterer function $v(\mathbf{r})$ is positive at the center ($\mathbf{r} = 0$) at $a = \lambda_0$, $\Delta c/c_0 \approx -0.059$ (Fig. 4) and negative at $a = 1.2\lambda_0$, $\Delta c/c_0 \approx -0.050$ (Fig. 3a); it may also be almost absent (for example, at $a = 1.18\lambda_0$, $\Delta c/c_0 \approx -0.050$). On the other hand, the error observed in the scatterer reconstruction is determined by the value of $\Delta\psi$ rather than by the size of the scatterer and its contrast separately. This conclusion is confirmed by the comparison between scatterers close in strength ($\Delta\psi \approx \pi/2$) but different in size (Fig. 3c and Fig. 5a, for which $a = 2\lambda_0$ and $\Delta c/c_0 \approx -0.059$) and opposite in the sign of contrast (Fig. 5b: $a = 1.2\lambda_0$ and $\Delta c/c_0 \approx 0.116$).

Finally, it should be noted that the resulting estimate $\hat{v}$ proved to be sufficiently robust against random noise that is present in the data. To study the noise robustness, we combined the scattering data $f(\mathbf{k}, \mathbf{l})$ with a normally distributed random noise characterized by the standard amplitude deviation $\sigma_{\mathrm{ns}} = \nu_{\mathrm{ns}}\bar{f}$, where $\bar{f} \equiv \sqrt{\dfrac{1}{(4\pi)^2}\int_0^{4\pi} d\Omega_{\mathbf{k}} \int_0^{4\pi} d\Omega_{\boldsymbol{l}} |f(\mathbf{k}, \boldsymbol{l})|^2}$ is the rms value of the scattering data (the averaging is performed over the directions of the vectors $\mathbf{k}, \boldsymbol{l} \in \mathbb{R}^3$; $d\Omega_{\mathbf{k}}$ and $d\Omega_{\boldsymbol{l}}$ are the corresponding elementary solid angles) and ν_{ns} is the background noise coefficient. Here, σ_{ns} is the deviation for the real and imaginary parts of noise separately; i.e., $\sqrt{2}\,\sigma_{\mathrm{ns}}$ is the total standard deviation for the noise as a complex

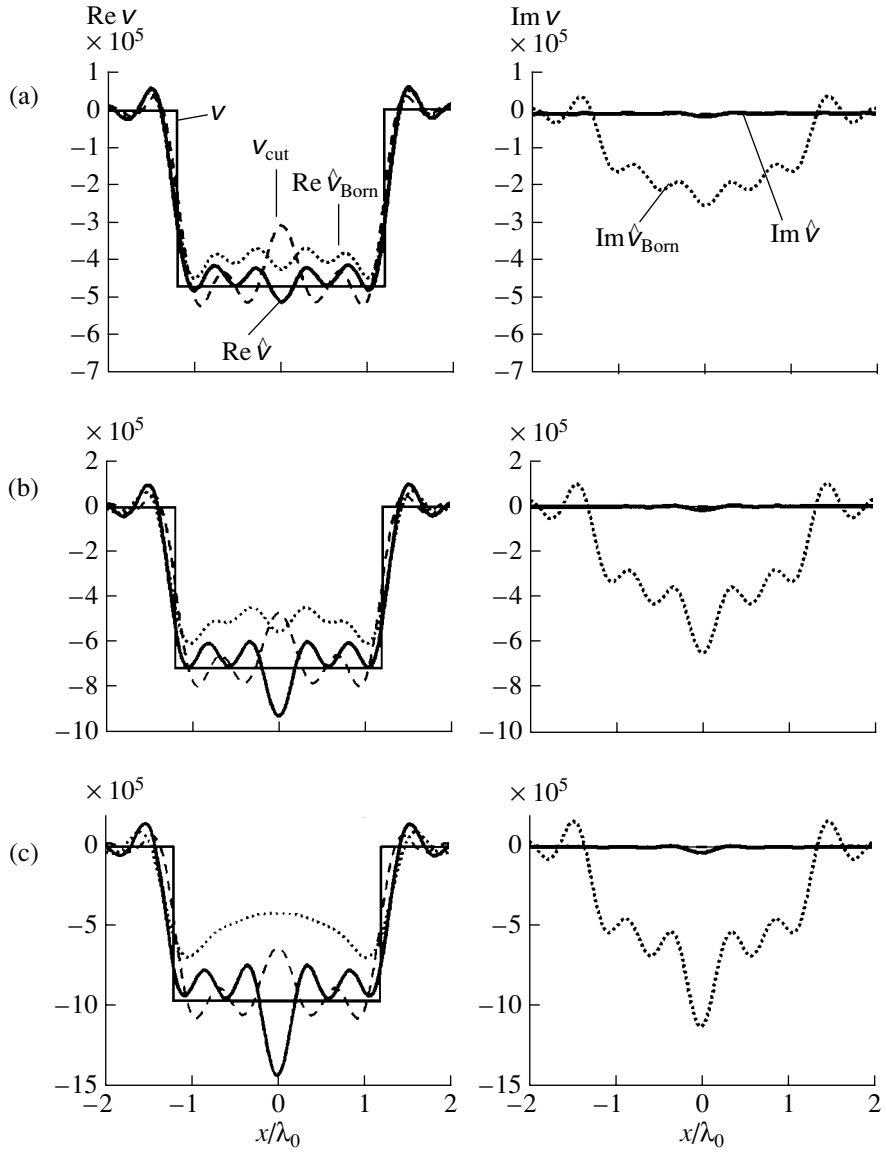

Fig. 3. Central sections of the real (left) and imaginary (right) parts of refractive scatterers in the form of spheres with the same radius $a = 1.2\lambda_0$; the sound velocity contrast $\Delta c/c_0 \approx$ (a) –0.050, (b) –0.085, and (c) –0.116; and the additional phase shift $\Delta\psi \approx$ (a) $\pi/4$, (b) $3\pi/8$, and (c) $\pi/2$: true scatterer v (thin solid line); scatterer form v_{cut} with the frequency band of its spatial spectrum being restricted by a sphere of radius $2k_0$ (dashed line); scatterer estimate in the absence of noise with allowance for multiple scattering, $\hat{v}$ (thick solid line); and scatterer estimate in the Born approximation, $\hat{v}_{\text{Born}}$ (dotted line).

quantity. In this case, the deviation of the spatial spectrum $\hat{\tilde{v}}_{\text{ns}}(-\mathbf{p})$ in the presence of noise in comparison with the noise-free estimate $\hat{\tilde{v}}(-\mathbf{p})$ is characterized by the relative rms error $\mu \equiv \sqrt{\int_{|\mathbf{p}|\le 2k_0} \left|\hat{\tilde{v}}_{\text{ns}}(-\mathbf{p}) - \hat{\tilde{v}}(-\mathbf{p})\right|^2 d\mathbf{p} \Big/ \int_{|\mathbf{p}|\le 2k_0} \left|\hat{\tilde{v}}(-\mathbf{p})\right|^2 d\mathbf{p}}$. For a scatterer causing a phase shift $\Delta\psi \le \pi/2$, the error in the reconstruction does not exceed $\mu \cong 0.03$–0.04 at $\nu_{\text{ns}} = 0.03$ and $\mu \cong 0.10$–0.12 at $\nu_{\text{ns}} = 0.09$. Hence, the relative error in the scatterer estimate only slightly exceeds the relative error in the scattering data.

It should be taken into account that, in these numerical simulations, the noise introduced in all the data corresponding to a single value of the scattering angle (the angle between $\mathbf{k}$ and $\boldsymbol{l}$) was the same. Hence, the redundancy of the three-dimensional problem was not used in the reconstruction, and such a correlated noise caused an increase in the error μ in comparison with the case of an uncorrelated noise. At the same time, in the presence of uncorrelated measurement errors, the dimensional redundancy of the data $f(\mathbf{k}, \boldsymbol{l})$ $(\mathbf{k}, \boldsymbol{l} \in \mathbb{R}^3)$ in the three-dimensional problem leads to an increase in the noise robustness of the solution. Indeed, for one

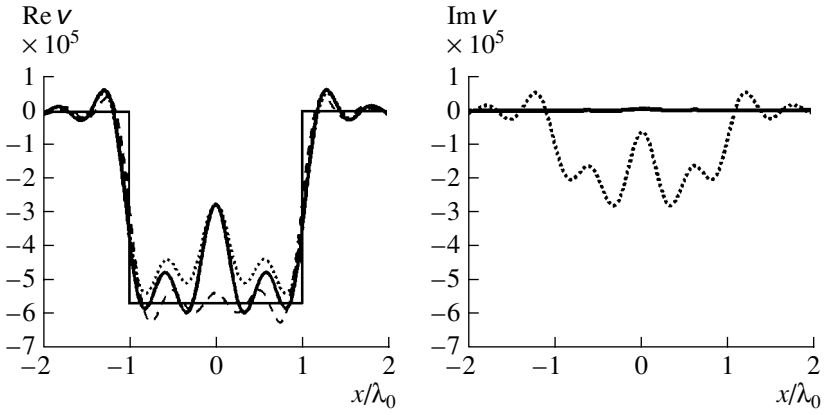

Fig. 4. Central sections of the real (left) and imaginary (right) parts of a refractive scatterer in the form of a sphere with radius $a = \lambda_0$, sound velocity contrast $\Delta c/c_0 \approx -0.059$, and phase shift $\Delta\psi \approx \pi/4$. The line notation is the same as in Fig. 3.

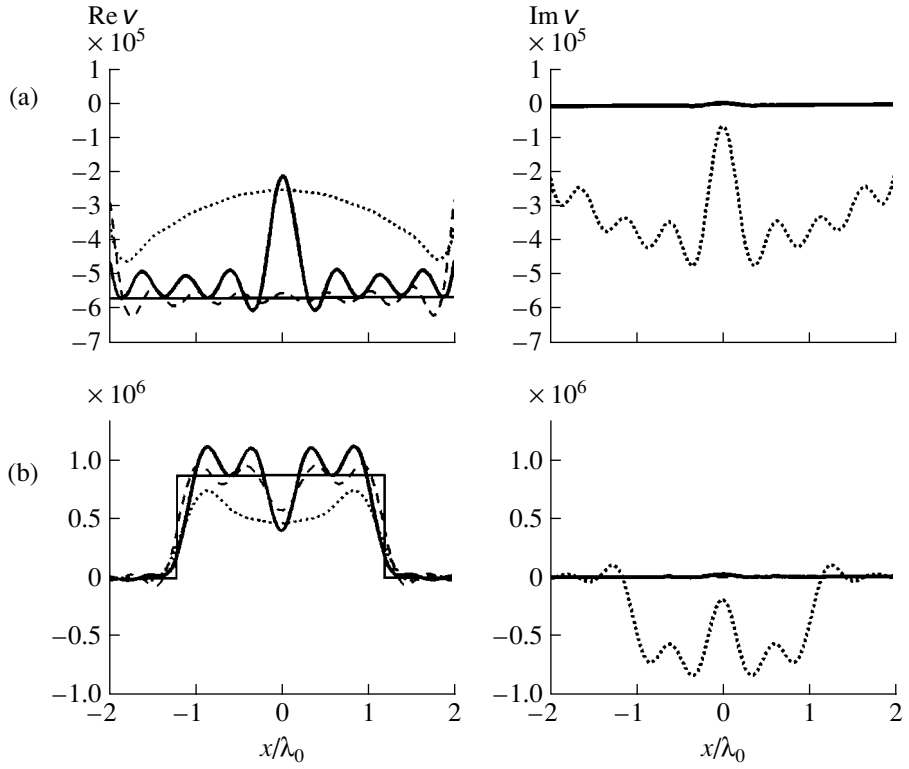

Fig. 5. Central sections of the real (left) and imaginary (right) parts of refractive scatterers in the form of spheres with radius a = (a) $2\lambda_0$ and (b) $1.2\lambda_0$ and with sound velocity contrast $\Delta c/c_0 \approx$ (a) –0.059 and (b) 0.116. The scatterers produce the same phase shift $\Delta\psi \approx \pi/2$. The line notation is the same as in Fig. 3.

vector $\mathbf{p} = \mathbf{k} - \boldsymbol{l}$, there is a corresponding continuum of pairs of vectors $\mathbf{k}, \boldsymbol{l} \in \mathbb{R}^3$ that differ in their directions. Namely, the end of the vector $\mathbf{k}$ can rotate in a circle in the plane perpendicular to the vector $\mathbf{p}$. In this case, the angular distance between the neighboring independent discretized directions is equal to the average lobe width of the scattering pattern; i.e., $\overline{\Delta\varphi} \cong \dfrac{\lambda_0/2}{L/2} = \dfrac{\lambda_0}{L} = \dfrac{2\pi}{k_0 L}$. By estimating the number of independent directions of the vector $\mathbf{k}$ in this way, we obtain $\cong 2\pi/\overline{\Delta\varphi} \cong k_0 L$. On the other hand, in the case of correlated measurement errors, the relative error in reconstructing a middle-strength scatterer is close to the rms relative error in the scattering data. However, in the case of estimating the scatterer by using the data for all of the possible directions of the vector $\mathbf{k}$ that lead to the same $\mathbf{p}$ but that have an uncorrelated measurement error, the error in the reconstruction of middle-strength scatterers is smaller

by a factor of $\cong\sqrt{k_0 L}$ in comparison with the case of correlated errors.

Thus, the estimate obtained with the approximate version of the algorithm proves to be acceptable for middle-strength scatterers that cause phase shifts smaller than $\pi/2$. For stronger scatterers, to obtain an adequate estimate, it is necessary to take into account the rejected integral term in algorithm (11) or to perform the passage to the limit in asymptotic algorithm (9).

ACKNOWLEDGMENTS

This work was supported by a grant from the President of the Russian Federation (grant no. NSh-1575.003.2) and by the Russian Foundation for Basic Research (project no. 04-02-16043).

REFERENCES

1. S. A. Johnson, Y. Zhou, M. L. Tracy, *et al.*, Ultrason. Imaging **6** (4), 103 (1984).
2. V. A. Burov, O. D. Rumyantseva, and A. V. Saskovets, Vestn. Mosk. Univ., Ser. 3: Fiz., Astron. **35** (6), 61 (1994) [Moscow Univ. Phys. Bull. **49** (6), 47 (1994)].
3. S. J. Norton, J. Acoust. Soc. Am. **106**, 2653 (1999).
4. L. D. Faddeev, Itogi Nauki Tekh., Ser.: Sovrem. Probl. Mat. **3**, 93 (1974) [J. Sov. Math. **5**, 334 (1976)].
5. R. G. Newton, *Inverse Shrödinger Scattering in Three Dimensions* (Springer, Berlin, 1989), p. 170.
6. R. G. Novikov and G. M. Henkin, Usp. Mat. Nauk **42** (3), 93 (1987) [Russ. Math. Surv. **42**, 109 (1987)].
7. K. Chadan and P. C. Sabatier, *Inverse Problems in Quantum Scattering Theory* (Springer, Berlin, 1977; Mir, Moscow, 1980).
8. L. D. Faddeev, Dokl. Akad. Nauk SSSR **165**, 514 (1965) [Sov. Phys. Dokl. **10**, 1033 (1965)].
9. V. A. Burov and O. D. Rumyantseva, Akust. Zh. **38**, 413 (1992) [Sov. Phys. Acoust. **38**, 226 (1992)].
10. R. G. Novikov, Teor. Mat. Fiz. **66** (2), 234 (1986) [Theor. Math. Phys. **66** (2), 154 (1986)].
11. P. G. Grinevich and S. V. Manakov, Funkt. Anal. Pril. **20** (2), 14 (1986) [Funct. Anal. Appl. **20** (2), 94 (1986)].
12. V. A. Burov, S. A. Morozov, and O. D. Rumyantseva, Acoust. Imaging **26**, 231 (2002).
13. V. A. Burov, I. M. Grishina, O. I. Lapshenkina, *et al.*, Akust. Zh. **49**, 738 (2003) [Acoust. Phys. **49**, 627 (2003)].
14. R. G. Novikov, J. Funkt. Anal. **103**, 409 (1992).
15. V. A. Burov and O. D. Rumiantseva, in *Ill-Posed Problems in Natural Sciences* (TVP, Moscow, 1992), pp. 463–471.
16. V. A. Burov and O. D. Rumyantseva, Akust. Zh. **49**, 590 (2003) [Acoust. Phys. **49**, 496 (2003)].
17. R. G. Novikov, Funkt. Anal. Pril. **22** (4), 11 (1988) [Funct. Anal. Appl. **22**, 263 (1988)].
18. V. A. Burov and O. D. Rumiantseva, Acoust. Imaging **21**, 101 (1995).
19. V. A. Burov, O. D. Rumyantseva, and T. V. Suchkova, in *Waves and Diffraction-90: Proceedings of X All-Union Symposium on Wave Diffraction and Propagation, Vinnitsa, 1990* (Fizicheskoe Obshchestvo, Moscow, 1990), Vol. 3, pp. 275–278.
20. A. Nachman, Ann. Math. **128**, 531 (1988).
21. P. M. Morse and H. Feshbach, *Methods of Theoretical Physics* (McGraw-Hill, New York, 1953; Inostrannaya Literatura, Moscow, 1958 and 1960), Vols. 1 and 2.

Translated by E. Golyamina

Acoustical Physics, Vol. 51, No. 4, 2005, pp. 376–384. Translated from Akusticheskiĭ Zhurnal, Vol. 51, No. 4, 2005, pp. 447–455.

Reconstruction of the In-Depth Temperature Distribution for Biological Objects by Linear Phased Arrays

A. A. Anosov* and L. R. Gavrilov**

** ELDIS Research Center for Electronic Diagnostic Systems, Russian Academy of Sciences, Starosadskiĭ per. 8, Moscow, 101000 Russia*

*** Andreev Acoustics Institute, Russian Academy of Sciences, ul. Shvernika 4, Moscow, 117036 Russia*

e-mail: anosov@hotmail.ru

Received December 2, 2003

Abstract—The feasibility of the reconstruction of two-dimensional temperature distributions in biological objects with the use of linear phased arrays is investigated theoretically with allowances made for the actual array directivity patterns and without using the data on the absorption coefficient. The method provides an opportunity to reconstruct the temperature distribution in the region under investigation with an accuracy of about 0.5 K from the data of 1.5-min-long measurements when the temperature of the region of interest is raised by 5–10 K. © *2005 Pleiades Publishing, Inc.*

An important characteristic of a human body is the spatial distribution of the in-depth temperature. Temperature monitoring is necessary for various therapeutic procedures, such as, for example, hyperthermia in oncology. In this procedure, it is important to heat a tumor up to a certain optimal temperature, for example, to 43–44°C, and, then, to maintain the temperature for several or several tens of minutes. Monitoring is effective if it is possible to measure the temperature at a depth of 3–8 cm in a volume of about 1 cm^3 with an accuracy of about 0.5 K. For such measurements it is desirable to use nondestructive and noninvasive techniques, for example, to receive the thermal acoustic radiation from a biological object in the ultrasonic frequency range.

In the previous publications [1, 2], the problem of reconstructing the in-depth temperature of a biological object was theoretically investigated and the reconstruction parameters were evaluated. However, in solving this problem, the directivity patterns of receivers were approximated by beams and the ultrasonic absorption coefficient in a biological object was assumed to be known, which is not always possible. Experiments on the reconstruction (using the indicated assumptions) of the in-depth temperature in glycerol and in a human hand were carried out in [2]. The authors of [3–5] theoretically and experimentally reconstructed the position of a heat source within model objects, in some cases, with the use of focused receivers [4, 5]. However, the temperature parameters of the distribution were not evaluated. The authors of [2, 6–8] theoretically and experimentally investigated the abilities of the correlation detection of thermal acoustic radiation in determining the internal temperature of a biological object. In this case, the accuracy of the reconstruction was not estimated.

The purpose of the present study is to theoretically investigate the feasibility of the reconstruction of a two-dimensional temperature distribution with the use of linear phased arrays by taking into account the actual directivity patterns of the arrays and by assuming that data on the absorption coefficient are absent. We propose to determine the form of the temperature distribution in two mutually perpendicular directions from the results of electronic scanning of a biological object by two phased arrays and to reconstruct the absorption coefficient in the medium from the difference between the signals measured by these arrays. Then, using the information on the form of the distribution and on the absorption coefficient, we propose to calculate the amplitude of the temperature peak and, thus, to completely reconstruct the temperature distribution.

Let us consider the measurement scheme (Fig. 1) proposed for the solution of a two-dimensional problem. (*1*) A biological object is located within the right angle formed by two rays, 0*x* and 0*z*. We assume that ultrasonic absorption within the biological object is constant and determined by the absorption coefficient α_0. The value of α depends on the frequency of the received signal. We assume that the measurement of thermal acoustic radiation is performed in soft tissue in a frequency range of about 1 MHz and that the amplitude absorption coefficient is $\alpha \approx 0.1$ cm^{-1} [9]. We also assume that the attenuation coefficient α is numerically equal to α_0, since the contribution of scattering to attenuation in soft tissues (usually no greater than 10–15%

[9]) can be ignored. Note that the attenuation and absorption of ultrasound in soft tissues of an organism may vary with temperature. However, in [10] (where the effect of 4-MHz ultrasound on fresh samples of dog's muscle, liver, and kidney tissues was studied), it was shown that, in the temperature range from 30 to 50°C (which is of interest to us), the attenuation and absorption coefficients of tissues remained virtually constant. It is necessary to note that an actual biological object containing different tissues is inhomogeneous in absorption. However, if we restrict our consideration to soft tissues [9], in which variations of the absorption coefficient are small, we can consider the region under investigation to be inhomogeneous in absorption.

Let a heat source created in the hyperthermia process be located within (*2*) a rectangular region under investigation (Fig. 1): $x \in [x_1 = 2.0\ \text{cm}, x_2 = 8.0\ \text{cm}]$, $z \in [z_1 = 0, z_2 = 6.0\ \text{cm}]$. We assume that the temperature distribution $T(x, z)$ produced by the source in the region under investigation is determined by the product of two functions, $f(x)$ and $g(z)$, each of them depending on only one coordinate and normalized to its own maximum value, so that $\max f(x) = \max g(z) = 1$:

$$T(x, z) = \Delta T_{\max} f(x) g(z) + T_0, \qquad (1)$$

where T_0 is the temperature of the biological object beyond the region under investigation, which is constant and known, and $\Delta T_{\max}$ is the maximum temperature increment in the heated region in comparison with T_0; below, this quantity will be called the temperature peak. The peak coordinates are $x_{\max}$ and $z_{\max}$. Contour *3* in Fig. 1 indicates the heated region, where the temperature peak is located. To reconstruct the temperature, it is necessary to determine the form of the distribution $f(x)g(z)$ and the value of the temperature peak $\Delta T_{\max}$, i.e., to determine the temperature increment $\Delta T(x, z) = \Delta T_{\max} f(x) g(z)$. Since we consider a two-dimensional problem, we assume that we have a cylindrical heat source extended along the axis perpendicular to the $x0z$ plane.

The receivers of thermal acoustic radiation are two linear phased arrays, LPA_1 and LPA_2, consisting of 33 rectangular elements 16.5 mm in length and 1.5 mm in width. The distance between the element centers is 1.6 mm. The central reception frequency is 1 MHz, and the passband is about 0.8 MHz. LPA_1 is placed 2 cm away from the boundary of the biological object (from the x axis), and LPA_2 is positioned at the boundary of the biological object (on the z axis). Due to the electronic scanning (indicated by arrows in Fig. 1), each of the arrays simultaneously receives thermal acoustic radiation with the help of thirteen directivity patterns $A_1(x, z), \ldots, A_{13}(x, z)$ (two directivity patterns are indicated in Fig. 1 by the gray color). The calculation of directivity patterns was performed by the method

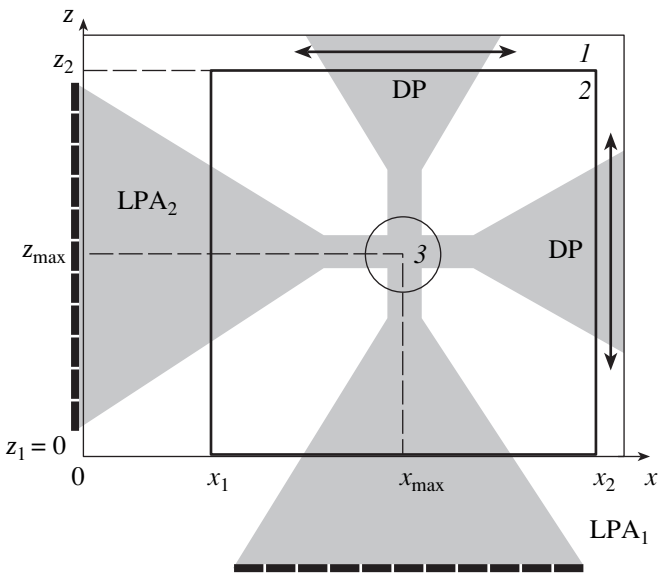

Fig. 1. Measurement scheme: (*1*) biological object, (*2*) the region under investigation (x_1, x_2, z_1, and z_2 are the region boundaries), and (*3*) the heated region; LPA_1 and LPA_2 are linear phased arrays, and DP are the directivity patterns (the arrows indicate the direction of scanning).

described in [11]. The map of the contours of intensity distributions of signals received by LPA_1 is shown in Fig. 2. The numbers from 1 to 13 correspond to the numbers of the directivity patterns. For each intensity distribution, three level lines corresponding to 0.75, 0.5, and 0.25 of the maximum value at the focus are shown. The central distribution is the narrowest and has the highest value in comparison with other distributions. The extreme 12^{th} and 13^{th} distributions are wider, and their maximum values are equal to 0.73 of the maximum of the first distribution. The z_A coordinates of all focuses are approximately equal, namely, $z_A \approx 40$ cm. The x_A coordinates of the focuses vary from 3.2 to 6.8 cm at a step of 0.3 cm. In addition, from Fig. 2 one can see that the distribution widths at a level of 0.25 are about 0.3 cm. The side lobes of the given distributions are small in value and mainly lie beyond the region under investigation. One can also see that the directivity patterns provide an opportunity to scan over the whole tested region of the biological object along the x axis, and, at the same time, that the intersection regions of the directivity patterns (at least, at the level of 0.25) are insignificant. This allows us to assume that we obtain 13 independent measurement results with the help of a single phased array. Note that LPA_2 allows us to scan over the region under investigation along the z axis. In total, we have 26 independent measurements.

If the received signal is expressed in degrees, the acoustic brightness temperature is measured [12]. The acoustic brightness temperature by definition is the temperature of an acoustic blackbody absorbing all

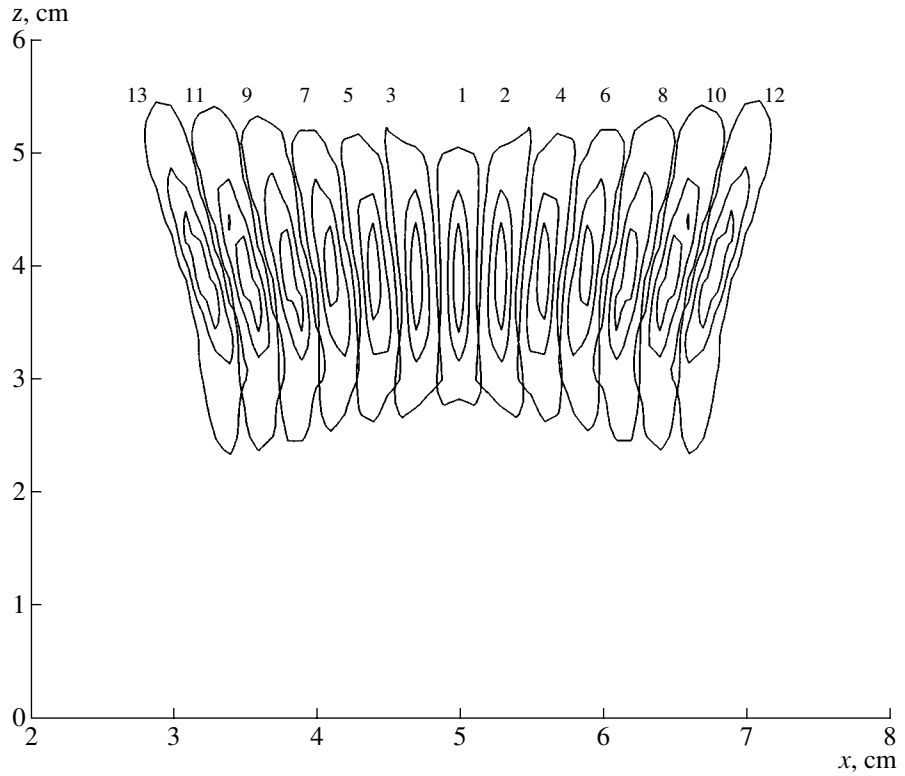

Fig. 2. Contour map of the intensity distribution of the received signals for LPA_1; numbers 1, …, 13 are the numbers of directivity patterns.

acoustic radiation incident upon it. It is expedient to measure the increment of the acoustic brightness temperature ΔT_A, i.e., the difference between the acoustic brightness temperature of the region under investigation and all other parts of the biological object: $\Delta T_A = T_A - T_0$. This quantity, with allowance for Eq. (1), can be expressed in the form [12–14]

$$\Delta T_A(i) = \Delta T_{\max} 2\alpha_0 \int_{z_1}^{z_2} dz \exp(-2\alpha_0 z) g(z) \times \int_{x_1}^{x_2} dx A_i(x, z) f(x), \quad i = 1, \ldots, 13; \tag{2a}$$

$$\Delta T_A(i) = \Delta T_{\max} 2\alpha_0 \int_{x_1}^{x_2} dx \exp(-2\alpha_0 x) f(x) \times \int_{z_1}^{z_2} dz A_i(x, z) g(z), \quad i = 14, \ldots, 26, \tag{2b}$$

where $A_i(x, z)$ in Eqs. (2a) and (2b) represent the directivity patterns of LPA_1 and LPA_2, respectively. Consider the contribution of the directivity patterns to the acoustic brightness temperature. The directivity patterns have different transverse dimensions and peaks. For example, the peak of A_1 is higher than that of A_{13} (see above), but A_{13} is wider. Nevertheless, for all directivity patterns $A_1(x, z)$, …, $A_{13}(x, z)$, the integrals $\int_0^{+\infty} dz \int_{-\infty}^{+\infty} dx A_i(x, z)$ are equal.

The increments of the acoustic brightness temperatures $\Delta T_A(i)$ ($i = 1, \ldots, 26$) in Eqs. (2) are measurable quantities. Using them, it is necessary to obtain the desired functions $f(x)$ and $g(z)$. For this purpose, we compare the transverse dimensions of the directivity patterns (0.3 cm), the region under investigation (6 cm), and the required spatial resolution (1 cm, see above). The transverse dimension of the directivity patterns is much smaller. If, for LPA_1 (or LPA_2), we approximate the directivity pattern by a beam perpendicular to the x (or z) axis and passing through the point $x_{Ai}(z_{Ai})$ of the focus of the ith directivity pattern, Eqs. (2) take on the form

$$\Delta T_A(i) \approx \Delta T_{\max} 2\alpha_0 f(x_{Ai}) \int_{z_1}^{z_2} dz \exp(-2\alpha_0 z) g(z), \quad i = 1, \ldots, 13, \text{ for } LPA_1; \tag{3a}$$

$$\Delta T_A(i) \approx \Delta T_{\max} 2\alpha_0 g(z_{Ai}) \int_{x_1}^{x_2} dx \exp(-2\alpha_0 x) f(x), \quad i = 14, \ldots, 26, \text{ for } LPA_2. \tag{3b}$$

As one can see from Eqs. (3), the measured signals are functions of the focus coordinate x_{Ai} (for LPA_1) or z_{Ai} (for LPA_2). Hence, for LPA_1 we have the dependence $\Delta T_A(i) \sim f(x_{Ai})$, and, for LPA_2, $\Delta T_A(i) \sim g(z_{Ai})$. Here,

$$f(x) = \Delta T_A(x)/\max_{\forall x}\Delta T(x), \quad i = 1, \ldots, 13; \quad (4a)$$

$$g(z) = \Delta T_A(z)/\max_{\forall z}\Delta T(z), \quad i = 14, \ldots, 26, \quad (4b)$$

where $\Delta T_A(x)$ and $\Delta T_A(z)$ are the functions approximating the sets of acoustic brightness temperatures $\Delta T_A(i)$ with $i = 1, \ldots, 13$ and $\Delta T_A(i)$ with $i = 14, \ldots, 26$, respectively. From Eqs. (3) and (4), we obtain an equation for the determination of the absorption coefficient α_0:

$$\int_{z_1}^{z_2} dz \exp(-2\alpha_0 z)\Delta T_A(z) - \int_{x_1}^{x_2} dx \exp(-2\alpha_0 x)\Delta T_A(x) = 0. \quad (5)$$

The possibility of the determination of the absorption coefficient by Eq. (5) is connected with the fact that the value of a thermal acoustic radiation signal propagating in an absorbing medium from a heated region to a receiver depends on the path length. The distance from the thermal acoustic radiation source to LPA_1 is smaller than that from the source to LPA_2 (see Fig. 1). Therefore, the increment of acoustic brightness temperature measured by LPA_1 must be greater. The difference of the measured increments and the information on the position of the temperature peak provides an opportunity to determine the absorption coefficient. In this connection, it is necessary to note the limitation for the temperature distributions symmetric with respect to x and z. It is necessary that the path lengths from the temperature peak in the biological object to LPA_1 and to LPA_2 be different.

Knowing α_0, $f(x)$, and $g(z)$, with the help of Eqs. (2), it is possible to calculate ΔT_{max} and, thus, to completely determine the desired temperature distribution $\Delta T(x, z)$.

The simulation was conducted in several stages.

(i) To preset the temperature distribution, we considered a symmetric distribution

$$\Delta T = 1.23 \times 10^{-2}\Delta T_{max}\exp[-(x - x_{max})^2 - (z - z_{max})^2/2d_1^2](x - x_1)(x - x_2)(z - z_1)(z - z_2) \quad (6a)$$

and an asymmetric distribution

$$\Delta T = 2.97 \times 10^{-2}\Delta T_{max} \times \exp[(x - x_2 + z - z_2)/d_2] \times (x - x_1)(x - x_2)(z - z_1)(z - z_2). \quad (6b)$$

In the case of the symmetric distribution given by Eq. (6a), the peak temperature value was reached at the point with the coordinates $x_{max} = 5.0$ cm, $z_{max} = 3.0$ cm; in the case of the asymmetric distribution given by Eq. (6b), at the point with $x_{max} = 5.7$ cm, $z_{max} = 3.7$ cm. Four factors after the exponent are introduced to reduce to zero the temperature values at the boundaries of the region under study in order to provide for the continuity of temperature variation. The dimensional coefficients 1.23×10^{-2} cm^{-4} and 2.97×10^{-2} cm^{-4} are introduced for the distribution peak as equal to ΔT_{max}. The spatial parameters d_1 and d_2 determine the form and characteristic transverse dimension of the distributions. Figure 3a shows the symmetric temperature distribution at $d_1 = 1.8$ cm and $\Delta T_{max} = 5$ K.

(ii) We calculated the exact values of the increments of acoustic brightness temperature ΔT_A, which were obtained from 26 "measurements," with the help of Eqs. (2). The results of the calculation are shown in Fig. 4. Figure 4a (4b) for LPA_1 (LPA_2) demonstrates 13 values of ΔT_A (squares *1*) as a function of the $x(z)$ coordinate of the directivity pattern focus. Note that the increments of acoustic brightness temperature for LPA_1 are greater than those for LPA_2, as was indicated above. Figure 4 also shows the increments of acoustic brightness temperature (curves *2*) that would be obtained with ideal directivity patterns approximated by beams. In their essence, curves *2* in Figs. 4a and 4b exactly reproduce the shape of the desired temperature distribution (the shapes of the functions $f(x)$ and $g(z)$, respectively).

(iii) The measurement errors $\Delta T_A = 0.1$ or 0.2 K were imposed upon the exact values of δT_A to obtain the acoustic brightness temperatures $\Delta\tilde{T}_A = \Delta T_A \pm \delta T_A$ "measured" with an error. The measurement error is distributed according to the Gaussian law with zero mean and an rms deviation δT_A. The choice of error is connected with theoretical and experimental estimates of the accuracy of acoustic brightness temperature measurements in [2, 3, 15]. In particular, the error can be reduced by increasing the measurement time. With typical characteristics of a thermal acoustic radiation receiver, it is possible to obtain the error $\delta T_A = 0.2$ K within 20 s; by increasing the time to 80 s, it is possible to reduce the error to $\delta T_A = 0.1$ K. Note that, for every type of preset condition, this stage was repeated 100 times to obtain statistically reliable results. Figure 4a (4b) for LPA_1 (LPA_2) presents one realization of the values of $\Delta\tilde{T}_A$ "measured" with the error $\delta T_A = 0.2$ K (asterisks *3*).

(iv) The increments of acoustic brightness temperatures "measured" with an error were approximated by quartic polynomials for LPA_1 and LPA_2, and the respective profiles $\Delta\tilde{T}_A(x)$ and $\Delta\tilde{T}_A(z)$ were obtained. If the profiles proved to be negative at some values of x or z, these segments were assumed to be equal to zero (because the heating of the biological object could not cause a temperature decrease). Figure 4 represents the approximated polynomials (curves *4*) as functions of the x and z coordinates. Note that, in Fig. 4a, the profile was

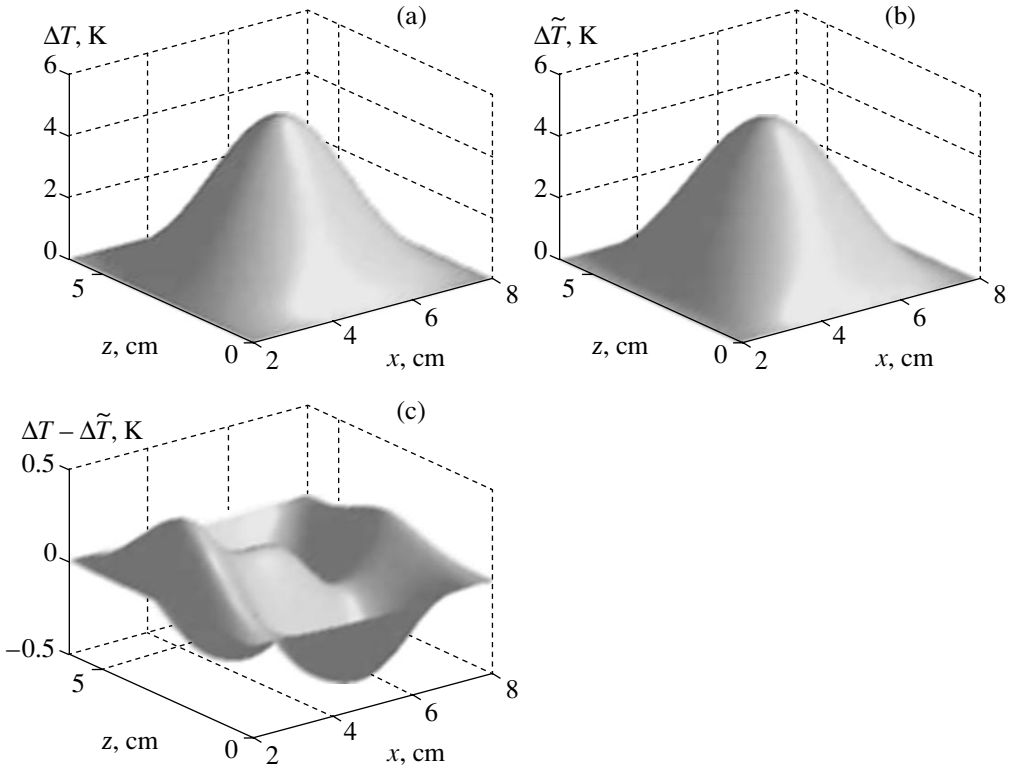

Fig. 3. Reconstruction of a temperature distribution: (a) the preset (symmetric) distribution $\Delta T(x, z)$, (b) the reconstructed distribution $\Delta\tilde{T}(x, z)$, and (c) the reconstruction error $\Delta T(x, z) - \Delta\tilde{T}(x, z)$.

made equal to zero on a segment close to the boundary $x = 2$ cm of the tested region. The desired approximated functions $\tilde{f}(x) \approx \Delta\tilde{T}_A(x)/\max_{x \in [x_1, x_2]} \Delta\tilde{T}_A(x)$ and $\tilde{g}(z) \approx \Delta\tilde{T}_A(z)/\max_{x \in [z_1, z_2]} \Delta\tilde{T}_A(z)$ had peaks at the coordinates $\tilde{x}_{\max}$ and $\tilde{z}_{\max}$. These coordinates approximated those of the temperature peak.

(v) Using the profiles $\Delta\tilde{T}_A(x)$ and $\Delta\tilde{T}_A(z)$ obtained with the discretization step $\Delta x = \Delta z = 0.1$ cm, we numerically solved Eq. (5). As a result, we obtained an approximate value of the absorption coefficient $\tilde{\alpha}_0$.

(vi) To calculate the approximate value of $\Delta\tilde{T}_{\max}$, various algorithms were tested. We sought the value of $\Delta\tilde{T}_{\max}$ that corresponded to the minimum value of $F(\Delta\tilde{T}_{\max})$:

$$F(\Delta\tilde{T}_{\max}) = \sum_{\forall i} Y_i(\Delta\tilde{T}_{\max}) \longrightarrow \min, \tag{7a}$$

$$F(\Delta\tilde{T}_{\max}) = \max_{\forall i} Y_i(\Delta\tilde{T}_{\max}) \longrightarrow \min,$$

$$F(\Delta\tilde{T}_{\max}) = \sum_{\forall i} Y_i^2(\Delta\tilde{T}_{\max}) \longrightarrow \min, \tag{7b}$$

where $Y_i(\Delta\tilde{T}_{\max}) = |\Delta\tilde{T}_A(i) - \Delta\tilde{T}_{\max} 2\tilde{\alpha}_0 \int_{x_1}^{x_2}\int_{z_1}^{z_2} dz dx \tilde{f}(x)\tilde{g}(z) A_i(x, z)\exp(-2\tilde{\alpha}_0 \xi)|$, $\xi = z$ for $i = 1, \ldots, 13$, and $\xi = x$ for $i = 14, \ldots, 26$. It is important to note that all methods give approximately the same results, but the minimization of Eq. (7a) gives the smallest systematic error. Therefore, precisely this method was used in the following calculations.

As the result of simulation, we obtained the approximation $\Delta\tilde{T}(x, z) = \Delta\tilde{T}_{\max}\tilde{f}(x)\tilde{g}(z)$ for the desired temperature distribution. Figure 3b shows an example of the reconstruction of the initial symmetric temperature distribution (see Fig. 3a) with the use of the "measurement" results given in Fig. 4. As one can see from the comparison of Figs. 3a and 3b, the distributions almost coincide on the scale in use. Figure 3c demonstrates the reconstruction error (the difference $\Delta T - \Delta\tilde{T}$), which does not exceed 0.5 K. The analysis of Fig. 3 allows us to make a preliminary conclusion about the possibility of applying the proposed algorithm. However, to determine the quality of the reconstruction, it is necessary to present statistically significant results. To obtain them, each reconstruction was repeated 100 times, and each time a random distribution of the measurement error was used (see the third stage of simulation). The results are shown in the table. Presetting the measurement

error δT_A (column 1), we calculated the average values of $\Delta\tilde{T}_{\max}$, $\tilde{x}_{\max}$, $\tilde{z}_{\max}$, and $\tilde{\alpha}_0$ and the rms deviations $\delta\tilde{T}_{\max}$, $\delta\tilde{x}_{\max}$, $\delta\tilde{z}_{\max}$, and $\delta\tilde{\alpha}_0$ for all desired parameters (columns 2–5, respectively). We also calculated the maximum absolute error of reconstruction $\delta T = \max_{\forall x(j)\forall z(k)} |\Delta T(x(j), z(k)) - \Delta\tilde{T}(x(j), z(k))|$, where $z(k)$ ($k = 1, \ldots, K$) and $x(j)$ ($j = 1, \ldots, J$) are the sampling points (column 6).

The parameter $\Delta\tilde{T}_{\max}$ allows us to estimate the systematic error of reconstruction, which is equal to the difference $\Delta T_{\max} - \Delta\tilde{T}_{\max}$ between the exact value of $\Delta T_{\max}$ and the value of $\Delta\tilde{T}_{\max}$ averaged over 100 realizations. The parameter $\delta\tilde{T}_{\max}$ determines the reconstruction accuracy for the temperature peak and the random error of reconstruction. This is one of the control parameters in hyperthermia, since it is important to know the maximum temperature in the heated region. The improvement of the accuracy of measurements for precisely the peak values of temperature distributions is a separate problem considered in [16]. The parameter δT characterizes the total error of reconstruction. The quantity δT allows us to estimate the accuracy of temperature reconstruction: in any part (with a size of 1 mm) of the tested region, the reconstruction error does not exceed δT. Precisely this parameter should be compared with the required accuracy of 0.5 K.

To test the proposed algorithm, we used it to solve several problems.

I. Investigation of the reconstruction quality with various values of the measurement error δT_A. To solve this problem, we preset a symmetric temperature distribution (Eq. (6a)) at $\Delta T_{\max} = 5$ K, $d_1 = 1.8$ cm, and the values of the measurement error $\delta T_A = 0$, 0.1, and 0.2 K. The reconstruction results for the distribution $\Delta\tilde{T}(x, z)$ are given in the table (see rows 1–3). We note the presence of a systematic error: $\Delta\tilde{T}_{\max} \neq 5$ K. This is connected with the fact that the form of the preset temperature distribution (even at $\delta T_A = 0$ K) cannot be perfectly approximated by a quartic polynomial (see Fig. 4, curves *1* and *2*). When δT_A increases, the values of $\Delta\tilde{T}_{\max}$, $\tilde{x}_{\max}$, $\tilde{z}_{\max}$, and $\tilde{\alpha}_0$ do not vary considerably, while the values of $\delta\tilde{T}_{\max}$, $\delta\tilde{\alpha}_0$, and δT grow by a factor of approximately 1.5–2. The variations of the parameters $\delta\tilde{x}_{\max}$ and $\delta\tilde{z}_{\max}$ at the given errors lie within 0.1 cm. This is an expected result: an exact reconstruction of the coordinates of temperature peaks is indicated in [2, 16, 17]. Note that the reconstruction accuracy for the parameters $\tilde{x}_{\max}$ and $\tilde{z}_{\max}$ is acceptable for all reconstructed temperature distributions. The value of δT at a zero measurement error is equal to the difference $\Delta T_{\max} - \Delta\tilde{T}_{\max}$; i.e., the maximum reconstruction error is observed at the peak. This well-known result is also discussed in [2, 16, 17]. In the case of a nonzero measurement error, the maximum error was not always observed at the point of the peak. All temperature parameters ($\Delta\tilde{T}_{\max} \pm \delta\tilde{T}_{\max}$ and δT) at $\delta T_A = 0.1$ K practically satisfy the requirements of hyperthermia (see above). If the measurement error increases to $\delta T_A = 0.2$ K, the temperature parameters $\pm\delta\tilde{T}_{\max}$ and δT lie within 1 K. This growth of the reconstruction error is the price for the decrease in the measurement time (see above) from 80 to 20 s. As one can see from the table (column 5), the absorption coefficient in all cases is reconstructed with a relative error no greater than 30% (at $\delta T_A = 0.2$ K). In analyzing the reconstruction of the absorption coefficient, it is necessary to take into account that, in the general case, the values of this parameter are different for different tissues of a biological object. The proposed algorithm reconstructs a cer-

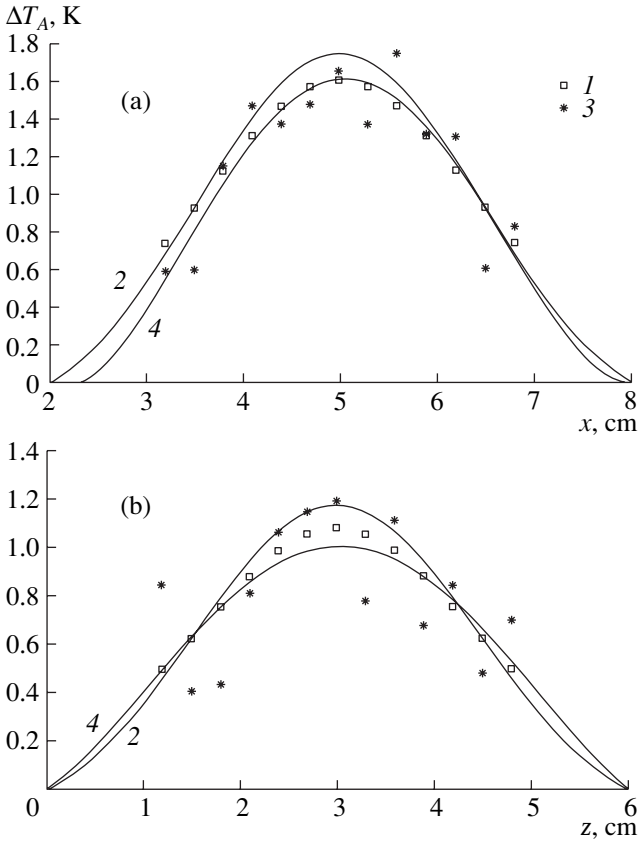

Fig. 4. Increments of acoustic brightness temperatures ΔT_A as functions of (a) *x* and (b) *z* coordinates: (*1*) results of "measurements" without any error with allowance for the actual directivity patterns; (*2*) results of "measurements" without any error with ideal directivity patterns (curves *2* demonstrate the shape of the preset distribution, Fig. 3a); (*3*) results of "measurements" with an error $\delta T_A = 0.2$ K and with allowance for the actual directivity patterns; and (*4*) temperature profiles reconstructed by polynomials (curves *4* demonstrate the shape of the reconstructed distribution, Fig. 3b).

Temperature and spatial parameters of the temperature distribution reconstructions

Row no.	δT_A, K	$\Delta\tilde{T}_{max} \pm \delta\tilde{T}_{max}$, K	$\tilde{x}_{max} \pm \delta\tilde{x}_{max}$, cm	$\tilde{z}_{max} \pm \delta\tilde{z}_{max}$, cm	$\tilde{\alpha}_0 \pm \delta\tilde{\alpha}_0$, cm^{-1}	δT, K
	1	2	3	4	5	6
Symmetric temperature distribution (Eq. (6a)), $d_1 = 1.8$ cm, $\Delta T_{max} = 5$ K						
1	0	4.6	5.0	3.0	0.10	0.4
2	0.1	4.7 ± 0.3	5.0 ± 0.1	3.0 ± 0.1	0.10 ± 0.02	0.6
3	0.2	4.7 ± 0.5	5.0 ± 0.1	3.0 ± 0.1	0.11 ± 0.03	1.0
Symmetric temperature distribution (Eq. (6a)), $d_1 = 1.8$ cm, $\Delta T_{max} = 10$ K						
4	0.1	9.3 ± 0.3	5.0 ± 0.1	3.0 ± 0.1	0.10 ± 0.01	0.8
5*	0.1	10.1 ± 0.3	5.0 ± 0.1	3.0 ± 0.1	0.10 ± 0.02	0.3
Symmetric temperature distribution (Eq. (6a)), $d_1 = 2.5$ cm, $\Delta T_{max} = 5$ K						
6	0.1	4.8 ± 0.3	5.0 ± 0.1	3.0 ± 0.1	0.10 ± 0.03	0.5
Symmetric temperature distribution (Eq. (6a)), $d_1 = 1.0$ cm, $\Delta T_{max} = 5$ K						
7	0.1	4.1 ± 0.4	5.0 ± 0.1	3.0 ± 0.1	0.10 ± 0.02	1.1 (0.8)
Asymmetric temperature distribution (Eq. (6b)), $\Delta T_{max} = 5$ K						
8	0.1	5.0 ± 0.2	5.5 ± 0.1	3.5 ± 0.1	0.10 ± 0.01	0.6
10	0.2	5.2 ± 0.5	5.5 ± 0.2	3.6 ± 0.3	0.11 ± 0.03	0.9

* The description of the algorithm used for the reconstruction is given in section *II*, "Investigation of the influence of the peak temperature on the reconstruction quality."

tain average parameter important for further determination of the temperature.

II. Investigation of the influence of the peak temperature on the reconstruction quality. The effect of hyperthermia depends on the temperature value to which the tissue is heated and on the time interval within which the elevated temperature is maintained. It is known that, starting from a temperature of 42–43°C, a temperature increase by one degree is equivalent to a twofold reduction of the heating time [18]. In other words, the effect achieved at a temperature of 42°C within 1 h is equivalent to the effect of heating, for example, to a temperature of 47°C within approximately 2 min. Therefore, it is important to consider the influence of the temperature peak value ΔT_{max} on the reconstruction quality. We note that a decrease in ΔT_{max} to 2.5 K did not lead to any deterioration of the reconstruction quality (the results are not given in the table). To evaluate the reconstruction quality in the case of a temperature increase, we preset a symmetric temperature distribution (Eq. (6a)) at $d_1 = 1.8$ cm, $\Delta T_{max} = 10$ K, and the value of the measurement error $\delta T_A = 0.1$ K (the reconstruction results are given in the table, row 4). Let us compare the results with those obtained at $\Delta T_{max} = 5$ K (row 2). In the case of a temperature increase, the systematic error increases to 0.7 K. In this case, the relative systematic error almost did not change: 7–8%. The random error of 0.3 K also did not change. As a result, the total error of reconstruction grows to 0.8 K and goes beyond the limits indicated above. To reduce the systematic error, it is necessary to change the method used for approximating the temperature distribution (i.e., the fourth stage of the algorithm). To evaluate the possibility of reconstructing the temperature with a peak of about 10 K, we considered the distribution approximation by a function of the type of Eq. (6a). In this case, the method of stage (v) was used to determine the absorption coefficient and, then, the distribution parameters ΔT_{max} and d_1 were determined. To do this, we used an algorithm analogous to that given by Eq. (7a). The results are given in row 5 of the table. Note that, in this case, the systematic error is approximately equal to zero. (This is connected with the choice of the "perfect" type of the approximating function. In the case of a different choice, the systematic error should arise.) The random error of 0.3 K did not change, but the total error was reduced to 0.3 K, which is quite admissible. Thus, in the case of reconstructing the temperature with peaks of about 10 K, it is necessary to vary the type of the approximating function. The optimal choice in this case needs additional study.

III. Investigation of the influence of the heated region width on the quality of temperature reconstruction. The characteristic transverse dimension of a temperature distribution is determined by the size of the heated region and by "smearing" of the temperature distribution due to thermal conductivity and blood flow. The estimate of the characteristic dimensions of the temperature distributions in the soft tissues of a human body was obtained on [19] on the basis of physiological data. The transverse dimension of a temperature distribution in a stationary state is about 1 cm. In the present study, a symmetric temperature distribution (Eq. (6a)) was preset at $\Delta T_{max} = 5$ K with different values of the

parameter d_1 = 1.8, 2.5, and 1.0 cm, and the temperature was reconstructed at a measurement error of δT_A = 0.1 K (rows 2, 6, and 7). Measurements of the parameter d_1 caused changes in the width of the heated region. If d_1 increases from 1.0 to 2.5 cm, the diameter of the heated region, where the temperature exceeded half the peak value, was 2.1, 3.1, and 3.6 cm, respectively. In the case of broader distributions, at d_1 = 1.8 and 2.5 cm, the reconstruction accuracy is approximately the same (δT = 0.6 and 0.5 K, respectively) and satisfies the necessary requirements. For the distribution with the minimum value d_1 = 1.0 cm, the reconstruction accuracy exceeds admissible values: δT = 1.1 K. This is connected with the fact that the temperature gradient increases. Note that a reconstruction accuracy of 0.5 K is presumed for the region with a size of 1 cm. In our algorithm, the quantity δT is calculated in the region with a size of 1 mm. If we assume that, in our study, it is important to know the temperature distribution $\Delta\bar{T}(x, z)$ averaged over a region 1 cm in size, the maximum absolute error δT should be determined according to the formula $\delta T = \max_{\forall x(j)\forall z(k)} |\Delta\bar{T}(x(j), z(k)) - \Delta\tilde{T}(x(j), z(k))|$. The results of this calculation are given in column 6 in parentheses. Naturally, this approach reduces the error to 0.8 K. Thus, the proposed algorithm provides a better reconstruction for smoother distributions. The reconstruction quality remains admissible for the characteristic dimension of the temperature peak region, namely, slightly greater than 2 cm.

IV. Investigation of the reconstruction quality in the case of an asymmetric temperature distribution. To solve the problem, we preset an asymmetric temperature distribution (Eq. 6b) at ΔT_{max} = 5 K and d_2 = 6.0 cm and reconstructed the temperature with different values of the measurement error: δT_A = 0.1 and 0.2 K (rows 8 and 9). Note that, in the case of the asymmetric distribution, the systematic error is connected not with the amplitude of the temperature peak but with its position: the reconstructed values of $\tilde{x}_{max}$ and $\tilde{z}_{max}$ are 2 mm smaller than the exact values. The random errors in the reconstructing of the spatial parameters are also greater. However, even at δT_A = 0.2 K, the maximum error for $\tilde{z}_{max}$ does not exceed 5 mm, which is quite admissible. The reconstruction quality for the temperature parameters with the preset distribution is no worse than in the case of a symmetric distribution.

Let us compare the results obtained above with the data given earlier in [2, 16, 17, 20], where different regularization algorithms and the "standard source" method were used for the reconstruction of temperature distributions. It should be noted that the parameters of the temperature distributions under reconstruction and the reconstruction quality are approximately the same as those in the present study. The advantage of our algorithm consists in that the ultrasonic absorption coefficient of the biological object is assumed to be unknown beforehand and is calculated from the "experimental" data. In addition, in contrast to [2, 15, 16, 19], where the directivity patterns approximated by beams were used to calculate the acoustic brightness temperature, we take into account the actual directivity patterns created by linear phased arrays. We note that actual directivity patterns of flat circular piezoelectric transducers were taken into account in [3], where the position of the heated region was determined but the temperature was not reconstructed.

All algorithms considered above imply the reconstruction of a two-dimensional temperature distribution; i.e., they imply the presence of a cylindrical heated region with its lateral surface perpendicular to the *x*0*z* plane in Figs. 1 and 2. However, our algorithm also allows one to consider a three-dimensional problem for a heated region shaped as, e.g., a sphere. This problem needs further investigation.

Thus, the results of this study demonstrate that, under the adopted assumptions, temperature distributions with peak values reaching 5–10 K can be reconstructed with an accuracy of approximately 0.5 K within a time interval of about 1.5 min. The proposed method does not need any *a priori* information on the absorption coefficient and takes into account actual directivity patterns of the receivers of thermal acoustic radiation.

In conclusion, it is necessary to note the limitation imposed upon the temperature distribution under reconstruction: its form should be determined by the product of functions depending on one coordinate each (the coordinates along which the scanning is performed). If the form of the temperature distribution is described by a more complex dependence, two linear arrays are insufficient for the determination of the temperature distribution. In the general case, the problem of reconstruction is reduced to a problem analogous to that solved in classical X-ray tomography. However, in the acoustical problem, it is necessary to take into account the actual dimensions of the directivity patterns of the arrays and the possible nonuniformity of absorption in biological objects.

ACKNOWLEDGMENTS

This work was supported by the Russian Foundation for Basic Research, project nos. 02-0-2-17371, 03-02-16232, and 03-01-00723.

REFERENCES

1. V. I. Passechnik, A. A. Anosov, and M. G. Isrefilov, Int. J. Hyperthermia **15** (2), 123 (1999).
2. V. I. Pasechnik, A. A. Anosov, and K. M. Bograchev, Biomed. Radioélektron., No. 2, 3 (1999).
3. E. V. Krotov, S. Yu. Ksenofontov, A. D. Mansfel'd, *et al.*, Izv. Vyssh. Uchebn. Zaved., Radiofiz. **42** (5), 479 (1999).

4. E. V. Krotov, A. M. Reĭman, A. D. Mansfel'd, *et al.*, in *Speech Acoustics. Medical and Biological Acoustics: Proceedings of XIII Session of the Russian Acoustical Society* (GEOS, Moscow, 2003), Vol. 3, pp. 195–199.
5. A. A. Anosov, V. I. Pasechnik, and V. V. Shablinskiĭ, Akust. Zh. **37**, 610 (1991) [Sov. Phys. Acoust. **37**, 315 (1991)].
6. V. V. Gerasimov, Yu. V. Gulyaev, A. V. Mirgorodskiĭ, *et al.*, Akust. Zh. **45**, 487 (1999) [Acoust. Phys. **45**, 433 (1999)].
7. V. A. Burov, P. I. Darialashvili, and O. D. Rumyantseva, Akust. Zh. **48**, 474 (2002) [Acoust. Phys. **48**, 412 (2002)].
8. A. A. Anosov, Yu. N. Barabanenkov, and A. G. Sel'skiĭ, Akust. Zh. **49**, 725 (2003) [Acoust. Phys. **49**, 615 (2003)].
9. F. Duck, *Physical Properties of Tissue* (Academic, London, 1990).
10. C. A. Damianou, N. T. Sanghvi, F. J. Fry, and R. Maass-Moreno, J. Acoust. Soc. Am. **102**, 628 (1997).
11. L. R. Gavrilov and J. W. Hand, IEEE Trans. Ultrason. Ferroelectr. Freq. Control **47**, 125 (2000).
12. V. I. Pasechnik, Akust. Zh. **36**, 718 (1990) [Sov. Phys. Acoust. **36**, 403 (1990)].
13. V. I. Babiĭ, Morsk. Gidrofiz. Issled., No. 2 (65), 189 (1974).
14. T. Bowen, US Patent No. 4,246,784 (1981).
15. V. V. Gerasimov, V. I. Mirgorodskiĭ, and S. V. Peshin, Zh. Tekh. Fiz. **65** (5), 149 (1995) [Tech. Phys. **40**, 489 (1995)].
16. K. M. Bograchev and V. I. Pasechnik, Akust. Zh. **49**, 474 (2003) [Acoust. Phys. **49**, 396 (2003)].
17. K. M. Bograchev and V. I. Pasechnik, Akust. Zh. **45**, 742 (1999) [Acoust. Phys. **45**, 667 (1999)].
18. S. A. Sapareto and W. C. Dewey, Radiat. Oncol. Biol. Phys. **10**, 787 (1984).
19. Yu. V. Gulyaev, K. M. Bograchev, I. P. Borovikov, *et al.*, Radiotekh. Élektron. (Moscow) **43** (9), 140 (1998) [J. Commun. Technol. Electron. **43**, 1061 (1998)].
20. M. S. Bosnyakov and Yu. V. Obukhov, Pattern Recogn. Image Anal. **13** (1), 74 (2003).

Translated by M. Lyamshev

Acoustical Physics, Vol. 51, No. 4, 2005, pp. 385–391. Translated from Akusticheskiĭ Zhurnal, Vol. 51, No. 4, 2005, pp. 456–462.

Determination of the Crack Configuration in an Anisotropic Elastic Medium

A. O. Vatul'yan* and I. V. Baranov**

** Rostov State University, ul. Zorge 5, Rostov-on-Don, 344090 Russia*

e-mail: vatulyan@aaanet.ru

*** Don State Technical University, pl. Gagarina 1, Rostov-on-Don, 344010 Russia*

Received July 10, 2003

Abstract—The problem of the identification of a single internal crack in an anisotropic elastic body is investigated. Using the dislocation theory approach, a system of boundary integral equations for the crack opening functions is constructed and studied by the boundary element method. A crack identification method is developed on the basis of the crack parametrization by a finite number of parameters, with their subsequent determination through the minimization of a certain nonquadratic residual functional. The problem of identifying a transverse tunnel crack in an orthotropic layer is solved for the cases of plane and antiplane deformations.

INTRODUCTION

The most effective experimental techniques used for nondestructive testing of elastic bodies include those based on the diffraction of elastic waves by the defects [1, 2]. A correct description of the diffracted field is given by systems of integral equations for the displacement jumps at a crack. To study the diffraction of elastic waves by internal and surface cracks, different analytical and numerical methods have been developed in recent years for analyzing these equations. All of the methods used for solving the direct problem of calculating the diffracted field in a medium with a single defect can be separated into two classes according to the type of the boundary integral equations to be analyzed: one of them includes the hypersingular equations described in many publications (see, e.g., [3–6]), and the other includes nonsingular equations [7] and also those using dual formulations [8, 9]. The methods of studying the aforementioned boundary integral equations can also be separated into two classes: high-frequency and low-frequency ones. The advantage of the high-frequency method consists in that the probing pulse length is of the same order of magnitude as the crack length or smaller than it. This leads to interference phenomena, which can easily be observed and used for the crack identification. The advantages of low-frequency vibrations include the possibility to use the static results of the theory of cracks for solving dynamic problems and also the possibility to derive a conclusion concerning the growth of the crack and the fracture of the sample. It should be noted that, by now, the methods of calculating the diffracted fields in isotropic bodies with cracks are developed in sufficient detail. These methods are based on either the boundary element method or asymptotic methods. At the same time, many metals and alloys subjected to technological processing acquire an anisotropy of their elastic properties. In this case, calculations with the isotropic medium model lead to large errors. Therefore, the study of wave processes in bodies possessing an anisotropy (presumed to be of the simplest type) in the presence of crack-type defects is quite topical. This study is the subject of the first part of the present paper. The second part of the paper is devoted to a poorly investigated class of inverse geometrical problems of the theory of elasticity: the localization of a single crack in an orthotropic medium from the known elastic displacement field of a stress-free boundary area of the body.

STATEMENT OF THE PROBLEM

Consider steady-state vibrations of an orthotropic elastic body V bounded by a piecewise smooth surface $S = S_1 \cup S_2$. The vibrations are caused by a load p_i applied in the boundary part $S_{20} \subset S_2$, while the boundary part S_1 is restrained. We assume that, in the boundary region $S_{21} \subset S_2$, displacements $u_i|_{S_{21}} = g_i$ are preset and that $S_{20} \cap S_{21} = \varnothing$. The body V is deteriorated by a crack bounded by internal surfaces $S_0^{\pm}$ (Fig. 1). At these surfaces, the components of the displacement vector experience jumps $\chi_i = u_i|_{S_0^+} - u_i|_{S_0^-}$. In addition, we assume that the crack edges do not interact in the course of vibrations. In terms of the dislocation theory approach, the boundary-value problem for a body containing a crack and performing steady-state vibrations has the form [6, 7]

$$\sigma_{ij,j} + \rho\omega^2 u_i + f_i = 0, \quad \sigma_{ij} = c_{ijkl}u_{k,l}; \tag{1}$$

1063-7710/05/5104-0385$26.00 © 2005 Pleiades Publishing, Inc.

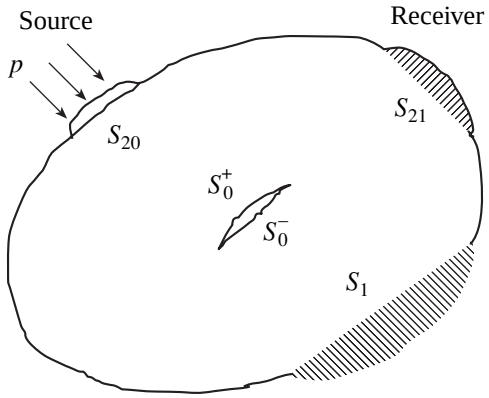

Fig. 1. Vibrations of a body with an arbitrary crack.

$\sigma_{ij}n_j|_{S_2} = p_i$, where p_i is nonzero within S_{20};

$$u_i|_{S_1} = 0; \tag{2}$$

$$\sigma_{ij}n_j^{\pm}|_{S_0^{\pm}} = 0; \tag{3}$$

and the fictitious mass forces are expressed through the jumps: $f_i = -[c_{ijkl}n_k^+\chi_l\delta(\zeta)]_{,j}$. Here, c_{ijkl} are the elastic constant tensor components, which satisfy regular symmetry conditions and are positively definite; u_i are the components of the displacement vector; σ_{ij} are the stress tensor components; n_j and $n_j^{\pm}$ are the components of the unit vectors that are normal to the surfaces S and $S_0^{\pm}$, respectively; $\delta(\zeta)$ is the Dirac delta function; ζ is the coordinate measured along the normal to S_0^+; ρ is the density; and ω is the frequency of vibrations.

The inverse problem of crack identification is formulated as follows: from the displacement field given in the load-free boundary region S_{21}, it is necessary to determine the surface S_0^+.

REDUCTION OF THE PROBLEM TO OPERATOR EQUATIONS

In studying the vibrations of a body with a crack, the most efficient method is to reduce the boundary-value problem of the elasticity theory to a system of boundary integral equations, which makes it possible to reduce the dimensionality of the problem by one. In this case, the elastic displacement field inside the body V can be determined using the Somyliana formulas [8]

$$u_m(\xi) = \int_S \sigma_{ij}n_jU_i^{(m)}(x,\xi)dS_x - \int_S \sigma_{ij}^{(m)}(x,\xi)n_ju_idS_x + \int_V U_i^{(m)}(x,\xi)f_idV_x, \quad \xi \in V, \tag{4}$$

where $U_i^{(m)}(x,\xi)$ and $\sigma_{ij}^{(m)}(x,\xi)$ are the fundamental and singular solutions for an anisotropic medium, respectively. Explicit representations of these solutions cannot be constructed, but it is possible to construct their integral representations in the form of single integrals (for a plane problem in the case of an orthotropic material, see, e.g., [10]).

Using the expressions for f_i and choosing $U_i^{(m)}(x,\xi)$ in Eq. (4) to be the fundamental solutions for the operator of the anisotropic elasticity theory given by Eqs. (1), which satisfy the boundary conditions

$$U_i^{(m)}|_{S_1} = 0, \quad \sigma_{ij}^{(m)}(x,\xi)|_{S_2} = 0, \tag{5}$$

we obtain

$$u_m(\xi) = u_m^{\text{ref}}(\xi) - \int_V U_i^{(m)}(x,\xi)[c_{ijkl}n_k^+\chi_l\delta(\varsigma)]_{,j}dV_x$$

$$= u_m^{\text{ref}}(\xi) - \int_V [U_i^{(m)}(x,\xi)c_{ijkl}n_k^+\chi_l\delta(\varsigma)]_{,j}dV_x + \int_V U_{i,j}^{(m)}(x,\xi)c_{ijkl}n_k^+\chi_l\delta(\varsigma)dV_x.$$

Applying the Gauss–Ostrogradski theorem to the first integral of the latter equality and taking into account that the crack is an internal one, we obtain that the integral is equal to zero, and the formula for calculating the displacement field inside V takes the form

$$u_m(\xi) = u_m^{\text{ref}}(\xi) + \int_{S_0^+} \sigma_{kl}^{(m)}(x,\xi)\chi_ln_k^+dS_x, \tag{6}$$

where $u_m^{\text{ref}}(\xi) = \int_{S_{20}} p_i(x)U_i^{(m)}(x,\xi)dS_x$ is the field in the medium without the defect (the reference field). Equation (6) allows one to calculate the displacement field everywhere in the region V if the crack opening functions χ_l are known. To determine the opening functions, with the standard method used in the theory of cracks, we construct a system of boundary equations by calculating the components of the stress vector at the surface S_0^+ and by applying boundary condition (3):

$$K\chi = \int_{S_0^+} k_{jl}(x,y)\chi_l(x)dS_x = F_j(y), \quad y \in S_0^+. \tag{7}$$

The kernels $k_{jl}(x,y)$ in Eq. (7) are hypersingular ones with a singularity on the order of $|x-y|^{-2}$ and have the form

$$k_{jl}(x,y) = c_{jimq}n_in_k\sigma_{kl,q}^{(m)}.$$

The corresponding integrals are interpreted in terms of the Hadamard finite value [11], and the functions $F_j(y)$ are expressed through the reference field:

$$F_j(y) = -c_{jiml}n_i^{\pm}u_{m,l}^{\text{ref}}.$$

In the inverse problem, on the basis of Eqs. (6) and (7), a system of nonlinear operator equations in $\chi_l(x)$ and S_0^+ is constructed:

$$\int_{S_0^+} k_{ml}^0(x, \xi)\chi_l dS_x = g_m^0(\xi) = g_m(\xi) - u_m^{\text{ref}}(\xi),$$

$$\xi \in S_{21}, \tag{8}$$

$$\int_{S_0^+} k_{jl}(x, y)\chi_l(x)dS_x = F_j(y), \quad y \in S_0^+, \quad m = 1, 2, 3,$$

where $k_{ml}^0(x, \xi) = \sigma_{kl}^{(m)}(x, \xi)n_k$.

The problem of deriving S_0^+ from system (8) is nonlinear and unstable under small perturbations of the preset functions $g_j(x)$. Thus, the inverse geometrical problem of crack identification is incorrect and should be solved with the use of regularizing algorithms [12]. One of the possible ways of regularization is the maximum possible narrowing of the search region, in particular, the reduction of the problem to a finite-dimensional one. The method used by us for the determination of S_0^+ is based on the preliminary parametrization of the surface by the introduction of a finite number of parameters c_p; in particular, for a planar elliptic crack, seven parameters are introduced (the coordinates of the center, the components of the normal vector, and the semiaxes of the ellipse). These parameters are determined using a discrete representation of integral operator (7) in terms of the nodal values of the opening functions and the subsequent determination of the parameters c_p ($p = 1, 2, \ldots, n$) from the minimum of the residual functional

$$\Phi(c_p) = \max_{y \in S_{21}} \left| u_m^{\text{ref}}(y) \right.$$
$$\left. + \int_{S_0^+} \sigma_{kl}^{(m)}(x, y)n_k(x)\chi_l(x)dS_x - g_m(y) \right|, \tag{9}$$

which, in the case of such a parametrization, represents a function of n variables.

Note that the efficiency of the proposed method strongly depends on the possibility to construct a fundamental solution satisfying boundary conditions (5). For some types of domains and boundary conditions, such solutions can be constructed rather well (a layer, an infinite cylinder, etc.). Let us consider the simplest examples of crack reconstruction.

EXAMPLES

We illustrate the proposed approach by solving the problem of crack identification in an orthotropic layer with a vertical tunnel crack for the cases of plane and antiplane deformations.

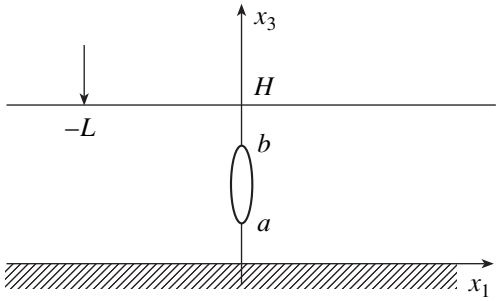

Fig. 2. Vibrations of a layer with a transverse crack.

Consider an orthotropic layer of thickness H with a rigidly fixed lower surface. Assume that the layer contains a transverse crack with tips a and b and that the crack does not reach the layer surfaces (i.e., $0 < a < b < H$). The coordinate system coincides with the elastic symmetry axes of the material. The crack lies on the Ox_3 axis, and the Ox_1 axis coincides with the lower surface of the layer (Fig. 2). Vibrations are excited in the layer by a concentrated force P applied to the upper surface of the layer at the point with the coordinates $(-L, H)$. To complete the problem, it is necessary to impose the radiation conditions, which are formulated using the principle of ultimate absorption [13]. The inverse problem consists in the determination of the coordinates of the tips a and b from the displacement field at the boundary $u(x_1, H) = g(x_1)$, where $x_1 \in [c, d]$. Below, we present equations of the type of Eq. (7) for some specific loads.

THE ANTIPLANE PROBLEM FOR A LAYER WITH A VERTICAL CRACK

Let the vibrations be excited by a tangential force directed along the x_2 axis. In this case, the displacement vector has only one nonzero component $u_2 = u(x_1, x_3)$. The equations of motion and the boundary conditions have the form

$$c_{66}u_{,11} + c_{44}u_{,33} + \rho\omega^2 u + f = 0, \tag{10}$$

$$u(x_1, 0) = 0, \quad \sigma_{23}|_{x_3 = H} = -P\delta(x_1 + L),$$
$$f = -[c_{66}\chi\delta(\zeta)]_{,1}, \quad \chi = \chi_2. \tag{11}$$

To determine the wave field in the layer, we apply the Fourier transformation in x_1 to Eqs. (10) and (11) and solve the boundary-value problem for the transform $\tilde{u}(\alpha_1, x_3)$. As a result, we obtain the wave-field representation

$$u(x_1, x_3) = \frac{1}{2\pi}\int_\sigma \tilde{u}(\alpha_1, x_3)\exp(-i\alpha_1 x_1)d\alpha_1, \tag{12}$$

where the contour σ is chosen according to the principle of ultimate absorption and coincides with the real axis everywhere except for the singularities of the inte-

grand function: it deviates to the complex plane to bypass the positive singularities from below and the negative singularities from above. Using the condition of zero stress at the crack edges, we arrive at a boundary integral equation with a hypersingular kernel:

$$\int_a^b \chi(\xi_3)K(\xi_3, x_3)d\xi_3 = F(x_3), \quad x_3 \in [a, b]. \quad (13)$$

Here, $K(\xi_3, x_3) = \dfrac{\nu^{-1/2}}{(\xi_3 - x_3)^2} + K_0(\xi_3, x_3)$, where $K_0(\xi_3, x_3)$ is the regular part representable in the form of a single integral over the contour σ:

$$K_0(\xi_3, x_3) = \int_\sigma \left\{ \frac{\nu\alpha^2}{2\lambda}\left[e^{-\lambda|x_3 - \xi_3|} - \frac{e^{-\lambda\xi_3}\cosh(\lambda(H - x_3)) - e^{-\lambda(H-\xi_3)}\sinh(\lambda x_3)}{\cosh(\lambda H)}\right] - \frac{\sqrt{\nu}}{2}|\alpha| e^{-|x_3 - \xi_3|\sqrt{\nu}|\alpha|}\right\} d\alpha; \quad (14)$$

$$\nu = c_{66}/c_{44}; \quad \lambda = \sqrt{\nu\alpha^2 - k^2}; \quad \alpha = \alpha_1;$$

$$k^2 = \rho\omega^2/c_{44};$$

$$F(x_3) = -P_0 \int_\sigma i\alpha \frac{\sinh(\lambda x_3)}{\lambda\cosh(\lambda H)} \exp(-i\alpha L)d\alpha, \quad (15)$$

$$P_0 = P/c_{44}.$$

THE PLANE PROBLEM FOR A LAYER WITH A VERTICAL CRACK

Let the vibrations be excited by a normal force directed along the x_3 axis. In this case, the nonzero components of the displacement vector are $u_1 = u_1(x_1, x_3)$ and $u_3 = u_3(x_1, x_3)$. The equations of motion and the boundary conditions have the form

$$c_{11}u_{1,11} + c_{55}u_{1,33} + (c_{13} + c_{55})u_{3,13} + \rho\omega^2 u_1 + f_1 = 0; \quad (16)$$

$$c_{55}u_{3,11} + c_{33}u_{3,33} + (c_{13} + c_{55})u_{1,13} + \rho\omega^2 u_3 + f_3 = 0;$$

$$u_1(x_1, 0) = u_3(x_1, 0) = 0;$$

$$\sigma_{33}\big|_{x_3 = H} = -P\delta(x_1 + L); \quad \sigma_{13}\big|_{x_3 = H} = 0; \quad (17)$$

$$f_1 = -(c_{11}\chi_1\delta(\zeta))_{,1} - (c_{55}\chi_3\delta(\zeta))_{,3};$$

$$f_3 = -(c_{55}\chi_3\delta(\zeta))_{,1} - (c_{13}\chi_1\delta(\zeta))_{,3}.$$

As in the case of the antiplane problem, we apply the Fourier transformation to Eqs. (16) and (17). Satisfying the boundary conditions at the crack and assuming that the crack edges do not interact, we obtain a system of boundary integral equations, which, in the case under consideration, divides into two independent equations in the displacement jumps:

$$\int_a^b k_{jj}(\xi_3, x_3)\chi_j(\xi_3)d\xi_3 = F_j(x_3), \quad x_3 \in [a, b], \quad j = 1, 3. \quad (18)$$

The kernels of these equations are representable in the form

$$k_{jj}(\xi_3, x_3) = \frac{M_j}{(\xi_3 - x_3)^2} + k^0_{jj}(\xi_3, x_3),$$

$$k^0_{jj}(\xi_3, x_3) = \int_\sigma K^0_{jj}(\alpha_1, \xi_3, x_3)d\alpha_1,$$

where M_j are constants determined by the elastic constants of the material, $k^0_{jj}(\xi_3, x_3)$ are kernels that are regular at $\xi_3 = x_3$, and the functions $K^0_{jj}(\alpha_1, \xi_3, x_3)$ that appear in the integral representations of the kernels are meromorphic in α_1 in the complex plane and have a finite number of poles on the real axis. The number and relative positions of the poles depend on the vibration frequency and determine the number of waves propagating in the layer. The functions $F_j(x_3)$ are representable as integrals over the contour σ and have a form similar to that shown at the end of the previous subsection. They characterize the stress vector components on the crack line in the layer without the crack under the effect of the initial load. The corresponding formulas are rather cumbersome and are not presented here.

Integral equations of the type of Eq. (13) are solved with the boundary element method [11]. For the case of the antiplane problem, the solution is realized in [14].

The inverse problem consists in the determination of the crack tips a and b from the known displacements u_k^{0m}, which are preset at the points x^m within the layer part S_{21} (by position probing). The solution to the problem is obtained by solving the system of boundary integral equations of the type of Eq. (7) and then minimizing the corresponding residual functional $\Phi(a, b) = \sum_m \left|u_k^m\big|_{S_{21}} - u_k^{0m}\right|^2$, where the quantities $u_k^m\big|_{S_{21}}$ are calculated according to representation (6).

RESULTS OF NUMERICAL EXPERIMENTS

By the collocation method, boundary integral equations (18) were reduced to a system of nonlinear equations

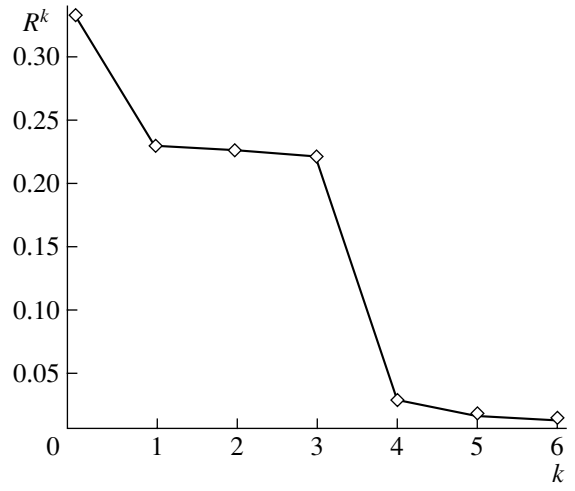

Fig. 3. Relative error R_k in the reconstruction of the crack tips versus the iteration number k for $\kappa = 2.2$, $\theta_1 = 0.1$, and $\theta_2 = 0.3$.

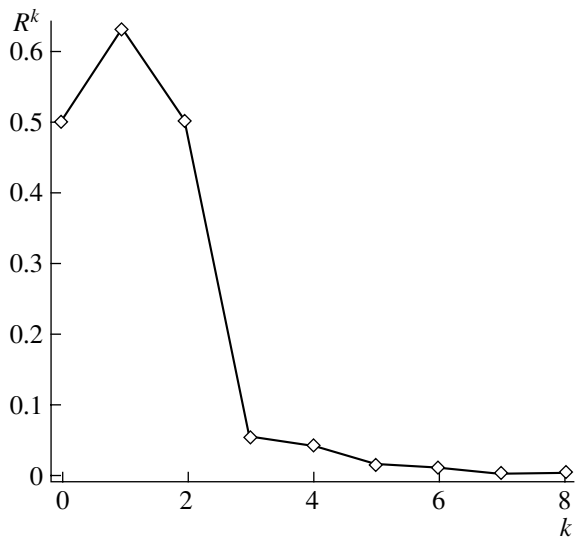

Fig. 4. Relative error R_k in the reconstruction of the crack tips versus the iteration number k for $\kappa = 2.2$, $\theta_1 = 0.4$, and $\theta_2 = 0.6$.

in the unknown crack parameters $\theta_1 = a/H$ and $\theta_2 = b/H$ and the nodal values $p_i^j = \chi_j(\eta_i^0 H)/\sqrt{(\theta_2 - \eta_i^0)(\eta_i^0 - \theta_1)}$:

$$\sum_{i=1}^{N} p_i^j \sqrt{(\theta_2 - \eta_i^0)(\eta_i^0 - \theta_1)} B_{ik}^j = F_j(y_k), \quad (j = 1, 3)$$

$$B_{ik}^j = M_j\left(\frac{1}{\eta_i - y_k} - \frac{1}{\eta_{i+1} - y_k}\right) + hk_{jj}^0(\eta_i, y_k), \quad (19)$$

$$y = x_3/H, \quad \eta = \xi_3/H.$$

Here, $\{\eta_i\}_{i=1}^{N+1}$ and $\{y_k\}_{k=1}^{N}$ are uniform grids on the segment $[\theta_1, \theta_2]$ with a mesh $h = (\theta_2 - \theta_1)/N$, ($\eta_1 = \theta_1$, $\eta_{N+1} = \theta_2$), η_i^0 is the center of the segment $[\eta_i, \eta_{i+1}]$, and the number N of the boundary elements was chosen so that no less than five to seven elements fell within the wavelength of the probing signal. An iteration process was developed for determining the values of θ_1 and θ_2. The process included the solution of the aforementioned system of equations and the minimization of the residual functional $\Phi^0(\theta_1, \theta_2) = \Phi(\theta_1 H, \theta_2 H)$. The initial approximation (θ_1^0, θ_2^0) was chosen with the help of a search over a uniform grid in the triangle $0 < \theta_1 < \theta_2 < 1$.

Figures 3–9 show examples of solutions to the inverse problem of locating a vertical crack with the crack tip coordinates θ_1 and θ_2 in an austenitic steel layer of thickness $H = 0.1$ m for the frequencies $\kappa = H\omega\sqrt{\rho/c_{33}} = 2.2$, 3.7, and 4.9 with two, three, and four traveling waves, respectively. In all of these figures, the horizontal axis represents the iteration number k, and the vertical axis, the relative error in the crack tip identification $R^k = \dfrac{1}{\theta_2 - \theta_1}\max(|\theta_2 - \theta_2^k|, |\theta_1 - \theta_1^k|)$. Figure 3 corresponds to a near-bottom crack, Fig. 4, to a crack in the middle of the layer, and Fig. 5, to a near-surface crack. The results of calculations testify that, for the near-surface crack, the convergence of the process is somewhat worse. Figures 4, 6, and 7 illustrate the change in the character of convergence with an increasing number of traveling waves in the layer. Figure 4 corresponds to two modes propagating in the layer, Fig. 6, to three propagating modes, and Fig. 7, to four modes. As the

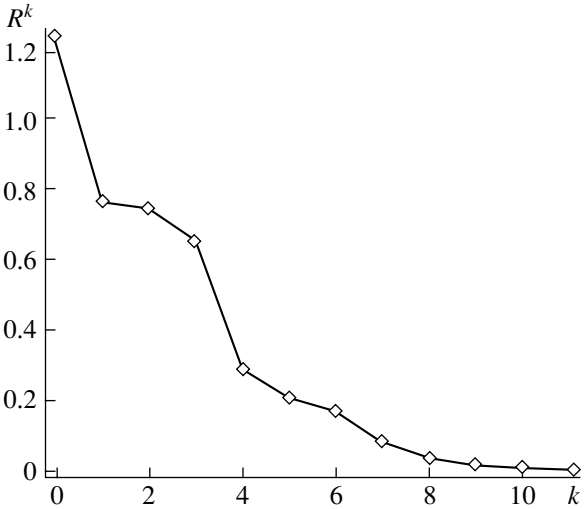

Fig. 5. Relative error R_k in the reconstruction of the crack tips versus the iteration number k for $\kappa = 2.2$, $\theta_1 = 0.75$, and $\theta_2 = 0.95$.

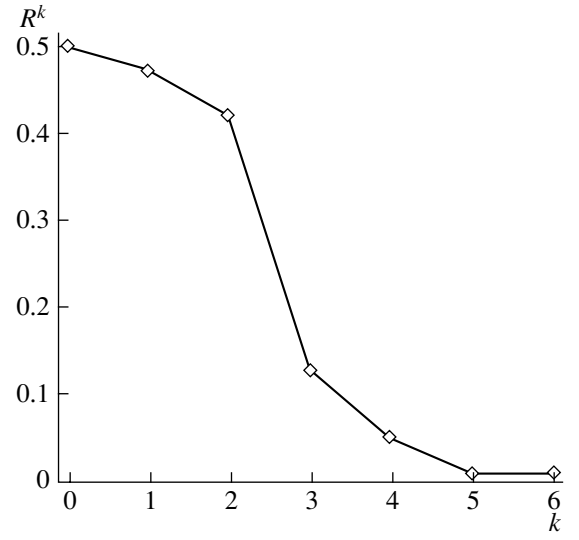

Fig. 6. Relative error R_k in the reconstruction of the crack tips versus the iteration number k for $\kappa = 3.7$, $\theta_1 = 0.4$, and $\theta_2 = 0.6$.

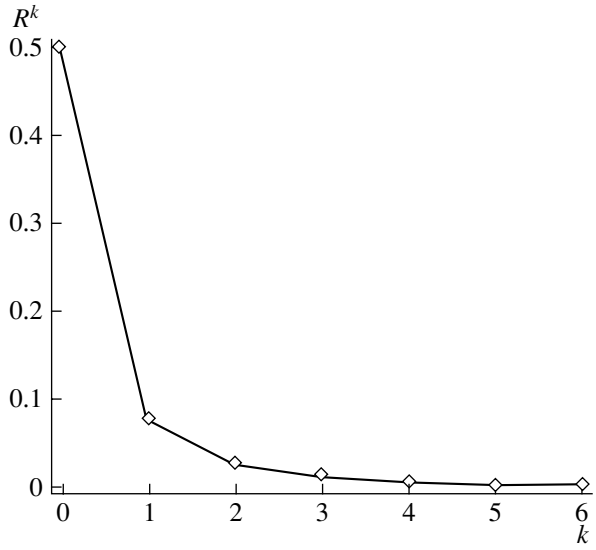

Fig. 7. Relative error R_k in the reconstruction of the crack tips versus the iteration number k for $\kappa = 4.9$, $\theta_1 = 0.4$, and $\theta_2 = 0.6$.

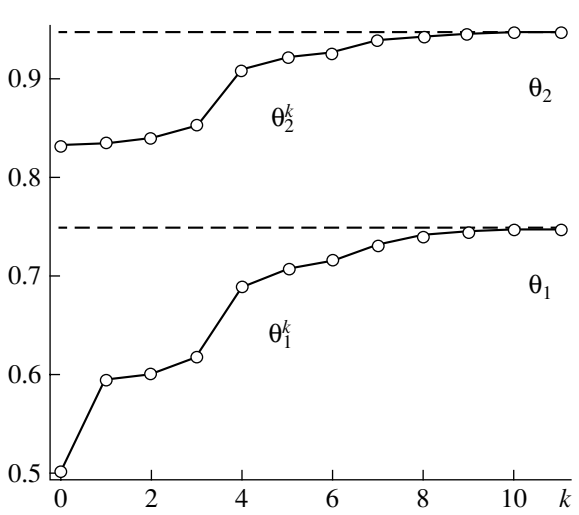

Fig. 8. Approximate values obtained for the crack tips θ_1^k and θ_2^k versus the iteration number k for $\kappa = 2.2$, $\theta_1 = 0.75$, and $\theta_2 = 0.95$.

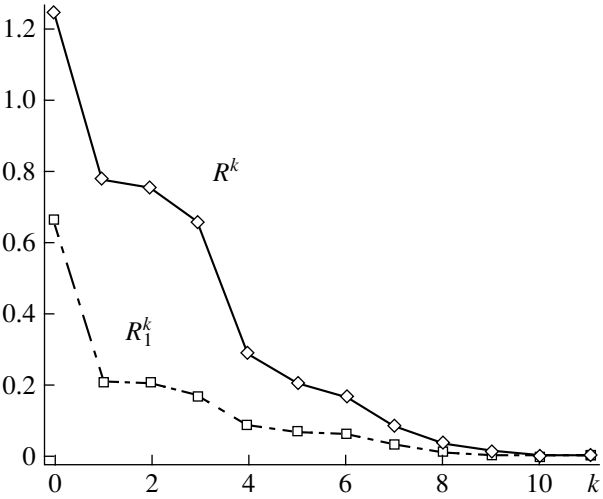

Fig. 9. Relative errors in reconstructing the crack tips, R^k, and the crack length, $R_1^k = \dfrac{\left|\theta_2^k - \theta_1^k - (\theta_2 - \theta_1)\right|}{\theta_2 - \theta_1}$, versus the iteration number k for $\kappa = 2.2$, $\theta_1 = 0.75$, and $\theta_2 = 0.95$.

frequency of vibrations increases, the rate of convergence of the identification process grows. It should be noted that, in all of the calculations, the crack length is reconstructed long before the crack tips are identified. This is illustrated in Figs. 8 and 9: Fig. 8 shows the results of reconstructing the tips of a near-surface crack, and Fig. 9, the results of reconstructing the tips (the solid line) and the length (the dotted–dashed line) of a crack at $\kappa = 2.2$.

The error in the reconstruction of the crack tips was studied as a function of the frequency and the input data error. Different numbers of position-probing points were used. A uniformly distributed random error δ (in percentage of the displacement field amplitude) was additively introduced into the input data of the inverse problem (the displacement amplitudes at the position-probing points). The numerical experiments showed that, when the number of position-probing points was small (one to three points), the accuracy of the reconstruction of the crack tips at the frequencies at which up to three travelling waves were present was as follows: when the input data error δ was about 1–2%, the error

in the tip reconstruction was 3–8%; when δ was about 5%, the error in the tip reconstruction was 15–32%.

Note that an increase in the number of traveling waves (at a fixed input data error) improves the resolution of the proposed method.

On the whole, we conclude that the proposed method allows one to reconstruct those cracks whose length is no smaller than one-fourth of the wavelength of the probing signal. From the point of view of the reconstruction problem, acceptable frequencies are those at which two to three travelling waves are present (when the error in the input data of the inverse problem is 1–5%).

ACKNOWLEDGMENTS

This work was supported by the Russian Foundation for Basic Research (project no. 02-01-01124) and by a grant from the President of the Russian Federation in Support of the Leading Scientific Schools (grant no. NSh-2113.2003.1).

REFERENCES

1. A. Boström and H. Wirdelius, J. Acoust. Soc. Am. **97**, 2836 (1995).
2. A. B. Roĭtman, Akust. Zh. **46**, 685 (2000) [Acoust. Phys. **46**, 601 (2000)].
3. V. Z. Parton and V. G. Boriskovskiĭ, *Dynamics of Brittle Fracture* (Mashinostroenie, Moscow, 1988) [in Russian].
4. D. E. Budreck and J. D. Achenbach, J. Appl. Mech. **55**, 405 (1988).
5. G. Krishnasamy, L. Schmerr, T. J. Rudolphi, and F. J. Rizzo, ASME Trans. J. Appl. Mech. **57**, 404 (1990).
6. S. Mukherjee and Y. X. Mukherjee, ASME Trans. J. Appl. Mech. **65**, 300 (1998).
7. V. Sladek and J. Sladek, Mech. Res. Commun. **17**, 281 (1990).
8. V. A. Babeshko, Dokl. Akad. Nauk SSSR **307** (2), 324 (1989).
9. E. V. Glushkov and N. V. Glushkova, Prikl. Mat. Mekh. **60**, 282 (1996).
10. A. O. Vatul'yan and I. A. Guseva, Prikl. Mat. Mekh. **57**, 149 (1993).
11. S. M. Belotserkovskiĭ and I. K. Lifanov, *Numerical Methods in Singular Integral Equations and Their Application in Aerodynamics, Elasticity Theory, and Electrodynamics* (Nauka, Moscow, 1985) [in Russian].
12. A. N. Tikhonov and V. Ya. Arsenin, *Methods for Solving Ill-Posed Problems* (Nauka, Moscow, 1979) [in Russian].
13. I. I. Vorovich and V. V. Babeshko, *Mixed Dynamic Problems of the Theory of Elasticity for Nonclassical Regions* (Nauka, Moscow, 1989) [in Russian].
14. A. O. Vatul'yan and I. V. Baranov, in *Proceedings of VI International Scientific and Engineering Conference on Dynamics of Technological Systems* (Rostov-on-Don, 2001), Vol. 1, pp. 105–109 [in Russian].

Translated by E. Golyamina

Acoustical Physics, Vol. 51, No. 4, 2005, pp. 392–396. Translated from Akusticheskiĭ Zhurnal, Vol. 51, No. 4, 2005, pp. 463–468.

The Influence of the Electrode Diameter on the Diffraction Effects in the Ultrasonic Field Generated by an Oscillating Piezoelectric Disk

V. V. Galanin and V. S. Kononenko

Volga State Academy of Telecommunications and Information Science, ul. L. Tolstogo 23, Samara, 443010 Russia

e-mail: galanin_v@mail.ru

Samara State Technical University, ul. Pervomaĭskaya 18, Samara, 443100 Russia

e-mail: physics@sstu.samara.ru

Received December 22, 2003

Abstract—The problem of ultrasound radiation by a finite-size source is considered. A boundary-value problem is formulated and solved for ultrasonic waves generated by an oscillating piezoelectric disk fixed along its edge and characterized by an eigenfrequency spectrum and a corresponding oscillation amplitude distribution. The influence of the size of electrodes on the diffraction effects arising in the ultrasonic field of the piezoelectric disk is theoretically investigated. © *2005 Pleiades Publishing, Inc.*

In the majority of publications devoted to the calculation of the ultrasonic field generated by a piston transducer, the dependence of the diffraction effects on the transducer parameters is not considered [1–7]. In [8, 9], an approach was proposed for calculating the diffraction field produced by an oscillating piezoelectric disk fixed along its edge and characterized by a specific eigenfrequency spectrum and a corresponding oscillation amplitude distribution. In connection with these studies, it has become possible to investigate how the ultrasonic field produced by a piezoelectric transducer in a liquid depends on the diameter of its electrodes. The topicality of this problem is determined by the wide practical application of ultrasonic transducers with diameters exceeding the diameters of their electrodes.

A general solution to the problem of plate oscillations has not yet been obtained [10–12]. Therefore, to solve the problem of interest, we consider a circular piezoelectric plate fixed along its edge and emitting radiation into a liquid layer, whose opposite side is represented by a rigid baffle with a receiving circular piezoelectric plate built into it. We seek an approximate solution for a narrow-band signal of finite duration under the assumption that the emitted and reflected pulses are separated in time and that multiple reflections can be ignored. In addition, since the effect of transverse and Lamb waves is negligible to a first approximation for sufficiently thin piezoelectric disks [8], the shear oscillations of the piezoelectric plate can be excluded from our consideration. With these assumptions, we can easily obtain a solution to the problem stated above and consider the dependence of the diffraction corrections on the parameters of the system.

Let us consider oscillations of a circular isotropic piezoelectric plate of radius a that is fixed along its edge in a hole of a rigid baffle of the same thickness. A similar plate is used as the receiver. We use a cylindrical coordinate system with the coordinates r, φ, z. Let the emitting and receiving piezoelectric plates have the same radius a and thickness d and be separated by a distance L from each other. The z axis passes through the centers of the plates. The surfaces of the emitting piezoelectric plate coincide with the planes $z = -d$ and $z = 0$, and the surfaces of the receiving plate, with the planes $z = L$ and $z = L + d$.

Since the plates are rigidly fixed along their contours, the following boundary conditions should be satisfied:

$$\begin{aligned} u_1 = 0 \text{ at } u_3 = 0 \text{ at } r = a, \\ u_{2,1} = 0 \text{ at } r \geq a, \quad z = 0 \text{ and } z = L, \end{aligned} \tag{1}$$

where u_1, $u_{2,1}$, and u_3 are the displacements of particles of the emitting piezoelectric plate, the liquid layer, and the receiving piezoelectric plate, respectively.

Taking into account that the electrode radius may be smaller than the radius of the piezoelectric plates, we should complement boundary conditions (1) with the following requirement for the electric induction D_1 in the emitting plate:

$$\begin{aligned} D_1 = D_{10} \text{ for } r \leq a_1, \\ D_1 = 0 \text{ for } r > a_1, \end{aligned} \tag{2}$$

where D_{10} is the electric induction of the field produced by the voltage applied to the electrodes and a_1 is the

radius of the electrode of the emitting piezoelectric plate.

Let ultrasonic waves generated in the emitting plate, the liquid layer, and the receiving piezoelectric plate be described by the Helmholtz equation

$$\frac{\partial^2 u_j}{\partial r^2} + \frac{1}{r}\frac{\partial u_j}{\partial r} + \frac{\partial^2 u_j}{\partial z^2} + \frac{\omega^2}{c_j^2}u_j = 0, \tag{3}$$

where u_j is the displacement of particles in the medium with number j ($j = 1, 2, 3$), c_j is the velocity of wave propagation in this medium, and ω is the cyclic frequency.

The solution to Eq. (3) for the liquid should take into account the pulsed nature of the ultrasonic signal: we assume that, within the duration of the exciting pulse, the oscillations in the disk are steady and the radiation is stationary. Because the exciting pulse and the reflected signal are separated in time, no reflected signal is present in the liquid at the boundary $z = 0$. By contrast, at the boundary $z = L$, the reflected wave should be included in the boundary conditions. Therefore, in view of the symmetry of the sound field with respect to the z axis and with allowance made for boundary conditions (1), we seek the solution to Eq. (3) in the form

$$u_1 = \sum_{n=1}^{\infty} J_0\left(\frac{\nu_{0n} r}{a}\right)\left(A_n e^{-ik_n z} + B_n e^{ik_n z}\right) \quad \text{for } -d \le z \le 0, \tag{4}$$

$$u_{2,1} = \int_0^{\infty} e^{-i\beta z} J_0(\alpha r) f(\alpha)\alpha d\alpha = C(r, z)e^{-ik_2 z} \quad \text{for } 0 \le z < L, \tag{5}$$

$$u_2 = u_{2,1} + u_{2,2} = C(r, z)e^{-ik_2 z} + D(r, z)e^{ik_2 z} \quad \text{for } 0 < z \le L, \tag{6}$$

$$u_3 = \sum_{m=1}^{\infty} J_0\left(\frac{\nu_{0m} r}{a}\right)\left(E_m e^{-ik_m z} + F_m e^{ik_m z}\right) \quad \text{for } L \le z \le L + d. \tag{7}$$

Here, the wave numbers $k_n^2 = k_1^2 - \nu_{0n}^2/a^2$ and $k_m^2 = k_3^2 - \nu_{0m}^2/a^2$ determine the eigenfrequencies of oscillations for the emitting and receiving piezoelectric plates; k_1, k_2, and k_3 are the wave numbers for the emitting piezoelectric plate, the liquid, and the receiving plate, respectively; ν_{0n} and ν_{0m} are the roots of the zero-order Bessel function; $\beta^2 = k_2^2 - \alpha^2$; α is an independent variable; $f(\alpha)$ is the distribution function of the radial wave amplitudes, which is determined from the boundary conditions; and A_n, B_n, E_m, F_m, $C(r, z)$, and $D(r, z)$ are quantities associated with the amplitudes of waves propagating along the z axis in the positive and negative directions. For the liquid layer, we have two expressions that take into account the pulsed nature of the piezoelectric plate excitation. Formula (5) describes the ultrasonic field at the emitting piezoelectric plate in the absence of the signal reflected from the receiving plate, and formula (6) describes the ultrasonic field at the receiving piezoelectric plate with both incident and reflected waves being present in the liquid.

The boundary conditions at the surfaces of the piezoelectric plates have the form

$$T_1 = 0 \text{ at } z = -d, \tag{8}$$

$$T_1 = T_2 \text{ at } z = 0, \tag{9}$$

$$u_1 = u_{2,1} \text{ at } z = 0, \tag{10}$$

$$T_2 = T_3 \text{ at } z = L, \tag{11}$$

$$u_{2,3} = u_3 \text{ at } z = L, \tag{12}$$

$$T_3 = 0 \text{ at } z = L + d. \tag{13}$$

Here, T_1 and T_3 are elastic stresses in the emitting and receiving plates; the quantity $T_2 = c_2^D(\partial u_2/\partial z)$ determines the sound pressure in the liquid; $c_2^D = \rho_2 c_2^2$; and ρ_2 and c_2 are the density of the liquid and the sound velocity in it, respectively.

The equations of the piezoelectric effect for the longitudinal oscillation mode have the form [13]

$$T_j = c_j^D \frac{\partial u_j}{\partial z} - hD_j, \tag{14}$$

$$E_j = -h\frac{\partial u_j}{\partial z} + \beta^s D_j, \tag{15}$$

where E_j and D_j are the strength and induction of the electric field in the emitting ($j = 1$) and receiving ($j = 3$) piezoelectric plates, $c_j^D = \rho_j c_j^2$ are the elastic moduli at a constant induction, ρ_j and c_j are the densities of the piezoelectric plates and the longitudinal wave velocities in them, h is the piezoelectric constant, and β^s is the inverse dielectric permittivity.

Substituting Eqs. (4)–(7) and (14) into boundary conditions (8)–(13), we obtain six equations in six unknowns: A_n, B_n, E_m, F_m, $C(r, z)$, and $D(r, z)$. Solving these equations, we determine the displacement u_3 as a function of the output voltage of the receiving piezoelectric plate. Let us consider the solution step by step. We substitute u_1 and $u_{2,1}$ given by Eqs. (4) and (5) into

Eqs. (6), (7), and (10); then, we multiply the resulting equalities by $(r/a^2)J_0(\nu_{0m}r/a^2)$ and integrate them with respect to r from 0 to a. Because of the orthogonality of the Bessel functions, the terms with $m \neq n$ will vanish from the sum. From the resulting set of equations in three unknowns A_n, B_n, and $C(r, 0)$, we derive an expression for $C(r, 0)$:

$$C(r, 0) = \frac{4ihD_{10}}{c_1^D}\sum_{n=1}^{\infty} J_0\left(\frac{\nu_{0n}r}{a}\right)\frac{k_n L_{1,n} R_n}{\nu_{0n}J_1(\nu_{0n})}\sin^2\frac{k_n d}{2}, \quad (16)$$

where

$$R_n^{-1} = \gamma_n \cos k_n d + i \sin k_n d,$$

$$\gamma_n = \frac{c_2^D k_2}{c_1^D k_n}, \quad L_{1,n} = \frac{a_1 J_1(\nu_{0n}a_1/a)}{aJ_1(\nu_{0n})}.$$

To determine the quantity $u_{2,1}$, in view of Eq. (1), we represent the boundary conditions for $z = 0$ from the side of the liquid layer in the following form:

$$\begin{cases} u_{2,1} = C(r, 0), & 0 \le r < a \\ u_{2,1} = 0, & r \ge a. \end{cases} \quad (17)$$

Applying the Hankel integral transformation to Eq. (5) with allowance for condition (17) and calculating the known integral of the Bessel functions, we obtain

$$f(\alpha) = \frac{4ihD_{10}a^2}{c_1^D}\sum_{n=1}^{\infty}\frac{k_n}{k}L_{1,n}R_n\sin^2\frac{k_n d}{2}\frac{J_0(x)}{(\nu_{0n}^2 - x^2)},$$

where $x = \alpha a$.

From this formula, in view of Eq. (5), we obtain an expression for $u_{2,1}$:

$$u_{2,1} = \frac{4ihD_{10}}{c_1^D}\sum_{n=1}^{\infty}\frac{L_{1,n}R_n}{k_n} \times \sin^2\frac{k_n d}{2}\int_0^{\infty} e^{-i\beta z} J_0\left(\frac{rx}{a}\right)\frac{J_0(x)x\,dx}{(\nu_{0n}^2 - x^2)}. \quad (18)$$

This expression describes the acoustic field produced by an oscillating piezoelectric plate fixed along its edge with allowance for diffraction.

Using boundary conditions (10)–(12), we obtain expressions for E_m and F_m. We substitute Eqs. (6) and (7) into Eqs. (10)–(12), multiply the resulting expressions by $(r/a^2)J_0(\nu_{0m}r/a^2)$, and integrate them with respect to r from 0 to a. As a result, for the displacements at the receiving plate, we obtain

$$u_3 = \frac{16ihD_{10}}{c_1^D}\sum_{m=1}^{\infty} J_0\left(\frac{\nu_{0m}r}{a}\right)\frac{\nu_{0m}R_m}{J_1(\nu_{0m})} \times \cos(k_m(z - L - d))\sum_{n=1}^{\infty}\frac{L_{1,n}R_n}{k_n}\sin^2\frac{k_n d}{2}I_{mn}, \quad (19)$$

where

$$I_{mn} = \int_0^{\infty} e^{-i\beta z}\frac{xJ_0^2(x)dx}{(\nu_{0m}^2 - x^2)(\nu_{0n}^2 - x^2)}. \quad (20)$$

Setting $D_3 = 0$ and using Eq. (15), we determine the voltage amplitude at the receiving piezoelectric plate:

$$U = \frac{2h}{a^2}\int_L^{L+d} dz \int_0^{a_2}(\partial u_3/\partial z)r\,dr,$$

where a_2 is the radius of the receiving plate electrode. Substituting expression (19) for u_3 in the above formula, we obtain

$$U = \frac{64ih^2 D_{10}}{k_2 c_2^D}U_{mn}, \quad (21)$$

$$U_{mn} = \sum_{m=1}^{\infty}\gamma_m L_{2,m}R_m\sin^2\frac{k_m d}{2} \times \sum_{n=1}^{\infty}\gamma_n L_{1,n}R_n\sin^2\frac{k_n d}{2}I_{mn}, \quad (22)$$

$$L_{2,m} = \frac{a_2 J_1(\nu_{0m}a_2/a)}{aJ_1(\nu_{0m})}. \quad (23)$$

Taking into account that $h = k_t c_1\sqrt{\rho_1/\varepsilon_1\varepsilon_0}$, $D_{10} = \varepsilon_1\varepsilon_0 U_1/d$ [13], and $k_1 d = \pi$, we arrive at the following expression for U:

$$U = \frac{64ik_t^2 U_1}{\gamma\pi}U_{mn}, \quad (24)$$

where $\gamma = c_2^D k_2/c_1^D k_1$ is the liquid-to-plate acoustic resistance ratio, k_t is the electromechanical coupling coefficient, ε_1 is the relative dielectric permittivity at constant strain, $\varepsilon_0 = 8.85 \times 10^{-12}$ F/m, and U_1 is the voltage amplitude at the exciting piezoelectric plate.

In Eq. (24), n is the number of a frequency in the oscillation spectrum of the excited piezoelectric plate

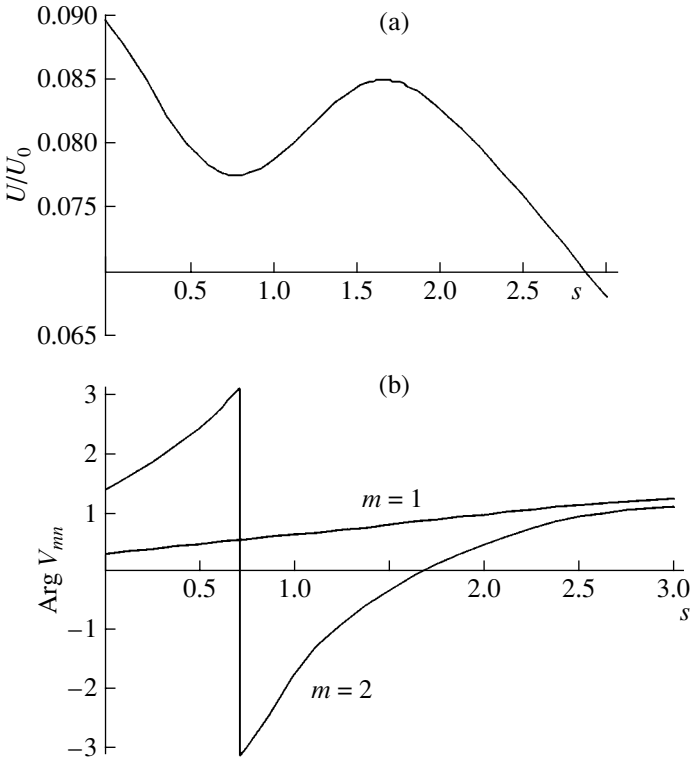

Fig. 1. (a) Ratio of the absolute values of the voltage amplitudes at the receiving plate $|U|/|U_0|$ and (b) the argument of U_{mn} for the natural oscillations of the receiving plate with $m = 1$ and $m = 2$ versus the generalized distance s at $k_2a = 100$, $\gamma = 0.1$, and $a_1/a = a_2/a = 1$.

and m is the number of a frequency in the oscillation spectrum of the receiving piezoelectric plate.

We determined the diffraction damping decrement A for the electric signal at the receiving plate as a function of the parameters k_2a, $s = \lambda z/a^2$, and γ according to the formula $A = 20\log(|U_0|/|U|)$, where U_0 is the value of U at $s = 0$. The ratio k_2/k_1 was set equal to 4, and the liquid-to-plate acoustic resistance ratio was $\gamma = 0.1$.

Figure 1a shows the ratio between the absolute values of voltage amplitudes at the receiving plate $|U|/|U_0|$ versus the generalized distance s. Figure 1b shows the argument of U_{mn} versus the distance s for the natural oscillations of the receiving plate with indices $m = 1$ and $m = 2$ (the inclusion of natural oscillations with $m \geq 3$ does not qualitatively change the situation because of their small amplitude). From the plots, one can see that, as s increases, the natural oscillations of the receiving piezoelectric plate are first combined in antiphase, then in phase, and then again in antiphase. Correspondingly, the minimum of the function $|U|/|U_0|$ changes to a maximum, whereas, for the dependence $A(s)$, an opposite dynamics is observed (Fig. 2).

Figure 2 presents the dependence of the diffraction damping decrement A on the generalized distance s for different values of the ratio between the electrode radius and the radius of the piezoelectric plates. To explain the behavior of the curves, we take into account that, in Eqs. (4) and (7), the distribution of the natural oscillation amplitude along the plate radius is determined by the zero-order Bessel function. As a result, the plate surface can be divided into parts oscillating with opposite phases. These parts are separated by

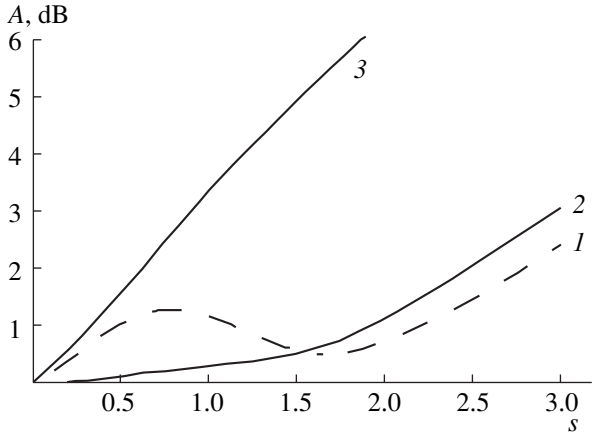

Fig. 2. Diffraction damping decrement A of the electric signal at the receiving plate versus the generalized distance s for different ratios between the electrode radii and the radius of the piezoelectric plates at $k_2a = 100$ and $\gamma = 0.1$: (*1*) $a_1/a = a_2/a = 1$; (*2*) $a_1/a = 1$ and $a_2/a = 0.68$; and (*3*) $a_1/a = a_2/a = 0.50$.

nodal curves of circular shape. The number of such parts is determined by the indices m or n, and the radius of the nodal curves corresponds to the roots of the Bessel function $J_0(\nu_{0m,n}r/a)$. Depending on the electrode radii, the radius mean for the displacement of particles of the piezoelectric plate particles varies; hence, the contribution made by each single mode to the amplitude of the resulting plate oscillation determined by Eq. (24) also varies. For example, the radius mean for the natural oscillation of the receiving plate with $m = 2$ is negative when the condition $\nu_{02}a_2/a < \nu_{11}$ is satisfied (see Eq. (23)), where ν_{02} is the second root of the zero-order Bessel function and ν_{11} is the first root of the first-order Bessel function. If the condition $\nu_{02}a_2/a \geq \nu_{11}$ is satisfied, the contribution made by the aforementioned natural oscillation is positive or equal to zero. The results of our calculations showed that, when the ratio of the electrode radius to the plate radius is the same for the emitting and receiving plates, the diffraction damping decrement A increases (curve *3* in Fig. 2), because the natural oscillations that make the greatest contribution to the amplitude of the received signal suppress each other. By contrast, the diffraction damping decrement A decreases (curve *2* in Fig. 2) when the size of the emitting plate coincides with the size of its electrodes and the radius of the receiving plate exceeds the radius of its electrodes. In this case, a mutual amplification of natural oscillations with small indices m and n takes place.

Thus, in this paper, we developed a theoretical approach to solving the boundary-value problem for an oscillating piezoelectric disk fixed along its edge when the diameter of the disk is greater than that of its electrodes. We studied the diffraction damping decrement of the ultrasonic signal as a function of the generalized distance between the emitting and receiving piezoelectric plates. We considered the influence of the parameters of the measuring system on the diffraction of the ultrasonic field generated by the oscillating piezoelectric plate. We analyzed the dependences of the diffraction damping decrement on the generalized distance s for different ratios between the electrode radii and the radius of the piezoelectric plates.

The results obtained can be used for the purpose of reducing the diffraction losses in precision measurements of the absorption coefficient and propagation velocity of ultrasonic waves in low-viscosity liquids at frequencies of ~1 MHz by choosing the appropriate parameters of the measuring system.

REFERENCES

1. M. Reewood, Proc. Phys. Soc. London **70**, 721 (1957).
2. E. F. Garome, J. M. Witting, and P. A. Fleury, J. Acoust. Soc. Am. **30**, 1417 (1961).
3. P. Tabuchi, Y. Tannaka, and T. Okuda, Mem. Ind. Res. Osaka Univ. **27**, 1 (1970).
4. Y. Tannaka, Acustica **23**, 328 (1970).
5. K. Brendel and C. Ludwig, Acustica **32**, 110 (1979).
6. L. Bosselar, R. C. Chivers, and P. R. Filmore, J. Acoust. Soc. Am. **68**, 80 (1980).
7. J. D. Aindov, R. C. Chivers, and A. Markiwicz, J. Acoust. Soc. Am. **78**, 1519 (1985).
8. V. S. Kononenko and P. K. Khabibullaev, Dokl. Akad. Nauk **340**, 39 (1995) [Phys. Dokl. **40**, 3 (1995)].
9. V. V. Galanin and V. S. Kononenko, Akust. Zh. **48**, 609 (2002) [Acoust. Phys. **48**, 535 (2002)].
10. B. Laulagnet, J. Acoust. Soc. Am. **103**, 2451 (1998).
11. T. Imamura, Bull. Natl. Res. Lab. Metrol. (Tokyo) **47** (4), 45 (1998).
12. L. Shuyu, Acust. Acta Acust. **86**, 388 (2000).
13. D. Berlincour, D. Kerran, and H. Jaffe, in *Physical Acoustics: Principles and Methods*, Ed. by W. P. Mason (Academic, New York, 1964; Mir, Moscow, 1966), Vol. 1, Part A.

Translated by E. Golyamina

Acoustical Physics, Vol. 51, No. 4, 2005, pp. 397–403. Translated from Akusticheskiĭ Zhurnal, Vol. 51, No. 4, 2005, pp. 469–476.

Correlation Characteristics of Pseudonoise Signals in the Ocean at a Highly Directional Reception

O. P. Galkin and S. D. Pankova

Andreev Acoustics Institute, Russian Academy of Sciences, ul. Shvernika 4, Moscow, 117036 Russia

e-mail: bvp@akin.ru

Received July 2, 2003

Abstract—Data of experiments with single-path and multipath reception of broadband continuous pseudonoise acoustic signals (0.8–1.3 kHz) in a deep ocean are discussed. The experiments were carried out on tracks from ~ 60 to ~ 420 km in length, which corresponds to the first seven convergence zones. The data on the cross-correlation coefficients and arrival time differences are presented (for the first, second, and seventh zones) for signals received by one highly directional (~2°) vertical array or by two such arrays simultaneously at depths of 200 and 450 m. The correlation characteristics of signals propagating over purely water paths, i.e., without reflections from the waveguide boundaries, and arriving under different angles in the vertical plane are compared. It is found that the origin of the decorrelation of signals received from various directions or at different depths (all other factors being the same) is the incomplete resolution of the received multipath signals in the arrival angle in the vertical plane. *© 2005 Pleiades Publishing, Inc.*

The study of the temporal and correlation structure of acoustic fields generated by the sound sources in the ocean is necessary for the development of an adequate model of an oceanic waveguide, as well as for the solution of a number of applied problems [1–4]. In this case, the experimental data received under actual oceanic conditions are of special value, because they automatically take into account the effect of various oceanographic factors. Such data allow one to modify the existing models of oceanic waveguides and to introduce corrections into the newly developed models, the construction of which is discussed in a number of publications [5–7].

In the deep ocean, the sound field at the reception point in most cases represents the superposition of the signals arriving from the sound source over various rays. In this case, individual components forming a multipath signal can differ from one another not only in the signal arrival angles in the vertical plane but also in the focusing factors and the times of arrival at the reception point.

The spatial resolution of the received signals in the arrival angle in the vertical plane can be realized with the use of highly directional arrays developed in the vertical direction. In order to separate individual components of a multipath signal by their arrival times, correlation processing is usually applied.

The aim of this paper is the experimental estimation of the effect of multipath propagation on the correlation characteristics and fluctuations in the arrival time differences of the received signals propagating to the reception point along different paths.

For the correct solution of the stated problem, it is necessary to eliminate completely (or to a large extent at least) the influence of other factors that in principle may lead to a decorrelation of the received signals. Because in the deep ocean (3–5 km), neither the receiving system nor the source can be rigidly fixed in space (at depths of 100–500 m), the experiments were carried out using drifting research vessels. This, naturally, led to a displacement of the acoustic track in space. Therefore, in the test region, during the period of the experiments, the sound velocity profiles should not undergo any significant changes for any position of the track. Besides, it was necessary to use only the signals that propagate without reflections from the waveguide boundaries, which allows one to eliminate the effect of the relief and structure of the bottom and the effect of the rough ocean surface. Note that, to obtain more reliable data on the correlation and temporal characteristics of the signals, most of the measurements should be carried out on those sections of the track where the received signal-to-noise ratio was maximum. As is known, this condition is satisfied in the convergence zones. Therefore, the experiments were mainly carried out in these zones.

With allowance for these considerations, the experiments were carried out in a deep-water region of the Atlantic ocean south west of the Canary Islands. This region is characterized by a very low spatial variability of oceanic conditions and almost completely satisfies the above-mentioned conditions.

The experiments were carried out as follows. At chosen points of the test track, one of the research ships of the Acoustics Institute, with the use of an omnidirec-

1063-7710/05/5104-0397$26.00

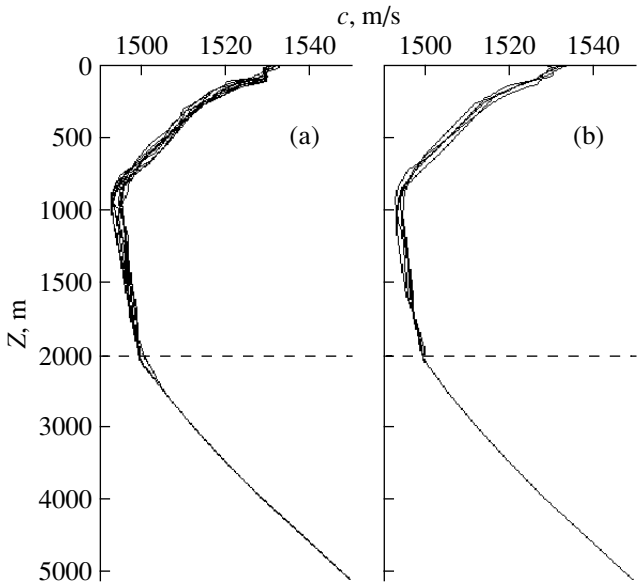

Fig. 1. Sound velocity profiles measured near (a) the receiving point and (b) the transmitting point during the whole time of the experiment.

tional source, emitted a continuous pseudonoise signal in a wide frequency band from 0.8 to 1.3 kHz. During the experiments, the source depth was 200 m. The other ship—the receiving one—carried two vertical 40-m-long arrays, which were lowered to various depths through specific trunks of bathyposts located on the ship diametral. The horizontal distance between the trunks was about 45 m. Each array had the form of a flexible pipe only 5 cm in diameter with 296 hydrophones mounted inside it and combined into 74 phase centers. For stretching the flexible arrays in the vertical position, 800-kg loads were attached to their lower ends. The central hydrophone of one of the arrays was at a depth of ~200 m, and that of the second array, at a depth of ~450 m. The signals arriving at each array from different directions in the vertical plane were simultaneously received by three directional patterns formed by the analog method. One of the main lobes of these patterns could be used not only in the guidance mode but also in the scanning mode in the angular range of ±(20°–23°). The spatial resolution in the arrival angle was ~2° at the mean frequency of the emitted range. The measurements of the angular, temporal, and correlation structures of the sound field were carried out at distances from ~60 to ~420 km, which corresponds to the convergence zones. The ocean depth in the test region was about 5 km and remained almost invariable along the whole propagation track up to a distance of 420 km.

The receiving ship with lowered arrays was drifting during the experiment, so that its position varied rather slowly. The transmitting ship passed from one point to another along the test track, and at the necessary distances it drifted and emitted signals. The total time of the experiment was 14 days, including the time necessary for passages. The depth dependences of the sound velocity $c(z)$ measured during the experiment at the receiving and transmitting ships are shown in Figs. 1a and 1b, respectively. As follows from the plots, the profiles $c(z)$ do not undergo any significant changes.

The underwater sound channel axis was located at a depth of about 900 m. During the experiments, the wind and the surface roughness were less than Beaufort 2–3. Therefore, the deflection of the arrays from the vertical was less than 1° and the maximum changes in the array depths did not exceed 1.5 m. Under such almost ideal conditions, the cross-correlation functions and the arrival time differences were measured for those signals propagating over water rays, i.e., arriving without reflections from the waveguide boundaries. Since the experiments were carried out in convergence zones, the signal-to-noise ratio noticeably exceed unity. Therefore, in the experiment, most attention was given to an estimation of the influence of the spatial resolution of signals in the arrival angle in the vertical plane on the aforementioned characteristics.

The normalized cross-correlation functions $R(\tau)$ between signals received from different directions in the vertical plane (including the case of arrays located at different depths) were calculated within 4–5 min (with an interval of 20 s) with a time of averaging T = 0.85 s. At this time of averaging, the error in the calculation of the coefficients $R(\tau)$ can be estimated from the formula $\xi = \frac{1}{\sqrt{\Delta f T}}$ [8], where Δf is the frequency band. For the given experimental conditions (Δf = 500 Hz and T = 0.85 s), the error does not exceed 5%.

The maximum interval of estimated time delays was $\tau_{max} = \pm 50$ ms with a step of 0.125 ms. The accuracy of the determination of arrival time differences, proceeding from the mean frequency of the emitted signal (about 1 kHz) and the possible change in the sign of the correlation peak, was no worse than 0.5 ms.

Let us consider the results of measurements of the angular, temporal, and correlation structure of the sound field that were carried out in the two near (the first and second) and one far (the seventh) convergence zones.

In the first zone (at a distance of 59.8 km), one of the realizations of the angular structure of the sound field recorded simultaneously at the above-mentioned depths of reception (450 and 200 m) is shown in Fig. 2. It exhibits a photograph of the screen of a sector scan indicator in the range of arrival angles in the vertical plane ±20° (for obtaining more accurate values of the angles, the range ±20° on the screen is expanded to ~±120°). The inner scan refers to a reception depth of 450 m, and the outer one, to a depth of 200 m. The thick radial dashes indicate the angles to which the main lobes of the directional patterns of each of the arrays were pointed in the course of the correlation measurements. The angular width of the response of both arrays

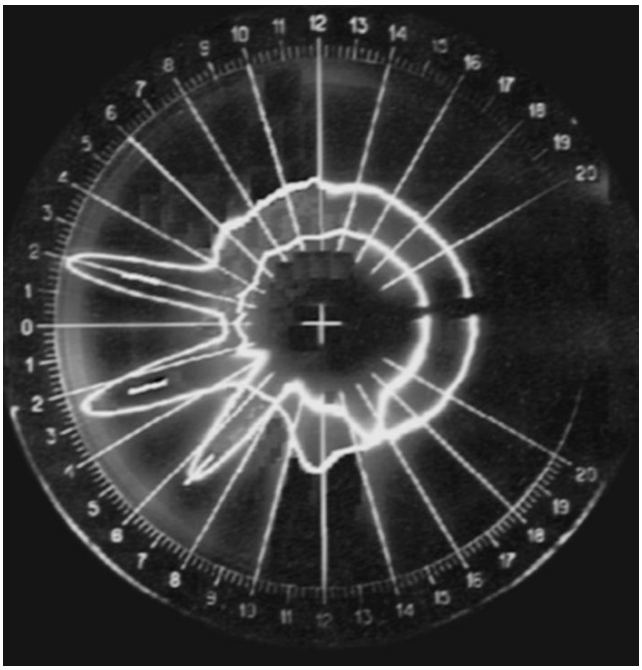

Fig. 2. Photograph of the screen of the sector scan indicator. The inner scan refers to a depth of 450 m, and the outer scan, to a depth of 200 m. The distance is 117.3 km. The strokes indicate the directions of signal arrivals.

in each of the signal arrival directions almost corresponds to that of a plane wave. This indirectly points to a complete spatial resolution of the received signals. The chosen signals arrived at angles $\alpha_1 = -6.5°$ (at a reception depth of 450 m) and $\alpha_2 = -2.5°$ and $\alpha_3 = +2°$ (for the array at a depth of 200 m). The minus sign means that the signal arrives at the array from below, and the plus sign, from above. The signals with indicated arrival angles propagated over purely water rays, i.e., without reflections from the waveguide boundaries; their recorded angles were smaller than the grazing angles of the rays touching the ocean surface (~10° for a depth of 450 m and ~7.5° for a depth of 200 m). Figure 3 (the upper plot) shows the autocorrelation functions $R_1(\tau)$, $R_2(\tau)$, and $R_3(\tau)$ of the signals arriving from each of the indicated directions. The lower plot in Fig. 3 exhibits the cross-correlation functions $R_{1-2}(\tau)$, $R_{1-3}(\tau)$, and $R_{2-3}(\tau)$ between the chosen signals (the subscripts 1–2, 1–3, and 2–3 indicate the numbers of the signals with the arrival angles α_1 and α_2, α_1 and α_3, and α_2 and α_3, for which these functions were calculated). Since each of the autocorrelation functions $R_1(\tau)$, $R_2(\tau)$, and $R_3(\tau)$ has a single pronounced maximum (peak), which corresponds to the complete spatial resolution of the` received signals, each of the cross-correlation functions also has one pronounced peak. Note that the form of these peaks almost coincides with the autocorrelation function of the emitted signal. Such a "single-path" signal reception simultaneously from two or three directions in the vertical plane was

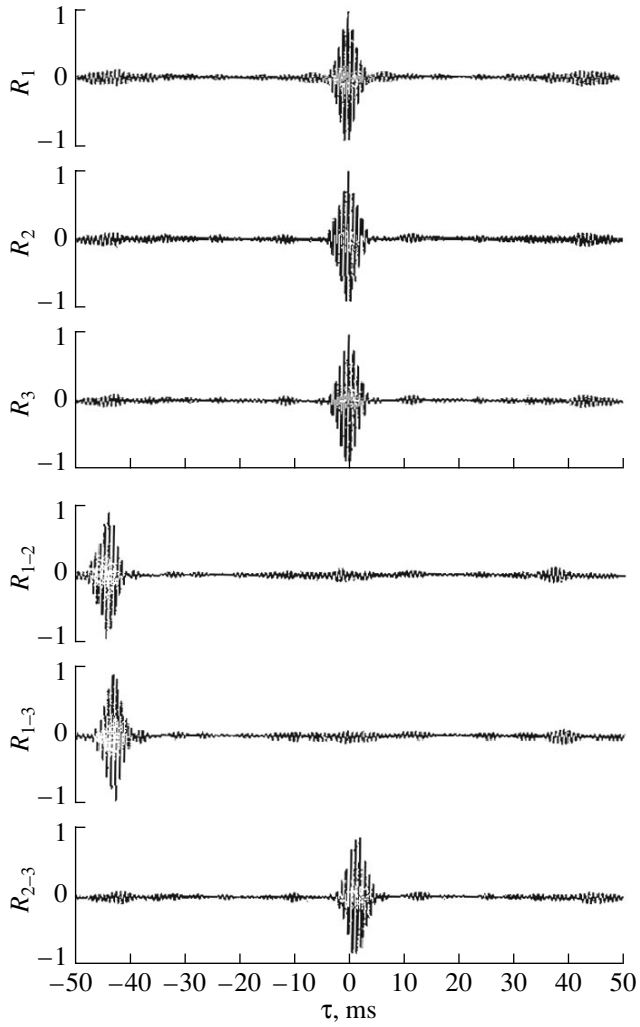

Fig. 3. Autocorrelation and cross-correlation functions of signals received in the first convergence zone with an almost complete spatial resolution of rays.

recorded in a number of other cases, especially in experiments in the first and second convergence zones. The results of calculating the cross-correlation coefficients and fluctuations of arrival time differences of the signals with an almost complete spatial resolution are presented in Table 1. The first four columns of Table 1 present the following: the distance r between the points of emission and reception and also the signal arrival angles α_1, α_2, and α_3 and the depths h at which the signals were received. The two right-hand columns (from top to bottom) present the values of the cross-correlation coefficients $R_{1-2}(\tau)$, $R_{1-3}(\tau)$, and $R_{2-3}(\tau)$ averaged, as was indicated above, over 4–5 min in 20–25 independent measurements and the fluctuations of the arrival time differences σ_τ for the same time intervals. The boldface print shows the results of the measurements described above and presented in Figs. 2 and 3.

The analysis of the data presented in Table 1 shows that, under an almost complete spatial resolution of the

Table 1

r, km	α_1°/h, m	α_2°/h, m	α_3°/h, m	$\lvert R\rvert$	σ_τ, ms
57.5	–11°/450	–6°/200	–7.5°/450	0.88	0.52
				0.87	0.39
				0.85	0.54
58.2	–6°/450	–8°/200	+3°/200	0.90	0.54
				0.90	0.46
				0.95	0.34
59.8	–6.5°/450	–2.5°/200	+2°/200	0.87	0.49
				0.89	0.54
				0.93	0.38
115.2	–10°/450	–7°/450		0.91	0.35
115.8	–6°/200	–2°/200		0.89	0.17
116.9	–7°/450	–3°/200		0.89	0.42
117.0	–8°/450	–6°/200	0°/200	0.87	0.38
				0.88	0.26
				0.91	0.31
117.5	–8.5°/450	–5.5°/200	–1.5°/200	0.84	0.49
				0.87	0.35
				0.95	0.15
118.2	–7°/200	–2°/200		0.91	0.35
118.5	+6°/200	–1.5°/200	–6°/200	0.91	0.31
				0.90	0.43
				0.91	0.43
119.7	+4°/200	–4°/200	0°/200	0.90	0.28
				0.89	0.30
				0.90	0.32
121.5	+1°/200	+8°/450		0.94	0.35

signals in arrival angle in the vertical plane, the cross-correlation coefficients are rather large and vary from 0.84 to 0.95, while the fluctuations of the arrival time differences vary from 0.15 to 0.54 ms. Their values are almost independent of both distance and reception depth (i.e., reception at one depth or at two different depths).

Here, it is necessary to note that similar conclusions (about the large values of the cross-correlation coefficients and the relatively small fluctuations of signal arrival time differences) were made for single-path signals received not only at different depths but at different distances, i.e., recorded in different convergence zones [9–12].

Consider now the results obtained in the cases when the arriving signals cannot be resolved in angle even using systems that are highly directional in the vertical plane. In these situations, the shape of the main lobe of the directional pattern is distorted: it is broadened and usually becomes asymmetric. A reliable determination of the number of received signals is only possible from the arrival time differences. Then, in the correlation processing, two variants are possible: a partial or a complete resolution of the signals in the arrival time. Figure 4 illustrates the first variant corresponding to the partial resolution of the received signals in the arrival time. The upper plot exhibits three autocorrelation functions, and the lower plot, three cross-correlation functions of the signals received in the second convergence zone at a distance of 117.3 km. The form of the uppermost autocorrelation function corresponding to the reception at a depth of 450 m at the angle $\alpha_1 \cong -6.6°$ is close to that of the autocorrelation function of the emitted signal. Hence, from this direction, an almost single-path reception is realized. Two other autocorrelation functions for $\alpha_2 \cong -6.3°$ and $\alpha_3 \cong +2°$, which correspond to the reception at a depth of 200 m (especially the second one for α_2), have a single but broadened correlation peak. Such a pattern arises when the arrival time differences of the signals getting into the main lobe of the directional pattern of the array are smaller than the correlation interval. Naturally, the peaks of the cross-correlation functions $R_{1-2}(\tau)$, $R_{1-3}(\tau)$, and $R_{2-3}(\tau)$ (especially where the second signal with the arrival angle α_2 is present) become asymmetric and differ in shape from one another.

The second variant arising under the correlation processing of signals that cannot be resolved in angle represents an almost complete resolution of the signals in their arrival times.

Figure 5 exhibits the autocorrelation functions (the upper plot) and the cross-correlation functions (the lower plot) of the multipath signals recorded in the seventh convergence zone at a distance of 416 km. It illustrates the two possible variants of the correlation determination of the number of the received signals with both incomplete and complete resolution of the signals in arrival times. The correlation function $R_1(\tau)$ refers to the signal reception at a depth of 450 m from the direction $\alpha_1 = -8°$; the other functions $R_2(\tau)$ and $R_3(\tau)$ refer to the signal reception at a depth of 200 m with the angles $\alpha_2 = -4°$ and $\alpha_3 = -1°$. From the number of correlation peaks and their positions, it follows that, in the first case ($R_1(\tau)$), the signals arrived over four rays, three of which are well-resolved but the fourth of which is combined with the third; in the second case ($R_2(\tau)$), the signals arrived over three rays, two of which were poorly resolved in time (broad maxima); in the third case ($R_3(\tau)$), the signals arrived over two rays with a good resolution in time. In the cross-correlation functions $R_{1-2}(\tau)$, $R_{1-3}(\tau)$, and $R_{2-3}(\tau)$, one can see several correlation maxima. However, they are clearly pronounced only in $R_{1-3}(\tau)$, where four correlation peaks point to the arrival of no less than four signals. In two other plots ($R_{1-2}(\tau)$ and $R_{2-3}(\tau)$), both complete and par-

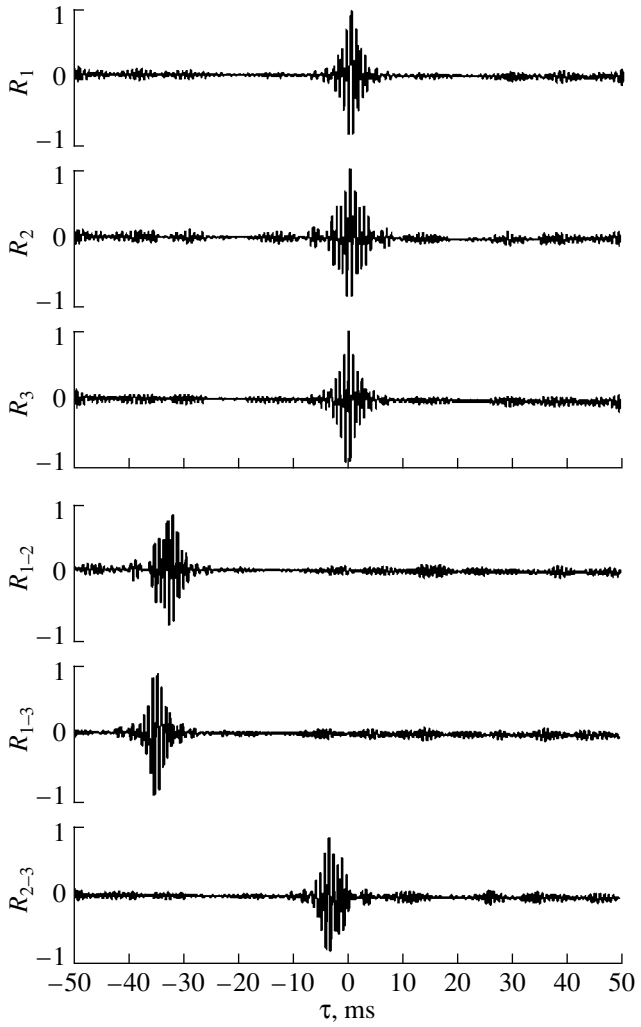

Fig. 4. Autocorrelation and cross-correlation functions of signals received in the second convergence zone with an incomplete spatial resolution of rays.

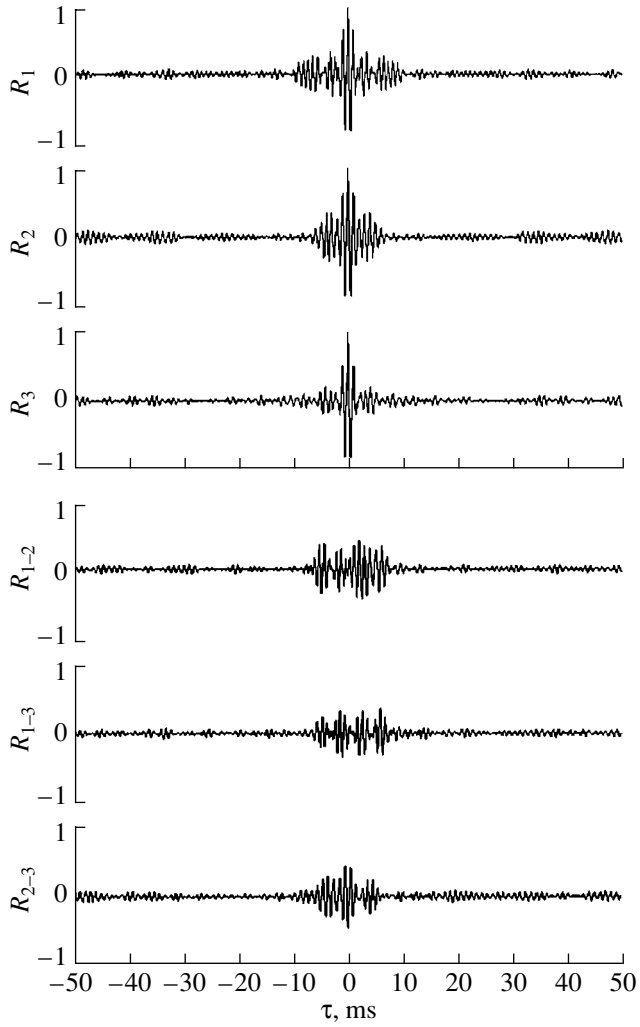

Fig. 5. Autocorrelation and cross-correlation functions of the signals received in the seventh convergence zone with both incomplete and complete resolution in arrival time.

tial resolutions of signals in the arrival time are observed. Thus, Fig. 5 allows one to state that each main lobe of the directional pattern received multipath signals arriving over two to four rays. Because their intensities were almost equal, the corresponding correlation peaks characterizing the energy of the received signals also proved to be practically equal. One can see that, in the case of the multipath reception, a noticeable decrease in the correlation coefficients is observed as compared to the single-path reception. This is related to the fact that the same signals arriving with slightly different times lead to a reduction of each separate peak, because they represent a kind of noise in the correlation processing. Such a singular noise is usually called signal-induced noise. That is why, in this case, the maximum values of the correlation coefficients did not exceed 0.5.

Table 2 presents the results of measurements of the cross-correlation functions for the case of the multipath reception in the first and second convergence zones, and Table 3 presents the results for the seventh convergence zone. The first three columns of these tables present the distance r between the points of emission and reception, the signal arrival angles α_1 and α_2, and the depths h at which the signals were received. The second-to-last column of each of these tables presents the magnitudes of the highest correlation maxima $|R|_{\max}$ (the upper numbers) and of the secondary peaks (the lower numbers). The last column presents the rms fluctuations of the arrival time differences σ_τ. The results of measurements that were described above and were presented in Figs. 4 and 5 are shown in boldface.

The data obtained in the Canary region of the Atlantic ocean and presented in this paper confirm the previous conclusions [9–12] that the fluctuations of the arrival time differences of signals, even including the measurement errors, almost coincide with the theoretical estimates [13], which relate them to the effect of

Table 2

r, km	α_1°/h, m	α_2°/h, m	$\frac{/R/_{max}}{/R/}$	σ_τ, ms	r, km	α_1°/h, m	α_2°/h, m	$\frac{/R/_{max}}{/R/}$	σ_τ, ms
60.2	+7°/200	+2°/200	0.83	0.36	117.0	–9°/450	–6°/200	0.64	0.31
			0.42	0.23				0.52	0.31
60.2	+2°/200	–2°/200	0.84	0.28	117.0	–8°/450	–1°/200	0.79	0.49
			0.47	0.36				0.30	0.44
66.6	+7.5°/200	+7°/450	0.74	0.24	117.3	–6.6°/450	+2°/200	0.87	0.38
			0.32	0.56	117.3	–6.6°/450	–6.3°/200	0.79	0.32
			0.47	0.51				0.44	0.43
68.5	+7°/450	+3°/450	0.79	0.41	117.3	–6.3°/200	+2°/200	0.81	0.37
			0.26	0.96				0.46	0.32
69.0	+11°/450	+7°/450	0.68	0.26	120.5	+6°/450	–7°/200	0.79	0.27
			0.62	0.38				0.31	0.46
			0.53	0.38	120.9	+6°/200	–6°/200	0.66	0.49
69.0	–11°/450	+7°/450	0.53	0.59				0.46	0.42
			0.47	0.50	120.9	–6°/200	+2.5°/200	0.64	0.50
115.2	–7.5°/450	–1°/200	0.57	0.27				0.45	0.36
			0.34	0.26	122.5	+2°/200	–0.5°/200	0.77	0.35
			0.32	0.29				0.40	0.62
115.2	–8°/450	–2°/200	0.66	0.34	122.8	–10.5°/450	+7.5°/450	0.50	0.69
			0.51	0.50				0.33	0.26
115.5	–5°/200	0°/200	0.66	0.23	123.4	+11°/450	+8.5°/450	0.56	0.27
			0.32	0.33				0.40	0.24
116.5	–7.5°/450	–5.5°/200	0.72	0.49	130.2	+10°/450	–10°/450	0.45	0.71
			0.60	0.50				0.37	0.62
116.5	–7°/200	–2°/200	0.66	0.50	132.4	+10°/450	–10°/450	0.46	0.56
			0.55	0.13				0.34	0.70
116.7	–7°/200	–3°/200	0.66	0.22	132.6	+10°/450	–7°/200	0.60	0.24
			0.40	0.12				0.40	0.58

inhomogeneities of the water column. The cross-correlation coefficients of the signals received by highly directional arrays at different depths separated by several hundreds of meters (the maximum separation of highly directional arrays in the experiments in other regions of the ocean reached 1200 m) can be rather large, especially at a good angular resolution of rays in the vertical plane (in the case under study, in the first and second convergence zones they may be up to 0.95). Thus, the vertical correlation interval can reach hundreds or even thousands of sound wavelengths. Such conclusions noticeably differ from those made on the basis of experiments carried out in a deep ocean with the use of omnidirectional hydrophones (see, e.g., [14]). These experiments showed that the vertical and horizontal correlation intervals are within approximately 10λ and 100λ (λ is the sound wavelength). However, in fact, such relatively small correlation intervals are not related to variations in the structure of individual signals propagating over different rays but rather are caused by the multipath propagation conditions in the waveguide. The latter phenomenon considerably reduces the cross correlation of signals at a spatial separation of the points of reception. Therefore, the key factor reducing the correlation coefficient between signals received by the arrays is the poor resolution of rays.

Thus, the results of the experiments with highly directional arrays (~2°) in the vertical plane, which were carried out in various regions of the ocean [9–12] at different distances and depths, showed that the main origin of the decorrelation of signals is the incomplete

Table 3

r, km	α_1°/h, m	α_2°/h, m	$\frac{\lvert R\rvert_{\max}}{\lvert R\rvert}$	σ_τ, ms
415.8	–3.5°/200	+1.5°/200	0.62	0.39
			0.43	0.45
415.9	–8°/450	–5°/200	0.68	0.33
			0.27	0.21
415.9	–5°/200	0°/200	0.59	0.68
			0.49	0.27
415.95	+2°/200	–5°/200	0.63	0.21
			0.39	0.25
415.95	+2°/200	–2°/200	0.59	0.31
			0.47	0.38
415.95	–5°/200	–2°/200	0.72	0.16
			0.51	0.0
416.0	–8°/450	–4°/200	0.53	0.25
			0.39	0.22
			0.31	0.30
			0.26	0.25
416.0	–8°/450	–1°/200	0.39	0.32
			0.35	0.40
			0.27	0.46
			0.24	0.48
416.0	–4°/200	–1°/200	0.51	0.51
			0.30	0.45
			0.26	0.38

resolution of multipath signals in arrival angle in the vertical plane. Therefore, for signals propagating without reflection from the waveguide boundaries, after the elimination of the multipath propagation feature, the intervals of spatial correlation almost reach the waveguide thickness in the vertical and exceed tens and hundreds of kilometers in the horizontal direction.

ACKNOWLEDGMENTS

This work was supported by the Russian Foundation for Basic Research (project no. 03-02-16565) and by the Ministry of Industry and Science of the Russian Federation (grant no. NSh-1277.2003.5)

REFERENCES

1. S. P. Czenszak and J. L. Krolik, J. Acoust. Soc. Am. **101**, 749 (1997).
2. G. J. Orris, M. Nicholas, and J. S. Perkins, J. Acoust. Soc. Am. **107**, 2563 (2000).
3. J. L. Spiesberger, J. Acoust. Soc. Am. **109**, 1997 (2001).
4. C. Soares and S. M. Jesus, J. Acoust. Soc. Am. **113**, 2587 (2003).
5. F. J. Beron-Vera and M. G. Brown, J. Acoust. Soc. Am. **114**, 123 (2003).
6. M. G. Brown, J. A. Colosi, S. Tomsovic, *et al.*, J. Acoust. Soc. Am. **113**, 2533 (2003).
7. M. A. Wolfson and S. Tomsovic, J. Acoust. Soc. Am. **109**, 2693 (2001).
8. J. Max, *Methodes et Techniques de Traitement du Signal et Applications aux Mesures Physigues* (Masson, New York, 1981; Mir, Moscow, 1983), Vol. 2.
9. O. P. Galkin and S. D. Pankova, Akust. Zh. **45**, 479 (1999) [Acoust. Phys. **45**, 426 (1999)].
10. O. P. Galkin and S. D. Pankova, Vopr. Sudostr., Ser. Akust., No. 15, 13 (1982).
11. O. P. Galkin and S. D. Pankova, Akust. Zh. **46**, 467 (2000) [Acoust. Phys. **46**, 400 (2000)].
12. O. P. Galkin and S. D. Pankova, Akust. Zh. **49**, 481 (2003) [Acoust. Phys. **49**, 402 (2003)].
13. N. G. Kuznetsova and L. A. Chernov, Vopr. Sudostr., Ser. Akust., No. 15, 5 (1982).
14. W. M. Carey, J. Acoust. Soc. Am. **104**, 831 (1998).

Translated by Yu. Lysanov

Acoustical Physics, Vol. 51, No. 4, 2005, pp. 404–409. Translated from Akusticheskiĭ Zhurnal, Vol. 51, No. 4, 2005, pp. 477–482.

Reversal of Waves in Forward-Scattering Location

V. A. Zverev

Institute of Applied Physics, Russian Academy of Sciences, ul. Ul'yanova 46, Nizhni Novgorod, 603600 Russia

e-mail: zverev@hydro.appl.sci-nnov.ru

Received August 27, 2003

Abstract—Potentialities of the pulsed acoustic forward-scattering location with the use of time separation of the intense direct and weak scattered signals propagating at a small angle to one another are considered. Two types of interference are taken into account: nonstationary observation conditions under the effect of currents, which affect the arrival times of the direct and scattered signals, and nonstationary reverberation. It is shown that, in the presence of these interferences, the application of the correlation transformation equivalent to the time reversal of waves has an advantage over the conventional location technique based on the determination of the signal travel times. © *2005 Pleiades Publishing, Inc.*

A problem of the detection of objects by their scattered radiation is considered in a series of publications [1–6]. In [1], from a full-scale experiment, the minimum target strength of a scatterer that can be separated from the direct signal by a multielement array at continuous radiation is determined. In [2, 3], the same problem is solved using the frequency shift that occurs in the scattered signal because of the scatterer motion. In [4], a method for constructing images of scatterers moving under a layer of inhomogeneities is proposed. In [5, 6], a pulsed location regime is considered. In [5], the spectrum of a pulsed signal is smoothed out with an extension of the effective frequency band to achieve the time separation of the direct and scattered signals. In [6], the problem of detecting the scatterers and determining their coordinates by scanning multi-element transmitting and receiving arrays under stationary conditions and in free space is solved. In [6], the signal processing used for the detection of scatterers and determination of their coordinates includes the time reversal of waves [7, 8]. The time reversal of waves allows one to eliminate the effect of inhomogeneities of the medium on the result of spatial focusing in it when the medium contains random inhomogeneities. However, in spite of the statement formulated in [6], nothing is known about the possibility of a noise-resistant observation of scattered signals with the use of the time reversal of waves. It is also unclear how one should apply the time reversal of waves to obtain a noise-resistant selection of scattered signals and what should be the results of this procedure. The authors of [6] concentrate on the spatial resolution of the method, which proves to be very high under the conditions of a stationary problem, a homogeneous medium, and the complete absence of noise and interference. The aim of the present paper is an investigation of the efficiency of the time reversal of waves [7, 8] for the selection of a weak scatterer under the combined action of two most widespread types of interference. First of all, these are the temporal variability of the wave propagation velocity and the nonstationary reverberation.

The time-reversed acoustics consists of the time reversal of a received pulses signal with a subsequent backward transmission of the reversed signal through the same medium. The result of the time reversal of waves [7, 8] can be represented as the convolution of the input signal with the correlation function of two responses of the medium, one of which is the response to the short pulse propagating in the forward direction and the other of which is the response to the same pulse propagating in the backward direction. A successful realization of this transformation requires retaining all parameters of the test medium during the whole experiment, including the forward and backward wave propagation. This is necessary for the corresponding signals to correlate with one another.

The time reversal of waves provides the spatial focusing of a reversed wave, which requires the propagation of the time-reversed signal in the backward direction. However, for the purpose of selecting the scattered signals, spatial focusing is not necessary: it is sufficient to receive the reversed wave at the point where it was initially emitted. In this case, the result of the time reversal can be obtained on the basis of one-way propagation of a wave from the transmission point to the point of reception, since, in this case, the cross-correlation function is reduced to the autocorrelation function. The autocorrelation function of the response to the input signal can be obtained on the basis of a one-way run of the wave. The resulting mathematical expression slightly differs (without any fundamental consequences) from the expression for the reversed wave received at the point of emission. In return, the requirement for the stationary state is completely removed, which is important for acoustics of liquid and

1063-7710/05/5104-0404$26.00

gaseous media. This is the main idea of achieving the noise immunity of the reversal of waves with respect to nonstationary conditions.

To illustrate the methods of calculations and their results, let us consider a specific example. The layout of the experiment is shown in Fig. 1. The pulsed signal is emitted from the point *A* (Fig. 1). This signal is received at the point *B*. The scatterer to be detected is at the point *O*. The delay time of the scattered signal with respect to the direct signal is also necessary to determine its target strength. The geometric difference ΔR in the path length between the direct and scattered signals can be estimated by the formula

$$\Delta R = a^2/R, \tag{1}$$

where *a* is the minimum distance between the point *O* and line *AB* (Fig. 1) and *R* is the length of the line *AB*. Formula (1) is valid for large distances *R* compared to *a* and for the position of point *O* relatively far from the end points of the interval *AB*. The pulse duration Δt is assumed to be sufficiently small for the direct and scattered signals to be separated in arrival time. For this purpose, it is necessary that

$$\Delta t < \Delta R/c, \tag{2}$$

where *c* is the wave propagation velocity.

Since our aim is to study the noise immunity of the time reversal of waves, it is sufficient to consider the simplest situation, shown in Fig. 1. In the general case, the number of scatterers can be more than one, as in [6]. The spectrum of the signal received at the point *B* has the form

$$G_B(\omega) = F(\omega)z(\omega). \tag{3}$$

Here, ω is the frequency, $F(\omega)$ is the spectrum of the emitted pulse, and $z(\omega)$ is the frequency characteristic of the wave propagation channel between points *A* and *B*. The frequency characteristic is the response of the channel to the transmission of the shortest possible pulse of unit area (a δ pulse). For realizing the time reversal of a wave, one needs to emit, from the point of reception, a signal reversed in time. The spectrum of such a signal is the complex conjugate of spectrum (3). In this case, the spectrum of the signal received at the point of emission will be [8]

$$G_A(\omega) = F^*(\omega)z^*(\omega)z(\omega). \tag{4}$$

To realize the procedure that leads to obtaining the signal spectrum described by Eq. (4), two sequential steps are necessary [7]: the first is to obtain spectrum (3), and second, to emit the time-reversed signal into the same medium. Under nonstationary conditions, this is impossible, since the medium varies. However, we can use the response that is already formed at the point *B* as a result of the arrival of the pulse sent from the point *A* for obtaining the spectrum of the following signal:

$$K(\omega) = G_B^*(\omega)G_B(\omega) = F^*(\omega)z^*(\omega)F(\omega)z(\omega). \tag{5}$$

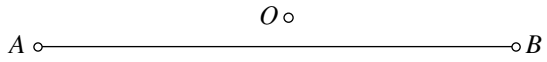

Fig. 1. Experiment layout used in the calculations. The source, receiver, and scatterer are positioned at the points *A*, *B*, and *O*, respectively.

Let us compare formulas (4) and (5). They differ by a factor that is equal to the spectrum of the emitted signal. This difference is insignificant for our purpose. Therefore, we assume that transformation (5), which will be used for noise-resistant separation of scatterers, represents the spectrum of the result of the time reversal of waves.

Now, we use a numerical example to show that transformation (5) possesses an enhanced noise immunity as compared to the separation of a scattered signal by the conventional location technique. First of all, we show that formula (5) is sufficient for separating the scattered signal. The spectrum of the signal received at the point *B* is the sum of the direct signal and the scattered one, which has the form of the direct signal delayed for the time determined by Eq. (3):

$$G_B(\omega) = F(\omega) + kF(\omega)\exp(i\omega\Delta t). \tag{6}$$

Here, *k* is the attenuation coefficient of the scattered signal with respect to the direct signal, which is determined by the target strength of the scatterer. In general, *k* is a function of ω. For simplicity, we first assume that *k* does not depend on ω. This is possible because the dependence of *k* on ω does not affect the noise immunity of interest. After considering the noise immunity of transformation (5), we will return to the problem of the dependence of *k* on ω. The common factor determining the decay of the direct and scattered signals along the path between *A* and *B* is omitted. Substituting Eq. (6) into Eq. (5), we obtain

$$\begin{aligned} K(\omega) &= F^*(\omega)F(\omega)(1 + kk^*) \\ &+ F^*(\omega)F(\omega)\{k\exp(i\omega\Delta t) + k^*\exp(-i\omega\Delta t)\}. \end{aligned} \tag{7}$$

The problem under consideration is of most interest for weak scatterers, for which the square modulus of *k* is small compared to unity and, therefore, can be neglected. In this approximation, Eq. (7) is generalized to the sum of a series of scatterers while retaining their additivity. As is seen from Eq. (7), transformation (5) is equivalent to the time reversal of waves and contains terms with information on both the magnitude of the scattered signal with respect to the direct signal and the value of the delay of the signal. These terms are delayed with respect to the maximum of the direct signal for the time given by Eq. (3). Therefore, condition (2) is quite sufficient for these terms to be separated and measured.

Figures 2a and 2b show the oscillogram of the initial pulse and its autocorrelation function, respectively. Using these oscillograms, one can clearly demonstrate the difference between Eqs. (4) and (5). In both cases, the respective oscillograms exhibit pulses repeated at

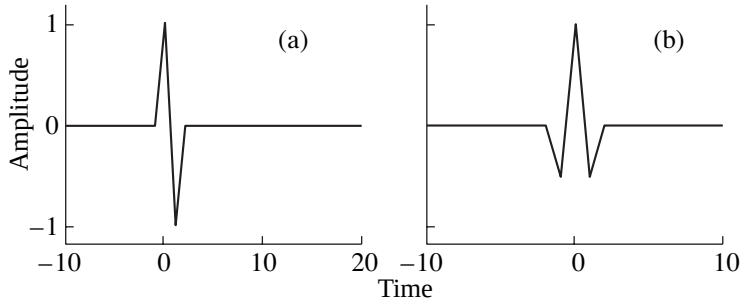

Fig. 2. (a) Oscillogram and (b) autocorrelation function of the emitted pulse.

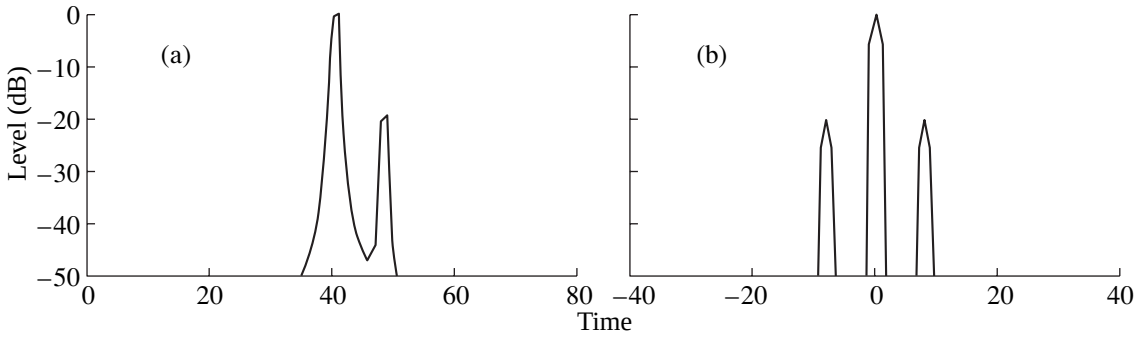

Fig. 3. (a) Level (logarithm of the modulus) of the oscillogram and (b) the autocorrelation function of the received signal.

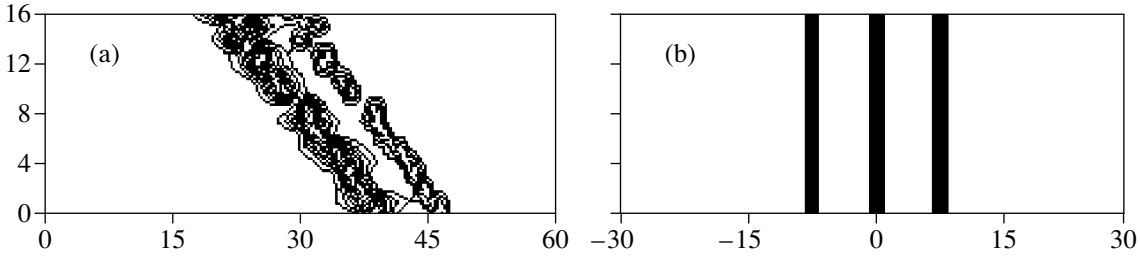

Fig. 4. Locator response as a function of time (vertical) and delay (horizontal) (a) for the conventional locator and (b) for the correlation locator realizing the signal processing according to Eq. (5) at a random variation of the signal travel time.

an interval Δt, but the shape of these pulses is different. Formula (4) corresponds to the pulse shown in Fig. 2a, while formula (5), to the pulse shown in Fig. 2b. Figure 3 shows the levels of the signals received without interference with the use of conventional location (Fig. 3a) and with the use of correlation transformation (5) (Fig. 3b). From these plots, it follows that both methods allow one to detect the presence of the scattered signal (or signals) and to determine its (their) relative magnitude with respect to the direct signal (in the given case, –20 dB), as well as the relative delay (eight units of distance). However, the patterns shown in Figs. 3a and 3b have different sensitivities to variations of such a significant parameter of the problem as the total delay of the direct and scattered signals. Indeed, if we change the total delay, this will be evident only in Fig. 3a, while Fig. 3b will remain unchanged. This is the basis for the higher noise immunity of correlation transformation (5) compared to the conventional location technique.

Let us consider a specific example. First, we introduce interference that is only detected by the conventional location. Assume that, under the effect of currents moving the eddies and temperature inhomogeneities of the medium, the total delay time varies with time. The pattern corresponding to a set of 16 instants is shown for the conventional location in Fig. 4a. In this pattern, both direct and scattered signals are clearly visible, and they perform the common motion in accordance with the variation of the total delay with time. The pattern corresponding to the same instants and processed by correlation method (5) is shown in Fig. 4b.

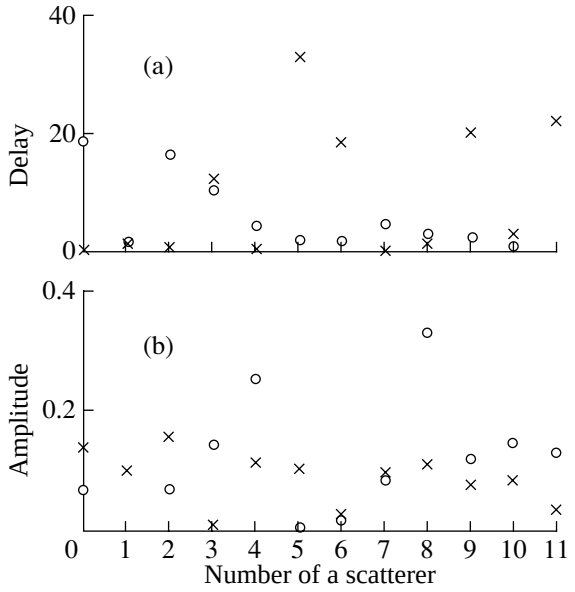

Fig. 5. (a) Delays and (b) amplitudes of signals scattered by scatterers for two (of 16) instants of time. The values corresponding to one instant are represented by crosses, and the values corresponding to the other instant, by circles.

This pattern exhibits a perfect stability, which we must use to gain the advantage in noise immunity. To this end, we add one more type of interference, namely, a time-dependent reverberation in the form of a set of extraneous scatterers. Each scatterer has a very small target strength. However, the number of scatterers is so great that their combined effect is noticeable. Reverberation is a spatial analog of shot noise in electronics. Because of the random character of the summation, the resulting maxima vary in both magnitude and position in space in a random manner [9]. We use this property of reverberation (the random positions and magnitudes of the local maxima) as the basis for the mathematical modeling of reverberation. Examples of such scatterers observed in the experiments on surface reverberation are presented in [10, 11]. From examples presented there, it follows that, in spite of the very large number of initial scatterers, only a few maxima create an actual interference for the location. This fact was taken into account in modeling.

Using random sequences generated by a computer, tables of random numbers were formed that determined the position (the delay with respect to the direct signal) and the amplitude of 12 scatterers for each of 16 instants of time. Figure 5a shows the positions of the scatterers at two instants of time, and Fig. 5b shows their amplitudes. The plot in Fig. 5a shows the path differences between the direct and scattered signals. These path differences were calculated from formula (1) on the basis of random numbers taken from the tables, which characterize the positions of the scatterers. To model the reverberation interference, we used two sets of scatterers that differ in amplitude by a factor of three (10 dB).

The results of adding the reverberation interference are shown in Fig. 6. From this figure, one can see the noise immunity of correlation transformation (5) in comparison with the conventional location. While in Fig. 6a*1*, under a relatively weak reverberation, the delayed signal is still visible, in Fig. 6a*2*, under an enhanced reverberation, this signal is not visible at all. At the same time, in Fig. 6b*1* and even in Fig. 6b*2*, the delayed signal is evident. As the reverberation level increases, the delayed signal rapidly (within several decibels) disappears from these patterns as well. In Fig. 6b*1*, the reverberation signal in most cases is still lower than the amplitude of the delayed signal distorted by the superposition of reverberation. In Fig. 6b*2*, the rever-

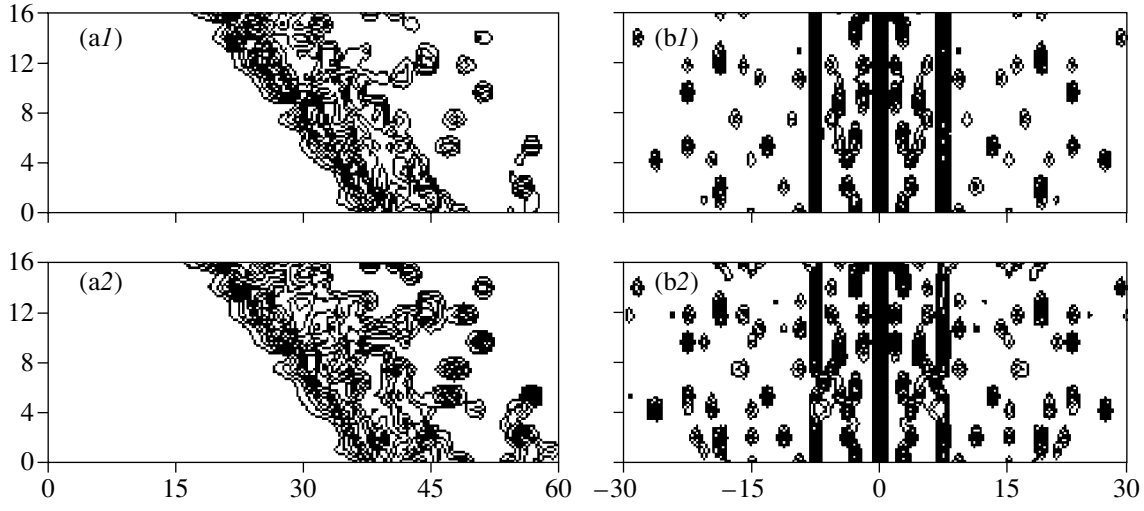

Fig. 6. Locator response as a function of time (vertical) and delay (horizontal) (a) for the conventional locator and (b) for the correlation locator realizing signal processing according to Eq. (5) at a random variation of the signal travel time with two levels of reverberation: (*1*) a low reverberation level and (*2*) a 10-dB-higher reverberation level.

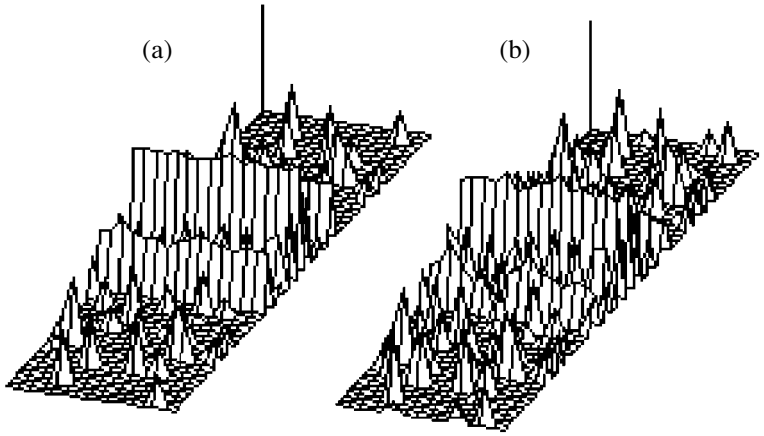

Fig. 7. Logarithm of the positive value of the locator response as a function of time (horizontal) and delay (depth) for the correlation locator realizing the signal processing according to Eq. (5) at a random variation of the signal travel time with two levels of reverberation: (a) a low reverberation level and (b) a 10-dB-higher reverberation level.

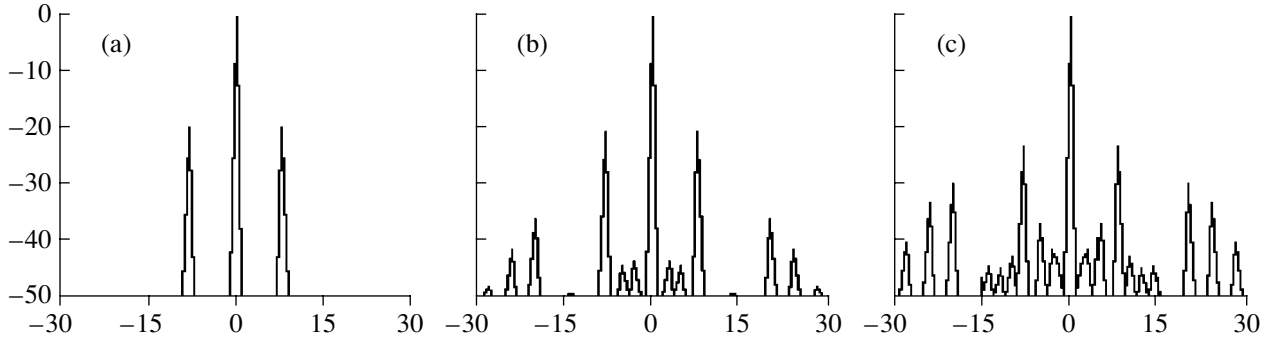

Fig. 8. Amplitudes of the positive values of signals accumulated over 16 instants of time in the correlation channel (a) in the absence of reverberation, (b) at a low reverberation, and (c) at a 10-dB-higher reverberation level. The signal level in decibels is plotted along the vertical, and time is plotted along the horizontal.

beration signal (in most pulses) is comparable to or even exceeds the amplitude of the scattered signal. This is evident from Fig. 7, where the data from 6b*1* and 6b*2* are represented on the amplitude scale. In spite of the fact that the desired signal in Fig. 6b*2* does not exceed the reverberation, it is clearly distinguished in this figure due to the effect of accumulation. The possibility of accumulation is provided by the stability of the desired signal position, which is a result of correlation processing (5).

The stability of the position of the desired signal in time gives an advantage in adding signals in time (a temporal accumulation). The result of the temporal accumulation is shown in Fig 8. From this figure, one can see that the cumulative signal exceeds the reverberation signal in all cases.

The specific value of the attainable noise immunity due to the time reversal of waves is determined by many factors, which are not discussed in this paper. For us, the important and sufficient result is the possibility to obtain additional noise immunity upon the reversal of waves.

Now let us return to the dependence of the coefficient k on ω. To determine the dependence of k on ω, one should use a short pulse with a high-frequency carrier, similar to the pulse used in [6]. Such a pulse can be formed so as to localize its spectrum in a very narrow frequency band, where the coefficient k can be considered as constant within the pulse spectrum. To obtain the frequency dependence, one has to change the frequency of the pulse carrier and repeat the measurements.

ACKNOWLEDGMENTS

This work was supported by the Russian Foundation for Basic Research (project no. 02-02-17056) and by the Ministry of Industry and Science (grant no. NSh-1641.2003.2).

REFERENCES

1. A. B. Gershman, V. I. Turchin, and V. A. Zverev, IEEE Trans. Signal Process. **43**, 2249 (1995).

2. V. A. Zverev, Akust. Zh. **46**, 75 (2000) [Acoust. Phys. **46**, 62 (2000)].
3. V. A. Zverev, P. I. Korotin, A. L. Matveev, *et al.*, Akust. Zh. **46**, 650 (2000) [Acoust. Phys. **46**, 569 (2000)].
4. N. V. Zuĭkova, T. V. Kondrat'eva, and V. D. Svet, Akust. Zh. **49**, 183 (2003) [Acoust. Phys. **49**, 148 (2003)].
5. V. A. Zverev, P. I. Korotin, and A. V. Tsiberev, Akust. Zh. **47**, 468 (2001) [Acoust. Phys. **47**, 419 (2001)].
6. S. K. Lehman and A. J. Devaney, J. Acoust. Soc. Am. **113**, 2742 (2003).
7. M. Fink, D. Cassereau, A. Derode, *et al.*, Rep. Prog. Phys. **63**, 1933 (2000).
8. V. A. Zverev, Akust. Zh. **50**, 792 (2004) [Acoust. Phys. **50**, 685 (2004)].
9. Yu. M. Sukharevskiĭ, Dokl. Akad. Nauk SSSR **55** (9), 825 (1947).
10. V. A. Zverev and P. I. Korotin, Akust. Zh. **48**, 340 (2002) [Acoust. Phys. **48**, 292 (2002)].
11. V. A. Zverev and P. I. Korotin, Akust. Zh. **49**, 71 (2003) [Acoust. Phys. **49**, 62 (2003)].

Translated by Yu. Lysanov

Acoustical Physics, Vol. 51, No. 4, 2005, pp. 410–413. Translated from Akusticheskiĭ Zhurnal, Vol. 51, No. 4, 2005, pp. 483–487.

Acoustic Properties of a Human Chest

V. I. Korenbaum* and A. A. Tagil'tsev**

** Il'ichev Pacific Oceanological Institute, Far-East Division, Russian Academy of Sciences, ul. Baltiĭskaya 43, Vladivostok, 690041 Russia*

*** Institute of Physics and Information Technologies, Far East State University, ul. Sukhanova 8, Vladivostok, 690600 Russia*

e-mail: v-kor@poi.dvo.ru

Received December 25, 2003

Abstract—A cross-spectral method for determining the longitudinal velocity of sound in the tissues of a human chest *in vivo* is proposed and substantiated. The method is based on the detection of a percussion stroke by two acoustic sensors positioned over opposite parts of a lung. Statistical estimates are obtained for the longitudinal velocity of sound in chest tissues (the middle part of the right lung) from a group of three men (40–47 years old) without any evident lung disorders in the frequency ranges of 80–130, 170–290, and 350–500 Hz. The adequacy of the double-resonance acoustic model of the human respiratory tract, which combines the resonance of the air volume in the human chest and the wave resonances of the bronchial tree as a narrow pipe, is experimentally verified. © *2005 Pleiades Publishing, Inc.*

INTRODUCTION

Despite exhaustive studies, the acoustic properties of the human respiratory system are still insufficiently investigated [1–3]. One of the acoustic parameters of practical importance [4] is the average velocity of longitudinal sound waves in the tissues of the human chest. This quantity is mainly determined by the sound velocity in the lung parenchyma, which is a complex three-phase medium (air, fluid, and tissue) [5]. The order of magnitude of this quantity estimated in full-scale experiments *in vitro* (for example, [6, 7]) agrees well with theoretical data [8, 5] and constitutes 5–70 m/s. However, other elements affecting sound generation and the velocity of perturbation propagation (the bronchial tree and the chest wall) are also present in the human chest in addition to the parenchyma. The estimates of the sound velocity value for the propagation along the respiratory system, i.e., from the trachea to the chest wall, are rather contradictory: for example, 30 [9] and 280 m/s [10]. Moreover, the value of the sound velocity in the human chest may widely vary depending on the part of the chest and on the specific individual, not to mention its dependence on the frequency range under investigation [11]. The purpose of this work is to study experimentally the distinctive features of the propagation of sound oscillations in a human chest *in vivo*.

ACOUSTIC MODEL

The respiratory system is a narrow branching air-filled pipe surrounded by lung tissue with an acoustic impedance greater than that of the air. The volume of air in the respiratory parts of a lung, i.e., in the acinuses, which are the totality of branching terminal bronchioles, together with the chest wall, form the so-called acoustic resonance circuit [12]. This acoustic system should be characterized by two fundamental resonances.

The frequency of the first of them (the resonance of the acoustic resonance circuit), according to the model of the resonance lid of a pipe [13], can be approximately represented in the form

$$f_{arc} \approx (K/m)^{0.5}/2\pi, \quad (1)$$

where $K = \rho_0 c_0^2/h$ is the stiffness; ρ_0 is the density of air; c_0 is the sound velocity in the air; h is the thickness of the air layer of the parenchyma, which on the average is about 5 mm, according to morphometric data [14]; $m = \rho_W l_W$ is the surface density of the mass of the chest wall; $\rho_W \approx 2000$ kg/m^3 is the average density of the chest wall tissues [4]; and l_W is the thickness of the chest wall, which is equal to 1–2 cm. With these data, the values of the fundamental frequency given by Eq. (1) have an order of magnitude of 110–150 Hz, which is close to the results of [12]. Since the resonance of a vibrating system does not depend on the application point of the driving action, the adequacy of the values obtained for the frequencies of the acoustic resonance circuit is confirmed by observations [15]: it was found that, in the case of a finger stroke (percussion) on the chest wall, "the fundamental frequencies of the percussion tone over healthy parts of lungs are about 100–130 Hz."

On the other hand, the whole bronchial tree as a system of narrow acoustic pipes is characterized by a series of wave resonances. Since, for the frequencies

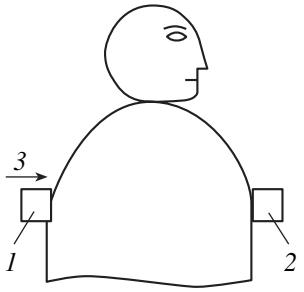

Fig. 1. Scheme of the experiment: (*1*, *2*) acoustic sensors and (*3*) the region of application of the percussion stroke.

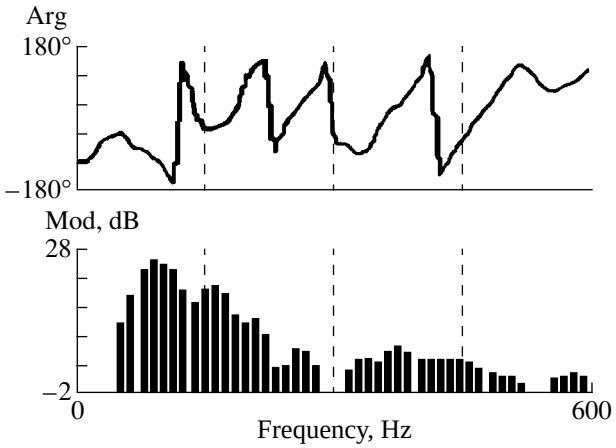

Fig. 2. Cross spectrum of the response of acoustic sensors to the percussion stroke.

$f > f_{arc}$, the impedance of the acoustic resonance circuit has a mass character and $2\pi f_m/\rho_0 c_0 \gg 1$, a quarter-wavelength series must be observed (if the patient breathes with an open mouth, one end of the pipe is open) in full accordance with the results of [16]. The sound velocity in the air ducts of the bronchial tree differs little from the sound velocity in the air [10], and the length of a bronchial tree branch, from the larynx to the chest wall, can be 23–38 cm for adults [14]. Then, the first frequency of the indicated series (the frequency of the quarter-wavelength resonance), under the assumption that the pipe walls are acoustically stiff, must be on the order of 215–350 Hz. Note that this resonance can also be lower in frequency because of a finite compliance of the walls. A standing wave can be excited at these frequencies. The maximum amplitude of sound pressure for this wave should occur at the closed end of the pipe. However, the increase in the total cross section of the pipe with decreasing distance to the chest wall leads to a situation wherein the maximum amplitudes of sound pressure are reached near the large bronchi and the intra-chest part of the trachea [17, 18].

METHOD AND MATERIALS

To estimate the average sound velocity in the chest tissues, we propose the following procedure (Fig. 1). Two identical (*1*, *2*) acoustic sensors (MKE-3 microphones provided with stethoscopic heads with a diameter of 20 mm and a conical cavity height of 10 mm) are positioned over the opposite parts of the right lung (the left lung was not used to exclude the influence of the heart on the results of measurements). The source of sound was a percussion stroke, which was applied near sensor *1* according to the traditional technique by an experienced doctor. The responses of the microphones were recorded by a measuring tape recorder and, after amplification and filtration within the frequency band 50–1500 Hz, were fed to an A/D converter (12 bit) and subjected to digital auto- and cross-spectral processing using a personal computer. The FFT procedure with the discretization rate of 6024 Hz was used (samples with a length of 512 readings, number of spectral readings of 256, weighting by the Hamming window, and averaging over 4–8 samples with a 75% overlap). The phase inaccuracy between the two channels of the measuring system did not exceed 10%.

The method of the sound velocity determination is based on the following considerations. It was assumed that the percussion stroke excites the resonance vibrations of the parenchyma part (the acoustic resonance circuit mechanism), which represents the source of a spherical wave propagating over the chest tissues. In this case, the experimental scheme and the design of the acoustic sensors provide an opportunity to separate the longitudinal sound waves. It is evident that, for a point source of radiation in a homogeneous medium, the phase cross spectrum of the sensors must have the frequency ranges where the phase shift varies according to a linear law. If we select the frequencies f_1 and f_2 within this linear part, the difference between the phase shifts $\Delta\varphi$ can be obtained in the form

$$\Delta\varphi = \varphi_2 - \varphi_1 = 2\pi(f_2 - f_1)L/c_{av}, \qquad (2)$$

where L is the distance between the two acoustic sensors and c_{av} is the average sound velocity in the medium. Since the quantities φ_2, φ_1, f_2, f_1, and L in Eq. (2) can be determined experimentally, the desired value of c_{av} is

$$c_{av} = 2\pi(f_2 - f_1)L/(\varphi_2 - \varphi_1). \qquad (3)$$

The studies were carried out with three volunteers (three men 40–47 years old without evident lung disorders). Four experiments were conducted with each patient (in the middle part of the right lung). The values obtained were averaged in three frequency ranges over the ensemble of the values of c_{av}.

RESULTS AND DISCUSSION

From the analysis of the phase parameters of the cross spectra (for example, Fig. 2), it follows that the probe and received signals contain frequency bands within which the phase shift varies according to a law that is close to linear, which testifies to the regularity of

Table 1. Velocity of longitudinal sound waves in the chest tissues (patient T., the middle part of the right lung)

f_1, Hz	f_2, Hz	φ_1, deg	φ_2, deg	c_{av}, m/s
82.4	117.7	–78.6	–157.8	32
176.5	223.6	–6.6	+155.2	20.1
235.3	294.1	–80.5	+151.1	18.2
341	411	–79.8	+170	20
423	517	–141	+136	24.5

Table 2. Averaged estimates of the velocity of longitudinal sound waves in human chest tissues: M (Q_{25}, Q_{75})

Frequency range, Hz	c_{av}, m/s	Number of measurements
80–130	36.8 (23.1; 46.6)	8
170–290	31.6 (20.1; 37)	10
350–500	52.3 (24.5; 56)	9

radiation from a small region of the chest. The values of the frequencies f_1 and f_2 were selected at the boundaries of this region (to increase the accuracy of linear approximation), and the values of c_{av} were calculated by Eq. (3). In particular, the results obtained for the case shown in Fig. 2 are given in Table 1. These values are certainly approximate estimates because of the nonstationary character of the percussion probe signal itself, the complexity of the chest structure, and the errors connected with the approximation of the actual phase characteristic by a linear dependence. However, despite the indicated inaccuracies, the value of c_{av} is determined *in vivo* and, due to the simplicity and availability of the procedure, can be averaged over large groups of patients and even over certain regions of the chest for uniform groups of patients.

As a preliminary estimate, we obtained the average values for the group of three persons under study. Some of the measurements (up to 30%) were discarded because of the strong irregularity of the phase spectrum. The results of all other measurements were averaged over the three frequency ranges that were present for all patients (80–130, 170–290, and 350–500 Hz). These results are given in Table 2 in the form of a mean value (M) and quartiles (Q_{25} and Q_{75}), since the distribution of variants turned out to be different from the normal distribution (the Shapiro–Vilk test). From Table 2 it follows that the values of c_{av} are sufficiently close to the values obtained *in vitro* for the lung parenchyma [6, 7]. One can also observe, although it is statistically insignificant (the Mann–Whitney test), a frequency dependence of c_{av} with a minimum in the frequency range of 170–290 Hz.

Now, let us consider in more detail the effects connected with the excitation of a probe signal by a percussion stroke. The high-frequency components of a percussion stroke would not be detected on the opposite side of the chest without the excitation of natural resonance vibrations of the chest elements by the same stroke. Indeed, we assumed that a percussion stroke locally excites the resonance of an acoustic resonance circuit. Thus, the presence of the part of the phase characteristic of the cross spectrum (Fig. 2) that is close to linear in the range of 100–150 Hz was presumed. However, apart from the range of 82–118 Hz, which fits into the model under consideration, linear phase regions are present in the ranges of 176–294 and 341–506 Hz in Fig. 2. What is their origin?

To clarify the nature of this effect, let us turn to Fig. 3, which presents an autospectrum for the response of the microphone (part of the record that directly follows the stroke) located near the point of application of the percussion stroke (the same realization as in Fig. 2). It is characterized by pronounced spectral peaks in the

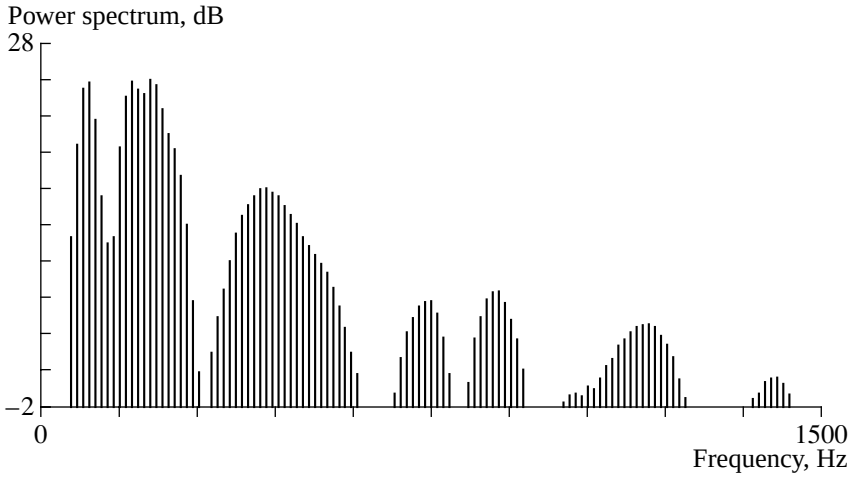

Fig. 3. Spectrum of the response of the nearest acoustic sensor to the percussion stroke.

regions of 100, 200–250, and 400 Hz and weaker peaks in the regions of 750, 900, and 1150 Hz. It is necessary to note that, according to the above acoustic model, the frequency value of 200–250 Hz is characteristic of the quarter-wavelength resonance of the bronchial tree as a narrow pipe. Therefore, the percussion stroke excites this resonance mechanism as well. A peak at the frequency of 450 Hz can be connected with the half-wavelength resonance of the bronchial tree as a narrow pipe. Its appearance is possible because of the complex frequency-dependent character of the impedance of the pipe "lids" at frequencies above 300 Hz or because of the breath arrest by the patient during percussion. In the latter case, the respiratory tract gets closed, which may lead to the appearance of the second rigid lid on the pipe. In this case, the higher-frequency spectral peaks (750, 1150, and 950 Hz) most probably characterize the next modes of the quarter- and half-wavelength series of natural frequencies for the pipe under consideration, respectively. The natural vibrations of the air column that are excited in the bronchial tree pipe are the source of a cylindrical wave propagating in the chest tissues on account of the transformation of a part of the standing wave energy into fluctuations of the lateral wall of the pipe, according to [16, 17]. Since the regions of the maximum amplitudes of the standing wave are located at different levels of the bronchial tree (the quarter-wavelength region is located in the area of the primary bronchi [17], and the half-wavelength region is closer to the chest wall), the propagation path length over the lung tissues for the sound waves in these frequency ranges considerably varies. Analogous considerations can be found in [11, 19]. Thus, it is possible that the observed minimum of c_{av} (Table 2) is connected not only with the dispersion of the longitudinal sound velocity in the tissue of the lung parenchyma but also with the variation of the propagation path length along the parenchyma. The propagation through the air channels presumably does not noticeably influence this effect, because the corresponding sound velocity is about an order of magnitude higher than the sound velocity in the parenchyma.

It is necessary to note that spectral peaks similar to those shown in Fig. 3 are observed for all patients, but the ratios of their amplitudes are different. Since, as follows from the above discussion, a percussion stroke excites the whole set of resonance frequencies (modes) of the respiratory system, one can expect that it is also possible to judge the functional state of the lungs according to the ratio of the amplitudes of spectral peaks.

CONCLUSIONS

A cross-spectral method for determining the longitudinal sound velocity in human chest tissues *in vivo* is proposed and substantiated. The method is based on the detection of a percussion stroke by a pair of acoustic sensors positioned over the opposite parts of a lung.

Estimates of the average values (quartiles) of the longitudinal sound velocity in the chest tissues are obtained *in vivo*: 36.8 (23.1, 46.6) m/s for the frequency range of 80–130 Hz; 31.6 (20.1, 37) m/s for the frequency range of 170–290 Hz; and 52.3 (24.5, 56) m/s for the frequency range of 350–500 Hz.

The adequacy of the two-resonance acoustic model of the human respiratory tract, which combines the resonance of the acoustic resonance circuit [12] and the wave resonances of the bronchial tree as a narrow pipe [16], is experimentally verified.

ACKNOWLEDGMENTS

We are grateful to Yu.V. Kulakov, I.Yu. Malyshenko, and G.G. Glukhomanyuk for their participation in the experiments.

REFERENCES

1. R. Loudon and R. L. Murphy, Am. Rev. Respir. Dis. **130**, 663 (1984).
2. F. Dalmay, M. T. Antonini, P. Marquet, and R. Menier, Eur. Respir. J. **8**, 1761 (1995).
3. H. Pastercamp, S. Kraman, and G. Wodicka, Am. Journ. Respir. Crit. Care Med. **156**, 974 (1997).
4. I. V. Vovk, V. T. Grinchenko, and V. N. Oleĭnik, Akust. Zh. **41**, 758 (1995) [Acoust. Phys. **41**, 667 (1995)].
5. J. J. Fredberg and S. K. Holford, J. Acoust. Soc. Am. **73**, 1036 (1983).
6. D. A. Rice, J. Appl. Physiol. **54** (1), 304 (1983).
7. M. Jahed, S. J. Laifook, and S. S. Kraman, J. Appl. Physiol. **76** (2), 565 (1994).
8. A. I. D'yachenko and G. A. Lyubimov, Izv. Akad. Nauk SSSR **5**, 3 (1988).
9. S. S. Kraman, J. Appl. Physiol. **55** (6), 1862 (1983).
10. D. A. Rice and J. C. Rice, J. Acoust. Soc. Am. **82**, 1139 (1987).
11. S. Lu, P. C. Doerschuk, and G. R. Wodicka, Med. Biol. Eng. Comput. **33** (3), 293 (1995).
12. L. I. Nemerovskiĭ, *Pulmophonography* (Meditsina, Moscow, 1981) [in Russian].
13. M. A. Isakovich, *General Acoustics* (Nauka, Moscow, 1973) [in Russian].
14. *Physiology of Respiration*, Ed. by I. S. Breslav and G. G. Isaev (Nauka, St. Petersburg, 1994), pp. 7–120 [in Russian].
15. M. I. Rederman, Ter. Arkh. **61** (4), 113 (1989).
16. G. Wodicka, K. Stevens, H. Golub, and D. Shannon, IEEE Trans. Biomed. Eng. **37**, 1130 (1990).
17. V. I. Korenbaum, A. A. Tagil'tsev, and Yu. V. Kulakov, Akust. Zh. **44**, 380 (1998) [Acoust. Phys. **44** (3), 322 (1998)].
18. V. I. Korenbaum, A. A. Tagil'tsev, and Yu. V. Kulakov, Akust. Zh. **49**, 376 (2003) [Acoust. Phys. **49**, 316 (2003)].
19. A. Leung, S. Sehati, D. Young, and C. McLeod, J. Appl. Physiol. **89** (6), 2472 (2000).

Translated by M. Lyamshev

Acoustical Physics, Vol. 51, No. 4, 2005, pp. 414–424. Translated from Akusticheskiĭ Zhurnal, Vol. 51, No. 4, 2005, pp. 488–499.

Experimental Studies of Flow Noise around a Surfacing Device

E. B. Kudashev

Space Research Institute, Russian Academy of Sciences, ul. Profsoyuznaya 84/32, Moscow, 117997 Russia

e-mail: eco@iki.rssi.ru

Received February 18, 2004

Abstract—The wall pressure fluctuations in turbulent boundary layers play an important role in acoustic measurements carried out in moving media. Results of measuring the frequency spectra of wall pressure fluctuations around a surfacing device are presented. The spatial resolution achieved in measuring the wall pressure fluctuations is investigated. It is demonstrated that the results of hydrodynamic flow noise measurements strongly depend on the aperture size of the measuring acoustic transducer and its orientation in the turbulent boundary layer. The pseudosound pressure fluctuation spectra observed in a series of experiments with surfacing devices show that the resolution of the pressure receivers operating in the turbulent boundary layers considerably varies. On the basis of systematic measurements of wall pressure fluctuations by miniature and distributed receivers at high Reynolds numbers, the effect of the geometric dimensions of a pressure receiver on its resolution in the flow noise measurements is studied. An experimental method is proposed for estimating the receiver-induced distortions. © *2005 Pleiades Publishing, Inc.*

1. INTRODUCTION

The frequency spectrum of pressure fluctuations in a turbulent boundary layer is one of the most important statistical characteristics of the wall pressure field [4]. The measurements of the wall pressure spectra remain of interest to researchers. The frequency spectrum of pressure is used in calculating the hydrodynamic flow noise, and the information on the energy spectrum of pressure is necessary for solving practical problems in aeroacoustics [9, 10]. Within the last forty years, numerous measurements of the frequency spectra of pressure fluctuations have been carried out under different conditions. The data obtained from these studies are most fully presented in [1–14].

The main difficulty in recording the frequency spectra of wall pressure fluctuations in a turbulent boundary layer is associated with the poor spatial resolution that is characteristic of pressure receivers with apertures of finite wave size. Attempts to reveal the influence of a distributed receiver on the results of measuring the wall pressure fluctuations were reported in many publications.

The importance of this problem is determined by the fact that the distorting effect of the receiver hinders the generalization of experimental data: a comparison between the results of wall pressure measurements performed with different measuring systems is virtually impossible. The spectra of pressure fluctuations obtained in different laboratories considerably diverge in the high-frequency region. It is commonly believed that this result is a consequence of the averaging effect associated with the geometric dimensions of a receiver [6, 9, 12].

The systematic error that arises in the pressure fluctuation measurements because of the finite size of the receiver aperture hinders the comparison of data obtained for the pressure spectra by different researchers with different experimental setups. The experimental data reported in [13] testify that the fluctuation intensity sharply increases when the contribution of small-scale turbulent pressure fluctuations are taken into account. The present paper reports on an experimental study of the resolution achieved with a receiver of a finite wave size in measuring the frequency spectra of wall pressure fluctuations in a turbulent boundary layer.

2. SPATIAL RESOLUTION OF PRESSURE RECEIVERS

The appearance of an error in hydrodynamic flow noise measurements is determined by the spatial resolution of the acoustic transducer of pseudosound wall pressure fluctuations. The aperture size and the orientation of the acoustic transducer in a turbulent flow strongly affect the results of hydrodynamic flow noise measurements. The study of the resolution of wall pressure transducers is one of the most interesting problems in hydrodynamic acoustics. By measuring the frequency spectra of pressure fluctuations at the walls of a surfacing device with the use of miniature and distrib-

1063-7710/05/5104-0414$26.00

uted receivers, it is possible to study the dependence of these spectra on the geometric dimensions of the sensing surface of the receiver.

The spatial filtering of wall pressure fluctuations by an acoustic transducer of a finite wave size leads to a systematic error in the hydrodynamic flow noise measurements. The error arises because of the averaging of the pressure fluctuations over the receiving surface of the sensing element of the transducer under the noncoherent action of turbulent pressures, whose correlation scale is commensurable with the geometric dimensions of the receiving surface.

The spatial resolution of a turbulent pressure receiver is determined by the expression [15, 16]

$$\gamma_T^2 = \gamma_{\text{sound}}^2 \alpha^2 \varphi(\bar{a}) \varphi(\bar{c}). \quad (1)$$

In estimating the error in measuring turbulent pressure fluctuations, the necessary condition is that the sensing element of the pressure fluctuation receiver be smaller in size than the turbulent vortices measured with its help. From the resolution representation by formula (1), it follows that the receiver sensitivity γ_{sound}^2 obtained from the acoustic calibration by sound pressure does not coincide with the receiver sensitivity γ_T^2 to pressure fluctuations. The selectivity of an acoustic transducer toward turbulent pressure fluctuations [15] is determined by the frequency characteristics of sensitivity, $\varphi(\bar{a})$ and $\varphi(\bar{c})$.

For the turbulent wall pressure field, the measurement error due to the averaging of pressure fluctuations is mainly a function of the dimensionless parameter $\omega S^{1/2}/U_C$ formed as a combination of the fluctuation frequency ω, the geometric dimension of the receiver $S^{1/2}$, and the convective flow velocity U_C with a correction factor α, which varies only slightly under specific experimental conditions.

In this paper, resolution representation (1) is used to propose a method for determining the error in measuring the wall pressure spectra with allowance for the averaging effect of the geometric dimensions of the receiver aperture.

The proposed method of determining the measurement error is based on obtaining experimental data on the vibration distributions $f(x)$ over the receiving surface of a pressure transducer. Let us briefly consider the method of error estimation.

After measuring $f(x)$, we determine the equivalent area of the receiving surface that interacts with pressure fluctuations:

$$s_{\text{surf}} = \int_s f(\vec{x}) ds(\bar{x}). \quad (2)$$

Then, we calculate the utilization factor α of the receiving surface:

$$\alpha = \frac{S_0}{S_{\text{surf}}}.$$

Finally, we calculate the calibration curve of the measurement error by the formulas

$$\varphi(\bar{a}) = 1/L_x^2 \int_0^{L_x} \int_0^{L_x} \exp(-a|x_0 - x_0'|) \times \cos b(x_0 - x_0') f(x_0) f(x_0') dx_0 dx_0', \quad (3)$$

$$\varphi(\bar{c}) = 1/L_y^2 \int_0^{L_y} \int_0^{L_y} \exp(-c|y_0 - y_0'|) f(y_0) f(y_0') dy_0 dy_0'.$$

Expressions (3) for analyzing the resolution achieved in the turbulent pressure measurement were obtained in [15]. They are based on the Corcos correlation model of the wall pressure field in a turbulent boundary layer [18].

In the Corcos model, the approximating function is an exponential function that depends on a single dimensionless combination of the fluctuation frequency, the spatial separation between the points of observation, and the velocity U_c of the convective transfer of the field components by the flow. Here, the quantities a and b represent the correlation coefficients of pressure fluctuations; $|x_0 - x_0'|$ and $|y_0 - y_0'|$ are the intervals between the points of observation on the surface about which the flow moves, which are taken along the longitudinal coordinate in the flow direction and along the transverse coordinate across the flow, respectively; and L_x and L_y are the geometric dimensions of the receiving surface of the transducer.

To use the wall pressure measurement error in practical calculations, sets of calibration curves were obtained [15–17]. The calibration curves were constructed for determining the sensitivities of different types of pressure receivers, namely, receivers with a uniform distribution over the aperture and flexural bimorph transducers. Figures 1 and 2 show typical examples of spectrum measurement errors for receivers with sensing surfaces in the form of a square and in the form of rectangles with side ratios of 1 : 5 and 5 : 1. Such pressure fluctuation transducers were used in the experiment to measure the pressure fluctuation spectra at the walls of a surfacing device.

To study the influence of the resolution of acoustic receivers on the results of flow noise measurements, piezoelectric plate transducers were designed with receiving surface areas equal to that of a circular receiver 20 mm in diameter. The structure of the plate receivers of flow noise is shown in Fig. 3. This structure is based on the scheme of a symmetric flexural bimorph

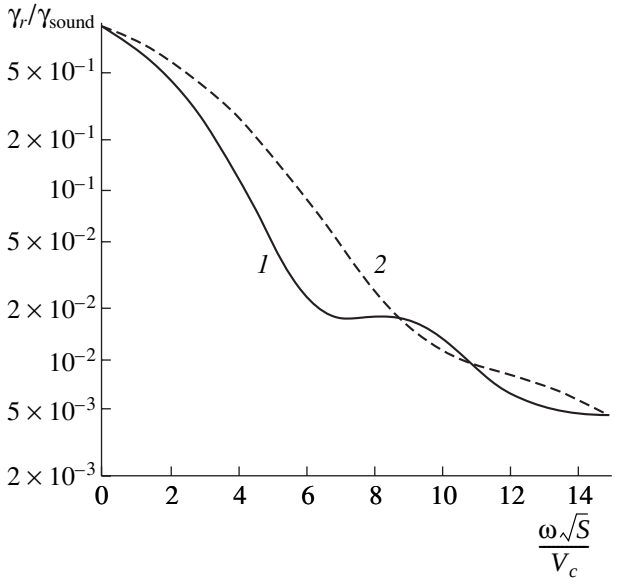

Fig. 1. Resolution of a receiver with a square aperture: (*1*) a flexural transducer and (*2*) a piston transducer.

(see Fig. 3). The transducer consists of two plate receivers electrically connected in parallel. The bimorph is formed by the plate of the receiver frame and a rigidly fixed barium titanate plate. This structure increases the vibration resistance of the acoustic receiver if a symmetry of electromechanical properties is achieved for the upper and lower bimorphs. When the electroacoustic transducer is excited by a plane flexural wave propagating over the frame of the surfacing device, elastic stresses of opposite sign arise in the upper and lower piezoelectric plates. If the upper plate is compressed, the lower plate is stretched, and the vibration signals from the two transducers electrically connected in parallel virtually cancel each other. The transducers were tested for sensitivity to vibration on a test bench. It was found that the parallel connection of the bimorphs reduced the sensitivity of the receivers to vibration by 8–10 dB compared to a single transducer.

One of the main problems in developing transducers with different resolutions in noise measurements was the necessity to suppress the effect of vibration and to provide for recording the turbulent pressure fluctuations by only the part of the receiving transducer surface that forms the bimorph with the piezoceramic plate. The condition of suppressing the vibrations excited by the wall pressure fluctuations complicates the structure of the receiver. In addition to the frame and the sensing elements of the transducers, a damping mass was introduced into the receiver structure. A brass cylinder with a hole for mounting the piezoceramic plates was attached by epoxy resin to the receiving surface of the transducer on the inner side of the frame.

Special studies of the spatial distribution of sensitivity over the receiver surfaces were performed. For all of the pressure receivers that were used in the hydrodynamic flow noise measurements, the distributions of vibrations over their apertures were determined by the contact method. The measurements were performed by a miniature B&K vibration receiver with a special needle-ended head. The vibration receiver moved over the sensing surface of the pressure fluctuation transducer.

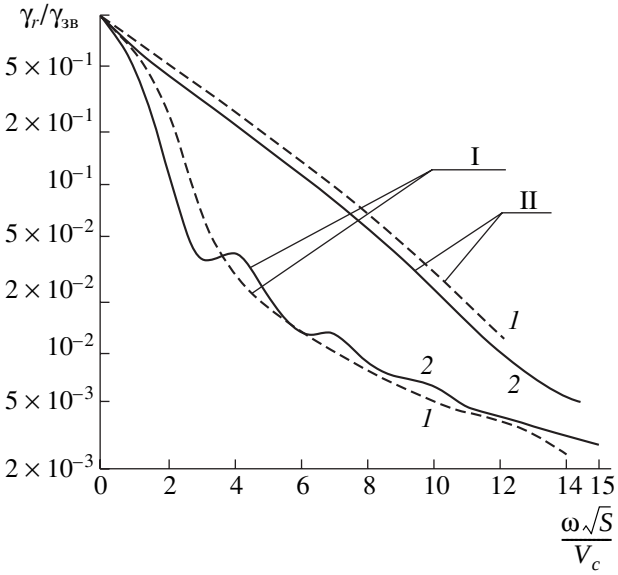

Fig. 2. Resolution of a receiver with a rectangular aperture: (*1*) a flexural transducer and (*2*) a piston transducer. The long side of the receiver is oriented (I) along the flow and (II) across the flow with the corresponding side ratios being (I) 5 : 1 and (II) 1 : 5.

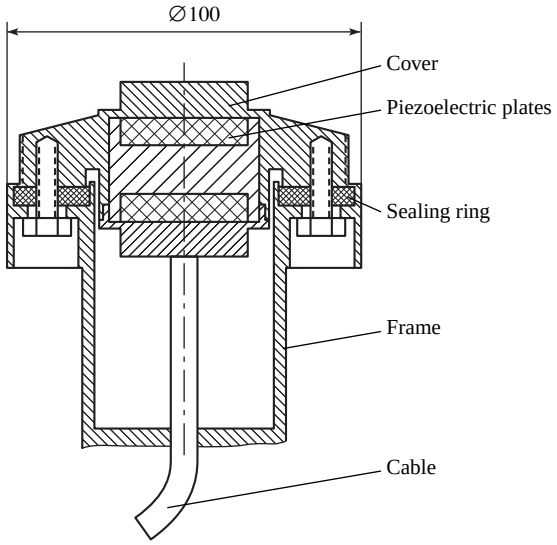

Fig. 3. Receiver of hydrodynamic flow noise.

The pressure transducer operated in the acoustic emission mode using the reversibility of the piezoelectric effect. The transducer was excited by a sine signal from an audio frequency oscillator in the subresonance region of the receiver. The signal was recorded in one-third-octave bands of the filters by a 2112 B&K spectrometer.

Figure 4 shows the effect of vibration damping achieved with the proposed structure of the pressure fluctuation transducer. In moving from the edge of the frame to the center of the receiving surface, the vibration receiver detected a 15-dB increase in the electric signal.

The study of the spatial distribution of sensitivity by the aforementioned method revealed a uniform distribution of the particle velocity over the surface for the receiver with a diameter of 20 mm. This receiver should be considered as a piston-type one or, in terms of the turbulent boundary layer studies, a uniform-sensitivity receiver.

Experiments with the miniature vibration receiver showed that rectangular plate transducers have the maximal particle velocity at the center of their receiving surfaces, and this velocity smoothly decreases toward the edge. The character of the particle velocity distribution testifies that, in rectangular receivers, more complex modes of vibration close to flexural ones are excited. Figure 5 shows the vibration distribution for a square receiver. Figures 6 and 7 show the corresponding distributions for rectangular electroacoustic transducers with side ratios of 3 : 1 and 5 : 1, respectively.

One can see that the introduction of the damping mass into the structure distorts the vibration distribution over the receiving surface that is typical of hinged bimorph transducers and described by the function $f(x) = \sin\pi x/L$ at low frequencies in the subresonance region of the transducer.

The spatial distribution of the plate sensitivity is proportional to the deflection of the plate under a point force. The deflection of a hinged plate decreases as the distance from its center to the point of the force application increases. Hence, the function characterizing the sensitivity of a bimorph receiver smoothly decreases from the center to the periphery. In the experiment, the simplest sensitivity distributions over the surfaces of receivers were investigated. The actual efficiency of taking into account the error in the spectrum measurements strongly depends on the correct determination of the actual distribution of vibrations over the surfaces of the receivers used in the experiment with the surfacing device.

The data on the particle velocity distributions over the receiver surfaces are presented in Table 1.

From an analysis of the data given in Table 1, it follows that, for receivers used in the experiment with a

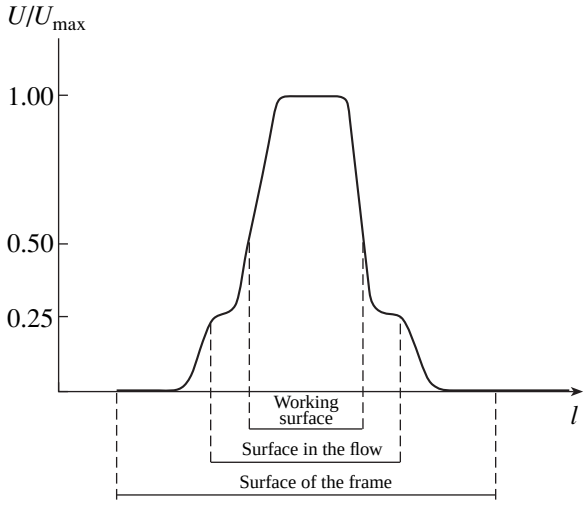

Fig. 4. Signal distribution along the receiving surface of a pressure fluctuation transducer.

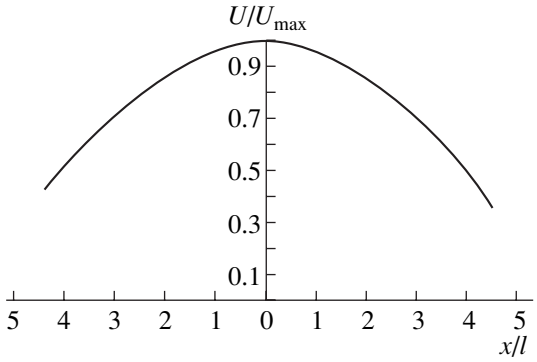

Fig. 5. Spatial distribution of sensitivity for a receiver with a square aperture.

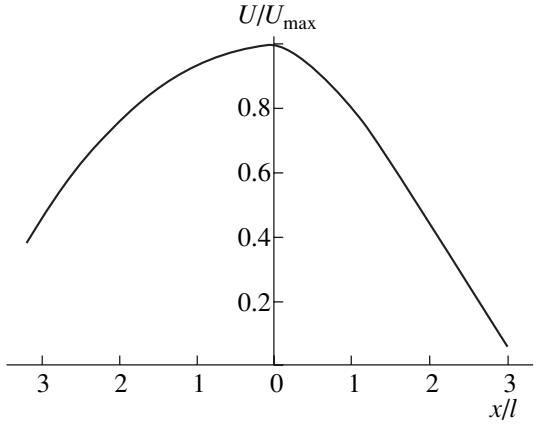

Fig. 6. Spatial distribution of sensitivity for a receiver with a rectangular aperture with a side ratio of 3 : 1.

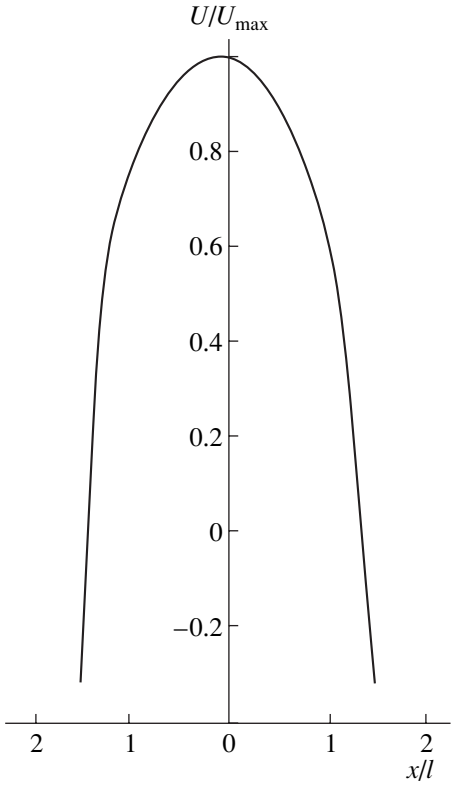

Fig. 7. Spatial distribution of sensitivity for a receiver with a rectangular aperture with a side ratio of 5 : 1.

surfacing device, the utilization factor of the sensitive surface, i.e., the parameter α, is close to the value typical of a flexural bimorph transducer.

In the practical calculations of the error in measuring the pressure fluctuation spectra, the first quantity to be determined is the dimensionless frequency $\omega S/U$ formed as the combination of the spectrum frequency ω, the geometric dimension of the receiver $S^{1/2}$, and the velocity of the surfacing device U. Then, from the data of Figs. 1 and 2, the corresponding distortion of the spectra is determined. Examples of such calculations of the spectrum measurement error are shown in Tables 2 and 3.

The results of studying the particle velocity distributions over the receiver surfaces provided the possibility to calculate the error in measuring the frequency spectra of wall pressure fluctuations by distributed receivers with rectangular apertures on the basis of the error calibration curves constructed for flexural receivers.

3. MEASUREMENT OF THE SPECTRA OF WALL PRESSURE FLUCTUATIONS AROUND A SURFACING DEVICE

To study the resolution of the pressure fluctuation receivers and to test the method of spectrum correction, a series of measurements of hydrodynamic flow noise produced by surfacing devices was carried out.

For the first time, the hydrodynamic flow noise of a surfacing device was measured by a research group headed by Skudrzyk at the Pennsylvania university [19]. In Russia, studies of similar devices and flow noise were independently performed at the Black Sea and at the Krylov Central Research Institute [20, 21].

The advantage of studying the wall pressure fluctuations around a surfacing device lies in the possibility to perform a complex acoustic–hydrodynamic experiment with Reynolds numbers far exceeding those available under laboratory conditions in a turbulent boundary layer formed at the outer surface of a long cylinder. The measurements of the flow noise produced by a surfacing device are almost free of distortion by extraneous noise.

In our experiments on studying the resolution and determining and eliminating the systematic measurement error in the pressure fluctuation measurement, the wall pressure fluctuations were recorded under identical conditions by miniature and distributed receivers. In the turbulent boundary layer formed around a long (more than 8 m in length) body of revolution cylindrical in shape, specially designed pressure receivers were introduced. The receivers had receiving surfaces that noticeably differed in size, shape, and orientation in the flow.

The distributed receivers were constructed so as to have identical areas of receiving surfaces; the apertures

Table 1. Study of the spatial distributions of sensitivity over the apertures of distributed receivers

Shape of the receiver	Characteristic linear dimension (cm)	Total area (cm^2)	Equivalent receiving surface (cm^2)	Utilization factor of the sensing surface α
Circle	2.0	3.14	3.14	1
Rectangle with ratio 5 : 1	4.0	3.14	1.52	0.485
Rectangle with ratio 3 : 1	3.0	3.14	2.24	0.715
Square	1.77	3.14	1.96	0.625

Note: The characteristic geometric dimension for the aperture of an acoustic receiver of circular shape is the diameter, while that for the aperture of an acoustic receiver of rectangular shape is the length of its longer side.

Table 2. Systematic error in measuring the pressure fluctuation spectra by a receiver with a diameter of 20 mm

Velocity of motion 9.5 m/s										
Frequency (Hz)	50	100	200	300	400	500	600	700	800	1000
Dimensionless frequency	0.4	0.8	1.6	2.4	3.2	4.0	4.8	5.6	6.4	8
Distortion of spectra (% with respect to the true spectrum)	76	56	26	9	2.6	1.4	1.2	0.8	0.5	0.36
Systematic error δ (dB)	1	2.5	6	10.5	16	19	19.5	21	23	24.5
Velocity of motion 20.5 m/s										
Frequency (Hz)	50	100	200	300	400	500	600	700	800	1000
Dimensionless frequency	0.2	0.4	0.8	1.2	1.6	2.0	2.4	2.8	3.2	4.0
Distortion of spectra (% with respect to the true spectrum)	87	76	56	40	26	16	9	4.8	2.6	1.4
Systematic error δ (dB)	0.5	1	2.5	4.0	6.0	8.0	10.5	13	16	19

Table 3. Systematic error in the measurement of pressure fluctuation spectra by a receiver with a diameter of 3 mm

Velocity of motion 9.5 m/s											
Frequency (Hz)	50	100	200	300	400	500	600	700	800	900	1000
Dimensionless frequency	0.06	0.12	0.24	0.36	0.48	0.6	0.72	0.84	0.96	1.08	1.2
Distortion of spectra (% with respect to the true spectrum)	95	90	84	78	71	66	60	54	50	47	39.6
Systematic error δ (dB)	–	–	–	1	–	1.7	–	–	3	–	4
Velocity of motion 20.5 m/s											
Frequency (Hz)	50	100	200	300	400	500	600	700	800	900	1000
Dimensionless frequency	0.028	0.057	0.114	0.17	0.228	0.285	0.34	0.4	0.456	0.51	0.57
Distortion of spectra (% with respect to the true spectrum)	–	96	92	88	85	82.5	78.5	75.8	73.5	70	67
Systematic error δ (dB)	–	–	–	–	–	–	–	1	–	–	1.7

were rectangles with side ratios of 3 : 1, 1 : 3, 1 : 5, and 5 : 1. In addition, pressure fluctuations were measured by square receivers and diamond-shaped receivers. Measurements were also performed with circular distributed receivers 20 mm in diameter and with miniature receivers 3 mm in diameter.

The measurements of wall pressure fluctuations in the turbulent boundary layer were carried out in the sea with the use of an experimental setup in the form of an elongated body of revolution cylindrical in shape with a length of more than 8 m; the body was surfacing from a large depth under the action of the excess buoyancy force alone. High values of the Reynolds number were achieved ($\mathrm{Re} = 3.5 \times 10^7$–$11.1 \times 10^7$) at a low level of extraneous noise. The working part of the vertical trajectory of the device was 80 m long. The velocity of the surfacing device was controlled by the on board ballast and varied from 9.5 to 20.5 m/s. The duration of the steady-state motion in the course of surfacing from the given depth was more than 10 s. The flow noise was recorded by distributed and miniature pressure fluctuation receivers mounted flush with the contour of the

surfacing device at two points on its body: on the bow and on the stern, with coordinates 2.68 and 8.34 m, respectively.

Sensing elements 3 mm in diameter were positioned in a multielement unit at equal distances from each other, so that the distance between the axes of neighboring elements was 7 mm. The multielement units of miniature receivers were mounted flush with the wall of the experimental setup on its cylindrical part.

Some of the results of systematic experimental studies of hydrodynamic flow noise produced by surfacing devices are reported in [22]. The spectral density of turbulent pressure fluctuations in a frequency band of 1 Hz is represented on a logarithmic scale along the ordinate axis (with respect to the pressure threshold of 2×10^{-5} Pa) for the whole frequency range studied, namely, from 40 to 10000 Hz. The measured values of turbulent pressure fluctuations are combined in groups of curves obtained for identical velocities of the surfacing object and coordinates of the point of measurement, i.e., positions of the electroacoustic transducer. Since the Reynolds numbers and the displacement thicknesses are the same within each group of curves, it is possible to estimate the influence of the geometric dimensions, shape of the receiving surface, and orientation of the receiver on the resolution achieved in the measurement of wall pressure fluctuations. For example, a receiver with an aperture in the form of a circle 20 mm in diameter has a much lower sensitivity to pressure fluctuations in the operating frequency range, as compared to a miniature circular receiver with a diameter of 3 mm.

In [23], it was shown that, in acoustic–hydrodynamic experiments, the main source of interference is noise and vibration. The effect of interference increases when turbulent pressure fluctuations are measured around objects of a complex shape under conditions close to full-scale ones. In [24], it was found that considerable interference is caused by the vibrations excited in the sensing element of the pressure receiver by the wall pressure fluctuations. In these experiments, the effect of vibration on spectrum measurements was investigated. The sensitivity of all the measuring transducers to vibration was determined in special experiments with a device buoying up in air. The following method was used to estimate the sensitivity of the transducers to vibration. Piezoelectric receivers were mounted flush with the frame of the device. The exciter of vibration—a tone machine—was placed at the stern of the device. The signal detected by the receivers and by miniature piezoelectric vibration receivers of the AMG type, which were rigidly fixed by epoxy resin to the skin of the device near the transducers, was recorded by a magnetic tape recorder.

The sensitivity of the vibration receiver in the audiofrequency range is constant and equal to 20 dB with respect to 1 *mV/g*. The sensitivity of the acoustic receivers to vibration was determined by the well-known expression typical of calibration by the comparison method:

$$\gamma_\xi = \upsilon \frac{u_{\text{tr}}}{u_\upsilon},$$

where υ is the sensitivity of the piezoelectric vibration receiver, u_{tr} is the electric signal at the transducer, u_υ is the electric signal at the vibration receiver, and γ_ξ is the sensitivity of the acoustic receiver to vibration.

The sensing elements of the electroacoustic transducers that were used in the experiments with a surfacing device were surrounded by sealant layers, which provided for a reliable sealing of the transducer under hydrostatic pressures of up to 20 kg/cm^2.

Special experiments were carried out to study the influence of vibration of the surfacing device on the measurement of the pressure fluctuation spectra. In the course of surfacing, the device vibration spectrum was determined at the acoustic receiver site with the use of a piezoelectric vibration receiver.

The equivalent sound pressure P_{eq} that was detected by the receiver in the course of surfacing was proportional to vibration and calculated by the formula

$$P_{\text{eq}} = \frac{u_\upsilon}{\upsilon} \frac{\gamma_\xi}{\gamma_p},$$

where γ_p is the sensitivity of the receiver to pressure (in volts per pascal), u_υ is the electric signal at the vibration receiver that was recorded by the magnetic recorder in the course of testing the device (in volts), and υ is the sensitivity of the miniature vibration receiver of the AMG type to vibration (in V/*g*).

Because of the effect of vibration in the course of surfacing, the pressure fluctuation receiver that is mounted flush with the surfacing device measures both the fluctuation pressure and the vibration pressure:

$$P_{\text{meas}} = P_{\text{eq}} + P_T,$$

where P_T is the fluctuation pressure.

If the spectral levels P_{eq} and P_T are close to each other, the extraction of the useful signal from the measured values is impossible. The comparison of the spectral levels of the equivalent pressure P_{eq} and the measured values P_{meas} is presented in Fig. 8 for a rectangular receiver with the side ratios 3 : 1 and 1 : 3 and in Fig. 9 for a circular receiver with a diameter of 20 mm for surfacing velocities of 12.4 and 20.5 m/s.

The distributed receivers with rectangular sensing surfaces and the circular receiver with a diameter of 20 mm are positioned on the stern of the device.

From an analysis of the curves shown in Figs. 8 and 9, it follows that the proposed acoustic transducers cannot detect the turbulent pressure fluctuations around a surfacing device in the following spectral regions:

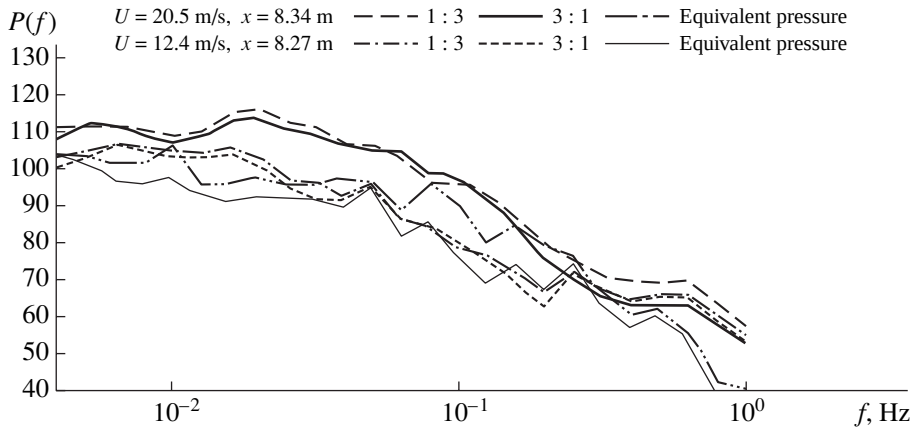

Fig. 8. Effect of vibration on the flow noise measurement by a receiver with a rectangular aperture (with a side ratio of 3 : 1).

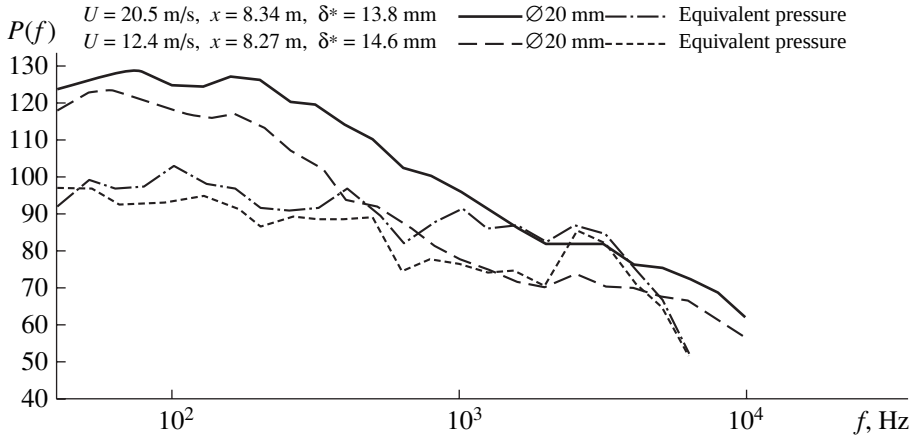

Fig. 9. Effect of vibration on the flow noise measurement by a receiver with a diameter of 20 mm.

above 500 Hz at the surfacing velocity $U = 12.4$ m/s and above 1000 Hz at the surfacing velocity $U = 20.5$ m/s. These frequency regions are excluded from subsequent consideration.

To compare the data of our experiment with the pressure fluctuation spectra measured on a flat plate, the frequency spectra shown in Figs. 10–12 are given in dimensionless form.

The normalization of pseudosound pressures is often performed using "mixed" scales of the velocity U_∞ and the length, i.e., the displacement thickness δ^* of the boundary layer [2]. This approach makes it possible to represent the dimensionless spectra of wall pressure fluctuations as functions of a single parameter, namely, the Strouhal number, a dimensionless combination of the circular frequency ω, the displacement thickness δ^* of the turbulent boundary layer, and the velocity U_∞ of motion at the outer boundary of the boundary layer. The value of this parameter noticeably varied in the course of the measurements: from 10^{-1} to 10^{1}.

The experimental results were compared with the universal spectrum of pressure fluctuations on a flat plate [13, 14].

Analyzing the curves shown in Figs. 10 and 11, one can conclude that the greater the aperture of a distributed receiver, the less it is capable of detecting small-scale high-frequency pressure fluctuations. The distortion of the pressure fluctuation spectra at high frequencies is related to the fact that, in spectral measurements by distributed sources, the well-known selectivity effect manifests itself [15]: a distributed receiver is insensitive to small-scale pressure fluctuations and is "not affected" by high-frequency pressure fluctuations [3].

The experimental data presented above demonstrate the influence of the geometric dimensions of the receiver on the resolution achieved in the flow noise measurements: as the frequency increases, the contribution of pressure fluctuations to the receiver signal decreases. On the basis of the data obtained at high frequencies, one can see a considerable change in the sen-

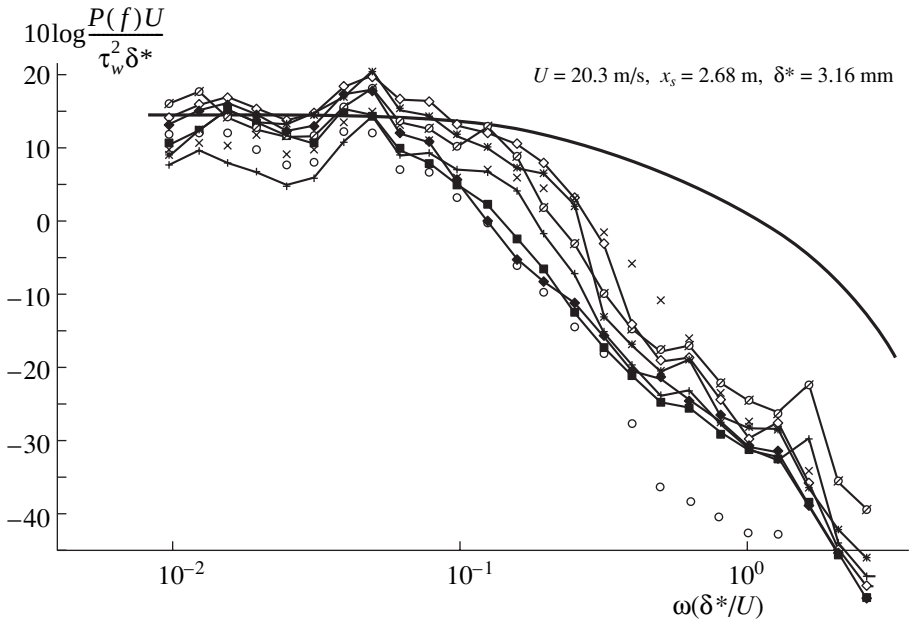

Fig. 10. Normalized flow noise spectra. The velocity of surfacing is 20.5 m/s. The receivers are mounted on the bow of the device. Symbol notation: (◗) 3 : 1, (×) 1 : 3, (–) 1 : 5, (●) 5 : 1, (◆) 1 : 1, (∅) diamond, (○) 20 mm, and (+) 3 mm.

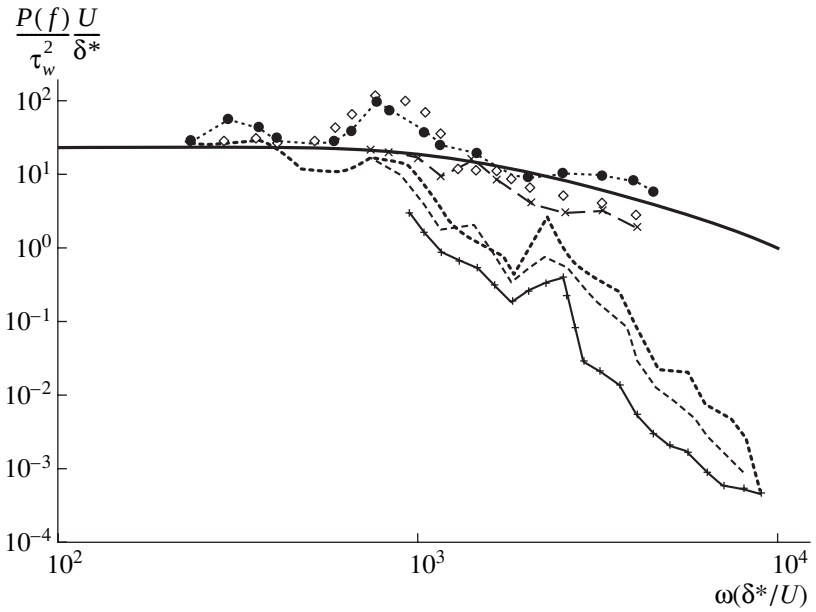

Fig. 11. Normalized flow noise spectra. The velocity of surfacing is 20.5 m/s. The receivers are mounted on the stern of the device. Symbol notation is the same as in Fig. 10.

sitivity to pseudosound pressure fluctuations for distributed pressure receivers calibrated by sound signals in an acoustic tank.

To illustrate the influence of the aperture size of a distributed receiver, Fig. 12 compares the results of hydrodynamic noise measurements by circular receivers with a diameter of 20 mm and by a miniature receiver with a diameter of 3 mm. One can see that, in the high-frequency region, the experimental data obtained by the distributed receiver with a circular aperture 20 mm in diameter and by the small-size receiver 3 mm in diameter differ by more than 25 dB. The introduction of the correction according to the proposed method results in the coincidence of the results of flow noise measurements by receivers with different

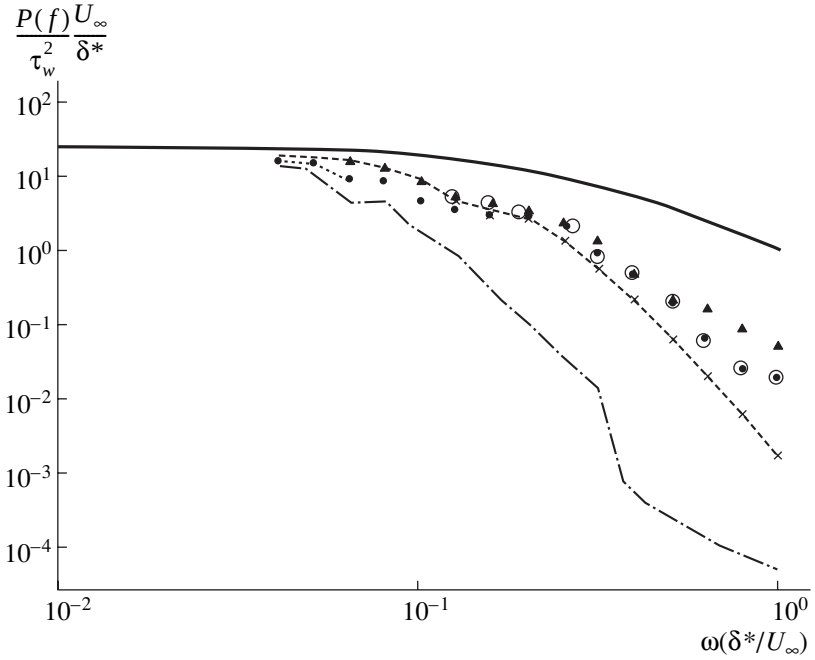

Fig. 12. Influence of the size of the receiver on the flow noise measurement at a constant velocity of surfacing equal to 20.5 m/s: data for the receivers with diameters of (○) 20 and (+) 3 mm.

resolutions. The miniature receiver reliably detects the flow noise produced by the surfacing device.

CONCLUSIONS

The main results of this study are as follows.

(i) In a series of in-sea experiments with a surfacing device, quantitative characteristics were obtained for the distortions introduced into the spectra of hydrodynamic flow noise by distributed receivers.

(ii) The method proposed for determining the error in the measurement of pressure fluctuation spectra was justified by experiments with a surfacing device on the basis of pressure fluctuation measurements by miniature and distributed receivers under identical conditions.

(iii) The experimental data revealed a considerable influence of the geometric dimensions of the receiver aperture on the resolution achieved in the flow noise measurements.

(iv) The effect of the vibration of the surfacing device on the results of measuring the pressure fluctuation spectra was investigated.

(v) The experiments with a surfacing device showed that the miniature receiver reliably measures the spectra of wall pressure fluctuations.

ACKNOWLEDGMENTS

A particular role in initiating and carrying out this study belongs to the well-known acoustician Professor V.S. Petrovskiĭ, who died in 2003. I was lucky to begin my work in hydrodynamic acoustics under his supervision, and, now, I dedicate this paper to his memory. The studies of hydrodynamic sound sources and turbulent flow noise represent one of the remarkable fields of Petrovskiĭ's scientific activity. Petrovskiĭ also made a substantial contribution to the design of low-noise moving sea objects.

I am grateful to A.A. Veĭp, A.A. Punin, and V.M. Tkachenko—members of the team that carried out the experiments with surfacing devices at the time when I worked at the Krylov Central Research Institute. I am grateful to them for their assistance in representing the experimental data and for their cooperation in the data processing and analysis.

This work was supported by the Russian Foundation for Basic Research, project no. 05-07-9002-b.

REFERENCES

1. M. K. Bull, J. Sound Vibr. **190**, 299 (1996).
2. A. V. Smol'yakov, Akust. Zh. **47**, 264 (2001) [Acoust. Phys. **47** (2), 218 (2001)].
3. I. P. Golyamina, E. M. Greshilov, M. A. Mironov, and D. L. Rastorguev, Akust. Zh. **47**, 460 (2001) [Acoust. Phys. **47**, 392 (2001)].
4. A. V. Smol'yakov, Akust. Zh. **46**, 401 (2000) [Acoust. Phys. **46**, 342 (2000)].

5. T. A. Brungart, W. E. Holmberg, A. A. Fontaine, *et al.*, J. Acoust. Soc. Am. **108**, 71 (2000).
6. S. P. Gravante, A. M. Naguib, C. E. Wark, and H. M. Nagib, AIAA J. **36**, 1808 (1998).
7. W. L. Keith, D. A. Hurdis, and B. M. Abraham, ASME Trans. J. Fluids Eng. **114**, 338 (1992).
8. T. M. Farabee and M. J. Casarella, Phys. Fluids A **3**, 2410 (1991).
9. W. K. Blake, *Mechanics of Flow-Induced Sound and Vibration* (Academic, New York, 1986).
10. V. E. Vlasov, A. S. Ginevskiĭ, B. M. Efimtsov, *et al.*, *Basic Problems of Aeroacoustic* (TsAGI, Moscow, 1996), Issue 2614 [in Russian].
11. B. M. Efimtsov, Akust. Zh. **30**, 58 (1984) [Sov. Phys. Acoust. **30**, 33 (1984)].
12. A. V. Smol'yakov and V. M. Tkachenko, *Mesurement of Turbulent Fluctuations* (Énergiya, Leningrad, 1980) [in Russian].
13. W. W. Wilmarth, Annu. Rev. Fluid Mech. **7**, 13 (1975).
14. Yu. G. Blyudze and O. N. Dokuchaev, Izv. Akad. Nauk SSSR, Mekh. Zhidk. Gaza **5**, 175 (1969).
15. E. B. Kudashev, Inzh.–Fiz. Zh. **17**, 416 (1969).
16. E. B. Kudashev and A. I. Popov, Metrologiya **7**, 51 (1971).
17. I. Ya. Miniovich, A. D. Pernik, and V. S. Petrovskiĭ, *Hydrodynamic Sources of Sound* (Sudostroenie, Leningrad, 1972) [in Russian].
18. G. M. Norcos, J. Acoust. Soc. Am. **35**, 192 (1963).
19. G. Haddle and E. Skudrzyk, J. Acoust. Soc. Am. **46**, 130 (1969).
20. N. K. Andreev, L. I. Afanas'ev, and A. A. Punin, in *Experimental Methods and Instruments for Turbulence Studies* (Inst. Teplofiz., Novosibirsk, 1976) [in Russian].
21. V. S. Petrovskiĭ, *Hydrodynamic Problems of Turbulence Noise* (Sudostroenie, Leningrad, 1966).
22. E. B. Kudashev, in *Proceedings of XIII Session of the Russian Acoustical Society* (GEOS, Moscow, 2003), Vol. 2, pp. 44–47 [in Russian].
23. E. B. Kudashev, Akust. Zh. **49**, 644 (2003) [Acoust. Phys. **49**, 545 (2003)].
24. E. B. Kudashev, Akust. Zh. **49**, 215 (2003) [Acoust. Phys. **49**, 176 (2003)].

Translated by E. Golyamina

Acoustical Physics, Vol. 51, No. 4, 2005, pp. 425–434. Translated from Akusticheskiĭ Zhurnal, Vol. 51, No. 4, 2005, pp. 500–510.

Wavelet Analysis of Ellipticity, Dispersion, and Dissipation Properties of Rayleigh Waves

M. A. Kulesh, M. S. Diallo, and M. Holschneider

University of Potsdam, Faculty of Applied and Industrial Mathematics, Am neuen Palais 10, Potsdam, 14469 Germany

e-mail: mkulesh@math.uni-potsdam.de

Received February 17, 2004

Abstract—This paper is devoted to the digital processing of multicomponent seismograms using wavelet analysis. The goal of this processing is to identify Rayleigh surface elastic waves and determine their properties. A new method for calculating the ellipticity parameters of a wave in the form of a time–frequency spectrum is proposed, which offers wide possibilities for filtering seismic signals in order to suppress or extract the Rayleigh components. A model of dispersion and dissipation of elliptic waves written in terms of wavelet spectra of complex (two-component) signals is also proposed. The model is used to formulate a nonlinear minimization problem that allows for a high-accuracy calculation of the group and phase velocities and the attenuation factor for a propagating elliptic Rayleigh wave. All methods considered in the paper are illustrated with the use of test signals. © *2005 Pleiades Publishing, Inc.*

INTRODUCTION

This paper studies Rayleigh surface elastic waves. The trajectory of volume elements oscillating in a Rayleigh wave is elliptic and coplanar with the wave propagation vector. In a classical elastic body, Rayleigh waves are nondispersive [1]; in the asymmetric Cosserat medium, they exhibit a dispersion due to microrotation [2]; and, in geological media, the dispersion of Rayleigh waves is caused by the variation of the elastic properties of rock with depth [3, 4]. In the latter case, a vibrational energy loss (dissipation) is also observed, which affects the oscillation amplitude. As a rule, Rayleigh waves in solids and geological media are observed only indirectly, namely, through interpreting the data obtained from vibration measurements in the form of seismograms. However, these seismograms do not contain exclusively Rayleigh waves, which makes it nessesary to apply high-quality filtering procedures. One of the possible methods for filtering Rayleigh waves relies on the polarization analysis serving to derive the parameters that characterize the ellipticity of the signal [5, 6].

For further interpretation, one should be able to retrieve the dispersion and dissipation parameters of the propagation medium from source seismograms. This data can be obtained by inversion of the Rayleigh waves with dispersion in an analysis of one-component [7] or multicomponent [8] signals.

Most of the experimental studies of Rayleigh waves (e.g., [3, 5, 6]) rely on Fourier analysis. However, Rayleigh waves are relatively difficult to study; their characteristic feature, namely, dispersion, is described by a function of frequency rather than by a single variable. In view of this, the time–frequency approach [4, 9] seems to be rather promising. This approach is particularly remarkable because of its ability to discriminate between signals according to their dispersion curves. The time–frequency approach known today as wavelet analysis [10, 11] has vigorously advanced in the last decades and has become one of the most important methods of digital signal processing.

Thus, the purpose of this work is to develop methods for processing multicomponent seismograms that are capable of retrieving the parameters of ellipticity (ellipticity, phase shift, and dip angle of the polarization ellipse), the dispersion (group and phase velocity), and the dissipation (attenuation function) of Rayleigh waves. As the basis for these methods, we choose wavelet analysis, in particular, the direct and inverse continuous wavelet transforms of complex signals.

1. THE BASIC RELATIONSHIPS OF THE SPECTRAL ANALYSIS OF COMPLEX SIGNALS

Let the raw signals be picked off from a multicomponent sensor: accelerometer, velocimeter, or seismometer. Let us combine different components to form a complex signal $S(t)$. To this end, we introduce a Cartesian coordinate system whose X axis is collinear with the phase velocity vector V_p and whose Y axis is perpendicular to the surface. Then, we have

$$S(t) = S_x(t) + iS_y(t), \tag{1.1}$$

where t is the time in seconds; $i = \sqrt{-1}$ is the imaginary unit; and $S_x(t)$ and $S_y(t)$ are two independent compo-

1063-7710/05/5104-0425$26.00 © 2005 Pleiades Publishing, Inc.

nents of the signal picked off from the seismic sensor, which have appropriate dimensions.

Consider the space $L^2(\mathbb{R})$ of complex functions $S(t)$ that are defined over the entire axis $\mathbb{R}(-\infty, \infty)$ and possess a finite energy (norm) [11]:

$$S(t) \in L^2(\mathbb{R}) \Rightarrow \int_{-\infty}^{+\infty} |S(t)|^2 dt < \infty.$$

We will use the pair of direct and inverse Fourier transforms serving as the basis of the spectral analysis in the form

$$\begin{aligned} \hat{S}(\omega) &= \frac{1}{\sqrt{2\pi}} \int_{-\infty}^{+\infty} S(t) e^{-i\omega t} dt, \\ S(t) &= \frac{1}{\sqrt{2\pi}} \int_{-\infty}^{+\infty} \hat{S}(\omega) e^{i\omega t} d\omega, \end{aligned} \tag{1.2}$$

where $\omega = 2\pi f$ is the angular frequency, f is the physical frequency in hertz, and the circumflex symbol means the complex Fourier transform.

In this paper, we will also use the Hilbert transform $\mathcal{H}S(t)$ [12], which allows us to obtain the progressive $S^+(t)$ and regressive $S^-(t)$ components. For the progressive component, the Fourier coefficients are nonzero only for $f > 0$; for the regressive component, for $f < 0$,

$$\begin{aligned} S(t) &= S^+(t) + S^-(t), \\ S^\pm(t) &= [S(t) \pm i\mathcal{H}S(t)]/2, \end{aligned} \tag{1.3}$$

where the Fourier transform of the function $\mathcal{H}\hat{S}(f)$ is defined as

$$\mathcal{H}\hat{S}(f) = \begin{cases} -i\hat{S}(f), & f \geq 0, \\ i\hat{S}(f), & f < 0. \end{cases} \tag{1.4}$$

To analyze the signal's frequency distribution versus time, we will use the continuous wavelet transform [10, 11]. The theory of the continuous wavelet transform is developed in [10]. Here, we only present the main relationships. The pair of direct and inverse wavelet transforms of a complex signal $S(t)$ has the form

$$\begin{aligned} {}^{\mathcal{C}}W_g S(t, a) &= \int_{-\infty}^{+\infty} \frac{1}{a} g^*\left(\frac{\tau - t}{a}\right) S(\tau) d\tau \\ &= \frac{1}{2\pi} \int_{-\infty}^{+\infty} e^{i\omega t} \hat{g}^*(a\omega) \hat{S}(\omega) d\omega, \\ S(t) &= \frac{1}{C_{g,h}} \int_{-\infty}^{+\infty} \int_{-\infty}^{+\infty} \frac{1}{a^2} h\left(\frac{t - \tau}{a}\right) {}^{\mathcal{C}}W_g S(\tau, a) d\tau da, \end{aligned} \tag{1.5}$$

$$C_{g,h} = \int_0^{+\infty} (\hat{g}^*(\omega)\hat{h}(\omega) + \hat{g}^*(-\omega)\hat{h}(-\omega)) \frac{d\omega}{\omega},$$

where $g(\cdot), h(\cdot) \in L^2(\mathbb{R})$ are real or complex wavelets, $C_{g,h}$ is the normalization coefficient, the asterisk superscript means complex conjugate, and ${}^{\mathcal{C}}W_g S(t, a)$ is the complex wavelet transform dependent on the dimensionless scaling factor $a \in \mathbb{R}$ and the dimensional time factor $t \in \mathbb{R}$. In contrast to the majority of works that use the continuous wavelet transform, the factor a here takes both positive and negative values.

In our case, it is convenient to choose as the scale the physical frequency, which is related to the dimensionless factor a as $a = f_0/f$, where f_0 is the characteristic (center) frequency of the wavelet. Then,

$$\begin{aligned} {}^{\mathcal{C}}W_g S(t, f) &= \int_{-\infty}^{+\infty} \frac{f}{f_0} g^*\left(\frac{f(\tau - t)}{f_0}\right) S(\tau) d\tau \\ &= \frac{1}{2\pi} \int_{-\infty}^{+\infty} e^{2\pi i \varphi t} \hat{g}^*\left(\frac{\varphi f_0}{f}\right) \hat{S}(\varphi) d\varphi, \end{aligned} \tag{1.6}$$

$$S(t) = \frac{1}{C_{g,h}} \int_{-\infty}^{+\infty} \int_{-\infty}^{+\infty} h(f(t - \tau)/f_0) {}^{\mathcal{C}}W_g S(\tau, f) d\tau \frac{df}{f_0}.$$

Thus, in contrast to the Fourier transform given by Eqs. (1.2), the wavelet transform provides a two-dimensional scan of the complex signal under study, the scale and time being treated as independent variables. As a result, the possibility appears to analyze the signal in the physical (time) and scaling (frequency) spaces simultaneously.

The wavelet for the inverse transform can be chosen in the form of the delta function, which yields a very efficient reconstruction formula [10]:

$$S(t) = \frac{1}{C_{g,\delta}} \int_{-\infty}^{+\infty} \frac{{}^{\mathcal{C}}W_g S(t, f)}{f f_0} df.$$

As a rule, the direct and inverse transforms use the same wavelet. The choice of the wavelet depends on what typical oscillation modes are present in the signal. For example, to analyze rectangular oscillations, the real HAAR wavelet or a similar but symmetric FHAT wavelet are most suitable. The most convenient for the seismic signals are real wavelets constructed on the basis of different-order derivatives of the Gaussian or complex wavelets, for example, the Morlet wavelet [10, 11]

$$g(t) = e^{2\pi i f_0 t} e^{-\frac{t^2}{2\sigma^2}}, \quad \hat{g}(\omega) = \sigma e^{-\frac{\sigma^2(\omega - 2\pi f_0)^2}{2}}, \tag{1.7}$$

where σ is the wavelet parameter. Strictly speaking, the Morlet wavelet does not satisfy relationship (1.5),

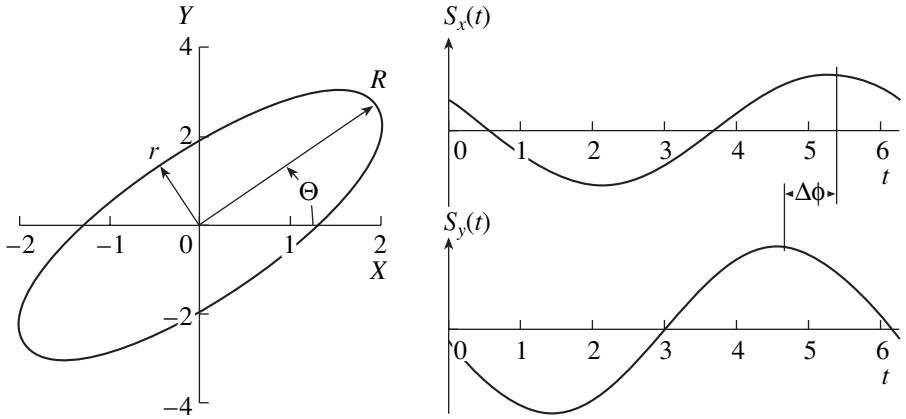

Fig. 1. Parameters that characterize an elliptic signal.

because it leads to singularities at frequencies close to zero. This property should be taken into account in practical implementation.

The Morlet wavelet is progressive; i.e., its Fourier coefficients for negative frequencies are zero. This feature allows the wavelet spectrum to be separated into progressive and regressive components, similar to formula (1.3):

$$\mathcal{W}_g S(t, f) = \mathcal{W}_g^+ S(t, f) + \mathcal{W}_g^- S(t, f), \qquad (1.8)$$

where

$$\mathcal{W}_g^+ S(t, f) = \begin{cases} \mathcal{W}_g S(t, f), & f \geq 0 \\ 0, & f < 0, \end{cases}$$

$$\mathcal{W}_g^- S(t, f) = \begin{cases} 0, & f \geq 0 \\ \mathcal{W}_g S(t, f), & f < 0. \end{cases}$$

To perform such a separation for nonprogressive (e.g., real) wavelets, one must first calculate the Hilbert transform of the source signal, which makes the numerical procedure more complex.

The spectrum $\mathcal{W}_g S(t, f)$ contains information about the distributions of the signal's amplitude $A(t, f)$ and phase $\Phi(t, f)$ in time and frequency:

$$\mathcal{W}_g S(t, f) = A(t, f) e^{i\Phi(t, f)}, \qquad (1.9)$$
$$A(t, f) = |\mathcal{W}_g S(t, f)|, \quad \Phi(t, f) = \arg \mathcal{W}_g S(t, f).$$

We will use this representation below to separately visualize the absolute value and phase of the complex wavelet spectrum.

2. THE ELLIPTICITY PROPERTIES OF RAYLEIGH WAVES

Since the form of a Rayleigh wave is comparatively stable, the polarization analysis is a convenient tool for processing it [5].

In the most general form, the properties of an elliptic signal are characterized by the following time-dependent parameters (Fig. 1):

(i) the major semiaxis of the ellipse, $R \geq 0$;

(ii) the minor semiaxis, r: $0 \leq r < R$;

(iii) the ellipticity $\rho = r/R$;

(iv) the inclination (rotation) angle of the ellipse, $\Theta \in (-\pi/2, \pi/2]$. For some time, the Rayleigh wave retains its geometry and exactly vertical orientation, i.e., $\Theta = \pi/2$, which is the criterion that allows this wave to be identified on a seismogram; and

(v) the phase shift between the components $S_x(t)$ and $S_y(t)$, $\Delta\phi \in (-\pi, \pi]$.

To determine the ellipticity parameters in the time domain, one can use the complex trace method [6]. It transforms the real components $S_x(t)$ and $S_y(t)$ of signal (1.1) to complex components through the Hilbert transform given by Eqs. (1.3) and (1.4):

$$C_x(t) = [S_x(t) + i\mathcal{H}S_x(t)]/2,$$
$$C_y(t) = [S_y(t) + i\mathcal{H}S_y(t)]/2.$$

The real and imaginary parts of the complex signals $C_x(t)$ and $C_y(t)$ obtained in this manner are considered separately, and the phase shift is calculated and used to determine the remaining ellipticity parameters:

$$\Delta\phi(t) = \arg[C_x^*(t) C_y(t)],$$
$$R^2(t) = [S_0(t) + \sqrt{S_1^2(t) + S_2^2(t)}]/2,$$
$$r^2(t) = [S_0(t) - \sqrt{S_1^2(t) + S_2^2(t)}]/2, \qquad (2.1)$$
$$\Theta = \frac{1}{2}\arg[S_1(t) + iS_2(t)] \bmod \pi,$$

where

$$S_0(t) = |C_x(t)|^2 + |C_y(t)|^2,$$
$$S_1(t) = |C_x(t)|^2 - |C_y(t)|^2,$$
$$S_2(t) = 2|C_x(t)||C_y(t)|\cos(\Delta\phi(t)).$$

Here, mod means modulo division.

The ellipticity parameters in the frequency domain. In seismology, the Nakamura method [13] (*H*/*V* method) is widely used. It calculates the ellipticity ρ as the ratio of the horizontal and vertical Fourier spectra:

$$\rho(f) \simeq F_h(f)/F_v(f), \tag{2.2}$$

where $F_h(f)$ and $F_v(f)$ are the smoothed power spectrum densities of the horizontal and vertical signals, respectively. This spectral density is calculated through Fourier transform (1.2) using special smoothing algorithms [14] (averaging the Fourier coefficients over several time windows).

The ellipticity parameters in the wavelet space. The method proposed in this paper for calculating the ellipticity parameters generalizes the above two methods. It determines the major and minor semiaxes, the dip angle, and the phase shift as functions of time and frequency. The key idea underlying the new method is the description of the ellipse on the complex plane in terms of two complex numbers, A^+ and A^-, and two real numbers, ω^+ and ω^-: $C(\tau) = A^+ e^{i\omega^+\tau} + A^- e^{-i\omega^-\tau}$.

This formula, along with geometrical considerations, yields the following relationships:

$$\Delta\phi = \arg\left(\frac{A^+ + (A^-)^*}{A^+ - (A^-)^*}\right) + \frac{\pi}{2},$$

$$R = |A^+| + |A^-|, \quad r = \big||A^+| - |A^-|\big|,$$

$$\Theta = \frac{1}{2}\arg(A^+A^-)\bmod\pi.$$

When a complex progressive wavelet is used, property (1.8) of the wavelet transform allows us to represent the wavelet spectrum as a superposition of the progressive and regressive components. Let us consider the instantaneous angular frequency defined as the derivative of the complex spectrum: $\omega^\pm(t, f) = \partial \arg \mathcal{W}_g^\pm S(t, f)/\partial t$. Then, in the vicinity of time instant t, each component can be represented as follows:

$$\mathcal{W}_g S(t+\tau, f) \simeq \mathcal{W}_g^+ S(t, f) e^{i\omega^+(t, f)\tau} + \mathcal{W}_g^- S(t, f) e^{-i\omega^-(t, f)\tau},$$

which yields a complex time–frequency spectrum for each of the parameters:

$$\Delta\phi(t, f) = \arg\left(\frac{\mathcal{W}_g^+ S(t, f) + (\mathcal{W}_g^- S(t, f))^*}{\mathcal{W}_g^+ S(t, f) - (\mathcal{W}_g^- S(t, f))^*}\right) + \frac{\pi}{2},$$

$$R(t, f) = |\mathcal{W}_g^+ S(t, f)| + |\mathcal{W}_g^- S(t, f)|,$$

$$r(t, f) = \big||\mathcal{W}_g^+ S(t, f)| - |\mathcal{W}_g^- S(t, f)|\big|, \tag{2.3}$$

$$\Theta(t, f) = \frac{1}{2}\arg[\mathcal{W}_g^+ S(t, f)\mathcal{W}_g^- S(t, f)]\bmod\pi.$$

Formulas (2.3) can be used to derive the parameters as a function of time alone or frequency alone, but, unlike direct methods (2.1) and (2.2), this inverse procedure offers rich opportunities for the frequency and time filtering of all ellipticity properties. Several algorithms for returning to the time or frequency domain are possible:

(i) The first possible algorithm calculates all parameters in the form of Eqs. (2.3) and averages them in frequency, but only over those regions of the wavelet spectrum where the ellipticity, which is characterized by the parameter $r(t, f)$, is most pronounced.

(ii) The second algorithm is as follows. In the original wavelet spectra $\mathcal{W}_g^+ S(t, f)$ and $\mathcal{W}_g^- S(t, f)$, the so-called ridges Γ^+ and Γ^- are selected. For the instant t, Γ^+ is the frequency corresponding to the local maximum of the absolute value of the progressive wavelet spectrum and Γ^- is that of the regressive wavelet spectrum. A ridge is actually the extremum of the region that describes the most typical behavior of the signal. If we consider the ridge as a function of time and replace the frequency in Eqs. (2.3) with it, we obtain the time-averaged parameters. If we consider the ridge as a function of frequency and replace the time variable in Eqs. (2.3) with it, we obtain the frequency average.

The main idea of these averaging operations is to extract only a particular mode from the complex signal for analysis, which cannot be achieved with the complex trace method or the *H*/*V* method.

Consider an example of a synthetic signal containing only one frequency mode. In Fig. 2a, the solid and dashed lines, respectively, represent the real and imaginary parts of this signal. Figure 2b shows the absolute values of the progressive and regressive wavelet spectra; and the solid lines are the ridges Γ^+ and Γ^-. Figure 2c is a plot of the signal on the complex plane.

Using the ridges $\Gamma_c^+(f)$ and $\Gamma_c^-(f)$, we can determine the ellipticity parameters as functions of frequency. Comparing the parameter $\rho(f)$ calculated by the *H*/*V* method (the dashed line in Fig. 2d) with that calculated by the method proposed in this paper (the solid line in Fig. 2d), we arrive at the conclusion that the results obtained with these methods basically agree with each other.

Figure 3a shows the lengths of the major and minor semiaxes of the elliptic signal on the time–frequency plane. The ellipticity parameters calculated by the complex trace method in the form of Eqs. (2.1) are shown in Figs. 3b–3d by dashed lines. The new ellipticity parameters, shown in Figs. 3b–3d by solid lines, are calculated in this case using the ridges in the form of $\Gamma_c^+(t)$ and $\Gamma_c^-(t)$. The results obtained with the complex trace method and the new method also agree with each other.

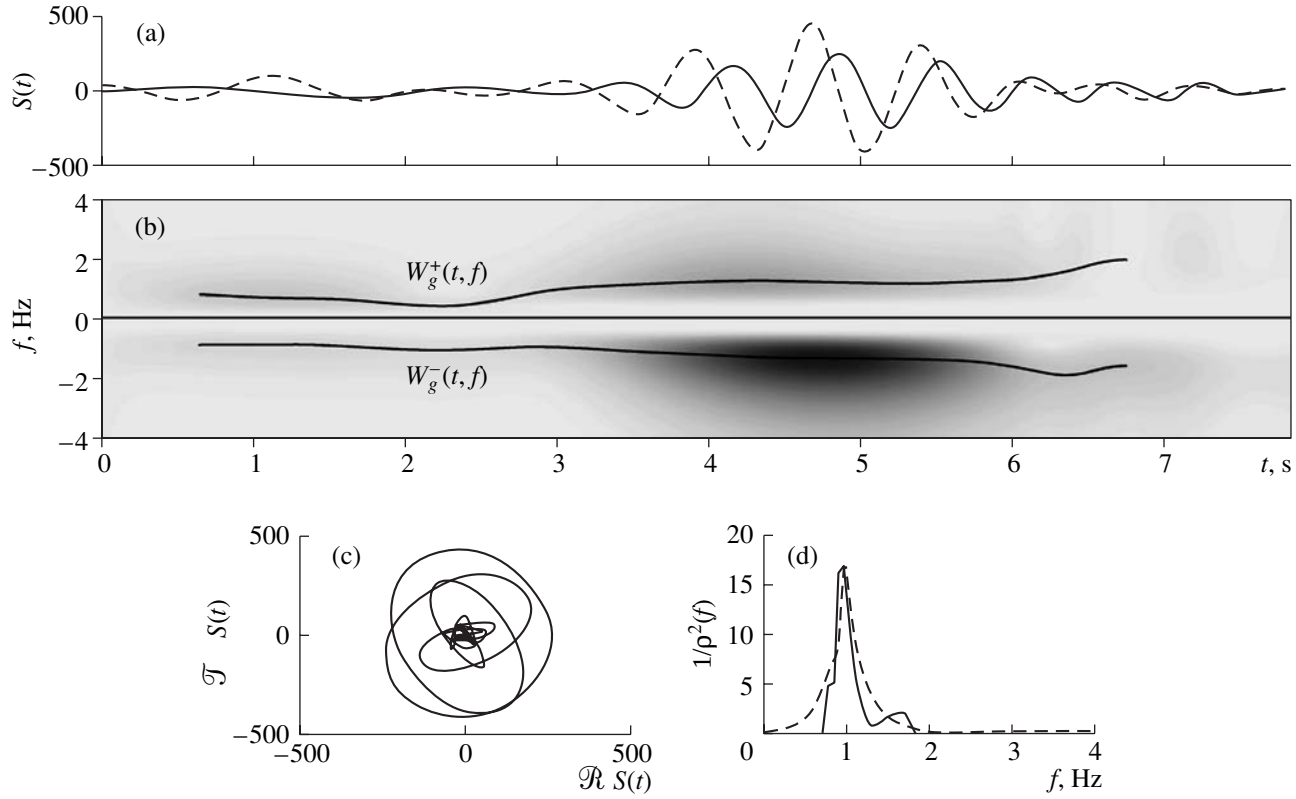

Fig. 2. Typical form of the elliptic signal.

3. THE DISPERSION AND DISSIPATION OF RAYLEIGH WAVES

Assume that the medium is stationary and consider two complex signals, $S_1(t)$ and $S_2(t)$, of the form of Eq. (1.1) that are read from two instruments separated by a distance Δx. In the case of more than two signals, all relationships provided below remain valid and apply to each pair of signals.

Description of the dispersion and dissipation in Fourier space. A model that relates the Fourier spectra of complex signals $S_1(t)$ and $S_2(t)$ in an isotropic medium was proposed in [3]:

$$\hat{S}_2(f) = e^{-[ik(f)+\alpha(f)]\Delta x}\hat{S}_1(f), \tag{3.1}$$

where the frequency-dependent parameter $\alpha(f)$ of the medium determines the dissipation (attenuation function) and the wave number $k(f)$ describes the dispersion.

As the dispersion parameters, the phase and group velocity functions determined by the wave number and its derivative are commonly used [4]:

$$k(f) = \frac{2\pi f}{V_p(f)}, \quad k'(f) = \frac{2\pi}{V_g(f)}. \tag{3.2}$$

If the phase velocity of the medium is known, the wave number can be found from Eqs. (3.2) and, thereby, the group velocity is determined as

$$V_g(f) = \frac{2\pi}{k'(f)} = \frac{2\pi V_p^2(f)}{V_p(f) - fV_p'(f)}. \tag{3.3}$$

An exact estimate of the group velocity from the phase velocity is impossible without additional information because of the unknown constant that appears when Eq. (3.3) is integrated. Formally, the group velocity function does not contain additional information about the medium, as compared to that contained in the phase velocity function; nevertheless, both of them are widely used. This occurs because, in some cases, the group velocity alone can be measured.

In our case, it should also be noted that physical considerations require that all functions be defined only for positive frequencies. However, we represent the spectrum of the complex signal as consisting of the progressive ($f > 0$) and regressive ($f < 0$) parts; therefore, we symmetrically extend all the functions to negative frequencies: $\alpha(-f) = \alpha(f)$, $V_p(-f) = V_p(f)$, and $V_g(-f) = V_g(f)$.

Description of the dispersion and dissipation in the wavelet space. Using relationship (1.6) for the wavelet transform in terms of the Fourier spectrum, we

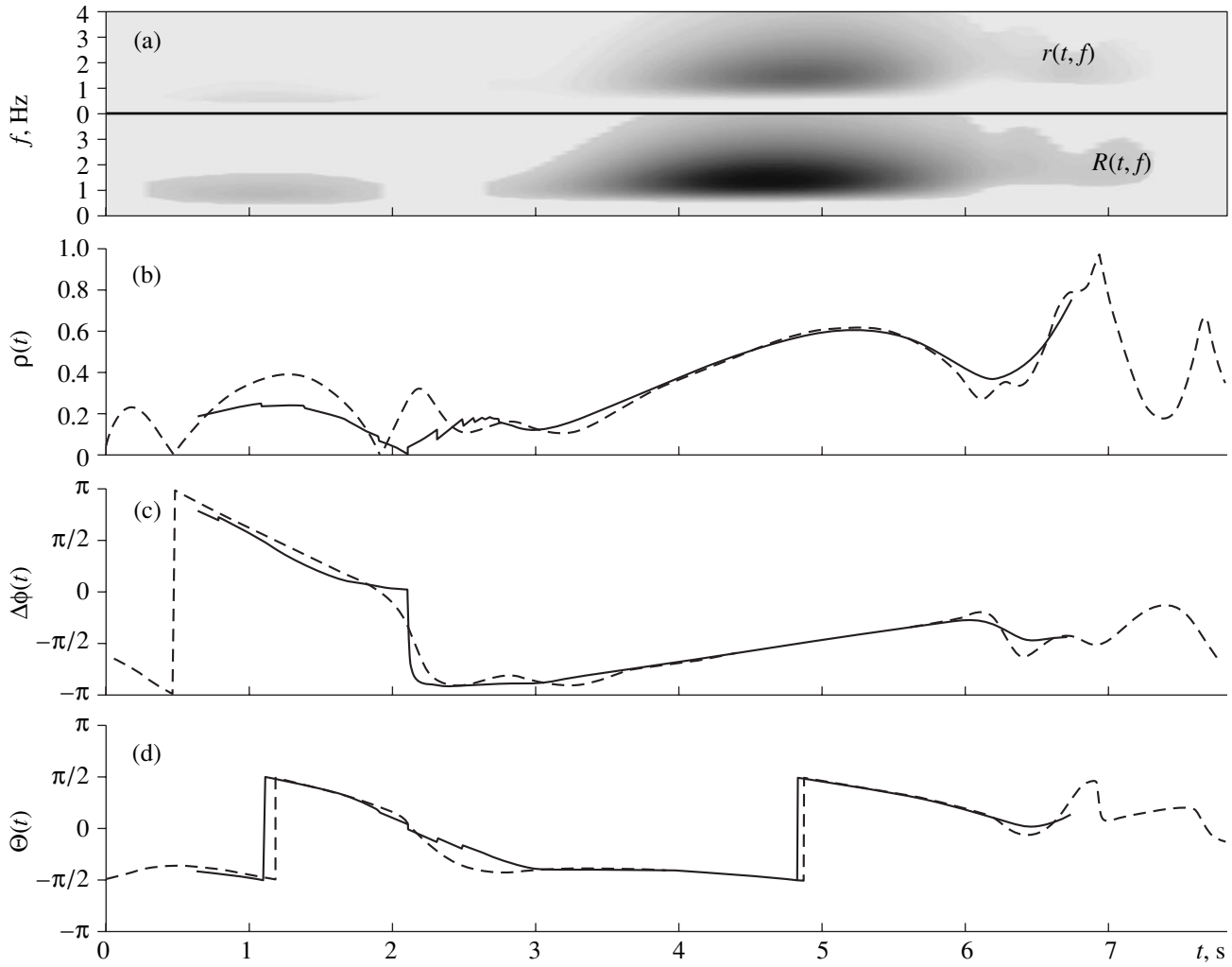

Fig. 3. Ellipticity parameters calculated by the complex trace method and by the new method.

obtain an analog of relationship (3.1) for the wavelet spectrum:

$$\mathcal{W}_g S_2(t, f) = \frac{1}{2\pi}\int_{-\infty}^{+\infty} e^{2\pi i\varphi t}\hat{g}^*\left(\frac{\varphi f_0}{f}\right)\hat{S}_2(\varphi)d\varphi$$

$$= \frac{1}{2\pi}\int_{-\infty}^{+\infty} e^{2\pi i\varphi t}\hat{g}^*\left(\frac{\varphi f_0}{f}\right)e^{-[ik(f)+\alpha(f)]\Delta x}\hat{S}_1(\varphi)d\varphi.$$

Let us expand the function $k(\varphi)$ in a Taylor series around the point f and keep the terms up to the first-order derivative:

$$k(\varphi) \simeq k(f) + (\varphi - f)k'(f). \tag{3.4}$$

Representing the attenuation function in a similar manner and transforming the integrand, we obtain

$$\mathcal{W}_g S_2(t, f) = e^{-i[k(f)-fk'(f)]\Delta x}e^{-\alpha(f)\Delta x} \times \mathcal{W}_g S_1(t - k'(f)\Delta x/(2\pi), f), \tag{3.5}$$

or, in terms of the group and phase velocity functions,

$$\mathcal{W}_g S_2(t) = e^{-2\pi if\left(\frac{1}{V_p(f)}-\frac{1}{V_g(f)}\right)\Delta x} \times e^{-\alpha(f)\Delta x}\mathcal{W}_g S_1\left(t - \frac{\Delta x}{V_g(f)}, f\right). \tag{3.6}$$

Due to expansion (3.4), the dispersion model in the wavelet space, unlike the model in the Fourier space, is an approximation. A better approximation can be achieved with a denser sampling in the frequency axis and a higher value for the wavelet parameter.

Using one of the Morlet wavelet properties, one more approximation can be obtained, which is on the one hand less accurate than Eq. (3.6) but which, on the other hand, very clearly illustrates the deformation of the wavelet spectrum in the course of propagation of a dispersive wave. The following relationship is valid for the Morlet wavelet [10]: $\arg\mathcal{W}_g S(t, f) \simeq 2\pi ft$. Representing the right-hand side of Eq. (3.5) in the

form of Eq. (1.9) and using the above expression for the argument of the complex spectrum, we obtain

$$\begin{aligned} {}^{\circ}W_g S_2(t) &= e^{-\alpha(f)\Delta x}\left|{}^{\circ}W_g S_1\left(t-\frac{\Delta x}{V_g(f)}, f\right)\right| \\ &\times \exp\left[i\arg {}^{\circ}W_g S_1\left(t-\frac{\Delta x}{V_p(f)}, f\right)\right]. \end{aligned} \tag{3.7}$$

Thus, the group velocity is a function that "deforms" the image of the absolute value of the source signal's wavelet spectrum, the phase velocity "deforms" the matrix of the wavelet spectrum phase, and the attenuation function determines the frequency-dependent real coefficient by which the spectrum is multiplied.

To demonstrate the model proposed above, consider the following example. As an approximation of the phase velocity function, let us use the three-parameter exponential approximation with the group velocity determined by Eq. (3.3):

$$V_p(f) = V_1 + \Delta V e^{-\frac{f^2}{2\sigma^2}}. \tag{3.8}$$

Let us use the simplest model of the attenuation function in the form of a linear dependence of the attenuation factor on frequency, $\alpha(f) = \beta f$, with one parameter β. The parameters of the problem have the following values: $V_1 = 1300$ m/s, $\Delta V = 200$ m/s, $\sigma = 6$ Hz, $\Delta x = 3500$ m, and $\beta = 3 \times 10^{-5}$ 1/(Hz s).

Figure 4a shows the phase velocity (the solid line) and the group velocity (the dashed line) for the given parameters. Figure 4b shows the variation of the Fourier coefficients due to attenuation: the solid line refers to the spectrum $\hat{S}_1(f)$, and the dashed line, to the spectrum $\hat{S}_2(f)$. Figure 4c illustrates the signal $S_1(t)$ (the solid line represents the real part, and the dashed line, the imaginary part); Fig. 4d shows the signal $S_2(t)$ calculated from Eqs. (3.6) (the black solid and dashed lines) and (3.1) (the gray lines). Figure 4e shows the absolute values of the wavelet spectra of signals $S_1(t)$ and $S_2(t)$, and Fig. 4f, the corresponding phases. The geometrical distortion of the spectrum ${}^{\circ}W_g S_2(t)$ with respect to ${}^{\circ}W_g S_1(t)$, which was illustrated above by Eq. (3.7), is due to the frequency dependence of the phase and group velocities. This example demonstrates a good agreement between model (3.1), defined in the Fourier space, and model (3.6), defined in the wavelet space.

4. THE CALCULATION OF THE GROUP AND PHASE VELOCITIES

As an example of practical application of the model reported in the previous section, let us formulate the nonlinear minimization problem to calculate the group and phase velocities from the known signals $S_1(t)$ and $S_2(t)$.

Let us use model (3.5) and the parametric approximation of the wave number $k(f)$ and the attenuation function $\alpha(f)$:

$$k(f) \approx k(f, p_i), \quad \alpha(f) \approx \alpha(f, q_j),$$
$$i = 1\ldots N, \quad j = 1\ldots M.$$

Then, in the general form, the unconstrained nonlinear minimization problem can be formulated as follows:

$$\begin{gathered} \chi^2(p_i, q_j, \Delta x) \longrightarrow \min, \quad p_i, g_j \in \mathbb{R}, \\ i = 1\ldots N, \quad j = 1\ldots M. \end{gathered} \tag{4.1}$$

Problem (4.1) can be solved numerically by the Levenberg–Marquardt method [14], in which the $\chi^2(\cdot)$ function is the mean-square cost function. For this function, several formulations that provide different parameter reconstruction accuracies can be considered. For space considerations, we will only focus on two of them.

(i) The simplest optimization problem to realize is when the cost function $\chi^2(\cdot)$ is defined as the difference between the absolute value of the wavelet spectrum of the second signal, $|{}^{\circ}W_g S_2(t, f)|$, and that of the function $|{}^{\circ}W_g S_n(t, f)|$ obtained by transforming the spectrum of the first signal with the use of Eq. (3.5). This algorithm is intended to reconstruct the group velocity and the dissipation parameters, because this cost function ignores the phase component of the signal:

$$\chi_1^2 = \int_t\int_f [|{}^{\circ}W_g S_2(t, f)| - |{}^{\circ}W_g S_n(t, f)|]^2 dt df. \tag{4.2}$$

(ii) To reconstruct the phase information from the signal and, consequently, to calculate the phase velocity, the cost function must allow for the phase component of the wavelet spectrum:

$$\chi_2^2 = \int_t\int_f [\arg {}^{\circ}W_g S_2(t, f) - \arg {}^{\circ}W_g S_n(t, f)]^2 dt df. \tag{4.3}$$

Here, it should be noted that the phase optimization is more sensitive to initial conditions. Therefore, as initial values of parameters p_i and q_i, it is necessary to use the results obtained by minimizing cost function (4.2). Also, the influence of the wavelet parameter is significant; an increase in this parameter improves the accuracy of the phase velocity reconstruction.

Methods that are capable of optimizing complex functions may use the cost function in the form of a sample squared absolute value of the difference between complex wavelet coefficients, $|{}^{\circ}W_g S_2(t, f) - {}^{\circ}W_g S_n(t, f)|^2$. However, in this case, statistical methods based on the Monte Carlo method are, in our opinion, more efficient than gradient methods, to which the Levenberg–Marquardt method belongs. If the source

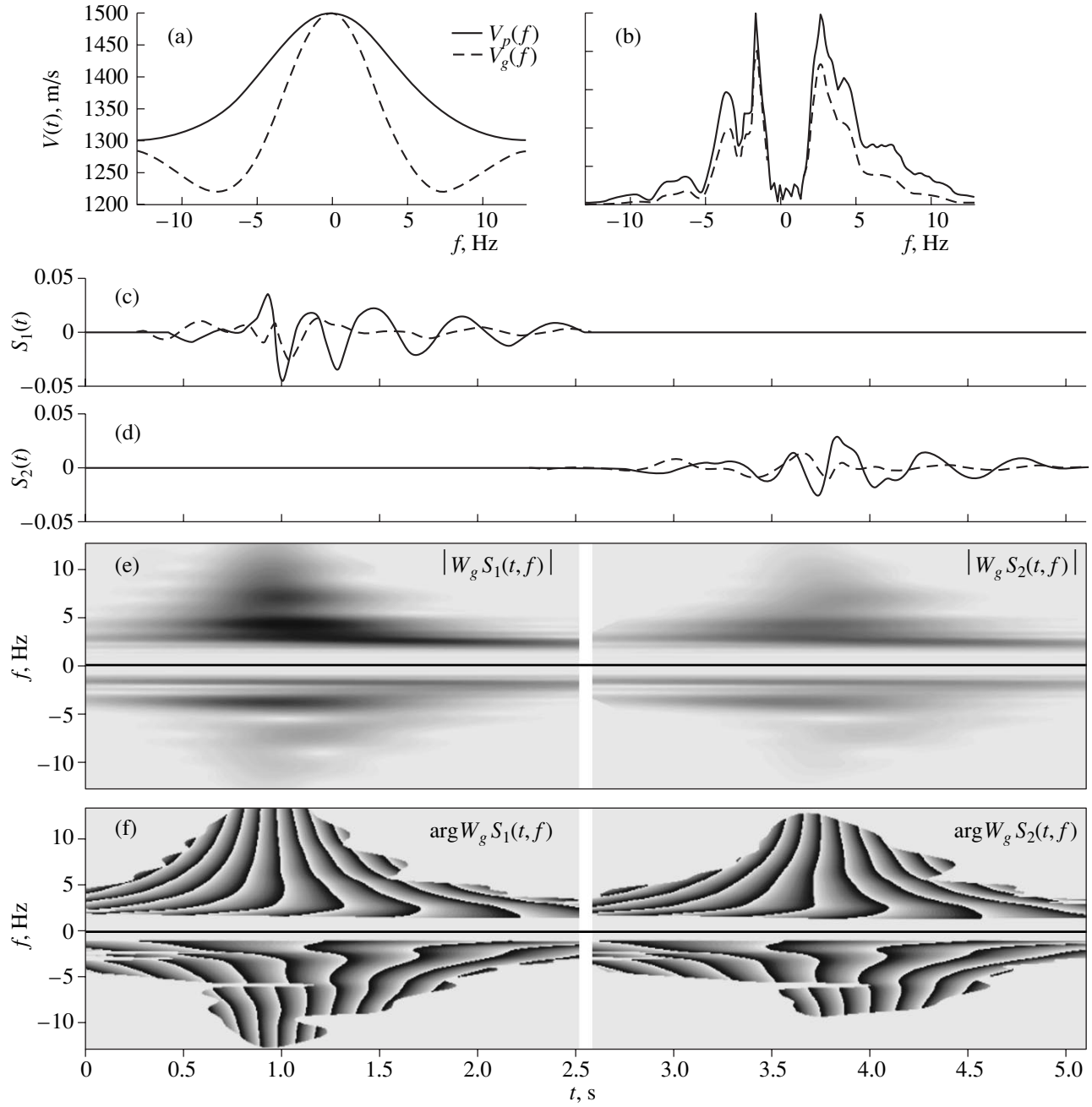

Fig. 4. Comparison of the dispersion models formulated in the Fourier and wavelet spaces.

seismogram is severely contaminated with noise, the optimization process may use the cost function in the form $|[\mathcal{W}_g T_{1,2}](t,f) - [\mathcal{W}_g T_{1,n}](t,f)|^2$, where the symbol $T_{i,j}$ means cross correlation of the signals: $\hat{T}_{i,j}(f) = \hat{S}_i(f)\hat{S}_j(f)$. Relationships (3.1)–(3.7) can readily be modified for this case. If the seismogram does not contain only the Rayleigh component, the double integral in Eqs. (4.2) and (4.3) is replaced with an integral over a region specified by ellipticity parameters (2.3). However, a detailed analysis of these and many other modifications is a subject of a separate study.

Consider an example. Let the signal propagate without attenuation and the three-parameter exponential approximation be chosen for the function $k(f, p_i)$:

$$k(f, p_i) = p_1 f + p_2 f e^{-\frac{f^2}{2p_3^2}}.$$

Let $S_1(t)$ and $S_2(t)$ be synthetic signals, where the second signal can be obtained from the first signal with

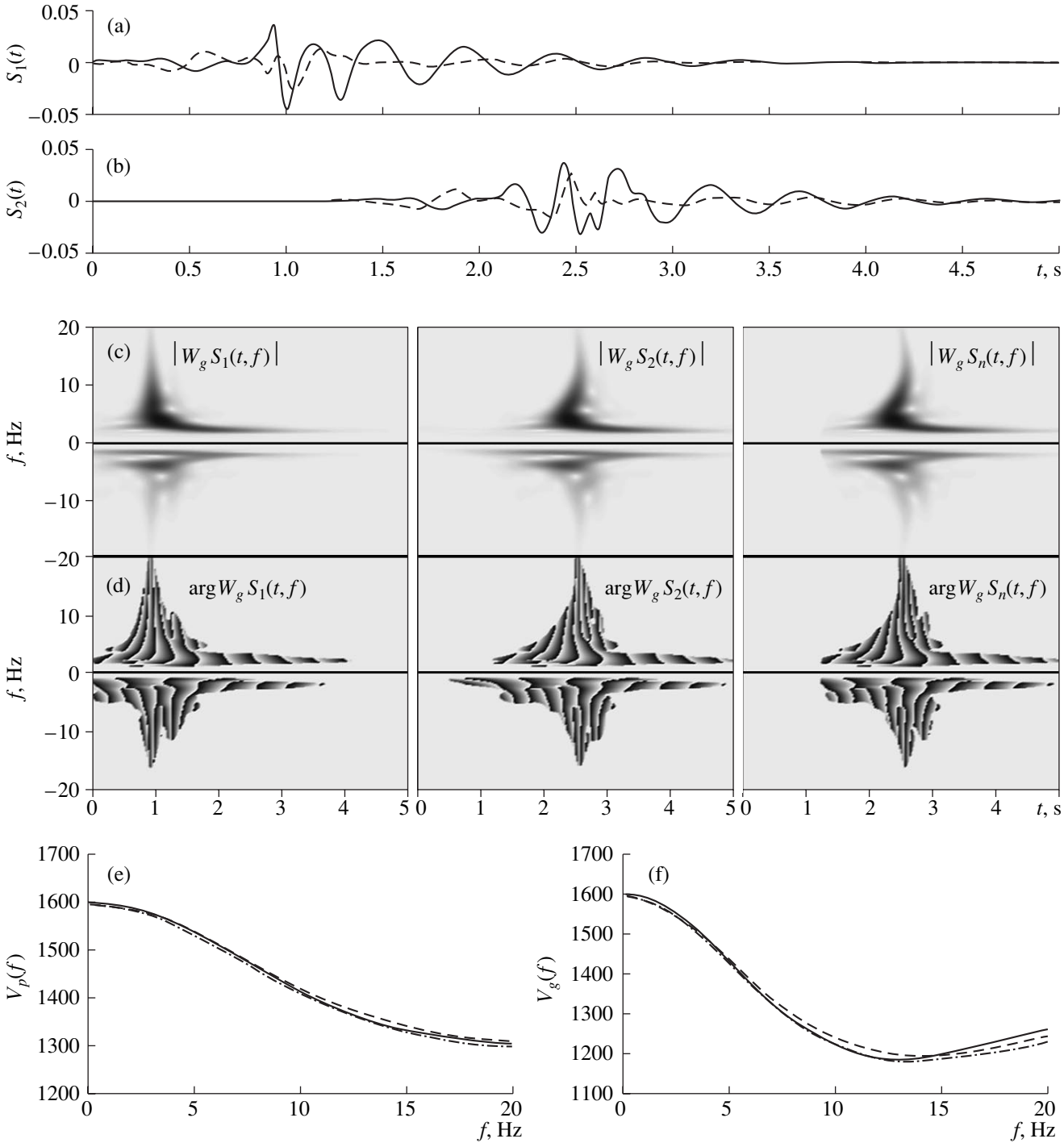

Fig. 5. Source signals, wavelet spectra of the source and reconstructed signals, and source and reconstructed phase and group velocities.

the help of dispersion model (3.1)–(3.3) with the phase velocity V_p given by Eq. (3.8) at V_1 = 1300 m/s, ΔV = 300 m/s, σ = 10 Hz, and Δx = 2000 m.

Figure 5a shows the real (solid line) and imaginary (dashed line) parts of the source signal $S_1(t)$. Figure 5b shows the source $S_2(t)$ (black lines) and reconstructed $S_n(t)$ (gray lines) signals.

Figure 5c shows the absolute values of the source wavelet spectrum and the one reconstructed by procedure (4.1)–(4.3), where $|\hat{W}_g S_n(t, f)|$ is the absolute value of the reconstructed signal spectrum. Figure 5d shows the phases of these spectra.

The solid line in Fig. 5e represents the theoretical phase velocity used to generate signals $S_1(t)$ and $S_2(t)$;

the dashed line represents the reconstructed phase velocity for cost function (4.2), and the dashed-dotted line, for cost function (4.3). Figure 5f shows similar curves for the group velocity. The conclusion may be drawn that the velocity reconstruction accuracy is quite satisfactory, the accuracy provided by cost function (4.3) being higher than that provided by cost function (4.2).

CONCLUSIONS

The following new results were obtained from this study:

(1) A new method based on the wavelet analysis formalism is proposed. The method determines the following ellipticity parameters of surface waves in the form of time–frequency spectra (matrices): the major $R(t, f)$ and minor $r(t, f)$ semiaxes of the ellipse and the ellipse dip angle $\Theta(t, f)$; the phase shift $\Delta\phi(t, f)$ between two components $S_x(t)$ and $S_y(t)$ of two-component signals; and the ellipticity $\rho(t, f)$. These parameters allow one to identify with fair accuracy a Rayleigh wave in seismograms.

(2) A model that relates the wavelet spectra of two complex signals $S_1(t)$ and $S_2(t)$ obtained from two multicomponent seismic receivers displaced by Δx is proposed. Parameters of the model are the amplitude attenuation function $\alpha(f)$, the phase velocity $V_p(f)$, and the group velocity $V_g(f)$.

(3) A nonlinear minimization problem is formulated, the solution of which determines the phase and group velocity functions and the attenuation function to a high accuracy from two complex signals $S_1(t)$ and $S_2(t)$.

(4) The combination of the minimization problem with the proposed method of calculating the ellipticity parameters allows one to determine the phase and group velocities and the attenuation function for the Rayleigh modes in the source seismograms.

ACKNOWLEDGMENTS

This work was supported by the German Research Society (Deutche Forschung Gemeinschaft, DFG) under the project no. DFG-1114 “Mathematical Methods in Time Series Analysis and Image Processing.”

REFERENCES

1. S. V. Biryukov, Yu. V. Gulyaev, V. V. Krylov, and V. P. Plesskiĭ, *Surface Acoustic Waves in Inhomogeneous Media* (Nauka, Moscow, 1991) [in Russian].
2. A. E. Lyalin, V. A. Pirozhkov, and R. D. Stepanov, Akust. Zh. **28**, 838 (1982) [Sov. Phys. Acoust. **28**, 494 (1982)].
3. B. Buttkus, *Spectral Analysis and Filter Theory in Applied Geophysics* (Springer, Berlin, 2000).
4. A. L. Levshin, T. B. Yanovskaya, A. V. Lander, *et al.*, *Seismic Surface Waves in the Horizontally Inhomogeneous Soil* (Nauka, Moscow, 1986) [in Russian].
5. V. G. Alkaz, N. I. Onofrash, and A. I. Perel’berg, *Polarization Analysis of Seismic Oscillations* (Shtiintsa, Chisinau, 1977) [in Russian].
6. R. M. Rene, J. L. Fitter, P. M. Forsyth, *et al.*, Geophysics **51**, 1235 (1986).
7. J. Xia, R. D. Miller, and C. B. Park, Geophysics **64**, 691 (1999).
8. C. B. Park, R. D. Miller, and J. Xia, Geophysics **64**, 800 (1999).
9. A. J. Deighan and D. R. Watts, Geophysics **62**, 1896 (1997).
10. M. Holschneider, *Wavelets: an Analysis Tool* (Oxford University Press, Oxford, 1995).
11. N. M. Astaf’eva, Usp. Fiz. Nauk **166** (11), 1145 (1996) [Phys. Usp. **39** (11), 1085 (1996)].
12. J. Bendat and A. Piersol, *Random Data: Analysis and Measurement Procedures* (Wiley, New York, 1986; Mir, Moscow, 1989).
13. Y. Nakamura, Quart. Rep. Railway Techn. Res. Inst. **30** (1), 25 (1989).
14. W. H. Press, S. A. Teukolsky, W. T. Vetterling, and B. P. Flannery, *Numerical Recipe in C: the Art of Scientific Computing* (Cambridge University Press, Cambridge, 1992).

Translated by A. Khzmalyan

Acoustical Physics, Vol. 51, No. 4, 2005, pp. 435–442. Translated from Akusticheskiĭ Zhurnal, Vol. 51, No. 4, 2005, pp. 511–519.

Noise Spectrum of a Gas Plume

A. O. Maksimov

Il'ichev Pacific Oceanological Institute, Far-East Division, Russian Academy of Sciences, ul. Baltiĭskaya 43, Vladivostok, 690041 Russia

e-mail: maksimov@poi.dvo.ru

Received January 22, 2003

Abstract—The spectrum of a "gas plume" formed by a marine hydrocarbon seep is described. The noise spectral density has maxima at frequencies corresponding to the natural (collective) oscillations of the bubble cloud, which are related to the size of the gas plume and to the mean volume gas content in the medium. The spatial distribution of noise in depth near a gas plume is highly nonuniform and modal in nature. The nonuniformity is localized in the horizontal plane, and the localization radius is the smaller the higher the mode number is. © *2005 Pleiades Publishing, Inc.*

In the mid-1980s, gas hydrate manifestations were detected in the Sea of Okhotsk near Paramushir Island and the Deryugin basin [1, 2]. Marine hydrocarbon seeps emitting methane bubbles from seafloor vents give rise to the so-called "gas plumes." The latter can be easily detected by regular echo sounders, because the resonant scattering cross section of a gas bubble is two orders of magnitude greater than the bubble size. The seeps found in the Sea of Okhotsk were mainly studied under the KOMEX joint Russian–German project [3–8]. Field measurements aimed at studying these phenomena were carried out with the use of both remote acoustic methods and underwater systems in the UK part of the North Sea [9–12], in the Gulf of Mexico [13, 14], and near the coast of California (the northern boundary of the Santa Barbara Channel) [15–17].

Along with the conventional (active) methods of gas plume sounding, the development of passive methods is proposed on the basis of analyzing the noise radiation in the vicinity of the object at frequencies corresponding to the natural (collective) oscillations of the bubble cloud. Two types of noise sources are analyzed. The formation of a single bubble is accompanied by noise radiation that is characterized by Longuet-Higgins as a "birthing wail" [18]. The second type of noise source is well known: the agitated upper layer of the ocean, where noise is produced by breaking waves. Broadband noise propagating in a bubble cloud gives rise to standing waves in the gas plume region. These collective oscillations manifest themselves as maxima in the spectral density of noise signals at frequencies related to the geometric dimensions of the gas plumes and to the mean gas content in the medium.

In constructing the model, it is reasonable to rely upon the world's most spectacular marine hydrocarbon seeps. They include primarily the SBC (Santa Barbara Channel) seep. In this region, bubbles rise from a relatively small depth (~60 m). Multiple backscattering measurements were performed at frequencies of 50 kHz and 3.5 MHz, and bubble size distributions were studied [14]. The bubbles fill the whole water column, from the vents in the bottom to the ocean surface, and the backscattering data show no anomalies in their distribution in depth. Below, a comparison is performed with the following marine hydrocarbon seeps [19]: the Thor CP Seep (TCS), (latitude 34°52.442′, longitude 119°23.650′) lying at a depth of 20 m and extending over an area of ~2 m^2; La Goleta Seep (LGS), (latitude 34°51.183′, longitude 119°22.500′) lying at a depth of 70 m and occupying an area of ~25 m^2; and Seep Tent Seep (STS), (latitude 34°53.350′, longitude 119°23.050′) at a depth of 70 m with an area of ~700 m^2. The simplest model (Fig. 1) that can be used to describe a gas

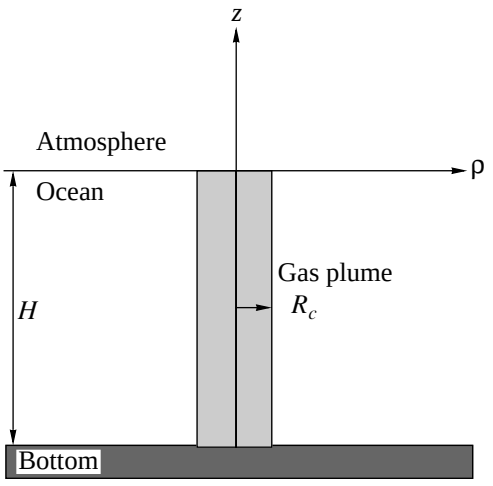

Fig. 1. Model of a gas plume: a cylinder with a height H and radius R_c filled with a gas–liquid mixture that is characterized by a sound velocity c_m much smaller than the sound velocity c in the surrounding liquid.

plume is a circular cylinder filled with a mixture of liquid and bubbles, whose height H is equal to the depth at which the bubbles depart from the vents and whose radius R_c characterizes the transverse size of the gas plume.

The linearity of the problem allows us to separate the solution into two parts. At the first stage, we analyze the radiation of a unit-amplitude monopole point source with a time dependence $\exp(-i\omega t)$. Eliminating the time variable, we reduce the problem to solving the Helmholtz equation for the pressure field P in pure liquid with the wave vector

$$k^2 = \omega^2/c^2, \quad R_c < \rho, \quad -H < z < 0, \tag{1}$$

where c is the velocity of sound in the pure liquid. The pressure perturbation P in the gas plume, i.e., in the aforementioned cylindrical column with $-H < z < 0$ and $0 < \rho < R_c$, is described by the Helmholtz equation with the wave vector [20]

$$k_m^2 = \frac{\omega^2}{c_m^2} = \frac{\omega^2}{c^2} + 4\pi\omega^2 \int \frac{g(R)RdR}{\Omega_0^2(R) - \omega^2 + 2i\delta\omega}. \tag{2}$$

Here, $g(R)$ is the distribution function representing the number of bubbles in a unit volume with radii from R to $R + \Delta R$ (the dimension of this functions is $\mathrm{m}^{-3}\ \mu\mathrm{m}^{-1}$); $\Omega_0(R)$ and δ are the eigenfrequency and damping factor of a bubble of radius R.

The applicability conditions for Eq. (2) deserve special consideration. Information on the distribution function of bubbles departing from the vents is rather scarce [2, 21–23]. In the most common case, that of continuous bubble generation, the distribution function has a maximum at $R_m \sim 2.5 \times 10^{-3}$ m and is characterized by a smooth decrease toward smaller and greater radii. A bubble with radius R_m has a resonance frequency $f_0 \sim$ 1.3 kHz near the surface; at a depth d, because of the hydrostatic pressure, the resonance frequency of a bubble of the same size is $f(d) = f_0\sqrt{1 + (d/h)}$ ($h \approx 10$ m). The distribution formed near the bottom can noticeably vary as the bubbles rise from the bottom to the surface [21–27]: the bubble size tends to decrease because of the dissolution of methane (CH_4) in water and tends to grow because of the decrease in hydrostatic pressure.

The present paper studies the low-frequency collective oscillations of the bubble cloud forming the gas plume; the periods of these oscillations are much greater than those of natural oscillations of individual bubbles. In this case, formula (2) is reduced to the well-known expression for the effective velocity of sound propagation in a gas–liquid mixture (Wood's equation) [28, 29]:

$$k_m^2 = \frac{\omega^2}{c_m^2}, \quad \frac{1}{c_m^2} = \frac{1}{c^2} + \frac{\beta\rho_0}{P}, \quad \beta = \frac{4\pi}{3}\int g(R)R^3 dR, \tag{3}$$

where β is the volume gas content, P is the hydrostatic pressure, and ρ_0 is the density of the liquid. The law governing the decrease in the volume gas content with decreasing distance to the surface depends on many factors [22] and differs from the linear law of hydrostatic pressure decrease. However, for depths smaller than 100 m, the ratio of these quantities can be considered to be constant within an order of magnitude. Precisely this simplest model with a constant sound velocity is used in the following calculations.

If, near the surface, the volume concentration β exceeds 10^{-4}, the effective sound velocity proves to be much smaller than the sound velocity in the pure liquid, and $c_m^2 \approx P(\beta\rho_0)^{-1}$. For $\beta \approx 0.01$, the sound velocity $c_m \approx$ 100 m/s is more than an order of magnitude smaller than c. This case is quite realistic because, in regions with an intense gas release, such as the SBC region, where methane production is organized, $\beta \approx$ 0.05 [15].

The Green function describing the propagation of sound from a point source satisfies the Helmholtz equation

$$\Delta G(\omega; \mathbf{r}|\mathbf{r}') + k^2(\rho)G(\omega; \mathbf{r}|\mathbf{r}') = -4\pi\delta(\mathbf{r} - \mathbf{r}'), \tag{4}$$

which should be complemented with boundary conditions. We use the free surface condition

$$G(\omega; \mathbf{r}|\mathbf{r}')\big|_{z=0} = 0 \quad (0 \le \rho < \infty) \tag{5a}$$

for regions occupied by the bubble mixture, as well as for regions occupied by pure liquid. At the bottom, in the presence of a sediment layer, we use the "soft" bottom condition

$$G(\omega; \mathbf{r}|\mathbf{r}')\big|_{z=-H} = 0 \quad (0 \le \rho < R_c); \tag{5b}$$

in the presence of rock, we use the "hard" bottom condition

$$\left.\frac{\partial G(\omega; \mathbf{r}|\mathbf{r}')}{\partial z}\right|_{z=-H} = 0 \quad (R_c \le \rho < \infty). \tag{5c}$$

Expanding the Green function in the eigenfunctions of the boundary-value problem and taking into account that the set of functions $\{\sin\lambda_n z\}$ is complete for both soft and hard boundaries, we obtain

$$\begin{aligned} G(\omega; \mathbf{r}|\mathbf{r}') &= \sum_{n=1}^{\infty}\sum_{m=-\infty}^{+\infty} G_{nm}(\rho|\rho') \\ &\times \sin(\lambda_n z)\sin(\lambda_n z')(\pi H)^{-1} e^{im(\varphi-\varphi')}, \\ &\frac{1}{\rho}\frac{\partial}{\partial\rho}\left(\rho\frac{\partial}{\partial\rho}G_{nm}(\omega; \rho|\rho')\right) \\ &+ \left[k^2(\rho) - \frac{m^2}{\rho^2} - \lambda_n^2\right]G_{nm}(\omega; \rho|\rho') = -\frac{4\pi}{\rho}\delta(\rho - \rho'), \end{aligned} \tag{6}$$

where, for the soft bottom given by Eq. (5b), $\lambda_n \equiv \lambda_n^S = (\pi/H)n$, whereas, for the hard bottom given by Eq. (5c),

$\lambda_n \equiv \lambda_n^R = (\pi/H)(n - 1/2)$ ($n = 1, 2, 3, \ldots$); (ρ, φ, z) are cylindrical coordinates. The explicit form of the radial part of Green's function $G_{nm}(\omega; \rho|\rho')$, which is the solution to Eq. (6), is determined by the formulas

$$G_{nm}(\rho|\rho') = 2\pi\begin{cases} J_m(\kappa_n\rho)[i\pi H_m^{(1)}(\kappa_n\rho') - d_1(n, m)J_m(\kappa_n\rho')] & \rho < \rho' < R_c, \\ [i\pi H_m^{(1)}(\kappa_n\rho) - d_1(n, m)J_m(\kappa_n\rho)]J_m(\kappa_n\rho') & \rho' < \rho < R_c, \\ (-\pi/d_2(n, m))J_m(\kappa_n\rho)K_m(k_n\rho') & \rho < R_c < \rho', \\ (-\pi/d_2(n, m))K_m(k_n\rho)J_m(\kappa_n\rho') & \rho' < R_c < \rho, \\ 2[I_m(k_n\rho) - c_1(n, m)K_m(k_n\rho)]K_m(k_n\rho') & R_c < \rho < \rho', \\ K_m(k_n\rho)2[I_m(k_n\rho') - c_1(n, m)K_m(k_n\rho')] & R_c < \rho' < \rho; \end{cases} \tag{7}$$

$$d_1 = \frac{K_m(k_nR_c)i\pi H_m^{(1)'}(\kappa_nR_c) - K_m'(k_nR_c)i\pi H_m^{(1)}(\kappa_nR_c)}{K_m(k_nR_c)J_m'(\kappa_nR_c) - K_m'(k_nR_c)J_m'(\kappa_nR_c)},$$

$$d_2 = -(\pi R_c/2)[K_m(k_nR_c)J_m'(\kappa_nR_c) - K_m'(k_nR_c)J_m(\kappa_nR_c)],$$

$$c_1 = \frac{I_m(k_nR_c)J_m'(\kappa_nR_c) - I_m'(k_nR_c)J_m(\kappa_nR_c)}{K_m(k_mR_c)J_m'(\kappa_nR_c) - K_m'(k_nR_c)J_m(\kappa_nR_c)},$$

$$k_n^2 = \lambda_n^2 - \frac{\omega^2}{c^2}, \quad \kappa_n^2 = \frac{\omega^2}{c_m^2} - \lambda_n^2,$$

where J_m, $H_m^{(1)}$, I_m, and K_m are Bessel functions and the prime denotes differentiation with respect to the coordinate.

As was mentioned above, the sound velocity in the mixture can be an order of magnitude smaller than the sound velocity in the liquid, and, therefore, the gas plume region represents an effective waveguide. Here, it is appropriate to refer to the analogy with an optical-fiber waveguide, which was mentioned in [30]. The presence of eigenmodes captured by this waveguide manifests itself as the poles of Green's function (6), (7). Indeed, at frequencies below the critical one, i.e., $\omega < \omega_0 = c(\pi/2H)$ (below, the calculations are performed for a hard bottom), all normal modes in the oceanic waveguide are damped and, hence, the Green function has no poles near the real axis. However, in the presence of a gas plume, the denominator $d_2(0, n) = (\pi R_c/2)]K_0(k_nR_c)\kappa_nJ_1(\kappa_nR_c) - k_nK_1(k_nR_c)J_0(\kappa_nR_c)$ involved in the axisymmetric ($m = 0$) part of Green's function $G_{0n}(\omega; \rho|\rho')$ may be equal to zero, which is the condition for the existence of natural oscillations localized in the horizontal plane. In the gas plume region, they are described by the singularity-free functions $J_0(\kappa_n\rho)$, and, outside the gas plume, by the exponentially decreasing functions $K_0(k_n\rho)$.

The presence of the small parameter $R_c/H \ll 1$ (for TCS, $R_c \sim 0.8$ m and $(R_c/H) \sim 0.04$; for LGS, $R_c \sim 3$ m and $(R_c/H) \sim 0.04$; and for STS, $R_c \sim 15$ m and $(R_c/H) \sim 0.2$) allows one to determine, in an explicit form, the eigenfrequencies of these localized oscillations. Taking only the first- and second-order terms of the Bessel function expansions in the small parameters $R_c\kappa_n \ll 1$ and $R_ck_n \ll 1$, we obtain

$$J_0(R_c\kappa_n) \simeq 1 - \frac{(R_c\kappa_n)^2}{4},$$

$$J_1(R_c\kappa_n) \simeq \frac{R_c\kappa_n}{2}\left(1 - \frac{(R_c\kappa_n)^2}{8}\right),$$

$$K_0(R_ck_n) \simeq -\left[\ln\frac{(R_ck_n)}{2} - \psi(1)\right],$$

$$K_1(R_ck_n) \simeq \frac{1}{(R_ck_n)} + \frac{(R_ck_n)}{2}\ln(R_ck_n),$$

$$d_2(0, n) \approx -(\pi/2)\left(1 + \frac{(R_c\omega/c_m)^2(1 - c_m^2/c^2)}{2}\ln(R_ck_n)\right).$$

The eigenfrequency of the nth mode, ω_{Rn}, is determined from the condition

$$(R_c\omega/c_m)^2(1 - c_m^2/c^2) = -2/\ln(R_ck_n). \tag{8}$$

As an illustration, Fig. 2 shows a graphical solution of this equation for the lowest mode with the geometrical parameters of the STS ($R_c/H \approx 0.2$). The gas flow from this seep is known to be rather intense [19], and, therefore, the calculations are performed by taking the sound velocity in the mixture to be much lower than the sound velocity in pure liquid: $ssr = (c_m^2/c^2) \approx 0.1$, 0.05, and 0.01. The low damping is ignored. Applying Wood's

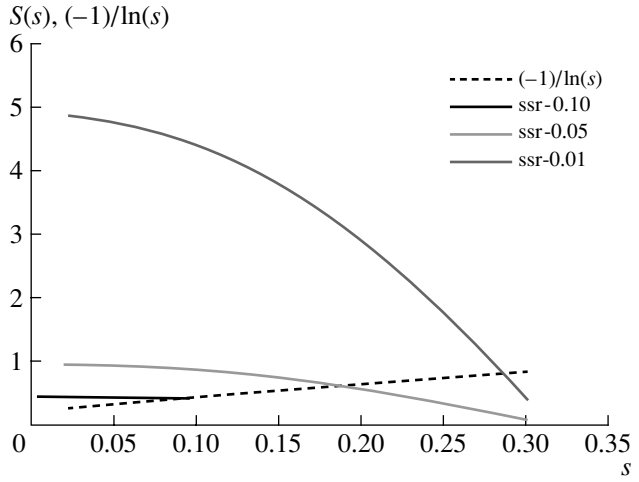

Fig. 2. Graphical solution of the dispersion equation for the lowest mode. The right-hand side of Eq. (8) is represented by the dashed line, and the left-hand side is represented by the solid lines, which are plotted for the sound velocity in the mixture c_m being much smaller than the sound velocity in the pure liquid c: $ssr = (c_m^2/c^2) \approx 0.1$, 0.05, and 0.01. The calculations are performed for the geometrical parameters of the STS, $(R_c/H) \approx 0.2$.

formula to these velocities in the mixture, we obtain the following volume concentration values: $\beta \approx 0.044$, 0.088, and 0.44%. Figure 2 represents the quantities $S(s) = (1/2)[1 - (c_m/c)^2](c_m/c)^{-2}[(\pi R_c)^2(2H)^{-2} - s^2]$ and $-1/\ln(s)$ plotted along the y axis versus the quantity $s \equiv R_c k_1$ ($k_1 = \sqrt{(\pi/2H)^2 - (\omega/c)^2}$) plotted along the x axis. The eigenfrequency of the trapped mode is determined by the point of intersection of the curves: $s(0.1) \simeq 0.087$, $s(0.05) \simeq 0.178$, and $s(0.01) \simeq 0.287$, which, according to the formula $f = (c/2\pi R_c)\sqrt{(\pi R_c/2H)^2 - s^2}$, yields $f(0.1) \approx 5.1$ Hz, $f(0.05) \approx 4.4$ Hz, and $f(0.01) \approx 2.1$ Hz. Note that it is the high concentration of bubbles in the mixture and, hence, the low sound velocity that is responsible for the noticeable deviation of the eigenfrequency from the continuous spectrum boundary $f_c = (c/4H) \approx 5.4$ Hz. In this case, it is possible to obtain an analytical dependence of the eigenfrequency on the determining parameters:

$$\omega_{R1}^2 \approx \frac{2c_m^2}{R_c^2|\ln(R_c/H)|}. \quad (9)$$

A similar expression can be obtained from simple physical considerations. Indeed, the model under study (Fig. 1) can be interpreted as the problem concerning the natural oscillations of a cylindrical bubble whose compressibility is expressed as

$$K = -\frac{1}{V}\frac{\partial V}{\partial P} = \frac{\beta}{P} = \frac{1}{\rho_0 c_m^2}$$

and whose inertial mass can be determined as follows. At distances smaller than the wavelength $\lambda = 2\pi/k \geq H$, the liquid can be considered incompressible; therefore, the potential satisfying the Laplace equation has the form $\varphi = -\varphi(t, R_c)\ln(\rho/H)$, and the pressure variations are expressed through the potential using the Bernoulli equation $\Delta P_{out} = -\rho_0(\partial\varphi/\partial t)$. The continuity conditions for the displacements and pressure variations at the cylindrical wall of the bubble yield

$$\Delta\dot{R} = -\frac{\varphi(t, R_c)}{R_c}; \quad \Delta P_{out} = \Delta P_{in},$$

$$\Delta P_{in} = -\frac{1}{K}\frac{2\Delta R}{R_c} = -\rho_0\frac{2c_m^2}{R_c}\Delta R, \quad (10)$$

$$\Delta P_{out} = \rho_0\frac{\partial\varphi(t, R_c)}{\partial t}\ln(R_c/H) = -\rho_0\ln(R_c/H)R_c\Delta\ddot{R},$$

$$-\ln(R_c/H)R_c\Delta\ddot{R} + \frac{2c_m^2}{R_c}\Delta R = 0,$$

which is an analog of the Rayleigh equation with the eigenfrequency determined by Eq. (9).

In the opposite case, when the deviation from the critical frequency is small, i.e., $f = f_c - \Delta f$ and $\Delta f \ll f_c$, dispersion equation (8) can be represented in the form

$$(R_c k_1)^2 = \exp\left[-\frac{4(c_m/R_c\omega)^2}{(1 - c_m^2/c^2)}\right]$$

$$\approx \exp\left[-\frac{4(c_m/R_c 2\pi f_c)^2}{(1 - c_m^2/c^2)}\right] = \exp\left[-\frac{4c_m^2H^2}{\pi^2c^2R_c^2(1 - c_m^2/c^2)}\right].$$

Replacing the left-hand side of this equation by an approximate expression $(R_c k_1)^2 = R_c^2[\pi^2/(4H^2) - 4\pi^2(f_c - \Delta f)^2c^{-2}] \approx (2\pi^2 R_c^2 c^{-1}H^{-1})\Delta f$, we obtain

$$\Delta f = \frac{cH}{2\pi^2R_c^2}\exp\left[-\frac{4c_m^2H^2}{\pi^2c^2R_c^2(1 - c_m^2/c^2)}\right]. \quad (11)$$

According to Eq. (11), for not as intense seeps (such as the LGS and TCS) with a smaller transverse size $(R_c/H) \sim 0.04$, the deviation of the lowest frequency from the continuous spectrum boundary ($f_c = (c/4H) \approx 5.4$ Hz for the LGS and $f_c \approx 19$ Hz for the TCS) is exponentially small. The physical parameter separating the two limiting cases is $\eta = (c_m H/cR_c)$. When $\eta \ll 1$, the deviation of the eigenfrequency is considerable and the eigenfrequency is described by Eq. (9); when $\eta \gg 1$, the deviation from the continuous spectrum boundary is exponentially small.

Dispersion equation (8) describes not only the lowest mode but also a set of higher localized modes satisfying the inequalities $R_c\kappa_n \ll 1$, $R_c k_n \ll 1$ and containing increasing numbers of nodes and antinodes in their ver-

tical structures. However, since these states fall within the continuous spectrum region, they are considered complex resonances.

The problem of captured modes in an acoustic waveguide, such as collective oscillations of a bubble plume, has been intensively studied in the last ten years (see [31–33] and the literature cited there). At the same time, rigorous mathematical results concerning the conditions for the presence (or absence) of captured modes were obtained for simple models, namely, objects of regular geometrical shape in configurations symmetric with respect to the walls or displaced from the symmetric configurations so as to allow one to use the perturbation theory. Moreover, the main results were obtained for the two-dimensional problem. In actual geometry, they may be applicable to a cylindrical object whose generatrix is parallel to the ocean surface.

Now, let us proceed to the comparison with the results of laboratory studies of sound radiation from a cylindrical column of bubbles in a tank [30, 34–36]. The bubbles were produced at the bottom by pumping air through nozzles (medical needles of identical size) uniformly distributed around concentric circles. Detailed measurements of the positions of the first five maxima in spectral density and their dependence on the volume gas content within 0.1–1.5% showed a total coincidence of the theoretical and experimental results. However, it should be noted that, in the presence of reflecting side walls, the dispersion equation for the eigenmodes in the tank with a cylindrical bubble cloud differed from that analyzed in this paper. This difference was most pronounced for lower volume concentrations, when the captured mode frequency (for definiteness, we consider the lowest mode) approached the boundary f_c of the continuous spectrum of the oceanic waveguide. Under the conditions of the experiment [36], $f_c = (c/4H) \approx 450$ Hz (the height is $H \approx 0.82$ m), but this value is not evident in the experiment, because the origin of localization in the horizontal direction is not affected by the damped nature of the field in the region $R_c \le \rho \le R_t$ (R_t is the tank radius) at $f < f_c$ or by its standing wave character at $f > f_c$: the localization is provided by the presence of the tank side walls. A totally different situation occurs in a waveguide that is infinite in the horizontal direction: there, the captured lowest mode can only exist at $f < f_c$.

The conditions of experiment [30] carried out in a tank that was relatively long in the transverse direction (the depth of the liquid was 0.28 to 0.47 m, and the tank radius was ~1.50 m) were closest to the STS in proportion. Figure 3 of the cited paper shows the dependence of the lowest mode frequency on the volume concentration for a cylindrical bubble plume of radius $R_c = 0.08$ m with the height of the liquid column $H = 0.41$ m. Since, in this case, we have $R_c/H \approx 0.2$, the comparison with the data of [30] verifies the results; in particular, this comparison confirms the validity of the dispersion equation in the relatively simple form of Eq. (8).

The explicit form of Green function as given by Eqs. (6) and (7) allows us to describe the spatial distribution of noise in the vicinity of a gas plume by combining the contributions of different sources. The Fourier component of the pressure measured at a frequency ω at the point $\mathbf{r}$ $P_T(\omega; \mathbf{r})$, is described by the integral

$$P_T(\mathbf{r}, \omega) = \int G(\omega; \mathbf{r}|\mathbf{r}')q(\omega; \mathbf{r}')d\mathbf{r}', \qquad (12)$$

where $q(\omega; \mathbf{r}')$ is a random distribution function of monopole noise sources. The spatial coherence of the noise field is described by the correlation function

$$\langle P_T(\mathbf{r}, \omega)P_T^*(\mathbf{r}_1, \omega)\rangle$$
$$= \int d\mathbf{r}'d\mathbf{r}''\langle q(\omega; \mathbf{r}')q^*(\omega; \mathbf{r}')\rangle G(\omega; \mathbf{r}|\mathbf{r}')G^*(\omega; \mathbf{r}_1|\mathbf{r}''),$$

where the asterisk indicates complex conjugation and the angular brackets denote averaging over an ensemble of random sources. Let us specify the types of sources.

Let us first consider noise caused by breaking waves. We use the conventional model [37, 38], according to which every point of the plane lying at a depth z_0 below the free surface corresponds to a monopole source described as $q(\omega; \mathbf{r}') = s(\omega; \mathbf{r}')\delta(z' - z_0)$. In this expression, the function $s(\omega; \boldsymbol{\rho}')$ is a random variable, and its correlation function is $\langle s^*(\omega; \boldsymbol{\rho}')s(\omega; \boldsymbol{\rho}'')\rangle = |q_0(\omega)|^2 N(|\boldsymbol{\rho}' - \boldsymbol{\rho}''|)$. In the important particular case of uncorrelated sources, $N(\rho) = 2\delta(\rho)(\omega^2\rho/c^2)^{-1}$ [37], and we have

$$C_\omega(\rho, z; \rho_1, z_1; \varphi - \varphi_1)$$
$$\equiv \langle P_T(\boldsymbol{\rho}, z; \omega)P_T^*(\boldsymbol{\rho}_1, z_1; \omega)\rangle = 4\pi\left(\frac{q(\omega)c}{\omega}\right)^2\int d^2\boldsymbol{\rho}'$$
$$\times G(\omega; \boldsymbol{\rho}, z|\boldsymbol{\rho}', z_0)G^*(\omega; \boldsymbol{\rho}_1, z_1|\boldsymbol{\rho}', z_0)$$
$$= 8\left(\frac{q(\omega)c}{\omega H}\right)^2\sum_{n=1}^{\infty}\sum_{l=1}^{\infty}\sin\left[\frac{\pi z}{H}(n-1/2)\right] \qquad (13)$$
$$\times \sin\left[\frac{\pi z_0}{H}(n-1/2)\right]\sin\left[\frac{\pi z_1}{H}(l-1/2)\right]\sin\left[\frac{\pi z_0}{H}(l-1/2)\right]$$
$$\times \sum_{m=-\infty}^{+\infty}\exp[im(\varphi - \varphi_1)]\int_0^{\infty}G_{nm}(\rho|\rho')G_{lm}^*(\rho_1|\rho')\rho'd\rho'.$$

However, the basic quantity measured in an experiment is the spectral density SD:

$$\mathrm{SD} = 10\log\left(\frac{4\pi|P_T(\omega; \mathbf{r})|^2}{T(P_{ref}^2/\mathrm{Hz})}\right). \qquad (14)$$

Here, T is the duration of the measurement interval and $P_{ref} = 1$ μPa. Assuming ergodicity, we express Eq. (14)

through the average over the ensemble of noise sources given by Eq. (13):

$$|P_T(\mathbf{r}, \omega)|^2 = |q_0(\omega)|^2 \int d\boldsymbol{\rho}' \int d\boldsymbol{\rho}'' G^*(\omega; \mathbf{r}|\boldsymbol{\rho}', z_0) \times G(\omega; \mathbf{r}|\boldsymbol{\rho}'', z_0) N(|\boldsymbol{\rho}' - \boldsymbol{\rho}''|) \approx 8\left(\frac{q(\omega)c}{\omega H}\right)^2 \times \sum_{n=1}^{\infty}\sum_{l=1}^{\infty} \sin\left[\frac{\pi z}{H}(n-1/2)\right]\sin\left[\frac{\pi z}{H}(l-1/2)\right] \times \sin\left[\frac{\pi z_0}{H}(n-1/2)\right]\sin\left[\frac{\pi z_0}{H}(l-1/2)\right] \times \sum_{m=-\infty}^{+\infty}\int_0^{\infty} G_{nm}(\rho|\rho')G^*_{lm}(\rho_1|\rho')\rho' d\rho'. \quad (15)$$

Near the frequencies corresponding to the natural collective oscillations of the bubble cloud (Eq. (8)), the major contribution to the spectral density is made by the pole singularities of Green function [37]. Retaining the components of the axisymmetric ($m = 0$) Green function that are diagonal in mode numbers n and that make the maximal contribution near the resonances, we obtain

$$|P_T(\mathbf{r}, \omega)|^2 \approx |q_0(\omega)|^2 \sin^2\left[\frac{\pi z}{H}(n-1/2)\right] \times \left[\frac{\pi z_0}{H}(n-1/2)\right]^2 \frac{1}{(\pi H)^2}\frac{8\pi^2}{(\omega/c)^2} \times \int_0^{\infty} d\rho'\rho' G^*_{n0}(\omega; \rho|\rho')G_{n0}(\omega; \rho|\rho'). \quad (16)$$

Taking the principal order in small parameters $R_c\kappa_n \ll 1$ and $R_c k_n \ll 1$, we arrive at the expression

$$\int_0^{\infty} d\rho'\rho' G^*_{n0}(\omega; \rho|\rho')G_{n0}(\omega; \rho|\rho') \approx \frac{4\pi^4 K_0^2(k_n\rho)}{|d_2(n,0)|^2}\int_0^{R_c} J_0^2(\kappa_n\rho')\rho' d\rho' + 16\pi^2|c_1(n,0)|^2 K_0^2(k_n\rho)\int_{R_c}^{\infty} K_0^2(k_n\rho')\rho' d\rho' \approx \frac{8\pi^2\left(R_c^2 + \dfrac{\omega^4 R_c^4}{c^4 k_n^2}\right)K_0^2(k_n\rho)}{\left\{1 - \dfrac{\omega^2}{\omega_{Rn}^2}\right\}^2 + \left\{4\pi\omega_{nR}^3 R_c^2 \ln\left[\dfrac{R_c\pi(n-1/2)}{H}\right]\int \dfrac{\delta g(R) R dR}{(\Omega_0^2(R) - \omega_{nR}^2)^2 + 4\delta^2\omega_{nR}^2}\right\}^2}.$$

From this formula, it follows that the contribution to the excitation of eigenmodes from the noise sources located above the gas plume (proportional to $\sim R_c^2$) is greater than the contribution from the sources located in the more extended region ($\sim k_n^{-2}$) outside the gas plume, but this occurs because of the Rayleigh-type ($\omega^4 R_c^4/c^4$) $\ll 1$ scattering leading to much smaller values of spectral density. Substituting this expression into Eq. (16), we obtain

$$|P_T(\mathbf{r}, \omega)|^2 \approx 16\pi^3 q_\infty^2(\omega)\frac{R_c^2(n-1/2)^2}{(\omega/c)^2 H^4}K_0^2(k_n\rho) \times \sin^2\left[\frac{\pi z}{H}(n-1/2)\right]\left\{\left[1 - \frac{\omega^2}{\omega_{Rn}^2}\right]^2 + Q_n^{-2}\right\}^{-1}. \quad (17)$$

Following [38], we eliminated the dependence on the parameter z_0 of the model, i.e., on the depth of the source layer. For this purpose, the noise level $q_0(\omega)$ was normalized [38], $q_0^2(\omega) = q_\infty^2(\omega)/(16\pi z_0^2)$, so as to reduce it to the level q_∞ produced by the same sources in an infinitely deep ocean. To describe the finite width of the resonance curve, the phenomenological parameter Q_n representing the Q factor of the nth localized mode was introduced in Eq. (17). If the major contribution to damping is made by the scattering by bubbles, we have

$$Q_n^{-1} \approx 4\pi\omega_{nR}^3 R_c^3 \ln\left[\frac{R_c\pi(n-1/2)}{H}\right] \times \int \frac{\delta g(R) R dR}{(\Omega_0^2(R) - \omega_{nR}^2)^2 + 4\delta^2\omega_{nR}^2}.$$

At the same time, this issue requires special investigation; in particular, it is necessary to take into account the permeability of the bottom, for example, in the Pekeris model, i.e., a fluid layer overlying a fluid half-space.

Now, let us calculate the distribution of noise generated by bubbles formed at the vents. Since the problem is linear, their contribution is additive with surface wave contribution (17). Then, the correlation

function of monopole sources is described by the formula [36]

$$\langle q^*(\omega; \mathbf{r}')q(\omega; \mathbf{r}'')\rangle = 4\rho_0^2\dot{n}T(\bar{R}_0/R_c)^4\left|(\ddot{R}_\omega)\right|^2[1-\theta(R_c-\rho')] \times \delta(z'-H)[1-\theta(R_c-\rho'')]\delta(z''-H),$$

where $\dot{n}$ is the number of bubbles formed at the vents per unit time, $\bar{R}_0$ is the average bubble radius, and $(\ddot{R})_\omega$ is the Fourier component of the bubble wall acceleration for a bubble of characteristic size $\bar{R}_0$. The physical interpretation of this expression is as follows: the base of the column is divided into N incoherent piston sources (vents), and each of them acts with the same pressure over an area of $\pi R_c^2/N$.

Retaining the diagonal (in mode number n) components of the axisymmetric ($m = 0$) Green function, we obtain the following noise distribution in the vicinity of a gas plume ($\rho > R_c$):

$$\begin{aligned}\left|P_T(\mathbf{r}, \omega)\right|^2 &= 4\rho_0^2\dot{n}T(\bar{R}_0/R_c)^4\left|(\ddot{R})_\omega\right|^2 \\ &\times\left|\int_0^{2\pi}\int_0^{R_c} d\varphi'\rho' d\rho' G(\omega; \mathbf{r}|\rho', \varphi', H)\right|^2 \\ &\approx 64\pi^2\rho_0^2\dot{n}T\frac{\bar{R}_0^4\left|(\ddot{R})_\omega\right|^2}{H^2}K_0^2(k_n\rho) \\ &\times\sin^2\left[\frac{\pi z}{H}(n-1/2)\right]\left\{\left[1-\frac{\omega^2}{\omega_{Rn}^2}\right]^2+Q_n^{-2}\right\}^{-1}.\end{aligned} \quad (18)$$

Thus, the spatial distribution of the spectral intensity of noise in depth near a gas plume is highly nonuniform and exhibits a mode character. This nonuniformity is localized in the horizontal plane, and the localization radius is smaller the higher the mode number is. The noise spectral density has maxima at frequencies directly related to the size of the gas plume and to the mean volume gas content in the medium.

In closing, let us estimate the noise spectrum described by Eqs. (17) and (18) and compare it with ambient noise in the ocean [40–42]. We use the estimate for the intensity of sources $q_0^2(\omega)$ [38] that produce a uniform pressure distribution q_∞ in an infinitely deep ocean with an intensity corresponding to 70 dB. According to Eq. (17), the spectral peaks associated with the gas plume manifestation exceed the ambient noise level only when $R_cQ_n > H$, i.e., for a sufficiently high Q factor of localized modes and sufficiently large seep areas, such as, e.g., the STS. The excess over the ambient noise level can be observed at distances equal to several depths. An indicator of the gas plume presence that is more efficient than noise intensity is the structure of spatial correlations of noise (Eq. (13)). However, these issues, as well as the "illumination" of a gas plume by ship noise, variations in the plume shape, and, in particular, the description of a conic waveguide, should be studied separately.

Let us estimate the noise level produced by bubbles appearing from vents at the bottom of the ocean. The spectral density of noise for the first normal modes of a bubble plume was investigated under laboratory conditions [36] in the frequency range 300–1200 Hz. The sampling interval was $T = 0.1$ s. At the axis of the plume (see Fig. 8 of the cited paper), the spectral density of the first mode was ~110 dB with respect to the wave with $P_{ref} = 1$ μPa in a 1-Hz frequency band. A full agreement with the experimental results was achieved for a model with the characteristic bubble size $R_0 \sim 2\times10^{-3}$ m and the rate of bubble generation at a single vent (medical needle) $\dot{n}_N = \dot{n}/N \sim 50$ s^{-1} (in the experiment under discussion, $N = 49$). In calculating the spectral density at the lowest mode frequency by formula (18), we use the same model of noise generation and the same value of the characteristic bubble radius as in [36]. To obtain a quantitative estimate, it is necessary to preset the Q factor of the lowest mode Q_1, the geometrical parameters of the seep (R_c, H), the mean rate of bubble generation at a single vent $\dot{n}_N$, and the total number of vents in the seep N ($\dot{n} \approx \dot{n}_N N$). Referring to the parameters of the STS, one can see that, for this seep, the rate of bubble generation at one vent is higher than in the laboratory experiment [36], but the density of vent distribution $N/(\pi R_c^2)$ is much smaller. To determine $\dot{n}$, we use the data from [39]. The methane production in the STS region is carried out with the use of two metal canopies fixed at the bottom and covering an area of 1800 m^2 and makes $\dot{V} \sim 9\times10^5$ m^3/month or 0.34 m^3/s [39]. Then, for the STS with an area of about 700 m^2, we obtain $\dot{n} = \dot{V}/(4\pi R_c^2/3) = 0.34(700/1800)[(4\pi/3)(2\times10^{-3})^3]^{-1} \approx 4\times10^6$ s^{-1}.

We use the same Q factor, namely, $Q_1 \sim 10$, as that realized in the experiment in [36], but, because of the higher permeability of the bottom at much lower frequencies corresponding to the eigenmodes of a natural seep, this value should be considered an estimate from above. Substituting these expressions into Eqs. (18) and (14), we estimate the peak value of spectral density at the first mode frequency at the cylinder axis: $SD \approx 128$ dB.

Comparison with the ambient noise level in the ocean at frequencies from several to ten hertz [40–42] shows that the above value considerably exceeds the minimal noise levels in this frequency range. With distance from the gas plume, the intensity of the spectral peak decreases according to the law $K_0^2(k_1\rho) \sim \exp(-k_1^2\rho^2)$, and, at a distance equal to several depths, $\rho \gg k_1^{-1} \sim H$,

the peak is lost in the ambient noise spectrum. As was noted above, at these distances, the presence of the plume can still be detected, although not by intensity measurements but rather by measuring more complex characteristics, namely, the spatial correlations of the spectrum (see Eq. (13)).

ACKNOWLEDGMENTS

This work was supported by the Russian Foundation for Basic Research (project no. 01-05-64915) and the Far-East Division of the Russian Academy of Sciences (project no. 04-3-A-07-038).

REFERENCES

1. A. I. Obzhirov, B. A. Kazanskiĭ, and Yu. I. Mel'nichenko, Tikhookean. Geol., No. 2, 119 (1989).
2. *Data on Gas Hydrates in the Sea of Okhotsk*, Text Supplement to the *Report on 11A Cruise of M. Keldysh Research Vessel* (IO AN SSSR, Leningrad, 1988) [in Russian].
3. GEOMAR Report 42. R/V *Professor Bogorov Cruise Report Paramushir–Okhotsk Sea Expedition to Investigate Venting* (Kiel, 1995).
4. GEOMAR Report 82. CRUISE REPORTS: KOMEX I and II, R/V *Professor Gagarinsky Cruise 22* and RV *Academik M. A. Lavrentyev Cruise 28* (Kiel, 1998).
5. GEOMAR Report 88. CRUISE REPORTS: KOMEX V and VI, R/V *Professor Gagarinsky Cruise 26* and RV *Marshal Gelovany Cruise 1* (Kiel, 1999).
6. E. Suess, G. Bohrmann, J. Greinert, and E. Lausch, Sci. Am. **281**, 76 (1999).
7. GEOMAR Report. CRUISE REPORTS: KOMEX and R/V *Akademik M.A. Lavrentiev Cruise 29* (Kiel, 2003).
8. A. S. Salomatin and V. I. Yusupov, in *Proceedings of XIII Session of the Russian Acoustical Society* (GEOS, Moscow, 2003), p. 776.
9. M. Hovland and J. H. Sommerville, Mar. Petrol. Geol. **2**, 319 (1985).
10. M. Hovland and A. G. Judd, *Seabed Pockmarks and Seepages* (Grahamand and Trotman, London, 1988).
11. A. G. Judd, D. Long, and M. Sankey, Bull. Geol. Soc. Den. **41**, 34 (1994).
12. R. P. Dando, *A Review of Pockmarks in the UK Part of North Sea: Technical Report TR_001, Strategic Environment Assessment—SEA 2* (Department of Trade and Industry, London, 2001).
13. J. M. Brooks, M. C. Kennicutt II, R. R. Fay, and T. J. McDonald, Science **223**, 696 (1984).
14. I. R. MacDonalds, N. L. Guinasso, Jr., S. G. Ackleson, *et al.*, J. Geophys. Res. **98** (C9), 16 351 (1999).
15. J. S. Hornafius, D. C. Quigley, and B. P. Luyendyk, J. Geophys. Res. **104**, 20 703 (1999).
16. D. C. Quigley, J. S. Hornafius, B. P. Luyendyk, *et al.*, Geology **27**, 1047 (1999).
17. I. Leifer, J. Clark, and R. Chen, Geophys. Rev. Lett. **27**, 3711 (2000).
18. M. S. Longuet-Higgins, in *Proceedings of Conference on Natural Physical Sources of Underwater Sound* (Cambridge, 1990), p. 1.
19. I. Leifer and J. Clark, Geol. Geofiz. **43**, 613 (2002).
20. V. E. Nakoryakov, B. G. Pokusaev, and I. R. Shreĭber, *Wave Propagation in Gas–Liquid and Vapor–Liquid Media* (Inst. Teplofiz., Sib. Otd. Akad. Nauk SSSR, Novosibirsk, 1983) [in Russian].
21. I. Leifer and A. G. Judd, Terra Nova **14** (6), 417 (2002).
22. I. Leifer and R. K. Patro, Cont. Shelf Res. **22**, 2409 (2002).
23. I. Leifer, Earth Planet. Sci. Lett. **210**, 411 (2003).
24. S. A. Thorpe, Philos. Trans. R. Soc. London, Ser. A **304**, 155 (1982).
25. V. N. Goncharov and N. Yu. Klement'eva, Akust. Zh. **42**, 371 (1996) [Acoust. Phys. **42**, 323 (1996)].
26. A. O. Maksimov, in *Marine Technologies* (IPMT DVO RAN, Vladivostok, 1998), No. 5, pp. 187–191 [in Russian].
27. A. O. Maksimov, in *Marine Technologies* (IPMT DVO RAN, Vladivostok, 2002), No. 2, pp. 167–175 [in Russian].
28. A. B. Wood, *A Textbook of Sound* (Bell, London, 1932).
29. L. van Wijngaarden, Annu. Rev. Fluid Mech. **4**, 369 (1972).
30. D. P. Koller and P. M. Shankar, J. Acoust. Soc. Am. **93**, 1362 (1993).
31. D. V. Evans, M. Levitin, and D. Vassiliev, J. Fluid Mech. **261**, 21 (1994).
32. E. B. Davis and L. Parnovski, Q. J. Mech. Appl. Math. **51**, 477 (1998).
33. N. S. A. Khallaf, L. Parnovski, and D. Vassiliev, J. Fluid Mech. **403**, 251 (2000).
34. N. Q. Lu, A. Prosperetti, and S. W. Yoon, IEEE J. Ocean. Eng. **15** (4), 275 (1990).
35. S. W. Yoon, L. A. Crum, A. Prosperetti, and N. Q. Lu, J. Acoust. Soc. Am. **89**, 700 (1991).
36. M. Nicolas, R. A. Roy, L. A. Crum, *et al.*, J. Acoust. Soc. Am. **95**, 3171 (1994).
37. W. A. Kuperman and F. Ingenito, J. Acoust. Soc. Am. **67**, 1988 (1980).
38. H. Schmidt and W. A. Kuperman, J. Acoust. Soc. Am. **84**, 2153 (1988).
39. J. R. Boles, J. F. Clark, I. Leifer, and L. Washburn, J. Geophys. Res. **106** (C11), 27 077 (2001).
40. *Oceanology. Physics of the Ocean*, Ed. by V. M. Kamenkovich and A. S. Monin (Nauka, Moscow, 1978), Vol. 2, pp. 60–62 [in Russian].
41. R. J. Urick, *Principles of Underwater Sound*, 3rd ed. (McGraw-Hill, New York, 1983; Sudostroenie, Leningrad, 1978).
42. D. G. Browning and U. A. von Vinkel, in *Underwater Acoustics and Signal Processing*, Ed. by L. Bjørnø (Plenum, New York, 1982; Mir, Moscow, 1985).

Translated by E. Golyamina

Acoustical Physics, Vol. 51, No. 4, 2005, pp. 443–448. Translated from Akusticheskiĭ Zhurnal, Vol. 51, No. 4, 2005, pp. 520–526.

Extraction of Signals from White and Colored Noise Using the Discrete Wavelet Transform

D. V. Perov and A. B. Rinkevich

Institute of Metal Physics, Ural Division, Russian Academy of Sciences, ul. S. Kovalevskoi 18, Yekaterinburg, 620219 Russia

e-mail: peroff@imp.uran.ru; rin@imp.uran.ru

Received December 2, 2003

Abstract—Methods based on wavelet analysis are used to study longitudinal elastic waves propagating in aluminum single crystals in the [111] and [001] directions at frequencies of 5 and 10 MHz. Results of the wavelet filtering of responses of the laser Doppler interferometer to these acoustic signals are reported. The efficiency of filtering the time dependencies of the interferometer response in the presence of white and colored noise is studied. Recommendations concerning the choice of the filtering parameters are given. © *2005 Pleiades Publishing, Inc.*

INTRODUCTION

Laser ultrasonic interferometry is one of the most advanced techniques for studying the structure of acoustic fields in solids [1]. Noncontact data acquisition combined with a high resolution determined by the diameter of the laser beam allow one to obtain the necessary amount of information about the acoustic field, which can subsequently be processed with appropriate software and represented in a form convenient for analysis.

Because the optical receiver is broadband and the surface of a solid is rough, the output signal of the laser interferometer is noisy, which hampers the correct interpretation of the results of the measurements. In addition, the signals detected by the interferometer usually have their own complex spectra, which makes the situation even more difficult. Also, the signal waveform may be different at different points of the acoustic field. All of these circumstances prevent digital filters based on conventional techniques from efficiently extracting the useful signals.

Earlier [2–4], it was shown that wavelet analysis can serve as a basis for universal algorithms intended for filtering complex signals. In this paper, we consider the application of the wavelet transform to the output signals of a laser ultrasonic interferometer that contain noise with different types of spectra. We also show that the surface roughness of a solid affects the interferometer output.

EXPERIMENTAL TECHNIQUE

The experimental part of this work was performed using the OFV-3001 laser ultrasonic interferometer that belongs to the Fraunhofer Institute of Nondestructive Testing (Dresden, Germany). The output signal of the interferometer was digitized by a digital oscilloscope. The data were analyzed and stored by a personal computer running LabView 5.0-based software. A more detailed description of the experimental setup can be found in [5].

Longitudinal elastic waves were excited in the samples under study by piezoelectric transducers with resonant frequencies of 5 and 10 MHz. The diameters of the piezoelectric plates of the 10- and 5-MHz transducers were 5 and 13 mm, respectively. Each sample had two planar surfaces. One of the surfaces carried the piezoelectric transducer, and the other was illuminated by a laser beam to detect the elastic field.

The time dependence of the response amplitude at each point of the scanned field, i.e., the type-A scan, consisted of 1000 sample values. The size of the scanned field was usually 14×14 mm. After scanning at different points, the type-A scans were stored in digital format and were available for subsequent computer processing.

The experimental samples were aluminum single crystals. The normal to the sample's parallel faces was parallel to the [001] or [111] crystallographic direction. The samples were approximately cylindrical and were 16 to 20 mm long. The sample with the [001] orientation had two polished plane-parallel faces. The second sample also had two parallel faces. One of them was exactly perpendicular to the [111] axis and polished so that the roughness height did not exceed 8 μm. The other face initially was not polished, and its roughness height was 30 to 40 μm with the average in-plane size of irregularities being about 100 μm. After a series of experiments, this face was polished and the measurements were repeated.

1063-7710/05/5104-0443$26.00

SIGNAL FILTERING USING THE DISCRETE WAVELET TRANSFORM

According to the theory of the orthogonal wavelet transform [6], a function of time t, $f(t) \in L^2(\mathbf{R})$, defined on the entire real axis $R(-\infty; +\infty)$ and possessing a finite norm $\|f\|$ can be represented in terms of the following spectral expansion:

$$\begin{aligned} f(t) &= f^A_{i_0}(t) + \sum_{i=i_0}^{+\infty} f^D_i(t) \\ &= \sum_{j=-\infty}^{+\infty} v^{(i_0)}_j \varphi_{i_0 j}(t) + \sum_{i=i_0}^{+\infty}\sum_{j=-\infty}^{+\infty} w^{(i)}_j \psi_{ij}(t), \end{aligned} \quad (1)$$

where $f^A_i(t)$ and $f^D_i(t)$ are, respectively, the large-scale component (approximation or approximation coefficients) and the small-scale component (refinement or refinement coefficients) of the function $f(t)$ on the ith level of resolution. Here, i_0 refers to a certain initial level corresponding to the lowest time resolution.

In formula (1), $v^{(i)}_j$ and $w^{(i)}_j$ are the coefficients of expansion of the function $f(t)$ in systems of basis functions $\varphi_{ij}(t)$ and $\psi_{ij}(t)$, respectively. The index i is the number of the resolution level; it determines the time span of the basis function, i.e., its resolution; the index j determines the position of the basis function on the time axis.

The functions $\varphi_{ij}(t)$ and $\psi_{ij}(t)$ are called scaling functions and wavelets, respectively. They determine the corresponding orthonormal bases in the orthonormal space $L^2(\mathbf{R})$ and are defined as follows [6]:

$$\varphi_{ij}(t) = 2^{i/2}\varphi(2^i t - j), \quad (2)$$

$$\psi_{ij}(t) = 2^{i/2}\psi(2^i t - j), \quad (3)$$

where i and j are integers.

The following orthogonality relationships are valid for the scaling functions and wavelets [6]: $(\varphi_{ij}, \varphi_{il}) = \delta_{jl}$, $(\psi_{ij}, \psi_{kl}) = \delta_{ik}\delta_{jl}$, and $(\varphi_{ij}, \psi_{il}) = 0$, where i, j, k, and l are integers and δ is the Kronecker delta.

The functions $\varphi(t)$ and $\psi(t)$ are called, respectively, the generative scaling function and the generative wavelet. They are used to generate orthogonal sets of basis functions through scaling by integer powers of number 2 and shifting in time by integer numbers, as defined by Eqs. (2) and (3). The expansion coefficients of the function $f(t)$ in these bases are given by the following formulas [6]:

$$v^{(i)}_j = \int_{-\infty}^{+\infty} f(t)\varphi_{ij}(t)dt, \quad (4)$$

$$w^{(i)}_j = \int_{-\infty}^{+\infty} f(t)\psi_{ij}(t)dt, \quad (5)$$

which are similar to the expressions for spectral coefficients of the generalized Fourier transform. The numerical sequences given by Eqs. (4) and (5) are called the scaling and wavelet coefficients, respectively.

Relationships (1), (4), and (5) express the concept of the multiple-scale analysis, i.e., the multilevel expansion of the function being analyzed in orthonormal systems of basis functions that differ only in the scaling factor of the argument. This expansion represents the space $L^2(\mathbf{R})$ as a sequence of embedded subspaces $V^{(i)}$ such that $\ldots \subset V^{(i-1)} \subset V^{(i)} \subset V^{(i+1)} \subset \ldots \subset \overline{\bigcup_i V^{(i)}} = L^2(\mathbf{R})$, $\bigcap_i V^{(i)} = \{0\}$. Then, for example, the approximation $f^A_{i_0}(t)$ corresponds to an orthogonal projection of the function $f(t)$ onto the subspace $V^{(i_0)}$ and contains the components of $f(t)$ whose time scale is no smaller than 2^{-i_0}.

The refinement $f^D_{i_0}(t)$ is a projection of the function $f(t)$ onto the subspace $W^{(i_0)}$, which is the orthogonal complement of the space $V^{(i_0)}$ in $V^{(i_0+1)}$: $V^{(i_0+1)} = V^{(i_0)} \oplus W^{(i_0)}$, which extracts from $f(t)$ the components whose time scale is on the order of $2^{-(i_0+1)}$. The possibility of using the multiple-scale analysis to construct the orthogonal wavelet transform was first shown by Mallat [7, 8].

It is known [6] that the scaling function and the wavelet must satisfy the following refinement relations:

$$\varphi(t) = \sqrt{2}\sum_k h_k \varphi(2t - k), \quad (6)$$

$$\psi(t) = \sqrt{2}\sum_k g_k \varphi(2t - k), \quad (7)$$

where k is an integer. The numerical sequences h_k and g_k are referred to as the coefficients of the scaling and wavelet filters, respectively. They are related by the expression $g_k = (-1)^k h_{1-k}$.

A straightforward implementation of the orthogonal dyadic wavelet transform based on Eqs. (1), (4), and (5) presents a heavy burden for the processor. However, the performance of the method can be considerably

improved and the method can best be adapted to the analysis of discrete signals by the technique described below. Let us perform the following transformations: substitute Eqs. (6), (7) into definitions (2), (3) and substitute the result into Eqs. (4), (5). Ultimately, we obtain the following recurrence relations [6], which give the fast wavelet transform (FWT) algorithm:

$$v_j^{(i)} = \sum_{k=0}^{K-1} h_k^* v_{2j-k}^{(i+1)}, \quad (8)$$

$$w_j^{(i)} = \sum_{k=0}^{K-1} g_k^* v_{2j-k}^{(i+1)}, \quad (9)$$

where $h_k^* = h_{K-k-1}$; $g_k^* = g_{K-k-1}$; and K is the length of sequences h^*, g^*, h_k, and g_k. Is clear that, in practice, calculations by formulas (8) and (9) must be performed a finite number of times and must end at a certain lowest level of resolution with index i_0. Consequently, the index i in Eqs. (8) and (9) must take the following values: $i = i_{\max} - 1$, $i_{\max} - 2$, …, $i_0 + 1$, i_0. The index j in Eqs. (8) and (9) ranges over the following values: $j = 0$, 1, 2, …, Int$[(N^{(i+1)} + K - 1)/2$, where $N^{(i+1)}$ is the length of the scaling and wavelet coefficient vectors at the resolution level number $i + 1$. Here, Int$[\cdot]$ is the integer part of the argument.

It should be noted that, at each step from an ith resolution level to the next level $i + 1$, the length of the vectors of the scaling and wavelet coefficients decreases by a factor of two.

As the initial coefficients, formulas (8) and (9) use the expansion coefficients of the signal $v_j^{(i_{\max})}$ being analyzed that correspond to the highest resolution level of number $i_{\max}$. As a rule, $v_j^{(i_{\max})} = f_j$, where f_j is the discrete signal being analyzed, which consists of $N = N^{(i_{\max})}$ samples taken with a sampling time interval Δt.

It can be shown [6] that the signal can be reconstructed from its scaling and wavelet coefficients by an algorithm called the inverse fast wavelet transform (IFWT), which can also be represented as the recurrence relation

$$v_j^{(i+1)} = \sum_{k=0}^{k=K-1} h_{j-2k} v_k^{(i)} + g_{j-2k} w_k^{(i)}. \quad (10)$$

In this paper, we will always implement the FWT and IFWT procedures using the Sym8 wavelet from the symlet family [6] and perform the transformations at four levels of resolution.

The wavelet filtering of signals relies on the FWT algorithm and is performed as follows. For all vectors of refining coefficients obtained at all resolution levels of the FWT algorithm, symmetric (about the zero level) thresholds, whose values are chosen by a certain strategy, are adjusted. The elements that are beyond the thresholds are left unchanged, and all the remaining elements are replaced by zeroes. This procedure is called hard thresholding. If the values of the nonzero vector elements that are left after applying the threshold limitation are additionally shifted towards the zero level by the corresponding threshold values, the procedure is called soft thresholding. Subsequently, IFWT procedure (10) is applied to the modified vectors of refining coefficients to obtain the denoised signal.

The wavelet filtering algorithm was first proposed by Donoho and Johnstone [2, 9], who formulated one of the possible rules for choosing the threshold levels on the ith resolution level as follows:

$$T_i = \pm \mathrm{med}(|w_j^{(i)}|)\frac{\sqrt{2\ln N}}{0.6745}, \quad (11)$$

where med$(\cdot)$ is the median of the argument vector $w_j^{(i)}$.

EFFECT OF ROUGHNESS

Consider the results of measuring the type-A scans, i.e., the time dependences of the interferometer's response, for two conditions of the reflecting surface: before and after polishing. Let us analyze the scans themselves and also the wavelet spectra and scalograms obtained by the continuous wavelet transform [6, 10], which we implement in this paper using the MHAT wavelet. The scalogram is a generalized characteristic of the time dependence. It shows the distribution of oscillation power in period. The maxima of the scalogram show the periods that predominate. The experimental and theoretical results are shown in Fig. 1 for the unpolished sample. Type-A scans for three beam points with the coordinate Y = 7.5 mm and different X coordinates are shown in Fig. 1a. The corresponding scalograms are shown in Fig. 1b. The realization for the point at X = 3 mm refers to a noise like signal. The corresponding scalogram has a maximum at a period of ≈0.1 μs, which is much smaller than the period of ultrasonic oscillations. The point at X = 6 mm refers to the periphery of the beam. In the realization for this point, an ultrasonic pulse is seen in the presence of noise. A second maximum appears in the scalogram in addition to the maximum due to noise. The point at X = 9.5 mm is at the center of the beam. Here, the amplitude of the ultrasonic pulse exceeds the noise level. In the scalogram, the highest maximum is now the one that corresponds to the ultrasonic pulse.

After these measurements, the reflecting surface was polished, so that the roughness height was reduced to 8 μm and the measurements were repeated. Figure 2a

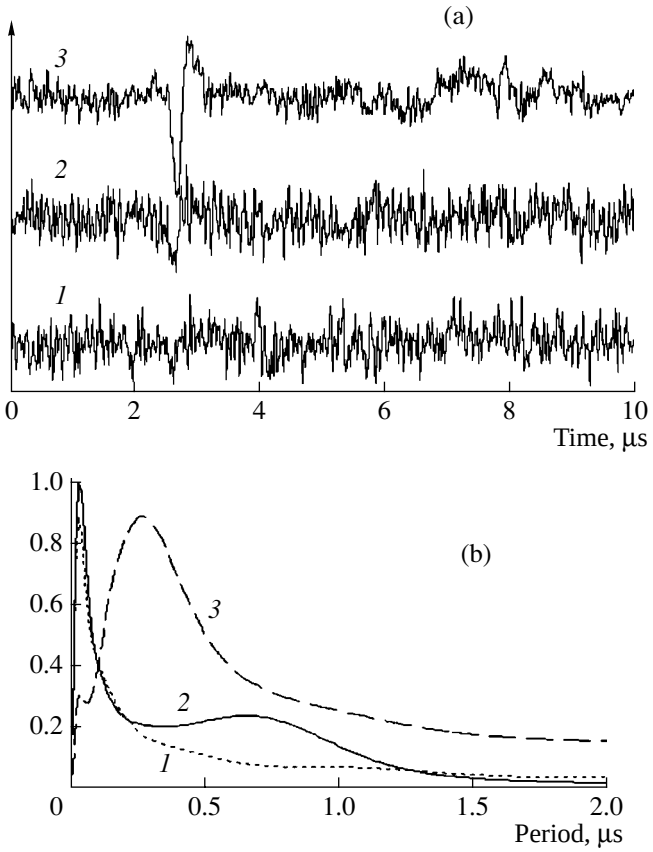

Fig. 1. (a) Time dependences of the interferometer response and (b) the corresponding scalograms for the [111]-oriented sample at three points: X = (*1*) 3, (*2*) 6, and (*3*) 9.5 mm and Y = 7.5 mm before polishing.

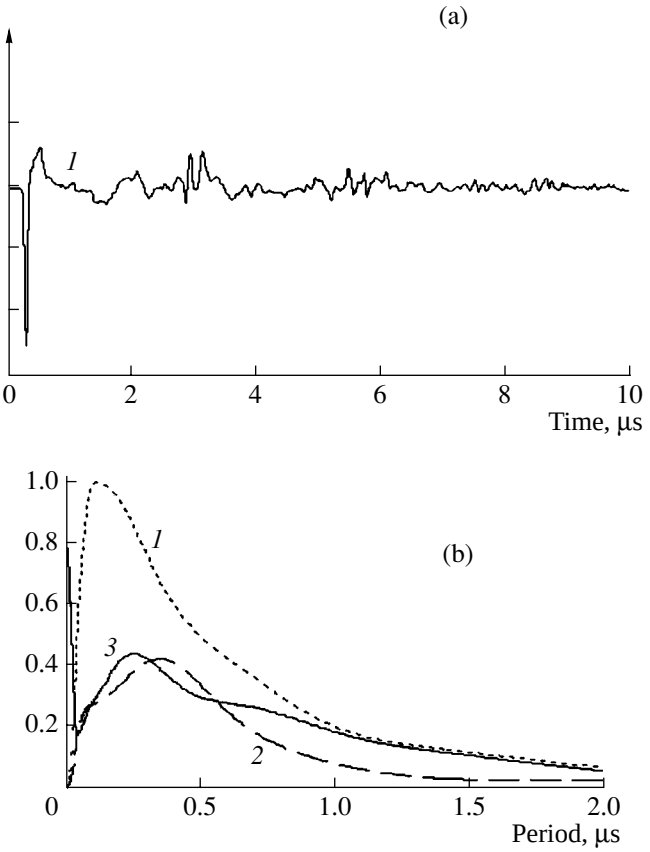

Fig. 2. (a) Type-A scans and (b) scalograms for three points: X = 7.5 mm (center of the beam), X = 13 mm (periphery of the beam), and X = 1 mm (region outside the beam).

shows a type-A scan for the central point of the beam; Fig. 2b, scalograms for three points: X = 7.5 mm (center of the beam), X = 13 mm (periphery of the beam), and X = 1 mm (region outside the beam). It is seen that the noise component is noticeably reduced. The maxima that refer to the ultrasonic pulse are seen in the scalograms even when the point is outside the ultrasonic beam.

WAVELET ANALYSIS AND FILTERING OF TYPE-A SCANS

In this section, we analyze the time dependence of the laser interferometer's response and the effect of noise with different spectra on it. We construct a filtering algorithm for this signal. The original signal, shown in Fig. 3a by curve *1*, is obtained at the central point of the beam for the sample with the [001] orientation. Longitudinal elastic waves were excited at a frequency of 10 MHz in the pulsed mode. The recording time was 10 μs. Two pulses can be seen, at 0.7–1.6 μs and 6.2–6.7 μs. The realization also contains an interference signal at 3.3–4 μs. This signal was combined with a noise like signal with a white-noise spectrum; the signal-to-noise ratio was 4.6 dB. The signal is shown in Fig. 3a by curve *2*. Now, it is impossible to distinguish the second low-amplitude ultrasonic pulse in the presence of noise.

The wavelet spectrum of this signal is illustrated in Fig. 3b. It has the form of a diagram, which displays the values of the wavelet transform coefficients in color or shades of gray. The abscissa axis represents the time, and the ordinate axis, the periods of oscillations of the signal. Thus, the wavelet spectrum represents the oscillation process in dynamics; i.e., it shows what frequencies or periods are present in the oscillations at particular time intervals. Examples of wavelet spectra of various signals can be found in [10, 11]. In Fig. 3b, the region 0.7–1.4 μs of the ultrasonic pulse contains loop-like structures. The interference signal in the region 3.2–3.8 μs also shows loop like structures, but with greater periods. The noise like signals are seen in the wavelet transform diagram as alternating vertical stripes. The frequency spectrum of the signal under study contaminated by noise and its scalogram are shown in Fig. 3c. The scalogram is seen in the figure as

the smoother curve. Maxima of the scalogram and the Fourier spectrum are at the ultrasonic signal's carrier frequency of ≈10 MHz. The signal shown in Fig. 3a by curve *2* was wavelet filtered with the use of hard thresholding, the thresholds being chosen in accordance with Eq. (11). The result is shown in Fig. 3a by curve *3*. Both pulses have again become visible. The comparison of signals 1 and 3 shows that the structure of oscillations in the first pulse is reproduced correctly. The interference pulse remained a series of small-amplitude oscillations. It can, in principle, be removed by appropriately choosing the parameters of the filtering procedure, but this would noticeably change the amplitude of the second ultrasonic pulse. Thus, the work reported above proves that this filtering procedure is efficient for pulsed ultrasonic signals contaminated by wideband noise.

A question arises about the efficiency of the filtering procedure for noise with a different spectrum. As an example of a colored noise, we considered noise with the spectral power density of 1/*f*. Such a noise can be acoustic in nature; i.e., it can arise in the medium through which the wave travels. Apart from the acoustic noise, there may be electric noise and interferences whose spectral density maximum is displaced from the maximum of the acoustic signal spectrum. The action of such an interference within the bandwidth of the receiver can be modeled by colored noise. As the original signal, we again used the type-A scan shown by curve *1* in Fig. 3a. It was additively contaminated by noise with a 1/*f*-type spectral density. This noisy signal is shown in Fig. 4a by curve *2*. The signal-to-noise ratio was 4.2 dB.

The random numerical sequences that modeled the 1/*f*-type noise were generated by the algorithm reported in [12]. It is specified by the expression

$$x_{n+1} = \rho x_n + r_n\sqrt{1-\rho^2}, \qquad (12)$$

where ρ is the required correlation coefficient between adjacent random numbers, this coefficient being related to the relaxation time τ as $\rho = \exp(-1/\tau)$, and the r_n are uniformly distributed random numbers. Formula (12) assumes that $x_0 = 0$.

We used a set of three values of τ: 1, 10, and 100. We substituted them one by one into Eq. (12) using different sets of r_n and then summed the realizations obtained to generate sequences of random numbers whose spectral density is characterized by a frequency dependence of 1/*f* throughout a range of almost three decimal orders of magnitude in width.

The noisy signal 2 shown in Fig. 4a was subjected to the following filtering procedure, which was performed in two stages. At first, the low-frequency noise was filtered out. For this purpose, the refining coefficients for

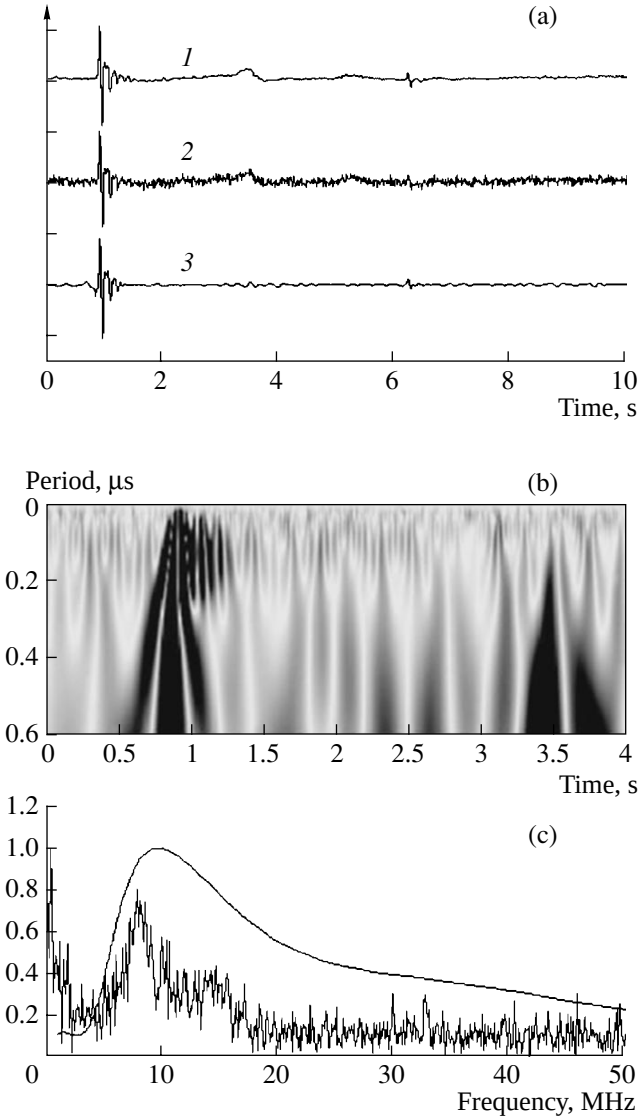

Fig. 3. Wavelet analysis and filtering of type-A scans in the presence of white noise. The direction of propagation is [001], and the frequency is 10 MHz. (a) Time dependences: (*1*) the interferometer response at the central point of the beam, (*2*) the signal contaminated by noise, and (*3*) the filtered signal. (b) Wavelet spectrum of signal 2. (c) Scalogram of signal 2 (the smoother curve) and its frequency spectrum.

all the four resolution levels were set equal to zero. Then, the signal obtained was subtracted from the original signal, and the result was subjected to the second stage of the filtering procedure. It used hard thresholding with the thresholds chosen according to Eq. (11). The filtered sequence is shown in Fig. 4a by curve *3*. The signal-to-noise ratio clearly became higher, and the second ultrasonic pulse became discernable. The wavelet spectrum of the filtered realization is shown in Fig. 4b. Its most important feature is that the first pulse near 1 μs on the abscissa axis is observable. Also, one can see a manifestation of the second ultrasonic pulse after

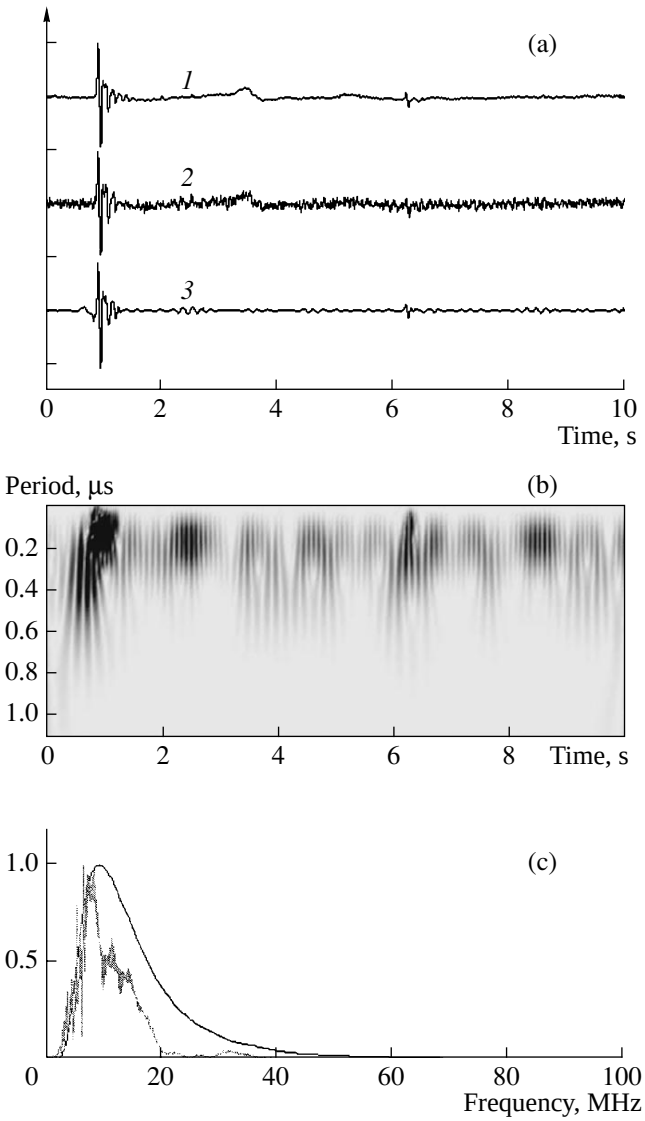

Fig. 4. Wavelet analysis and filtering of type-A scans in the presence of noise with the $1/f$ spectrum. The direction of propagation is [001], and the frequency is 10 MHz. (a) Time dependences: (*1*) the interferometer response at the central point of the beam, (*2*) the signal contaminated by noise, and (*3*) the filtered signal. (b) Wavelet spectrum of signal 3. (c) Scalogram of signal 3 (the smoother curve) and its frequency spectrum.

6 μs. The Fourier power spectrum and the scalogram of the filtered signal are shown in Fig. 4c. (Here, the scalogram is the smother curve with one maximum.)

CONCLUSIONS

Acoustic fields in aluminum single crystals are studied by a laser Doppler interferometer. The time dependences of the acoustic field at different points of the ultrasonic beam are analyzed with the use of the continuous wavelet transform for different conditions of the reflecting surface: before and after polishing.

The application of wavelet signal filtering algorithms based on the discrete wavelet transform theory is considered. It is shown that the use of symlets with sufficiently large indices, for example, Sym8, as the basis functions of the discrete wavelet transform gives good results in the image filtering. The number of resolution levels can be limited to four.

A dual filtering algorithm that is capable of efficiently extracting one-dimensional signals (time dependences of the interferometer response) from white and colored noise is developed. The fixed-threshold hard thresholding strategy is shown to be most efficient for filtering one-dimensional functions.

The most important advantage of the discrete wavelet transform filtering algorithm is that it does not require any special fitting to the particular function being analyzed. Consequently, the advantages of the wavelet filtering are realized without applying an operator.

ACKNOWLEDGMENTS

This work was supported by the Russian Foundation for Basic Research, project no. 01-02-96410; D.V. Perov acknowledges the support of the Foundation in Support of the Russian Science. We are grateful to Prof. M. Krőning and Dr. B. Köhler for the opportunity to work with the laser ultrasonic interferometer. We also thank A.S. Krivonosova for providing us with aluminum single crystals.

REFERENCES

1. C. B. Scruby and L. E. Drain, *Laser Ultrasonics: Techniques and Applications* (Adam Hilgar, Bristol, 1990).
2. D. Donoho, IEEE Trans. Inf. Theory **41**, 613 (1995).
3. D. V. Perov and A. B. Rinkevich, Defektoskopiya, No. 4, 78 (2002) [Rus. J. Nondestr. Test. **37**, 889 (2001)].
4. D. V. Perov, A. B. Rinkevich, and Ya. G. Smorodinskiĭ, Defektoskopiya, No. 12, 3 (2002) [Rus. J. Nondestr. Test. **38**, 869 (2002)].
5. A. S. Krivonosova, A. B. Rinkevich, and Ya. G. Smorodinskiĭ, Akust. Zh. **47**, 76 (2001) [Acoust. Phys. **47**, 76 (2001)].
6. I. Daubechies, *Ten Lectures on Wavelets* (SIAM, Philadelphia, 1992; Regul. Khaot. Din., Izhevsk, 2001).
7. S. Mallat, IEEE Trans. Pattern Anal. Mach. Intell. **11**, 674 (1989).
8. S. Mallat, Trans. Am. Math. Soc. **315**, 69 (1989).
9. D. L. Donoho and I. M. Johnstone, Biometrika **81**, 425 (1994).
10. N. M. Astaf'eva, Usp. Fiz. Nauk **166**, 1145 (1996) [Phys. Usp. **39**, 1085 (1996)].
11. D. V. Perov, A. B. Rinkevich, Ya. G. Smorodinskiĭ, and B. Keler, Defektoskopiya, No. 12, 67 (2001) [Rus. J. Nondestr. Test. **37**, 889 (2001)].
12. M. R. Schroeder, *Fractals, Chaos, Power Laws* (Freeman, New York, 1991; Regul. Khaot. Din., Izhevsk, 2001).

Translated by A. Khzmalyan

Acoustical Physics, Vol. 51, No. 4, 2005, pp. 449–456. Translated from Akusticheskiĭ Zhurnal, Vol. 51, No. 4, 2005, pp. 527–535.

The Effect of Internal Waves on the Sound Propagation in the Shelf Zone of the Sea of Japan in Different Seasons

A. N. Rutenko

Il'ichev Pacific Oceanological Institute, Far-East Division, Russian Academy of Sciences, Baltiĭskaya ul. 43, Vladivostok, 690041 Russia

e-mail: rutenko@poi.dvo.ru

Received November 12, 2003

Abstract—Results of the observation of seasonal variations in the vertical distribution of water temperature in the shelf zone of the Sea of Japan are presented, and the effect of this variability on the parameters of internal waves and on sound propagation is studied. The measurements were carried out in different seasons using a vertical acoustical–hydrophysical measuring system. The propagation of sound (tone and noise signals) was studied on a 510-m-long track at a constant depth of 38 m. Using a self-contained resonance (320 Hz) transmitter of the electromagnetic type, which was bottom-moored at a depth of 65 m, a 10.6-km-long stationary acoustic track crossing the shelf was set up. During the in-sea experiments, the spatial characteristics of internal waves were measured along with the distributions of temperature, salinity, sound velocity, and sea level variations. © *2005 Pleiades Publishing, Inc.*

INTRODUCTION

At present, despite considerable progress in the theory and numerical modeling of the effect of hydrophysical fields on the sound propagation in a shallow sea [1–3], some problems remain of interest to researchers, namely, the problems related to the experimental investigation of hydrophysical fields and hydrodynamic processes that occur in the shelf zone in different seasons and the influence of these fields and processes on sound propagation.

In the presence of a fully developed pycnocline, the main hydrodynamic sources of acoustic inhomogeneities in the water layer are the tidal internal wave and the shorter internal waves (IWs). The tidal internal wave induced by the tidal current at the edge of the shelf [4–7] propagates along the shelf as a long internal wave (LIW). Because of nonlinearity and interaction with the bottom, it undergoes transformations accompanied by the generation of shorter IWs and packets of quasi-harmonic and soliton-like nonlinear IWs [5–7]. Therefore, the field of IWs on the shelf, as well as the acoustic wave fields, have a number of features related to the influence of the bottom and to the seasonal variability of the spatial parameters of the density field in the water layer. The refraction and scattering of acoustic waves by inhomogeneities of the sound velocity field, which are induced by the IW in the water layer, lead to both focusing and defocusing of acoustic waves in the horizontal plane and to energy transfer from propagating acoustic modes with low numbers to those of higher numbers. This interaction can be of a resonance character [3, 8, 9].

In 1978, Il'ichev Pacific Oceanological Institute began to establish a research base at the Schulz Cape (see the chart in Fig. 1). Over a period of 25 years, experimental data on the variability and dynamics of basic oceanological fields that affect the sound propagation in the shelf region of the Sea of Japan in various seasons were collected. Numerous observations of the IW parameters were carried out [10–14], and the effect of these parameters on sound propagation was studied [14–18]. The present paper is a logical development of the previous investigations, with an emphasis on studying the features of the sound propagation from the deep-water part of the shelf to the shallow-water coastal region and also the influence of the IWs on the sound propagation along tracks oriented across and along the direction of IW propagation.

THE TEST REGION AND THE MEASURING SYSTEM

Figure 1 shows a chart of the test region with the measurement sites and the tracks on which the measurements were carried out. In this shelf region of the Sea of Japan, an unusual semidiurnal tide is observed with a height of 35 cm. At the same time, a surge related to wind currents and surface waves plays a considerable part in sea surface displacements. The summer monsoon displaces the seasonal thermocline from the shallow-water part of the shelf, and the water layer becomes almost homogeneous in temperature. However, in autumn, due to the long-term action of the north and northwest winds, the cool near-bottom water returns to the shallow-water region, and this process is accompanied by intense nonlinear IWs [17, 18].

1063-7710/05/5104-0449$26.00

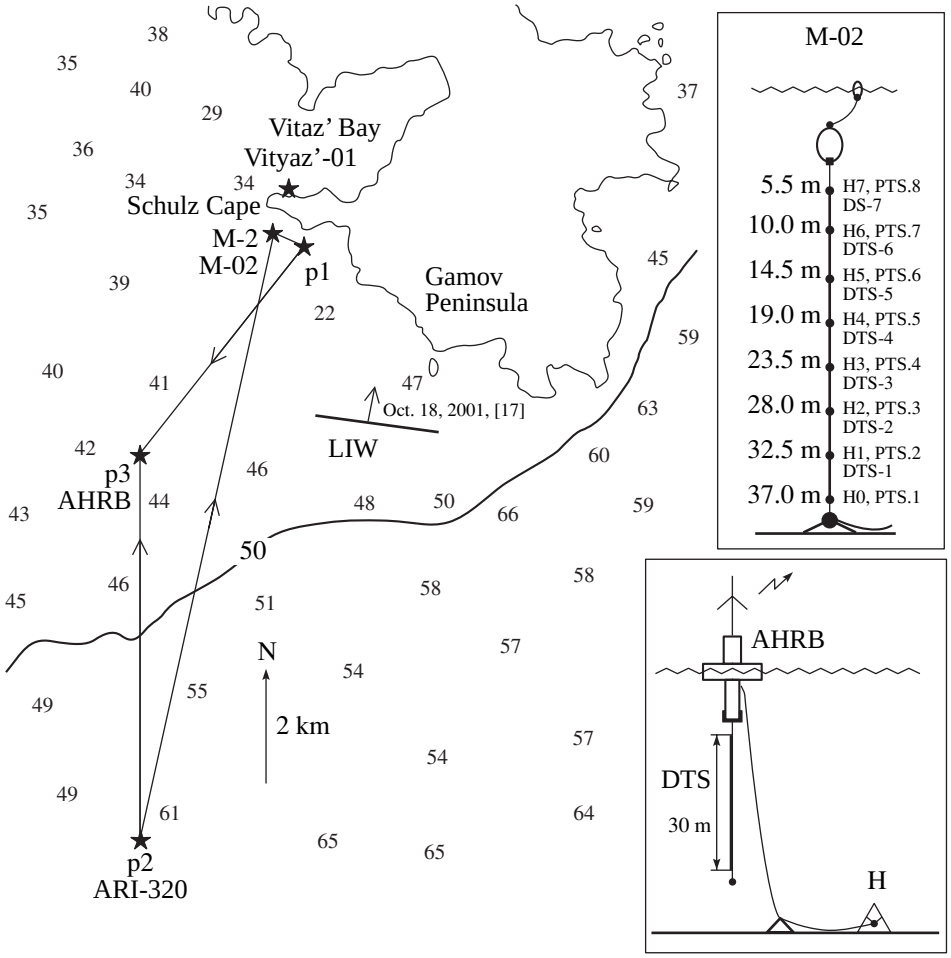

Fig. 1. Chart of the test region with the positions of the measuring means, the acoustic tracks, and the crests and propagation directions of long internal waves (LIWs) measured in autumn of 2001 [17]. Schemes of positioning the Mollusk-02 vertical acoustic–hydrophysical measuring system and the acoustic–hydrophysical radio buoy (AHRB) in the sea of Japan. Notation: Vityaz'-01 is the level meter, M-02 is the Mollusk-02 measuring system, ARI-320 is the self-contained resonance transmitter of an acoustic signal with a frequency of 320 Hz, H is the hydrophone, PTS is the point temperature sensor, and DTS is the distributed temperature sensor of the resistance type.

The emission of tone and noise acoustic signals was performed by a piezoceramic transmitter, which was stationarily positioned at a depth of 37 m at the point p1[19]. Using the Mollyusk-02 vertical acoustical–hydrophysical measuring system [20], a self-contained resonance transmitter (ARI-320), and acoustical–hydrophysical radio buoys (AHRB), stationary tracks up to a length of 10.6 km were set up (Fig. 1). The basic technical characteristics of the measuring means are presented in [21].

RESULTS OF ACOUSTIC–HYDROPHYSICAL MEASUREMENTS AND NUMERICAL MODELING

In April 2003, at the point p3 (see Fig. 1), an acoustic–hydrophysical radio buoy was placed, and the ARI-320 transmitter positioned at the point p2 emitted a TON-320 tone acoustic signal. Signals TON-295 and TON-450 were emitted at the point p1. The results of synchronous measurements of acoustic signals and variations of water temperature at the points M-2 and p3 are presented in Fig. 2. The variations of the mean temperature within a 30-m-thick water layer are represented by the plot of $\eta(t)$ and were obtained using a distributed temperature sensor of the AHRB positioned at the point p3. This plot characterizes the profile of the IWs propagating over the thermocline [22]. The vertical displacements of the sea surface are represented by the plot of $\xi(t)$ (the solid line) and were obtained using the Vityaz'-01 level meter placed near the entrance to the Vityaz' Bay (see Fig. 1). In the same figure, the dotted line shows the tide line calculated analytically. From Fig. 2, one can see that the theoretical curve correctly predicts the phases and the character of the tide in this region. Therefore, in analyzing the data obtained in the experiments in which $\xi(t)$ was not measured, we will use the theoretical curves.

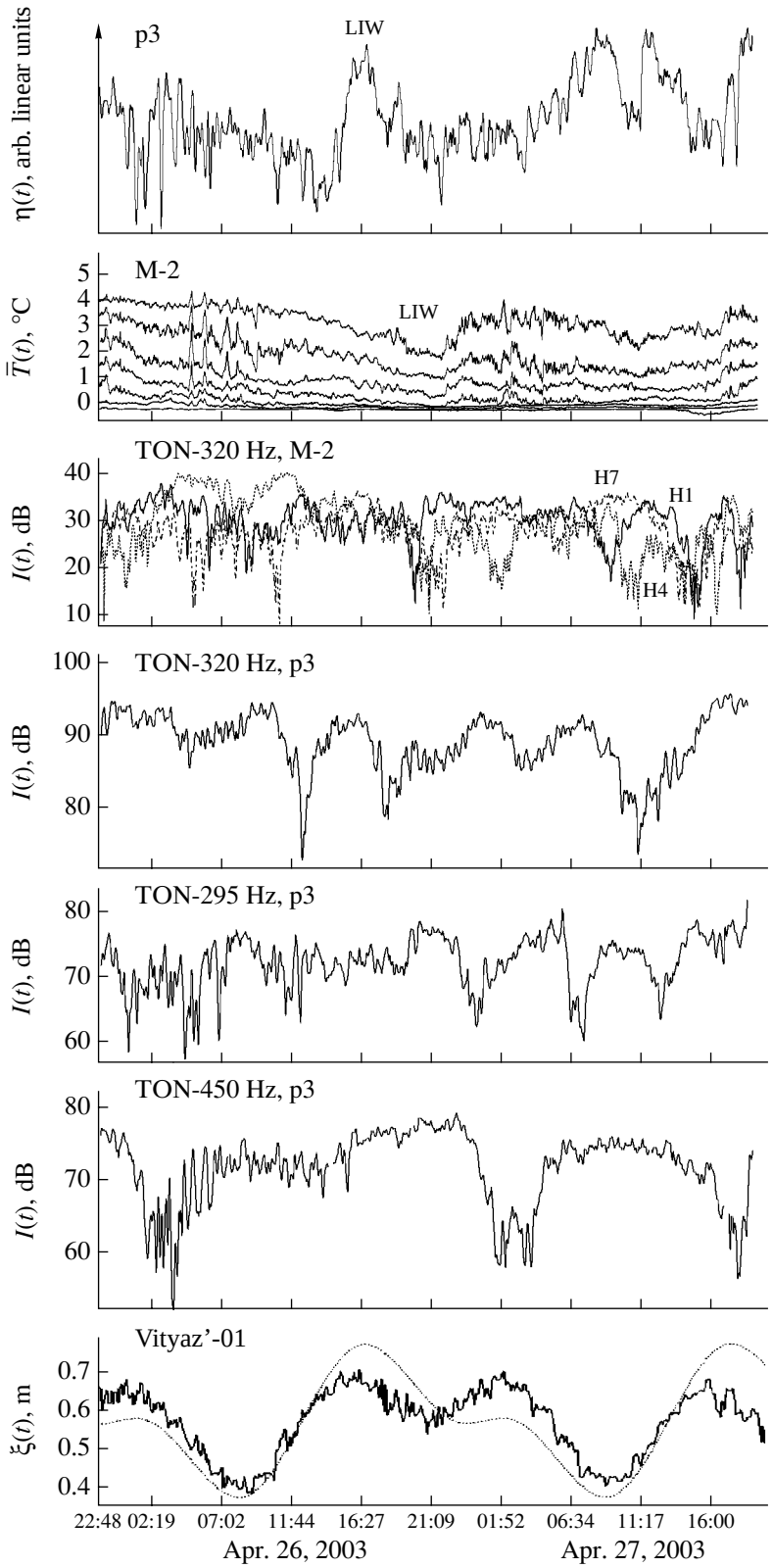

Fig. 2. Results of synchronous acoustic-hydrophysical measurements carried out in the spring–time experiment. The TON-320 signal was generated near the bottom at a depth of 65 m at the point p2 by the self-contained transmitter. The TON-295 and TON-450 signals were generated at a depth of 37 m at the point p1. The profile of the IW at p3 represented by the plot $\eta(t)$ was obtained using the AHRB. The plot $\xi(t)$ shown by the solid line refers to the full-scale measurements of the sea level, and the dotted line refers to the analytical estimate.

In Fig. 2, it is possible to select a group of intense IWs arriving at the point p3 at about 02:19 on April 26, 2003 (see the plot of $\eta(t)$). It is known [17] that, in this region, the long internal waves (LIWs) induced by the tidal current and the shorter IWs related to them [7] propagate nearly along the p2–M-2 track with a speed of ≈0.30–0.45 m/s. Therefore, this group of IWs should arrive at the point M-2 within approximately 4 h. In the plots of $\bar{T}(t)$ obtained with the use of seven distributed temperature sensors of the M-02 measuring system at nearly the same time (5:00 to 9:00 on April 26, 2003), a group of nonlinear IWs is clearly visible. As follows from Fig. 2, the intense IWs causing synchronous vertical displacements of isotherms by ≈4.5 m in a 27-m-thick water layer are observed when bases of the LIWs pass by (see the curves $\bar{T}(t)$ at 07:02, April 26 and 01:52, April 27). Theoretically, the LIW can be generated at the shelf edge by a hydraulic jump [4]. Such a jump can begin to propagate upstream, in the coast direction, as an LIW undergoing considerable nonlinear transformations [7] that are accompanied by energy transfer to the shorter IWs (see the plot of $\eta(t)$ in the interval 00:00 to 07:00 on April 26, 2003). However, the jump can also retain its space–time scale (see the plot of $\eta(t)$ in the interval 15:00 to 20:00 and the curves $\bar{T}(t)$ in the interval 20:00 to 22:00 on April 26, 2003). Now consider in more detail the spatial–temporal formation of cool water, which is conditionally denoted as LIW in Fig. 2. The speed of its propagation from the point p3 to M-2 is 0.4 m/s, which agrees well with the results of measurements carried out in this region in October 2001 [17]. According to the plot of $\xi(t)$, the speed of the tidal current at the shelf edge was maximum approximately at 04:00 on April 26, 2003. If the LIW induced at this phase of the surface tide propagated with a speed of 0.4 m/s, it would arrive at the point p3 within 12 h. Therefore, we can assume that the LIW is truly related to the tide and began its motion toward the beach against the tidal current, which agrees well with the model proposed in [4]. Its spatial scale in the shallow-water part of the shelf is about 6.5 km, according to the measurements at the point p3.

Let us consider the results of the acoustic measurements. Figure 2 shows the plots of intensity variations $I(t)$ of acoustic signals with different frequencies and propagating along different tracks: TON-320 Hz propagated along the p2–p3 (6.6 km) and p2–M-2 (10.6 km) tracks; TON-295 and TON-450 Hz were generated at the point p1 and propagated along the p1–p3 (4.7 km) and p1–M-2 (510 m) tracks. The results of synchronous measurements at the points p3 and M-2 (see Fig.1) allow one to estimate the effect of IWs at different distances from the emission point of the TON-320 signal (p2); the acoustic signals TON-320 and TON-295 propagated along nearly the same track but in opposite directions. Let us compare the variations of signal intensities within the time interval from 22:48 (April 25) to 11:44 (April 26) that corresponds to the transmission of a group of intense nonlinear IWs along the p2–M-2 track. From Fig. 2, it is seen that, at the deep-water part of the p2–p3 track, the IWs do not produce any considerable effect on the sound field formed near the bottom by the TON-320 signal at the point p3 (variations of $I(t)$ do not exceed 5 dB). At the transmission of the IWs near the point M-2, the short-period variations of $I(t)$ at this point reached 15 dB in both the near-bottom (plot *1*) and subsurface (plot *7*) water layers. The variations $I(t)$ of the TON-295 signal measured at the point p3 also reach ≈15 dB at the passage of the IWs over the emission and reception points. For this time interval, the plot of $I(t)$ (TON-450) is similar to that of $\eta(t)$.

The observed intensity variations of the acoustic field, which were measured by hydrophones at fixed depths at the passage of IWs near the point of reception, can be caused by changes in the vertical interference structure of the acoustic field. The inteference can be induced by the refraction of acoustic waves by spatial acoustic inhomogeneities generated by the IWs. Apparently, it is also necessary to take into account the effect of IWs on the mode structure of the sound field, since the IWs change the spatial distribution of the sound velocity field over the source. For estimating these effects, numerical modeling was performed in the mode adiabatic approximation. The results of the numerical experiment are presented in Fig. 3. The model waveguide has the form of a three-layer structure with a liquid sediment layer and a liquid basement. The water layer consists of a subsurface homogeneous layer with sound velocity C = 1490 m/s and a near bottom homogeneous layer with C = 1470 m/s. Between these layers, a 10-m-thick thermocline is present, with the sound velocity linearly varying from 1490 to 1470 m/s. The sound source is located at the initial point of the track at a depth of 64 m. The dotted line shows the shift of thermocline boundaries caused by a model solitary internal wave 10 m in height and 300 m in width at the base. In the numerical experiment, a spatial inhomogeneity formed by this wave in the sound velocity field propagated with a speed of 0.4 m/s along an inhomogeneous waveguide whose geometry was similar to that of the full-scale experiment.

Figure 3b shows the results of calculating the transmission loss by using a modified MOATL code [23] for eight depths for 320-Hz sound propagating in the given waveguide [23]. The zero instant of time corresponds to the internal wave passage above the sound source, while the time instant 7.2 h corresponds to the passage of the model internal wave through the point on the track where the vertical measuring system was positioned. From Fig. 3b, it is seen that, at the point of reception, relatively short time variations of the acoustic field intensity are maximum when the model acoustic inhomogeneity moves near the points of emission and reception. The greatest amplitudes of variations are observed at depths corresponding to minima in the spatial interference structures of the acoustic field formed in the waveguide. Thus, the results of modeling agree

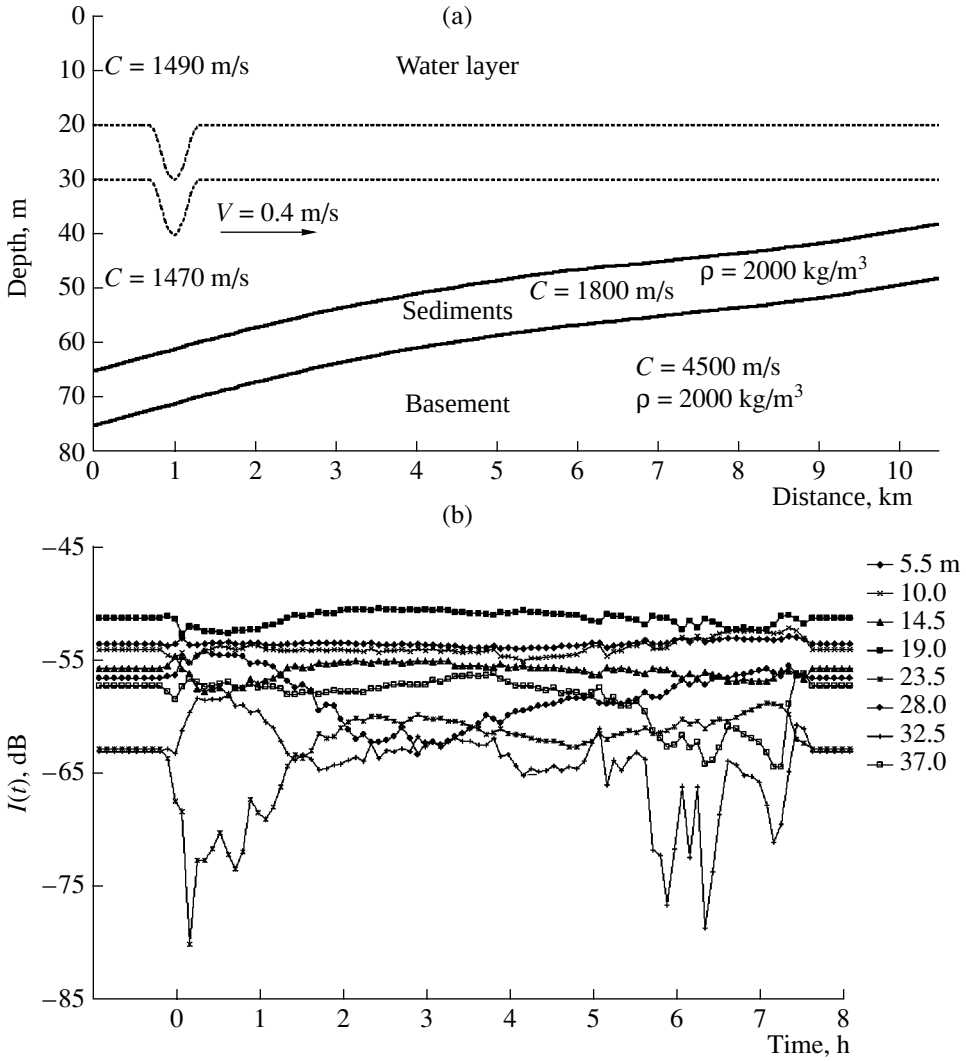

Fig. 3. (a) Geometry and parameters of the model waveguide. (b) Intensity variations $I(t)$ of sound with a frequency of 320 Hz at eight depths in the course of the motion of the acoustic inhomogeneity along the waveguide, where the inhomogeneity is formed from the thermocline by a model internal wave propagating through it.

well with the full-scale data. Besides, from Fig. 2b, it is seen that short-period variations of $I(t)$ are truly maximum in the acoustic signals measured by the hydrophones located at the interference minima of the acoustic field. This effect was interpreted in [15].

As an example, Fig. 4 illustrates the effect of waveguides generated by the crests of the IWs on the vertical interference structure of the acoustic field formed by tone (with a frequency of 310 Hz) and noise signals emitted at the point p1. The sound propagated along the p1–M-2 track oriented almost parallel to the crests of the IWs. An analysis of the influence of IWs on the interference structure of the acoustic field generated by a noise signal [15, 17] showed that the IWs noticeably effect both the spatial and frequency interference structures of the acoustic field. Therefore, it is possible, by means of averaging the power spectral density of the acoustic field in a wide frequency band and using algorithm (1), to eliminate the effects caused by the IWs in the frequency interference and to select the synchronous (in the frequency range $f_n - f_m$) variations in the vertical interference structure of the noise field:

$$\bar{I}(f_n;\ f_m) = 10\log\left(\frac{G(f_n) + \ldots + G(f_m)}{m - n + 1}\right) \text{dB}, \quad (1)$$

where $G(f_n)$ is the value of the periodogram at the frequency $f_n = \dfrac{n f_\text{d}}{N}$, f_d is the digitization frequency, and N is the length of the series used to calculate the periodogram by the fast Fourier transformation (FFT).

As follows from Fig. 4, the effects caused by the IWs are more pronounced in the plots of $\bar{I}(t)$ obtained by algorithm (1). However, the mean intensity of the acoustic field varies with the periods exceeding those of

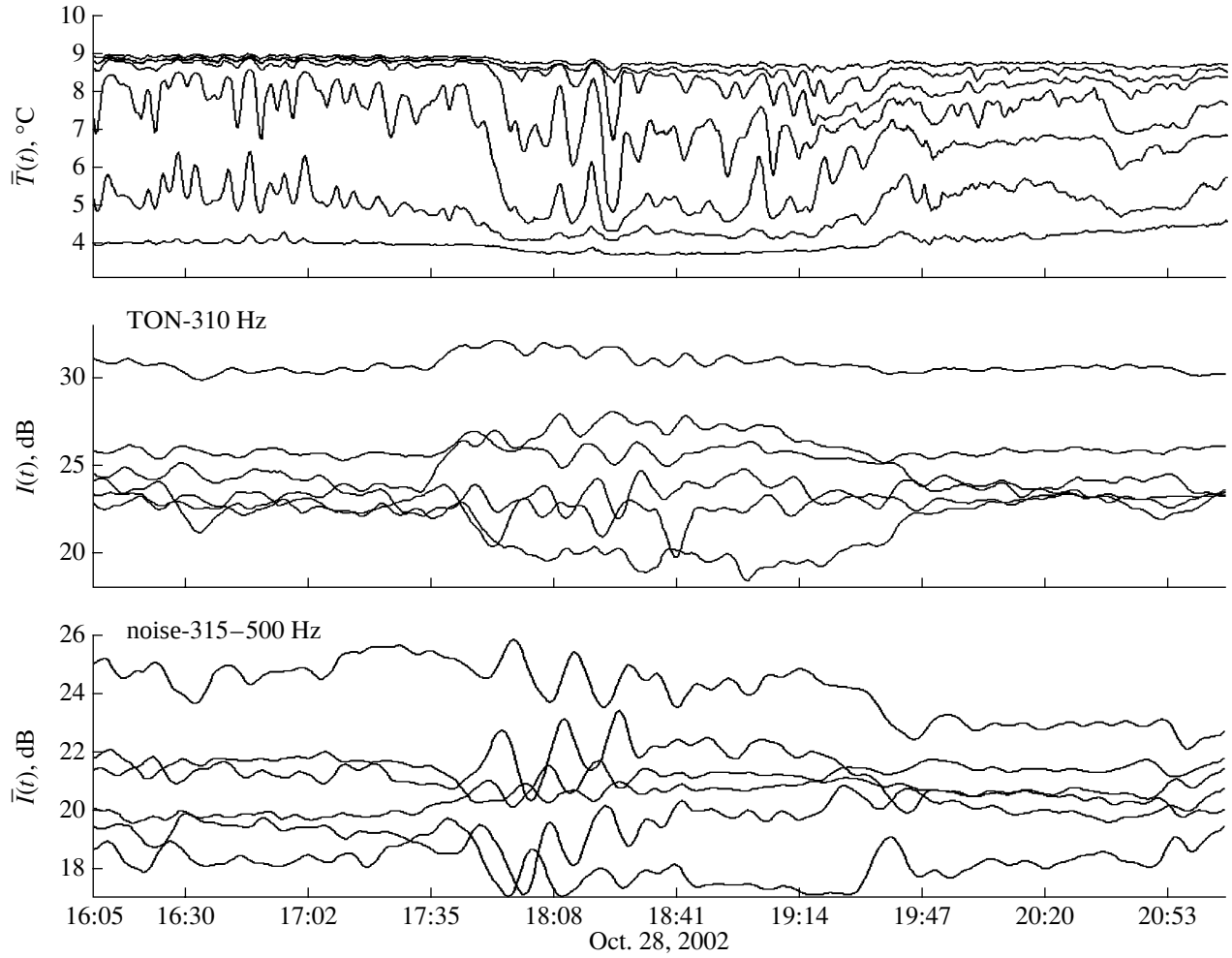

Fig. 4. Effect of IWs on the propagation of tone and noise signals along the p1–M-2 track.

the IWs observed at the point M-2 (see the plots of $\bar{T}(t)$). Apparently, the IWs intersected the p1–M-2 track at an angle smaller than 90°.

RESULTS OF OBSERVATIONS IN WINTER HYDROLOGICAL CONDITIONS

In February of 1995, in the given shelf region, a stationary acoustic track was set up with a transmitter located in the coastal zone and a receiving radio hydroacoustic station positioned 15 km away from the coast and providing measurements of acoustic pressure near the bottom during 2.5 days [24]. The temperature measurements performed with the use of reversing mercury thermometers showed that, in winter in the coastal zone, a relatively cold (–1.8°C) and, therefore, heavy water mass is formed, which moves toward the shelf edge. On the other hand, a horizontal advection of the warmer water (0.5°C) of the Sea of Japan into the shelf zone is observed, which leads to the formation of a dynamic temperature front extending along the shelf and affecting the sound propagating through it.

Figure 5 shows the results of acoustic–hydrophysical measurements carried out on the p1–M-2 track in December 2002, and in March 2003. Tone (TON-240, TON-450) and noise acoustic signals were continuously emitted at the point p1. The plots of $T(t)$ shown in Fig. 5 correspond to the measurements carried out with eight point temperature sensors of the M-02 system. These plots quantitatively illustrate the variations in the vertical distribution of the temperature field during the active phase of convective cooling of water (Fig. 5a), as evidenced by the temperature inversions. Unfortunately, the figure is black and white and, therefore, the inversions are not visible. Figure 5 (see the plots of $T(t)$) shows that, under winter hydrological conditions, the LIWs play an important role in the hydrodynamic processes on the shelf. The IWs induce synchronous vertical displacements of isotherms in the whole 30-m-thick test water layer.

Thus, from the results of measurements carried out in different seasons by the Mollusk-02 vertical acoustic–hydrophysical measuring system, it follows that the LIW and the IWs related to it are present in this shelf

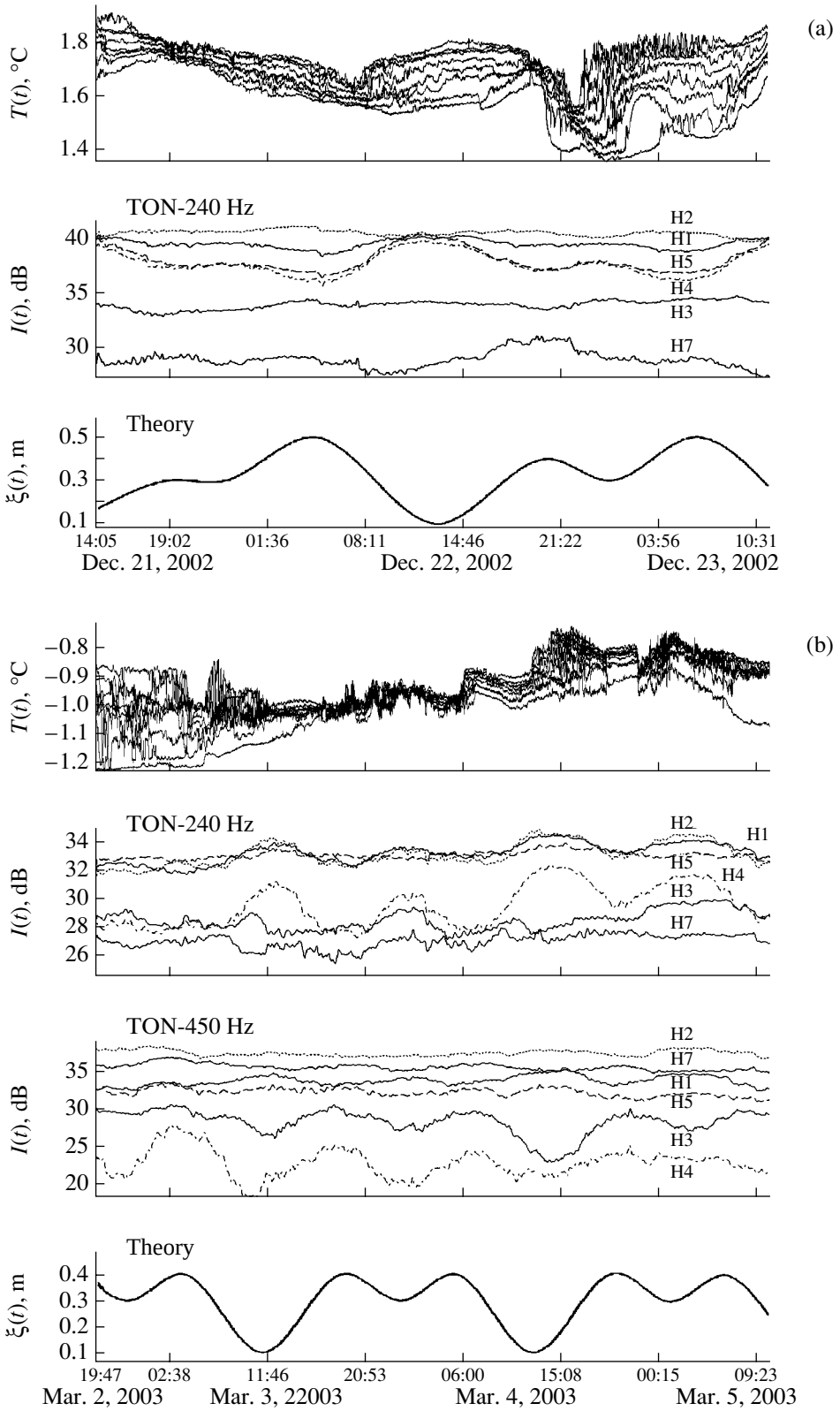

Fig. 5. Variations of water temperature and intensities of tone acoustic signals propagating along the p1–M-2 track. The measurements were carried out under winter hydrological conditions using the M-02 system. The plots of $\xi(t)$ refer to the theoretical surface tide.

region of the Sea of Japan at all times of the year. Apparently, the orbital motions of water particles in the IWs play an important role in winter convective processes on the shelf. As follows from Fig. 5, in winter, because of the small value of the vertical temperature gradient in water (≈0.032°C/m) and, hence, the small sound velocity gradient, the effect of the LIWs and IWs on the sound propagation along the p1–M-2 track becomes insignificant compared to the effect of the surface tide, which causes changes in the water layer thickness according to the plots of $\xi(t)$ presented in Fig. 5.

ACKNOWLEDGMENTS

I am grateful to S.V. Borisov, A.V. Gritsenko, R.A. Korotchenko, V.V. Likhachev, and S.I. Penkin for their participation in the experiments, to M.V. Kruglov for assistance in the numerical experiment, to Yu.N. Morgunov for the possibility to use the broadband transmitter positioned at p1, and to V.V. Navrotskiĭ for interest in this work and useful discussions.

This work was supported by the Russian Foundation for Basic Research, project nos. 00-05-64844 and 03-05-65213.

REFERENCES

1. D. Tielbuger, S. Finette, and S. Wolf, J. Acoust. Soc. Am. **101**, 789 (1997).
2. B. G. Katsnel'son and V. G. Petnikov, *Acoustics of a Shallow See* (Nauka, Moscow, 1997) [in Russian].
3. B. G. Katsnel'son, S. A. Pereselkov, V. G. Petnikov, *et al.*, Akust. Zh. **47**, 494 (2001) [Acoust. Phys. **47**, 424 (2001)].
4. V. I. Il'ichev and V. V. Navrotskiĭ, Dokl. Akad. Nauk SSSR **294** (1), 587 (1987) [Dokl. Phys. **294** (1), 216 (1987)].
5. K. V. Konyaev and K. D. Sabinin, *Waves within the Ocean* (Gidrometeoizdat, St. Petersburg, 1992) [in Russian].
6. P. E. Holloway, E. Pelinovsky, T. Talipova, and B. Barnes, J. Phys. Oceanogr. **27**, 871 (1997).
7. V. V. Navrotskiĭ, V. L. Izergin, and E. P. Pavlova, Dokl. Akad. Nauk **388** (2), 249 (2003).
8. J. X. Zhou, X. Z. Zhang, and P. H. Rogers, J. Acoust. Soc. Am. **90**, 2042 (1991).
9. B. G. Katsnel'son and S. A. Pereselkov, Akust. Zh. **44**, 786 (1998) [Acoust. Phys. **44**, 684 (1998)].
10. A. N. Serebryanyĭ, Okeanologiya **25**, 744 (1985).
11. A. N. Serebryanyĭ, Okeanologiya **27**, 225 (1987).
12. K. V. Konyaev, Okeanologiya **27**, 896 (1987).
13. V. V. Navrotskiĭ, A. Yu. Lazaryuk, and A. A. Malyshev, Dokl. Akad. Nauk SSSR **309** (1), 95 (1989) [Sov. Phys. Dokl. **309** (1), 187 (1989)].
14. N. G. Borisov, A. V. Gritsenko, S. B. Kozitskiĭ, *et al.*, Akust. Zh. **40**, 749 (1994) [Acoust. Phys. **40**, 664 (1994)].
15. A. N. Rutenko, Akust. Zh. **46**, 259 (2000) [Acoust. Phys. **46**, 207 (2000)].
16. A. N. Rutenko, in *Proceedings of VIII School–Seminar of Academician L.M. Brekhovskikh on Acoustics of the Ocean* (GEOS, Moscow, 2000), pp. 151–155.
17. A. N. Rutenko, Akust. Zh. **49**, 535 (2003) [Acoust. Phys. **49**, 449 (2003)].
18. L. F. Bondar', L. K. Bugaeva, and A. N. Rutenko, Akust. Zh. **46**, 613 (2000) [Acoust. Phys. **46**, 534 (2000)].
19. V. A. Akulichev, V. V. Bezotvetnykh, S. I. Kamenev, *et al.*, Dokl. Akad. Nauk **381** (2), 243 (2001).
20. A. N. Rutenko, Prib. Tekh. Eksp. **5**, 141 (1998).
21. S. V. Borisov, A. V. Gritsenko, D. G. Kovzel', *et al.*, Vestn. DVO **108** (2), 16 (2003).
22. K. V. Konyaev and K. D. Sabinin, Dokl. Akad. Nauk SSSR **209** (1), 291 (1973) [Sov. Phys. Dokl. **209** (1), 86 (1973)].
23. J. F. Miller and S. N. Wolf, *Modal Acoustic Transmission Loss (MOATL): A Transmission Loss Computer Program Using a Normal-Mode Model of the Acoustic Field in the Ocean* (Naval Research Laboratory, Washington, 1980).
24. A. N. Rutenko, Akust. Zh. **43**, 98 (1997) [Acoust. Phys. **43**, 84 (1997)].

Translated by Yu. Lysanov

Acoustical Physics, Vol. 51, No. 4, 2005, pp. 457–462. Translated from Akusticheskiĭ Zhurnal, Vol. 51, No. 4, 2005, pp. 536–542.

Primary Analysis of Speech Signals

V. N. Sorokin and D. N. Chepelev

Institute of Information Transmission Problems,
Bol'shoĭ Karetnyĭ per. 19, Moscow, 101447 Russia
e-mail: vns@iitp.ru

Received May 15, 2003

Abstract—Operations of the type of taking the logarithm, summation, and time delay can be used by a simple operator, which, with different values of frequency and time parameters, creates different transformations of the current spectrum. This operator simulates such properties of auditory perception as temporal and frequency masking, effects of turning on and off a stimulus, selective response to transients with different rates, detection of amplitude and frequency modulations, and adaptation to the mean signal level. © *2005 Pleiades Publishing, Inc.*

Most of the modern automatic speech recognition systems use formal mathematics for the primary description of the speech signal. This may be either the Fourier transformation in a moving window with a weighting function or 10–12 coefficients of the current cepstrum, often together with the first and second time derivatives. Such a description only gives a vague idea of the actual speech signal features. Therefore, the properties of the auditory system have become of special interest to researchers.

Different models of auditory analysis were proposed and then implemented in speech recognition systems [1–4]. In [5], the synchronism of responses in different frequency channels was studied, and the results were used to determine the formant frequencies. The data on the critical bands of hearing and on the nonuniform frequency dependence of hearing sensitivity were realized in a "perceptual linear predictive" (PLP) system [6].

At the same time, the physiology of hearing has some properties that may be directly related to the description of the speech signal but that are not implemented in automatic speech recognition systems. The auditory cortex contains neurons selectively responding to switching on and off a stimulus [7, 8]. Structures specializing in the detection of amplitude modulations are also present in the auditory system [9, 10], and some of the neurons possess a threshold for the rate of change of the sound signal envelope [11]. Auditory neurons also respond to frequency modulations in the signal [12]. Some neurons of the auditory cortex selectively respond to an increase or decrease in frequency [13, 14].

The auditory system was found to possess different integration time constants. A value close to 2 ms was obtained in [15], and a time constant of about 10 ms was reported in [16, 17]. In [18], adaptation intervals of 150–300 ms with the corresponding time constants of 50–100 ms were determined. Even greater time constants (200–300 ms) characterize the mechanism of hearing adaptation to the mean sound level. The authors of [19] proposed a smoothing of the spectral components of the speech signal with a time constant of 170–220 ms.

Effects of temporal masking, i.e., a dependence of the perception of a stimulus or a speech segment on the preceding and following signals, were observed for test signals [20] and in the perception of speech [21].

The reproduction of the known properties of perception in mathematical models of the primary analysis of speech signals may contribute to the stability of automatic speech recognition systems against external noise and distortions and also reduce the effect of the speaker-related variability of speech patterns.

In what follows, the spectrum $S(\omega, t)$ means the power spectrum $S(\omega, t) = |\tilde{S}(j\omega, t)|^2$, where $\tilde{S}(j\omega, t)$ is the complex spectrum of the speech signal. The dynamic spectrum of a distorted speech signal at the input of a recognition system has the form

$$S(\omega, t) = K(\omega, t)[V(\omega, t)X(\omega, t) + \zeta(\omega, t)], \quad (1)$$

where $X(\omega, t)$ is the frequency–time characteristic of the vocal tract, $V(\omega, t)$ is the characteristic of the source of excitation, and $\zeta(\omega, t)$ is the dynamic spectrum of additive noise. The transfer function of the channel $K(\omega, t)$ can be represented in the form of the product of components depending on the speech signal and independent of it:

$$K(\omega, t) = m(\omega, t)r(X, \omega, t), \quad (2)$$

where $m(\omega, t)$ is the speech-independent amplitude–frequency characteristic of the microphone and the communication channel and $r(X, \omega, t)$ is the characteristic of the frequency–time distortions depending on the speech signal, such as microphone-related nonlinear

1063-7710/05/5104-0457$26.00

distortions or room reverberation. A logarithmic transformation of Eq. (1) yields

$$\log S(\omega, t) = \log m(\omega, t) + \log r(X, \omega, t) + \log[V(\omega, t)X(\omega, t) + \zeta(\omega, t)]. \quad (3)$$

The presence of additive noise prevents the separation of the characteristics of the source of excitation $V(\omega, t)$ from those of the vocal tract $X(\omega, t)$. Let us assume that additive noise is suppressed to a negligibly small level, for example, by a spectral subtraction [22]. Then, we have

$$\log S(\omega, t) \approx \log m(\omega, t) + \log r(X, \omega, t) + \log V(\omega, t) + \log X(\omega, t). \quad (4)$$

Generally speaking, by filtering out additive noise, it is also possible to distort the frequency–time characteristic of the speech signal. However, to simplify the following discussion, we assume that this distortion is absent. The extraction of the speech signal characteristics from the mixture given by Eq. (4) is only possible when their spectral–time parameters do not intersect with the distortion parameters. The amplitude–frequency characteristic of the communication channel $m(\omega, t)$ may slowly vary with time in comparison with the speech signal characteristic $X(\omega, t)$, whereas the characteristic of the source of excitation $V(\omega, t)$ may vary much faster. In this case, the filtering in the region of the modulation spectra, i.e., spectra of the time signal for each of the frequency components ω, suppresses the spectral components outside the region of the speech modulation spectrum. Experimentally, it was found that the modulation spectra of speech signals can be confined within a band of 2–16 Hz [23], and this property was used to increase the stability of speech recognition systems [24, 25].

Along with the suppression of distortions and noise, it is necessary to describe the speech signal so as to reproduce most adequately the variety of properties of phonetic and acoustic speech segments. According to [26], the responses to transient processes and to a steady sound stimulus occur in different parts of the human auditory cortex. This testifies that the analysis of the dynamics of a sound signal and its quasi-stationary spectral composition is likely to be performed by applying different types of processing to the data arriving from the internal ear.

Consider an operator that uses only those mathematical operations whose analogs are known to exist in the auditory system: summation, subtraction, integration with respect to time and frequency, delay in time, smoothing with different time constants, and an almost logarithmic transformation of the input signal amplitude

$$A(\omega, t) = \log\frac{S(\omega + \Delta\Omega, \theta_1, t \pm \Delta T_1, \tau_1) + C}{S(\omega - \Delta\Omega, \theta_2, t \mp \Delta T_2, \tau_2) + C}. \quad (5)$$

This operator describes the acoustic (nonspecific) detectors of spectrum–time inhomogeneities of the signal and models many of the known properties of auditory perception. Here, S is the power spectrum of the received signal separated from additive noise, $\Delta\Omega$ is the frequency shift of the spectrum reading, ΔT is the time shift of the spectrum reading, θ_1 and θ_2 are the moving intervals of smoothing the spectrum in frequency, τ_1 and τ_2 are the time constants of smoothing the spectral components by a first-order filter, and $C \geq 1$.

At certain values of the parameters $\Delta\Omega$, θ_1, θ_2, and C, the function $A(\omega, t)$ is invariant with respect to the time-constant amplification coefficient $K(\omega)$ for each of the frequency components ω, which provides for the independence from the stationary amplitude–frequency characteristic of the communication channel, including the independence from the amplification coefficient. However, this property only holds for the channels in which the amplification coefficient is nonzero at certain frequencies. At other values of the parameters $\Delta\Omega$, θ_1, θ_2, and C, the function $A(\omega, t)$ weakly depends on $K(\omega)$.

A total invariance to the sound level is undesirable, because, in this case, weak noise fluctuations in the communication channel acquire weight equal to that of the speech signal. In addition, the speech intelligibility is known to depend on the sound level, which manifests itself most clearly in the perception of foreign speech when the listener is not quite familiar with the language. The choice of the constant C is determined by the compromise between the sensitivity of the detector to small signal fluctuations and its sensitivity to the nonuniform amplitude–frequency characteristic of the channel. To describe most clearly the properties of operator (5), we set $C = 0$ and ignore the possibility of the situation with log(0).

Let us consider several particular cases. At $\tau_1 = 0$, $\tau_2 = 0$, $\Delta\Omega = 0$, $\theta_1 = 0$, $\theta_2 = 0$, $\Delta T_1 \longrightarrow 0$, and $\Delta T_2 \longrightarrow 0$, operator (5) calculates the logarithmic derivative with respect to time:

$$A(\omega, t) = \log S(\omega, t + \delta t) - \log S(\omega, t - \delta t) \underset{\delta t \to 0}{=} 2\delta t[\log S(\omega, t)]', \quad (6)$$

because the second term in Eq. (6) is the central difference converging to the derivative $\partial S(\omega, t)/\partial t$ at $\delta t \longrightarrow 0$. The operator $A(\omega, t)$ given by formula (6) possesses the properties of the detector of the beginning and end of the signal: the rise of the signal (positive derivative) corresponds to $A(\omega, t) > 0$, and the drop of the signal (negative derivative) corresponds to $A(\omega, t) < 0$; within the stationary part of the signal with zero derivative, $A(\omega, t) = 0$. At finite values of $\Delta T_1 = \Delta T_2 = \Delta T$, $A(\omega, t)$ is invariant with respect to the constant amplification coefficient $K(\omega)$. A finite interval of $2\Delta T$ corresponds to sampling of the function $A(\omega, t)$ in time at a step of $2\Delta T$, and, according to the Nyquist–Kotel'nikov theorem, an increase in this interval leads to a decrease in the highest frequency retained in the spectrum $A(\omega, t)$, i.e., to

the smoothing of the function $A(\omega, t)$ in time. Therefore, the calculation of the finite difference on the interval $2\Delta T$ leads to the smoothing of the first derivative of the signal. This contributes to the suppression of high-frequency noise. When $\tau_1 \neq 0$ and $\tau_2 \neq 0$, an additional smoothing of the signal with the suppression of different high-frequency components takes place.

At $\theta_1 = 0$, $\theta_2 = 0$, and $\Delta\Omega = 0$, i.e., in the case of only temporal signal processing, operator $A(\omega, t)$ simultaneously responds to changes in both amplitude and spectral composition of the signal. The time interval $\Delta T_1 + \Delta T_2$ determines the duration of the segment, at the ends of which signal readings are taken and the rate of the relative spectrum variation is estimated. This interval is different for different combinations of articulatory or acoustic events, i.e., transitions from one state to another. The time constants τ_1 and τ_2 should also be different. For example, for an estimate of the transient process between a nonaspiratory stop consonant and the following vowel, the time constants and the interval of analysis should be small. At the same time, the spectrum of fricative consonants varies within a relatively long interval of time, and the parameters τ_1, τ_2, ΔT_1, and ΔT_2 should correspond to these features.

Vowels, fricatives, and nasal, voiced, and voiceless closures have quasi-stationary segments characterized by their own spectra. It is desirable to find such a spectrum description that is little sensitive to distortions of the amplitude–frequency characteristic of the channel but that retains the informative features of the speech sound spectra.

At $\theta_1 = 0$, $\theta_2 = 0$, $\tau_1 = 0$, $\tau_2 = 0$, $\Delta T_1 = 0$, $\Delta T_2 = 0$, and $\Delta\Omega \longrightarrow 0$, as in Eq. (6), $A(\omega, t)$ taken in the limit estimates the instantaneous derivative of the spectrum, however, with respect to frequency rather than with respect to time:

$$\begin{aligned} A(\omega, t) &= \log S(\omega + \Delta\Omega, t), \\ -\log S(\omega - \Delta\Omega, t) &\underset{\Delta\Omega \to 0}{=} 2\Delta\Omega[\log S(\omega, t)]', \end{aligned} \tag{7}$$

where the prime now denotes the derivative with respect to ω. Representing Eq. (7) in the form

$$A(\omega, t) = 2\Delta\Omega \frac{S'(\omega, t)}{S(\omega, t)}, \tag{8}$$

one can see that Eq. (8) estimates the rate of spectrum variation in frequency, this rate being normalized by the spectral value at the given frequency. As in the case of Eq. (6), an increase in the interval between the spectrum readings in frequency is equivalent to a smoothing of the derivative, which suppresses random fluctuations of the spectrum readings. The logarithmic derivative with respect to frequency is sensitive to the nonuniformity of the amplitude–frequency characteristic of the channel:

$$\frac{S'(\omega, t)}{S(\omega, t)} = \frac{K'(\omega, t)}{K(\omega, t)} + \frac{[V(\omega, t)X(\omega, t)]'}{V(\omega, t)X(\omega, t)}.$$

Nevertheless, when the amplitude–frequency characteristic of the channel does not vary with time, the subsequent processing of the dynamic spectrum of the signal with the calculation of the logarithmic time derivative provides for invariance to the perturbing term $K'(\omega)/K(\omega)$ or reduces its influence, as in the case of Eq. (6).

Spectral peaks corresponding to the resonance frequencies can merge, as often happens for the first and second resonances of the vowels */o, u/*. In this case, an exact estimate of formant frequencies through the search for the extrema of the spectrum is impossible. The value of the frequency interval between the maxima of the positive and negative frequency derivatives and its comparison with the expected bandwidth of the formant at a given frequency may indicate the presence of two formants and will allow an approximate estimate of their frequencies. In some cases, the position of the maximum of the negative derivative in the low-frequency region clearly discriminates the voiced and nasal closures, while the position of the maximum of the positive derivative in the high-frequency region distinguishes the fricatives */s, sh/*.

At $\tau_1 = 0$, $\tau_2 = 0$, $\theta_1 = 0$, $\theta_2 = 0$, $\Delta T_1 = \Delta T_2 \longrightarrow 0$, and $\Delta\Omega \longrightarrow 0$, operator (5) estimates the combined derivative with respect to frequency and time with normalization to the spectrum reading at the frequency ω at the instant t; i.e., it calculates the energy gradient of sonograms.

Parameters θ_1 and θ_2 normalize the signal spectrum to the moving average:

$$\bar{S}(\omega, t) = \theta_2 \int_{\omega - \theta_1}^{\omega + \theta_1} S(\omega, t)d\omega \Big/ \left[\theta_1 \int_{\omega - \theta_2}^{\omega + \theta_2} S(\omega, t)d\omega\right]. \tag{9}$$

This operation is analogous to the so-called lateral suppression in the frequency domain. If the average over the interval $2\theta_1$ is equal to the average over the interval $2\theta_2$, we have $\bar{A}(\omega, t) = 0$. This corresponds to the spectrum parts with a strictly linear dependence on frequency, in particular those with a constant level. Positive values $\bar{A}(\omega, t) > 0$ occur only for convex parts of the locally normalized spectral section $\bar{S}(\omega, t)$. For concave parts, the spectral section normalized by Eq. (9) is $\bar{S}(\omega, t) < 1$ and, hence, $\log \bar{S}(\omega, t) < 0$. If we impose a limitation on the negative values of $\bar{A}(\omega, t)$, i.e., if we require that $\bar{S}(\omega, t) = 1$ each time when

$$\theta_1 \int_{\omega - \theta_2}^{\omega + \theta_2} S(\omega, t)d\omega > \theta_2 \int_{\omega - \theta_1}^{\omega + \theta_1} S(\omega, t)d\omega, \tag{10}$$

then such parts of the spectrum will also be "invisible," because $\bar{A}(\omega, t) = 0$. As a result, the spectral section will contain local maxima determined within different

frequency intervals. These maxima may be identified as the resonances of the mouth cavity and subglottal area.

A local normalization of the spectrum leads to a kind of equalization of the high and low levels by reducing the sensitivity to transformations of the Lombard-effect type, changes in the spectrum slope due to differentiation or integration in the time domain (which are equivalent to multiplication or division by ω), and different spectral characteristics of the sources of acoustic vibration excitation in the vocal tract. Transformation (9) retains the dependence on $K(\omega)$, but, in the determination of the frequencies of the spectral maxima, the influence of the nonuniform amplitude–frequency characteristic of the communication channel can be negligible.

In the particular case, at $\theta_1 = 0$ and $\theta_2 = \Theta$, where Θ is the upper bound of the frequency spectrum of the signal, the normalization to the total signal energy in the whole frequency range at every instant of time is performed:

$$\bar{S}(\omega, t) = \Theta S(\omega, t)/\int_0^\Theta S(\omega, t)d\omega. \quad (11)$$

Then, the normalized detector is represented as

$$\bar{A}(\omega, t) = \log\frac{\bar{S}(\omega + \Delta\Omega, t \pm \Delta T_1, \tau_1)}{\bar{S}(\omega - \Delta\Omega, \Theta, t \mp \Delta T_2, \tau_2)}. \quad (12)$$

Let the spectral composition of the signal be constant in time and only the amplitude of the signal vary: $S(\omega, t) = G(t)H(\omega)$. Then, the normalized spectrum does not vary with time:

$$\bar{S}(\omega, t) = \Theta G(t)H(\omega)/\int_0^\Theta G(t)H(\omega)d\omega = \bar{S}(\omega). \quad (13)$$

In the case of, e.g., $\tau_1 = 0$, $\tau_2 = 0$, and $\Delta\Omega = 0$, we obtain

$$\bar{A}(\omega, t) = \log\frac{\bar{S}(\omega, t \pm \Delta T_1, \tau_1)}{\bar{S}(\omega, t \mp \Delta T_2, \tau_2)} = 0, \quad (14)$$

because the values of $\bar{S}(\omega)$ are the same at different instants ΔT_1 and ΔT_2. If $\tau_1 \neq 0$ and $\tau_2 \neq 0$, $\bar{A}(\omega, t) =$ const after the termination of the transient processes. This case corresponds to an idealized description of the beginning of a vowel or a fricative after a pause or their termination before a pause, when the spectral composition of the sound does not change, while its energy either increases or decreases. The detectors of normalized signals, $\bar{A}(\omega, t)$, for all frequency components of the sound spectrum will notice the passage from the pause spectrum to the speech segment spectrum (or in the opposite direction) but will not respond to the change in amplitude, whereas the detectors of nonnormalized signals $A(\omega, t)$ will notice the transient processes. Thus, the detectors $\bar{A}(\omega, t)$ mainly respond to energy redistribution over the spectrum, while the detectors $A(\omega, t)$ respond to both amplitude variations and changes in the spectral composition of the signal. Detectors $\bar{A}(\omega, t)$ retain the properties of $A(\omega, t)$ for a time-invariable amplitude–frequency characteristic of the channel.

The spectral–time patterns of the speech signal differ depending on whether the operations are performed in only the time or only the frequency domain or the temporal processing is performed before or after the frequency processing.

The figure shows the results of the speech signal processing for the sequence of words *odin, shest', chetyre* by using the operator with different parameters. The apostrophe marking the symbols means palatalized consonants, the symbol *vh* means aspiration at the end of a word, the symbol *Th* means aspiratory stop, the symbol *T*! means nonaspiratory stop, and the symbol *z#* means the beginning of a pause between words. The plot below the speech signal represents the sonogram calculated on the mel scale and smoothed in frequency by triangular filters (with slopes of +25 dB/Bark and –10 dB/Bark). The plot below the sonogram shows the "detectograms," i.e., the positive responses of the operator with the parameters $\theta_1 = 0$, $\theta_2 = 0$, $\Delta\Omega = 0$, $\tau_1 = 5$ ms, $\tau_2 = 15$ ms, $\Delta T_1 = 0$, and $\Delta T_2 = -25$ ms, and the inverted "detectogram" for the negative responses of the operator with the same parameters. The next plot below is the sonogram that was frequency normalized on moving intervals $\theta_1 = 40$ mel and $\theta_2 = 600$ mel. The lowest plot shows the positive finite differences of the spectrum in frequency, which are calculated on a 120-mel interval.

As one can see from the figure, the detectors of the rise and fall of energy in time notice the beginning and end of transients. However, this is not the only role of the dynamic detectors. The energy distribution in frequency at every given instant also characterizes the spectral composition of transients. The locally normalized spectrogram more clearly distinguishes between the trajectories of the energy peaks, as compared to the initial sonogram. The positive "derivative" emphasizes the difference in the cutoff frequencies of the spectra for the fricatives /*sh*/ and /*s*/.

Operator (5) reproduces many properties observed in the auditory system. By choosing the parameters θ_1, θ_2, $\Delta\Omega$, τ_1, τ_2, ΔT_1, and ΔT_2 with an allowance made for the dynamic and spectral characteristics of phonetic and acoustic segments of the speech signal, it is possible to reduce the influence of amplitude–frequency distortions of the speech signal and to emphasize the characteristic features of speech segments. Thus, one obtains a multilayer description of a speech flow with different resolving powers in the frequency and time domains, which is necessary for an adequate segmentation and subsequent decoding of the speech signal.

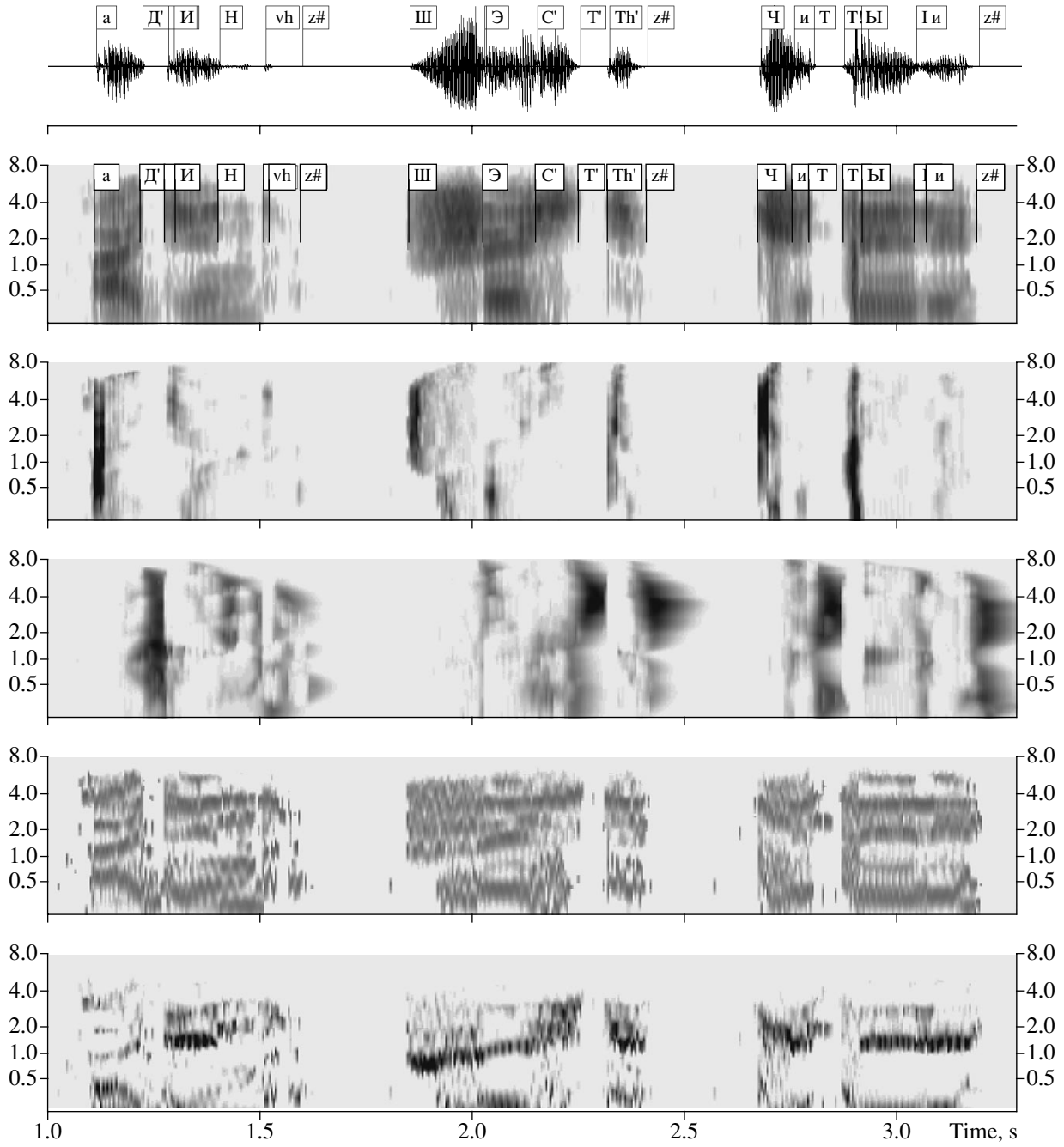

Words *odin*, *shest'*, *chetyre*. From top to bottom: oscillogram of the speech signal, sonogram, response of the dynamic detector to the energy rise, response of the dynamic detector to the energy drop, sonogram normalized by an interval moving in frequency, and finite difference in frequency (explanations are given in the main body of the paper).

A system of dynamic detectors in chosen frequency bands was tested in the recognition of Russian numerals from a speech data base obtained from 47 speakers with the use of three types of microphones placed at different distances from a speaker, two types of handsets, two types of nonprofessional A/D converters, and a simulator of a telephone communication channel. For some speakers, the signal-to-noise ratio in this base did not exceed 10 dB. The structure of the speech recognition system was described in [27]. The mean error in the recognition of single words was found to be about 11.7%.

ACKNOWLEDGMENTS

This work was supported in part by the Russian Foundation for Basic Research (project no. 03-01-0016).

REFERENCES

1. T. Dau, D. Püschel, and A. Kohlrausch, J. Acoust. Soc. Am. **99**, 3615 (1996).
2. R. P. Lippmann, Speech Commun. **22** (1), 1 (1997).
3. B. E. D. Kingsbury, N. Morgan, and S. Greenberg, Speech Commun. **25** (1–3), 117 (1998).
4. J. Tchorz and D. Kollmeier, J. Acoust. Soc. Am. **106**, 2040 (1999).
5. S. Seneff, J. Phonetics **16**, 55 (1988).
6. H. Hermansky, J. Acoust. Soc. Am. **87**, 1738 (1990).
7. B. Delgutte and N. Y. S. Kiang, J. Acoust. Soc. Am. **75**, 866 (1984).
8. D. G. Sinex, J. Acoust. Soc. Am. **94**, 1351 (1993).
9. W. Rhode and S. Greenberg, J. Neurophysiol. **71**, 1797 (1994).
10. N. G. Bibikov, *Description of Sound Features by Neurons of the Auditory System of Land Vertebrates* (Nauka, Moscow, 1987) [in Russian].
11. N. Suga, J. Physiol. **217**, 159 (1971).
12. K. Wang and S. A. Shamma, IEEE Trans. Speech Audio Process. **3** (5), 382 (1995).
13. S. A. Shamma, J. W. Fleshman, P. R. Wiser, and H. Versnel, J. Neurophysiol. **69**, 367 (1993).
14. N. Kowalski, Y. Versnel, and S. A. Shamma, J. Neurophysiol. **73**, 1513 (1995).
15. D. M. Green, J. Acoust. Soc. Am. **54**, 373 (1973).
16. D. H. Raab, J. Acoust. Soc. Am. **33**, 137 (1961).
17. H. Babkoff and S. Sutton, J. Acoust. Soc. Am. **44**, 1373 (1968).
18. L. L. Elliot, J. Acoust. Soc. Am. **34**, 1116 (1962).
19. H. Hermansky and N. Morgan, IEEE Trans. Speech Audio Process. **2** (4), 578 (1994).
20. E. Zwicker and R. Feldtkeller, *Das Ohr als Nachrichtenempfänger* (*The Ear as a Communication Receiver*) (Hirzel, Stuttgart, 1967; Svyaz', Moscow, 1971; Acoust. Soc. Am., New York, 1999).
21. B. Delgutte and N. Y. S. Kiang, J. Acoust. Soc. Am. **75**, 887 (1984).
22. S. F. Boll, IEEE Trans. Acoust., Speech, Signal Process **27**, 113 (1979).
23. R. Drullman, J. M. Festen, and R. Plomp, J. Acoust. Soc. Am. **95**, 1053 (1994).
24. H. Hermansky, Speech Commun. **25** (1–3), 3 (1998).
25. N. Kanedera, T. Arai, H. Hermansky, and M. Pavel, Speech Commun. **28**, 43 (1999).
26. E. Seifritz, F. Esposito, F. Hennel, *et al.*, Science **297**, 1706 (2002).
27. V. N. Sorokin, A. N. Izhnin, A. I. Tsyplikhin, and D. N. Chepelev, in *Proceedings of International Seminar: Dialog-2003* (Moscow, 2003), p. 657.

Translated by E. Golyamina

Acoustical Physics, Vol. 51, No. 4, 2005, pp. 463–468. Translated from Akusticheskiĭ Zhurnal, Vol. 51, No. 4, 2005, pp. 543–549.

The Effect of the Liquid Flow in the Outlet of a Centrifugal Pump on the Acoustic Resonance

V. L. Khitrik

Chemical Machinery Research Institute, Sergiev Posad, Moscow oblast, 141300 Russia
e-mail: mail@niichimmash.ru

Received August 27, 2003

Abstract—The effect of a radially nonuniform steady-state liquid flow in the outlet of a centrifugal pump on the excitation of sound waves in it by a source of oscillations positioned in the inlet cross section of the impeller is analyzed. It is shown that a change in the velocity of the potential rotation of the liquid in the outlet almost does not affect the resonance frequency values in the frequency range of sound oscillations under consideration (the difference is less than 2%). A similar change (an increase) in the velocity of the solid-state rotation of the flow leads to a small (from 2 to 10%) increase in the resonance frequencies within the same frequency range.

Centrifugal pumps are known to be capable of working in a wide range of volume discharges (capacities) [1]. The use of centrifugal pumps in the whole range of possible capacities is primarily limited by the hydrodynamic vibration that arises when they operate at low capacities. The hydrodynamic vibration reduces the performance of pumps, causes an increase in the power consumption, wears out the equipment, and produces an adverse ecological effect. One of the sources of this type of vibration may be the resonance excitation of sound by the disturbances of liquid that arise, for example, at the interaction of moving and stationary blade cascades. In this connection, it is of interest to consider the effect of a radially nonuniform steady-state liquid flow in the outlet of a centrifugal pump on the excitation of sound waves in it by a source of oscillations positioned in the inlet cross section of the impeller. This problem is close to that of a silencer with a hole in the screen separating the moving and stationary media and operating in the presence of an air flow. The study of the effect of a flow on the acoustical characteristics of holes while taking into account their finite width is a complicated problem, various aspects of which are considered in [2–6].

As an initial set of equations describing the propagation of sound waves in the outlet, we use the following linearized equations:

the continuity equation

$$i\omega r\rho + \rho_0 r\frac{\partial v}{\partial r} + \rho_0 v + U_0\frac{\partial \rho}{\partial \varphi} + \rho_0\frac{\partial u}{\partial \varphi} = 0, \qquad (1)$$

the projections of the Euler vector equation of motion on the circular and radial directions of a cylindrical coordinate system r, φ, z (figure)

$$\frac{v}{r}\frac{d(rU_0)}{dr} + \frac{U_0}{r}\frac{\partial u}{\partial \varphi} + i\omega u + \frac{1}{r\rho_0}\frac{\partial p}{\partial \varphi} = 0, \qquad (2)$$

$$i\omega v + \frac{U_0}{r}\frac{\partial v}{\partial \varphi} - \frac{2U_0 u}{r} + \frac{1}{\rho_0}\frac{\partial p}{\partial r} = 0, \qquad (3)$$

and the equation of state

$$\rho = p/c^2, \qquad (4)$$

where u and v are the circular and radial components of the oscillating particle velocity in the outlet, respectively; ρ and p are the fluctuations of density and pressure of the liquid in the outlet, respectively; ρ_0 and U_0 are the steady-state values of the density (ρ_0 = const) and of the projection of the liquid velocity vector in the outlet on the circular direction, respectively; c is the sound speed in the stationary medium; ω is the angular frequency of oscillations; r and φ are the radial and angular coordinates, respectively; and i is the imaginary unit.

Equations (1)–(3) were derived under the following assumptions:

(i) the sound source generates harmonic oscillations of frequency ω;

(ii) the steady-state flow in the outlet is mainly realized in the circular direction with the velocity U_0 varying in the radial direction and independent of the axial coordinate z, which is perpendicular to the plane of the outlet drawing in the figure; the oscillating components of the dependent variables in Eqs. (1)–(3) are also assumed to be independent of the z coordinate;

1063-7710/05/5104-0463$26.00 © 2005 Pleiades Publishing, Inc.

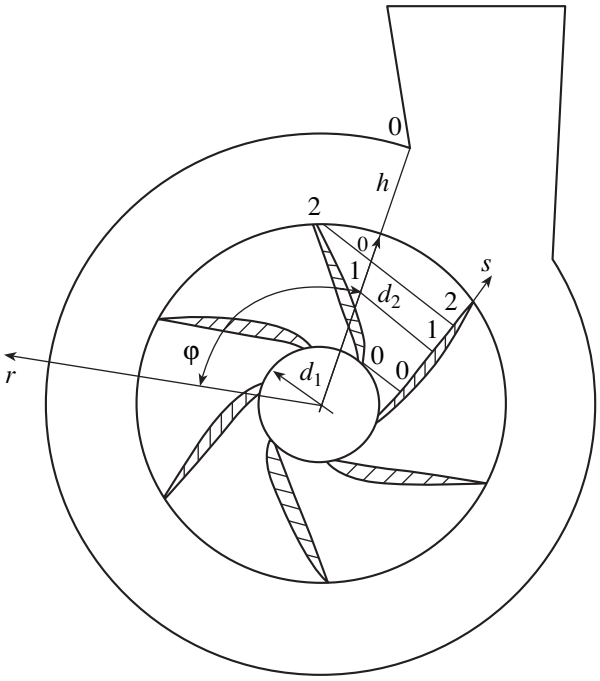

A centrifugal pump.

(iii) the effect of the impeller rotation on the sound propagation is neglected; the effect of the outlet orifice is also neglected.

Since the dependent variables involved in set of equations (1)–(4) should be periodic in the φ coordinate, the solution to this set of equations can be written as

$$f(r, \varphi) = f(r)\exp(-im\varphi), \tag{5}$$

where $f(r, \varphi)$ denotes the dependent variables involved in set of equations (1)–(4): ρ, v, u, and p. Then, taking into account Eqs. (4) and (5), set of equations (1)–(3) takes the form

$$i\omega r\rho + \rho_0 r\frac{\partial v}{\partial r} + \rho_0 v - imU_0\rho - im\rho_0 u = 0, \tag{6}$$

$$\frac{1}{r}\frac{d(rU_0)}{dr}v - im\frac{U_0}{r}u + i\omega u - \frac{imc^2}{r\rho_0}\rho = 0, \tag{7}$$

$$i\omega v - im\frac{U_0}{r}v - \frac{2U_0}{r}u + \frac{c^2}{\rho_0}\frac{\partial\rho}{\partial r} = 0. \tag{8}$$

Considering Eqs. (7) and (8) as a set of algebraic equations with respect to the unknowns v and u, we find the expressions for v and u in terms of ρ:

$$v = i\frac{-m2\dfrac{U_0}{r^2}\dfrac{c^2}{\rho_0}\rho + \left(\omega - m\dfrac{U_0}{r}\right)\dfrac{c^2}{\rho_0}\dfrac{\partial\rho}{\partial r}}{\left(\omega - m\dfrac{U_0}{r}\right)^2 - 2\dfrac{U_0}{r^2}\dfrac{d(rU_0)}{dr}}, \tag{9}$$

$$u = -\frac{\dfrac{1}{r}\dfrac{d(rU_0)}{dr}\dfrac{c^2}{\rho_0}\dfrac{\partial\rho}{\partial r} - \left(\omega - m\dfrac{U_0}{r}\right)\dfrac{c^2}{\rho_0}\dfrac{m}{r}\rho}{\left(\omega - m\dfrac{U_0}{r}\right)^2 - 2\dfrac{U_0}{r^2}\dfrac{d(rU_0)}{dr}}. \tag{10}$$

By substituting Eqs. (9) and (10) into continuity equation (6), it is possible to obtain an equation for the density perturbation for an arbitrary dependence of the steady-state circular component of liquid velocity in the outlet U_0 on the radial coordinate r. This equation is not given here because of its awkwardness. In addition, it should be noted that the analytical solution of this equation is rather complicated. However, for some particular forms of the function $U_0 = U_0(r)$ that are of practical importance, this equation can be simplified and its solution becomes possible.

If the solution for the density perturbation $\rho(r)$ is found, then, using Eqs. (4), (9), and (10), it is possible to obtain the functions $p(r)$, $v(r)$, and $u(r)$. To complete the problem formulation, we specify the boundary conditions.

At the outer radius of the outlet, the no-leakage condition is satisfied, which implies that the radial component of the oscillating particle velocity equals zero:

$$v = i\left[\left(\omega - m\frac{U_0}{r}\right)\frac{c^2}{\rho_0}\frac{\partial\rho}{\partial r} - m2\frac{U_0}{r^2}\frac{c^2}{\rho_0}\rho\right] = 0 \quad \text{for } r = \frac{d_2}{2} + h, \tag{11}$$

where d_2 is the diameter of the impeller and h is the height of the outlet (h = const).

The other boundary separates the moving medium in the outlet from the medium in the blade channels of the impeller, which, on the average, is stationary. This boundary is given by the equation $r = \dfrac{d_2}{2} + \eta(\varphi, t)$ and is characterized by the continuity of the small boundary displacement $\eta(\varphi, t)$:

$$\eta_1(\varphi, t) = \eta_2(\varphi, t) \text{ for } r = \frac{d_2}{2}, \tag{12}$$

as well as by the continuity of the pressure fluctuation

$$\rho(r)c^2 e^{-im\varphi} = P_{k2} \text{ for } r = \frac{d_2}{2}. \tag{13}$$

Here, P_{k2} is the pressure fluctuation of the liquid at the outlet of the blade channel of the impeller.

The radial component of the oscillating particle velocity of liquid in the outlet at the boundary separating the moving medium in the outlet from the stationary

(on the average) medium in the blade channels of the impeller is determined by the formula

$$v = \frac{\partial \eta_2}{\partial t} + U_0 \frac{1}{r}\frac{\partial \eta_2}{\partial \varphi} = i\omega\eta_2 + \frac{2U_0}{d_2}\frac{\partial \eta_2}{\partial \varphi}, \quad (14)$$

and the radial component of the oscillating particle velocity of liquid in the blade channel of the impeller at the same boundary v^r_{k2} is determined by the formula

$$v^r_{k2} = \frac{\partial \eta_1}{\partial t} = i\omega\eta_1. \quad (15)$$

Using condition (12) and Eqs. (14) and (15), we obtain the following differential equation:

$$v = v^r_{k2} + \frac{2U_0}{i\omega d_2}\frac{\partial v^r_{k2}}{\partial \varphi}. \quad (16)$$

Substituting the function $v(r)$ found from the solution of set of equations (1)–(4) for $r = d_2/2$ into the left-hand side of Eq. (16), we obtain

$$v\left(\frac{d_2}{2}\right)\exp(-im\varphi) = v^r_{k2} + \frac{2U_0}{i\omega d_2}\frac{\partial v^r_{k2}}{\partial \varphi}. \quad (17)$$

The solution to inhomogeneous differential equation (17) has the form

$$v^r_{k2} = C\exp\left(-\frac{i\omega d_2}{2U_0}\varphi\right) + \frac{v(d_2/2)}{1 - \dfrac{m2U_0}{\omega d_2}}\exp(-im\varphi), \quad (18)$$

where C = const.

In the framework of the problem formulation considered in this paper, the solution to Eq. (18) should be periodic in the variable φ. Consequently, the constant C has a nonzero value only when

$$\frac{\omega d_2}{2U_0} = n, \quad (19)$$

where n is an integer.

When condition (19) is violated, the boundary condition for the radial component of the oscillating particle velocity at the boundary separating the moving medium in the outlet from the stationary (on the average) medium in the blade channels of the impeller is determined by the formula

$$v^r_{k2} = \frac{v(d_2/2)}{1 - \dfrac{m2U_0}{\omega d_2}}\exp(-im\varphi).$$

Let the steady-state flow in the outlet represent a potential rotation with the velocity

$$U_0 = \Gamma/r, \quad (20)$$

where Γ = const.

Then, continuity equation (6) can be represented as

$$\frac{\partial^2 \rho}{\partial r^2} + \left[-\frac{4m\Gamma}{r^3\left(\omega - m\dfrac{\Gamma}{r^2}\right)} + \frac{1}{r}\right]\frac{\partial \rho}{\partial r} + \left[\frac{\omega\left(\omega - m\dfrac{\Gamma}{r^2}\right)}{c^2} + \frac{8m^2\Gamma^2}{r^6\left(\omega - m\dfrac{\Gamma}{r^2}\right)^2}\right. \quad (21)$$
$$\left. + \frac{4m\Gamma}{r^4\left(\omega - m\dfrac{\Gamma}{r^2}\right)} - \frac{m\Gamma\left(\omega - m\dfrac{\Gamma}{r^2}\right)}{r^2c^2} - \frac{m^2}{r^2}\right]\rho = 0.$$

We restrict our consideration to the high-frequency oscillations that are generated in high-speed turbomachines, for example, in aerodynamic interaction between moving and stationary cascades [7]. In this case, it is possible to assume that $\varepsilon = \left|\dfrac{m\Gamma}{\omega r^2}\right| \ll 1$.

Writing Eq. (21) in the linear approximation with respect to ε, we obtain

$$\frac{\partial^2 \rho}{\partial r^2} + \left[\frac{1}{r} - \frac{4m\Gamma}{r^3\omega}\right]\frac{\partial \rho}{\partial r} + \left[\frac{\omega^2}{c^2} - \frac{2m\Gamma\omega}{r^2c^2} + \frac{4m\Gamma}{r^4\omega} - \frac{m^2}{r^2}\right]\rho = 0. \quad (22)$$

By a direct substitution, one can verify that, within the accepted accuracy, the following expression is the solution to Eq. (22):

$$\rho = \exp\left(-\frac{m\Gamma}{\omega r^2}\right)Z_\nu(\alpha r) = \exp\left(-\frac{m\Gamma}{\omega r^2}\right)[AJ_\nu(\alpha r) + BN_\nu(\alpha r)], \quad (23)$$

where $J_\nu(\alpha r)$ and $N_\nu(\alpha r)$ are the Bessel and Neumann functions, respectively; A = const; B = const; $\nu^2 = m^2 + \dfrac{2\omega\Gamma m}{c^2}$; and $\alpha^2 = \dfrac{\omega^2}{c^2}$.

Substituting Eq. (23) into Eq. (9), we use boundary conditions (11), (13), and (18) to obtain expressions for A and B and, then, the relation between the pressure and the radial velocity at the beginning of the outlet:

$$v_{k2}^r = \frac{i\alpha\omega}{\left(\omega - m\frac{\Gamma}{(d_2/2)^2}\right)^2\rho_0}P_{k2}\frac{-N_\nu'\left[\alpha\left(\frac{d_2}{2}+h\right)\right]J_\nu'\left[\alpha\left(\frac{d_2}{2}\right)\right] + J_\nu'\left[\alpha\left(\frac{d_2}{2}+h\right)\right]N_\nu'\left[\alpha\left(\frac{d_2}{2}\right)\right]}{D} + C\exp\left(-i\frac{\omega}{\Gamma}(d_2/2)^2\varphi\right), \quad (24)$$

where the prime designates differentiation with respect to the argument and

$$D = J_\nu'\left[\alpha\left(\frac{d_2}{2}+h\right)\right]N_\nu\left[\alpha\left(\frac{d_2}{2}\right)\right] - N_\nu'\left[\alpha\left(\frac{d_2}{2}+h\right)\right]J_\nu\left[\alpha\left(\frac{d_2}{2}\right)\right].$$

Note that, in the case of high-frequency oscillations under consideration, it is possible to use the asymptotic representations of the Bessel and Neumann functions. Then, Eq. (24) takes the form

$$v_{k2}^r = \frac{i\alpha\omega}{\left(\omega - m\frac{\Gamma}{(d_2/2)^2}\right)^2\rho_0}P_{k2}\frac{\sin(\alpha h)}{\cos(\alpha h)} + C\exp\left(-i\frac{\omega}{\Gamma}(d_2/2)^2\varphi\right). \quad (25)$$

Substituting the expressions from [8] that relate the fluctuation amplitudes of the radial velocity and the pressure at the blade channel outlet, v_{k2}^r and P_{k2}, to the corresponding amplitudes at the blade channel inlet, v_{k1}^r and P_{k1}, into Eq. (25), we obtain the impedance relation at the impeller inlet:

$$v_{k1}^r\left[\frac{\sin\beta_2}{\sin\beta_1}\left(1 - \frac{\tan kl}{ks_2}\right)\cos kl - \frac{c\omega\alpha\tan(\alpha h)}{\left(\omega - m\frac{\Gamma}{(d_2/2)^2}\right)^2}\frac{\sin kl}{\sin\beta_1}\right]$$
$$= P_{k1}\left[\frac{i\omega\alpha\tan(\alpha h)}{\left(\omega - m\frac{\Gamma}{(d_2/2)^2}\right)^2\rho_0}\left(1 + \frac{\tan kl}{ks_1}\right)\cos kl + \frac{i\sin\beta_2}{\rho_0 c}\left(1 + \frac{1}{k^2 s_1 s_2} - \frac{l}{ks_1 s_2}\cot kl\right)\sin kl\right] + C\exp\left(-i\frac{\omega}{\Gamma}(d_2/2)^2\varphi\right), \quad (26)$$

where k is the wave number of sound oscillations in the blade channel of the impeller, $k = \frac{\omega}{c}$; l is the length of the blade channel of the impeller; β_1 and β_2 are the angles of the blade orientation at the inlet and outlet of the impeller, respectively; s_1 and s_2 are the coordinates of the inlet and outlet cross sections of the blade channel; and $P_{k1} = P_1 = \text{const}$.

The condition for the resonance sound excitation in the pump is the zero value of the coefficient multiplying v_{k1}^r in Eq. (26):

$$\frac{\sin\beta_2}{\sin\beta_1}\left(1 - \frac{\tan[\omega l/c]}{\omega s_2/c}\right)\cos(\omega l/c) - \frac{\omega^2\tan[\omega h/c]}{\left(\omega - m\frac{\Gamma}{(d_2/2)^2}\right)^2}\frac{\sin(\omega l/c)}{\sin\beta_1} = 0. \quad (27)$$

The resonance frequencies at the impeller inlet are determined from the solution of transcendental equation (27), and their values depend on the flow velocity in the outlet only for nonzero modes of sound oscillations in the outlet ($m \neq 0$). It should be noted that, in the absence of the flow and when the outlet height is small compared to the outer radius of the impeller, i.e., $2h/d_2 \ll 1$, Eq. (27) transforms into the formula for determining the resonance frequencies derived for the conditions indicated in [8].

We consider the case when the steady-state flow in the outlet represents a solid-state rotation with the velocity

$$U_0 = \Omega r. \quad (28)$$

We introduce the notation $\lambda = \omega - m\Omega$. Let $\lambda \neq 2\Omega$. Then, substituting Eqs. (9) and (10) into Eq. (6) with allowance for Eq. (28), we obtain

$$r^2\frac{\partial^2\rho}{\partial r^2} + r\frac{\partial\rho}{\partial r} + \left[-m^2 + r^2\frac{\lambda^2 - 4\Omega^2}{c^2}\right]\rho = 0. \quad (29)$$

Let us assume that the velocity of the solid-state rotation of the liquid in the outlet is much smaller than the sound speed, $\Omega^2 r^2/c^2 \ll 1$. Then, Eq. (29) can be written in the simplified form

$$r^2\frac{\partial^2\rho}{\partial r^2} + r\frac{\partial\rho}{\partial r} + \left[\frac{r^2\lambda^2}{c^2} - m^2\right]\rho = 0. \tag{30}$$

Obviously, the solution to Eq. (30) has the form

$$\rho = Z_m\left(\frac{\lambda}{c}r\right) = CJ_m(\mu r) + EN_m(\mu r),$$

where $\mu = \lambda/c$, C = const, and E = const.

Now, for the case under consideration, we use a procedure similar to that described above in the investigation of the effect of a potentially rotating flow on the acoustic resonance in a centrifugal pump. As a result, we obtain the impedance relation at the impeller inlet in the form

$$v_{k1}^r\left\{\frac{\sin\beta_2}{\sin\beta_1}\left(1-\frac{\tan kl}{ks_2}\right)\cos kl - \frac{c\sin kl}{\sin\beta_1}(\lambda+m\Omega)\frac{\tan(\mu h)\left[(\lambda\mu)^2 + \dfrac{(2\Omega m)^2}{\left(\frac{d_2}{2}+h\right)\frac{d_2}{2}}\right] - \lambda\mu\dfrac{2\Omega mh}{\frac{d_2}{2}\left(\frac{d_2}{2}+h\right)}}{\lambda(\lambda^2-4\Omega^2)\left[\lambda\mu - \dfrac{2\Omega m}{\frac{d_2}{2}+h}\tan(\mu h)\right]}\right\}$$

$$= iP_{k1}\left\{(\lambda+m\Omega)\frac{\tan(\mu h)\left[(\lambda\mu)^2 + \dfrac{(2\Omega m)^2}{\left(\frac{d_2}{2}+h\right)\frac{d_2}{2}}\right] - \lambda\mu\dfrac{2\Omega mh}{\frac{d_2}{2}\left(\frac{d_2}{2}+h\right)}}{\lambda(\lambda^2-4\Omega^2)\rho_0\left[\lambda\mu - \dfrac{2\Omega m}{\frac{d_2}{2}+h}\tan(\mu h)\right]}\left(1+\frac{\tan kl}{ks_1}\right)\cos kl\right. \tag{31}$$

$$\left. + \frac{\sin\beta_2}{\rho_0 c}\left(1+\frac{1}{k^2 s_1 s_2} - \frac{l}{ks_1 s_2}\cot kl\right)\sin kl\right\} + C\exp\left[-i\frac{\lambda+m\Omega}{\Omega}\right].$$

From Eq. (31) it follows that the condition for the resonance sound excitation in the pump is the zero value of the coefficient multiplying v_{k1}^r.

If, in the coefficient of v_{k1}^r, we retain the terms linear in the small parameters $\varepsilon_1 = (r\mu)^{-1}$ and $\varepsilon_2 = \dfrac{\Omega r}{c}$, we obtain the condition for resonance sound excitation in the pump for the case of solid-state rotation:

$$\frac{\sin\beta_2}{\sin\beta_1}\left(1-\frac{\tan kl}{ks_2}\right)\cos kl - \frac{(\lambda+m\Omega)}{\lambda}\frac{\sin kl}{\sin\beta_1}\tan(\mu h) = 0. \tag{32}$$

Using the dimensionless frequency of sound oscillations $\bar{\omega} = \omega l/c$, the dimensionless velocity of potential rotation $\bar{U}_{0p} = \dfrac{\Gamma}{cd_2/2}$, the dimensionless velocity of

Table 1. Resonance frequencies in the pump for a potential rotation of the liquid in the outlet

$m\bar{l}\bar{U}_{0p}$	Resonance frequency, $\bar{\omega}$									
0.05	2.50	3.72	4.71	5.65	6.88	7.85	8.80	10.03	10.99	11.94
0.5	2.51	3.67	4.71	5.69	6.85	7.85	8.82	10.00	10.99	11.96

Table 2. Resonance frequencies in the pump for solid-state rotation of the liquid in the outlet

$m\bar{l}\bar{U}_{0t}$	Resonance frequency, $\bar{\omega}$									
0.05	2.52	3.75	4.76	5.68	6.90	7.90	8.82	10.05	11.04	11.96
0.5	2.77	3.97	5.21	5.90	7.14	8.35	9.04	10.29	11.49	12.18

solid-state rotation $\bar{U}_{0t} = \dfrac{\Omega d_2/2}{c}$, the dimensionless length of the blade channel of the impeller $\bar{l} = \dfrac{l}{d_2/2}$, and the dimensionless height of the outlet $\bar{h} = h/l$, expressions (27) and (32) can be represented in the form

$$\frac{\sin\beta_2}{\sin\beta_1}\left(1 - \frac{\tan\bar{\omega}}{\bar{\omega}s_2/l}\right)\cos\bar{\omega}$$

$$- \frac{\tan(\bar{\omega}\bar{h})}{\left(1 - m\dfrac{\bar{U}_{0p}\bar{l}}{\bar{\omega}}\right)^2}\frac{\sin\bar{\omega}}{\sin\beta_1} = 0,$$

$$\frac{\sin\beta_2}{\sin\beta_1}\left(1 - \frac{\tan\bar{\omega}}{\bar{\omega}s_2/l}\right)\cos\bar{\omega}$$

$$- \frac{\tan\left(\bar{\omega}\left(1 - m\dfrac{\bar{U}_{0t}\bar{l}}{\bar{\omega}}\right)\bar{h}\right)}{\left(1 - m\dfrac{\bar{U}_{0t}\bar{l}}{\bar{\omega}}\right)}\frac{\sin\bar{\omega}}{\sin\beta_1} = 0.$$

Calculations with these formulas for $s_2/l = 2$, $\bar{h} = 1$, $\beta_2 = \pi/6$, $m\bar{U}_{0p}\bar{l} = 0.05$ and 0.5, and $m\bar{U}_{0t}\bar{l} = 0.05$ and 0.5 are presented in Tables 1 and 2. These calculations show that the potential rotation of the flow in the centrifugal pump outlet almost does not change the resonance frequencies values (the difference is less than 2%). In the case of solid-state rotation, there is a slight increase (by ~2 to ~10%) in the values of the resonance frequencies for the same increase in the flow velocity as in the case of the potential rotation.

REFERENCES

1. S. I. Perevoshchikov, Izv. Vyssh. Uchebn. Zaved., Neft' Gaz, No. 4, 50 (1997).
2. M. A. Mironov, Akust. Zh. **28**, 528 (1982) [Sov. Phys. Acoust. **28**, 310 (1982)].
3. D. Ronnenberger, J. Sound Vibr. **24** (1), 133 (1972).
4. A. S. Hersh, B. Walker, and M. Bucka, AIAA Pap., No. 78-1125 (1978).
5. M. S. Howe, J. Fluid Mech. **109**, 125 (1981).
6. P. M. Radavich, A. Selamet, and J. M. Novak, J. Acoust. Soc. Am. **109**, 1343 (2001).
7. B. V. Ovsyannikov and B. I. Borovskiĭ, *Theory and Calculation of Power Systems of Liquid-Propellant Rocket Engines* (Mashinostroenie, Moscow, 1986) [in Russian].
8. V. L. Khitrik, Akust. Zh. **46**, 698 (2000) [Acoust. Phys. **46**, 613 (2000)].

Translated by A. Svechnikov

Acoustical Physics, Vol. 51, No. 4, 2005, pp. 469–476. Translated from Akusticheskiĭ Zhurnal, Vol. 51, No. 4, 2005, pp. 550–557.

Diffraction Distortion of Surface Acoustic Waves in Crystals

V. I. Cherednick and M. Yu. Dvoesherstov

Lobachevski State University,
pr. Gagarina 23, Nizhni Novgorod, 603950 Russia
e-mail: Dvoesh@rf.unn.ru

Received March 17, 2003

Abstract—A method for the numerical modeling and visualization of the diffraction of surface acoustic waves propagating in anisotropic crystals is described. Examples of two-dimensional wave energy distributions are presented for some crystal orientations widely used in acoustoelectronics. © *2005 Pleiades Publishing, Inc.*

A theoretical analysis of the properties of surface acoustic waves (SAW) propagating in piezoelectric media is usually based on the assumption that the wave front is planar [1, 2]. However, an actual acoustic wave beam, which, as a rule, is excited by an interdigital transducer (IDT), has a finite cross-sectional dimension. Therefore, in the general case, a diffraction of the acoustic wave beam always takes place. If the distance between the IDTs exciting and receiving an electroacoustic surface wave is large, the energy loss owing to the diffraction of the acoustic beam may be considerable. Consequently, the problem of analyzing the diffraction distortion of surface acoustic waves propagating along the surfaces of various piezoelectric crystals and the problem of finding the "optimal" (from the point of view of minimal diffraction distortion) orientations for SAW in these media are important and urgent [1–6].

These problems can be solved using the methods employed in optics [7], i.e., considering the superposition of scalar secondary waves at the point of observation. As indicated in [1], the neglect of the vector character of oscillations is justified for two-dimensional diffraction problems, when the diffraction is considered only in the surface plane of the crystal and the depth dependence is ignored. The essential distinction of the diffraction in anisotropic crystals from the diffraction in optics consists in the fact that the velocity of a surface acoustic wave propagating in an anisotropic medium depends on the direction of propagation. If this dependence can be approximated by a parabola, the diffraction problem can be solved analytically [1, 2]. In the general case, numerical calculations are needed.

In this paper, we present the method and the results of numerical modeling of SAW diffraction in some cuts of quartz (SiO_2), lithium tantalate ($LiTaO_3$), and langasite (LGS) crystals. The amplitude of the resulting wave at an arbitrary point of the crystal surface was calculated as a superposition of waves arriving at this point from various points of the wave source. In this superposition, both plane and cylindrical waves were used. Both variants give practically the same profiles of the transverse amplitude distribution, but, in the case of cylindrical waves, the energy conservation law is additionally obeyed. The dependences of the SAW velocity on the propagation direction in SiO_2, $LiTaO_3$, and LGS piezoelectric crystals were calculated beforehand using the methods described in [8, 9]. The program for calculating the diffraction was done in the Borland C++ Builder visual programming environment. The results of the calculations were automatically passed to the Excel worksheet and were displayed as graphs of two-dimensional wave energy distributions. These graphs clearly show how various cuts and directions in piezoelectric crystals appear from the point of view of diffraction distortion of a SAW. These dependences also contain the quantitative information that allows one to calculate the propagation loss due to the diffraction divergence of an acoustic beam. The visualization of the results of calculation in the form of two-dimensional dependences of radiation energy on the coordinates distinguishes this work from the most recent papers on the same subject, where one-dimensional energy distributions in one coordinate (usually in the transverse one) for some fixed values of the other coordinate are presented (see, for instance, [1–5]). Two-dimensional distributions for quartz, lithium tantalate, and lithium niobate are presented in [6], but they refer to other conditions and orientations.

Let us consider the method for analyzing the diffraction divergence of an acoustic wave beam in more detail. The wave amplitude $A(X, Y)$ at an arbitrary point

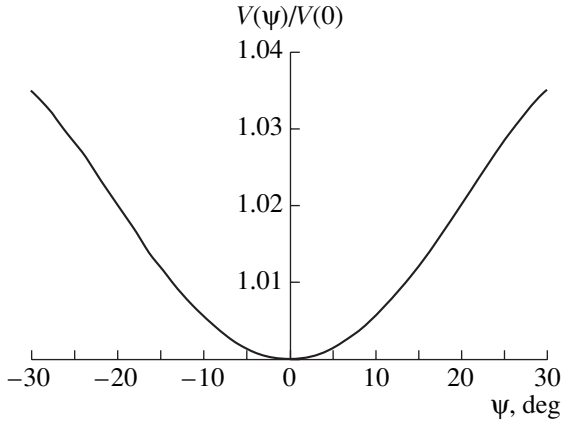

Fig. 1. Normalized phase velocity of a SAW as a function of the third Euler angle ψ in quartz with the (0°, 132.75°, ψ) orientation.

of a plane with the coordinates X, Y can be computed as a superposition of secondary waves [1–6]:

$$A(X, Y) = \int_{-a/2}^{a/2} A_0(Y')K(\alpha)G(R) \times \exp\left[i2\pi\frac{v(0)}{v(\alpha)}R\right]dY'. \quad (1)$$

Here, $X' = 0$, Y' are the coordinates of the source points, $A_0(0, Y')$ is the distribution of the secondary wave amplitude over the source (the input IDT), $G(R) = 1$ for plane waves, $G(R) = \frac{1}{\sqrt{R}}$ for cylindrical waves, $R = \sqrt{X^2 + (Y - Y')^2}$ is the distance from the source point to the point of observation, $\frac{v(\alpha)}{v(0)}$ is the dependence of the normalized phase velocity of a wave on the propagation direction α, $\alpha = \arctan\frac{Y - Y'}{X}$ is the angle of the propagation direction, a is the source width (the aperture), and $K(\alpha)$ is a function that equals unity at $\alpha = 0$ and monotonically decreases with increasing $|\alpha|$ (the simplest variant is $K(\alpha) = \cos(\alpha)$). In [1], the function $K(\alpha) \sim \sin(\alpha)/\alpha$ is used. All of the sizes are normalized by the wavelength λ.

The proposed method makes it possible to model the diffraction of pseudosurface waves as well. It is only necessary to take into account two additional factors: first, the pseudosurface waves attenuate along the direction of propagation and the attenuation coefficient depends on this direction, and, second, these waves do not exist for all spatial orientations. Some examples of the diffraction of pseudosurface acoustic waves are presented in [10]. In the present paper, we only consider the diffraction of surface waves.

The integration in Eq. (1) can be performed analytically if we suppose that $G(R) = 1$ (plane secondary waves), $A_0 = \text{const}$, and the dependence of the SAW velocity v on the direction of propagation is of a parabolic character:

$$\frac{V(\alpha)}{V(0)} = 1 + \frac{1}{2}\gamma\alpha^2. \quad (2)$$

The quantity γ involved in this expression is called the anisotropy parameter [1]. From the analytical theory, it follows that the optimal value of the anisotropy parameter is $\gamma = -1$. For this value of the anisotropy parameter, the diffraction divergence of the acoustic beam is absent and the beam profile remains unchanged at any distance from the aperture [1]. Although the parabolic approximation of the SAW velocity is not always valid, the anisotropy parameter is often used to estimate whether the calculated orientation of a piezoelectric crystal is optimal from the point of view of the diffraction distortion. The anisotropy parameter for an arbitrary specific orientation in a crystal can be calculated by the expression

$$\gamma = \frac{\partial(pfa)}{\partial\Psi}, \quad (3)$$

where

$$pfa = \arctan\left(\frac{1}{v}\frac{\partial v}{\partial\Psi}\right) \quad (4)$$

is the power flow angle.

Here, ψ is the third Euler angle, which determines the direction of SAW propagation in the crystal cut. The crystal cut is defined by the first (ϕ) and second (θ) Euler angles [11].

Note that, in an isotropic medium, the wave velocity does not depend on the propagation direction and the anisotropy parameter γ equals zero. In anisotropic crystals, the behavior of the wave phase velocity strongly depends on all of the three Euler angles determining the orientation in the crystal. For example, Fig. 1 shows the dependence of the normalized SAW phase velocity on the third Euler angle for ST-cut (0°, 132.75°, ψ) quartz in the vicinity of the X direction ($\psi_0 = 0$). The phase velocity is normalized to the velocity corresponding to $\psi_0 = 0$; i.e., this curve can be used for calculations by Eq. (1) ($\alpha = \psi - \psi_0$). Using Eqs. (3) and (4), from the curve given in Fig. 1 for the direction $\psi_0 = 0$, we obtain $\gamma = 0.38$. The positive value of γ corresponds to a greater diffraction divergence than that in the isotropic case; i.e., from the point of view of diffraction distortion, the ST-X quartz is worse than an isotropic medium. Figure 2 displays the calculated two-dimensional isolines of γ for a SAW in the space of the two Euler angles: θ = 0°–180° and Ψ = 0°–180°, at a fixed ϕ = 0° for (0°, θ, Ψ) quartz. As is seen from Fig. 2, there are a number of spatial orientations in which, according

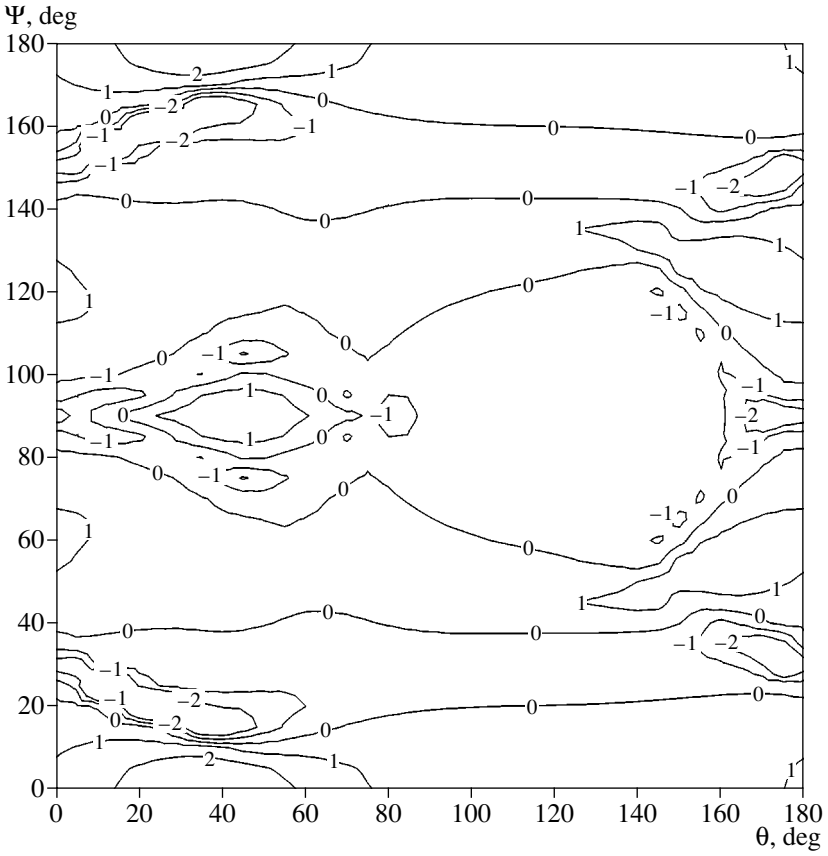

Fig. 2. Dependence of the anisotropy parameter γ on the second (θ) and third (ψ) Euler angles for quartz. The first Euler angle ϕ is equal to zero. The isolines of γ are shown only in the range from –2 to +2.

to the analytical theory, the diffraction distortion of SAW is absent ($\gamma = -1$).

The search for optimal spatial orientations for a SAW in a piezoelectric crystal also includes the following conditions: in the direction found, the SAW should have the minimal power flow angle ($pfa \approx 0$), minimal temperature coefficient of delay ($tcd \approx 0$), maximal electromechanical coupling coefficient (K^2), etc. [2]. The search for the optimal orientation consists in finding the minimum of the objective function Φ_c [12], which is a linear combination of the main parameters of the wave (*tcd*, *pfa*, K^2, γ, etc.) with the corresponding weight coefficients. As a result of such a search, the orientation determined by using the contour maps can be refined to yield the optimal orientation from the point of view of all of the main wave parameters. For instance, for quartz, such an orientation is the orientation near the Euler angles (0°, 45°, 24°). Figure 3 illustrates the dependence of the phase velocity for (0°, 45°, ψ) quartz in the neighborhood of the propagation direction $\psi_0 = 24°$. Near this direction, the velocity reaches its maximum and Eqs. (3) and (4) give $\gamma = -0.79$, which approaches the ideal value $\gamma = -1$. For this direction, $tcd = 0.2 \times 10^{-6}/°\mathrm{C}$, $K^2 = 0.13\%$, $pfa \approx 0$, and the phase velocity is $V = 3.626$ km/s.

If the phase velocity curve for the propagation direction ψ_0 does not have an extremum, then, along with the beam divergence, beam deflection takes place ($pfa \neq 0$).

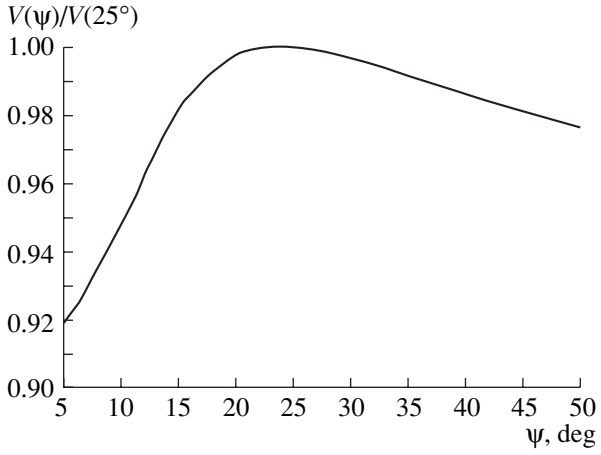

Fig. 3. Normalized phase velocity of a SAW as a function of the third Euler angle ψ in quartz with the (0°, 45°, ψ) orientation.

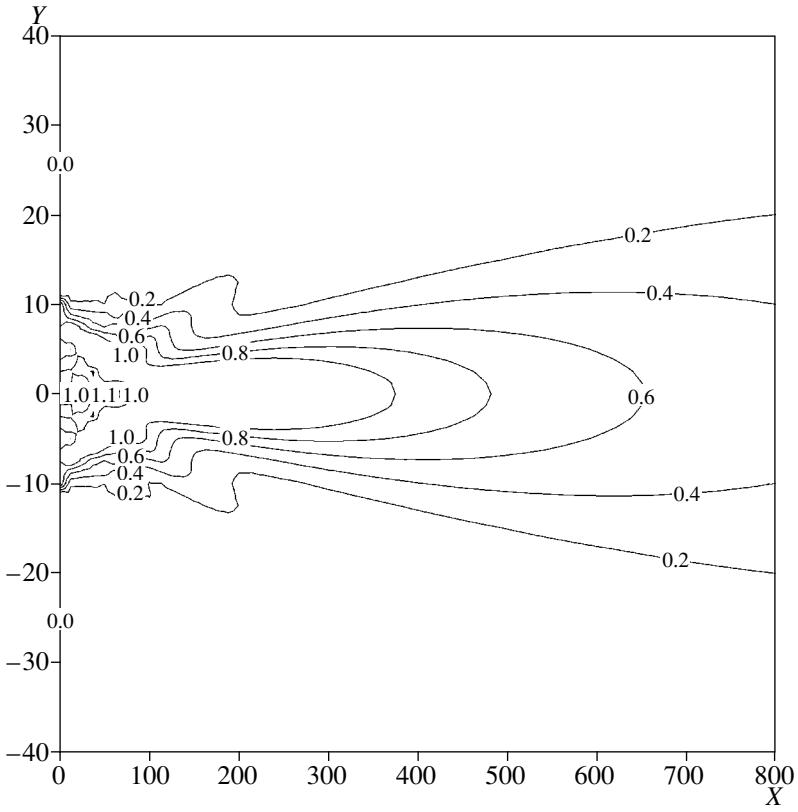

Fig. 4. Isotropic medium, $\gamma = 0$.

For example, in the commonly used orientation of ST + 25 (0°, 132.75°, 25°) quartz, the power flow angle is *pfa* = 5° (see Fig. 1, $\psi_0 = 25°$).

To calculate integral (1), it is necessary first to calculate the wave phase velocity in the angle interval $\Psi_0 \pm 90°$. The values obtained for v were used in the form of tables with a small step in the range from $\psi_0 - 90°$ to $\psi_0 + 90°$. The values at the intermediate points were determined using a linear interpolation.

In the calculation of integral (1), both plane and cylindrical secondary waves were used. Both types of secondary waves gave practically the same profiles of the energy distribution along the transverse *Y* coordinate, but plane waves did not ensure a decrease in the wave amplitude with distance from the source; i.e., they did not satisfy the energy conservation law. They give an incorrect distribution along the *X* propagation direction and do not allow one to obtain a two-dimentional image of the energy distribution. In this case, it is possible to obtain a correct result by applying a special normalization procedure on every line *X* = const. Then, both types of secondary waves give practically the same two-dimensional distributions of wave energy. Some of these distributions are displayed in Figs. 4–9. In all cases, A_0 = const and the aperture is equal to 20 wavelengths. Figures 4–9 show the normalized values of $|A(X, Y)/A_0|^2$, which are proportional to the wave energy.

Figure 4 displays the distribution corresponding to an isotropic medium ($\gamma = 0$). Figures 5–9 represent the energy distributions for the surface acoustic waves corresponding to certain known cuts and orientations in some of the widely used crystals. Figure 5 shows the diffraction pattern for ST-*X* (0°, 132.75°, 0°) quartz. The comparison with Fig. 4 shows that this widely used thermostable cut is rather poor from the point of view of the diffraction divergence. This is caused by the behavior of the SAW velocity in the neighborhood of the propagation direction (the corresponding curve has a minimum). For large distances between IDTs, this orientation is inappropriate. Figure 6 shows the energy distribution for ST + 25 (0°, 132.75°, 25°) quartz. This orientation corresponds to a particular phase relation between the electric potential and the longitudinal displacement of the wave, and, therefore, it can be used for unidirectional IDTs (NSPUDT) [13]. For this orientation, Eqs. (3) and (4) yield $\gamma = -0.22$ and the diffraction divergence is smaller than that in an isotropic medium; however, a 5° deflection of the beam takes place, because the phase velocity curve contains no extremum for this direction. Figure 6 clearly shows how the input and output IDTs should be positioned with respect to each other to avoid energy loss due to this deflection.

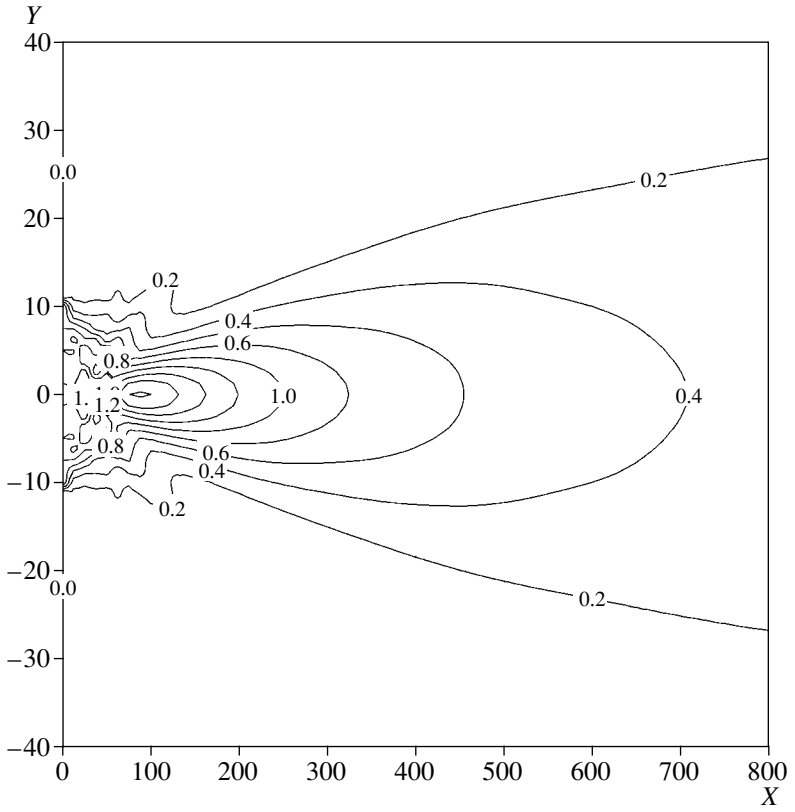

Fig. 5. Quartz with the (0°, 132.75°, 0°) orientation, $\gamma = 0.38$.

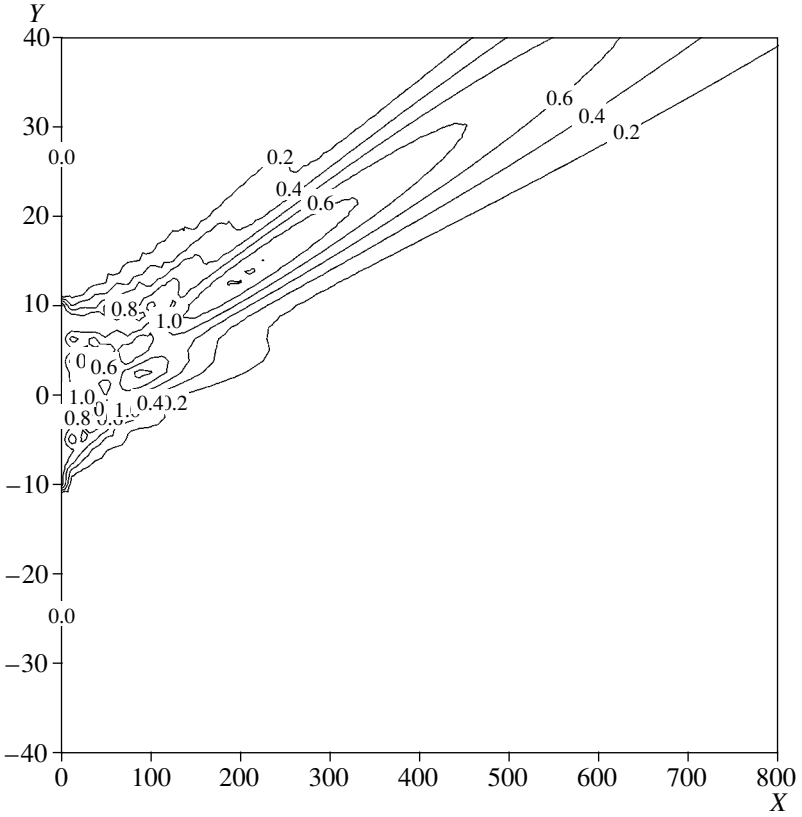

Fig. 6. Quartz with the (0°, 132.75°, 25°) orientation, $\gamma = -0.22$.

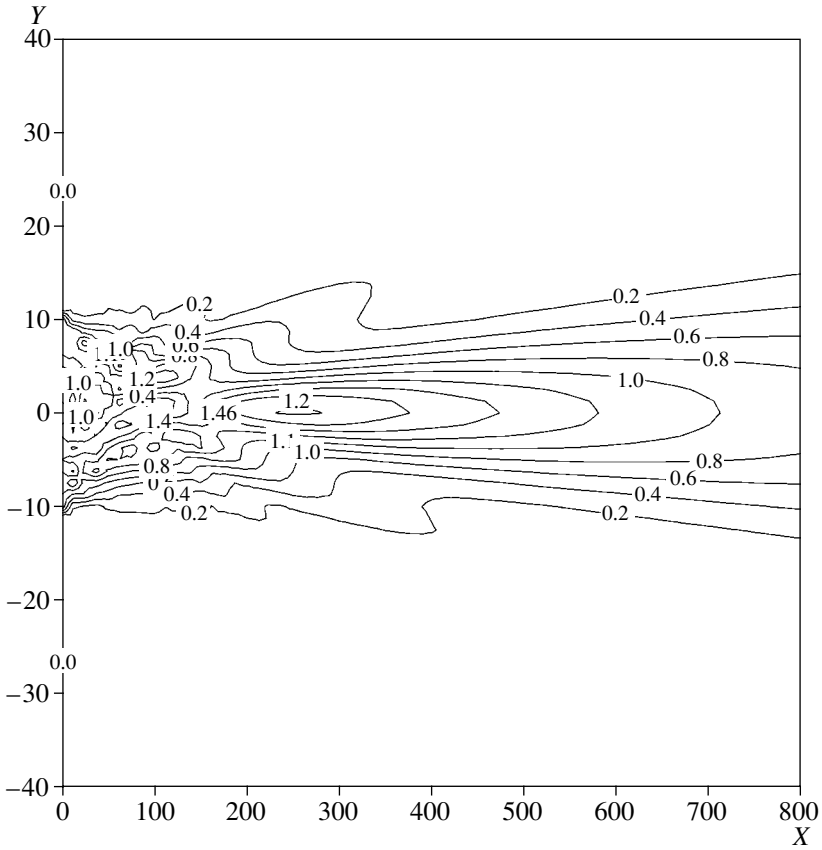

Fig. 7. Quartz with the (0°, 45.1°, 23.95°) orientation, $\gamma = -0.79$.

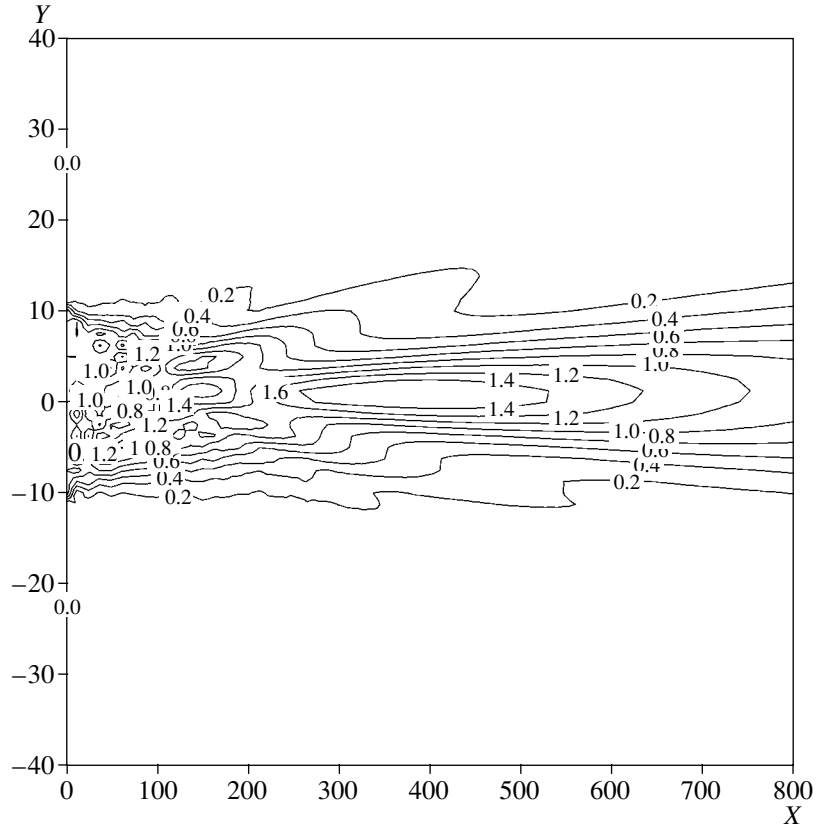

Fig. 8. LGS with the (0°, 140°, 25°) orientation, $\gamma = -1.48$.

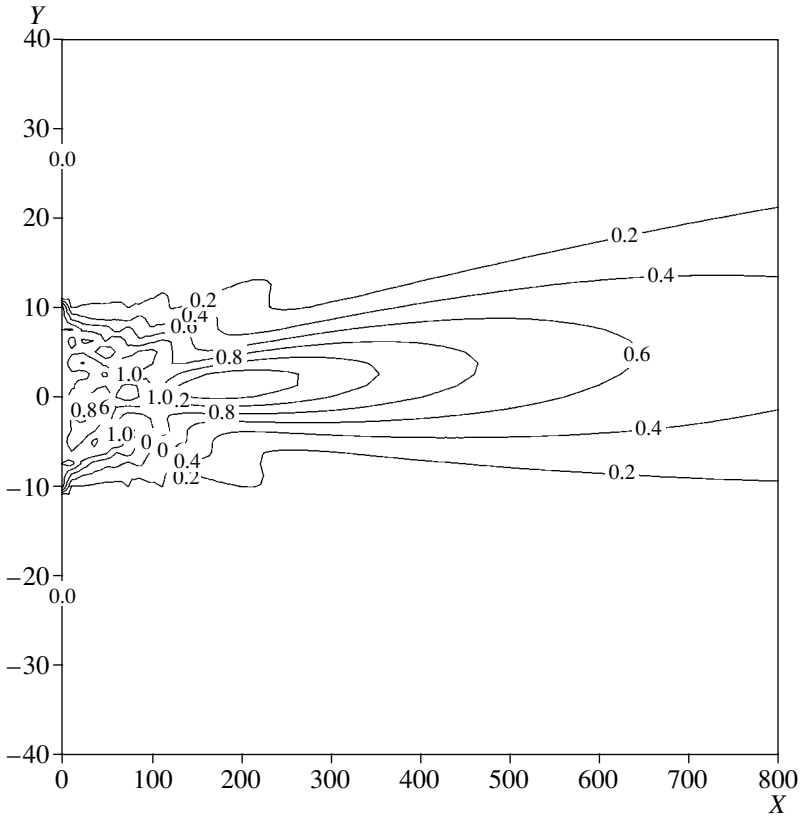

Fig. 9. $LiTaO_3$ with the (90°, 90°, 112°) orientation, $\gamma = -0.3$.

Figure 7 presents the diffraction pattern for a quartz of the (0°, 45.1°, 23.95°) orientation. In the vicinity of this orientation, a SAW has parameters that are close to the optimal ones, in particular, a high thermal stability and a zero power flow angle (the velocity curve has a maximum, see Fig. 3). In addition, for this direction, the anisotropy parameter is $\gamma = -0.79$ and the diffraction divergence is relatively small.

Figure 8 displays the energy distribution for (0°, 140°, 25°) LGS. Near this orientation, all of the wave parameters for this crystal are very good ($v = 2.744$ km/s, $tcd \approx 0$, $K^2 = 0.36\%$, $pfa \approx 0.1°$, and $\gamma = -1.48$). The diffraction divergence is fairly small, as is seen from Fig. 8. However, an asymmetry of the wave beam arises because of the asymmetry of the phase velocity curve near this direction. The material constants for langasite (LGS) were taken from [14].

Finally, Fig. 9 shows the diffraction pattern for (90°, 90°, 112°) $LiTaO_3$. The anisotropy parameter is $\gamma = -0.3$. As is seen from Fig. 9, the wave beam has a small diffraction divergence, but it exhibits a slight deflection, because this direction does not exactly correspond to the maximum of the phase velocity curve ($pfa = 1.2°$). The material constants for $LiTaO_3$ were taken from [15].

Thus, in this paper, we described a method for calculating and visualizing the two-dimensional energy distribution of a propagating surface acoustic wave, which allows one to obtain visual diffraction patterns for any orientation of a piezoelectric crystal of any crystallographic symmetry class. This makes it possible to evaluate different crystal orientations from the point of view of the diffraction loss and the loss associated with the deflection of the power flux of the acoustic beam. In addition, from these distributions, quantitative data can be obtained for calculating the diffraction loss.

REFERENCES

1. *Acoustic Surface Waves*, Ed. by A. A. Oliner (Springer, New York, 1978; Mir, Moscow, 1981).
2. *Surface Wave Filters: Design, Construction and Use*, Ed. by H. Mathews (Wiley, New York, 1977; Radio i Svyaz', Moscow, 1981).
3. R. Milsom, *Proc. IEEE Ultrason. Symp*. (1977), pp. 827–833.
4. G. Kerber and G. Alsup, *Proc. IEEE Ultrason. Symp*. (1977), pp. 834–839.
5. I. Streibl, B. Syrett, and M. Suthers, *Proc. IEEE Ultrason. Symp*. (1983), pp. 62–65.
6. A. Ronnekleiv, *Proc. IEEE Ultrason. Symp*. (2000), pp. 219–222.

7. G. S. Gorelik, *Oscillations and Waves* (Fizmatgiz, Moscow, 1959) [in Russian].
8. M. Yu. Dvoesherstov, V. I. Cherednik, and A. P. Chirimanov, Izv. Vyssh. Uchebn. Zaved. Radiofiz. **43**, 801 (2000).
9. M. Yu. Dvoesherstov, V. A. Savin, and V. I. Cherednik, Akust. Zh. **47**, 847 (2001) [Acoust. Phys. **47**, 682 (2001)].
10. V. I. Cherednick and M. Yu. Dvoesherstov, in *Procceedings of 16 European Frequency and Time Forum, 2002* (St. Peterburg, 2002), p. C107.
11. M. P. Shaskol'skaya, *Acoustic Crystals* (Nauka, Moscow, 1982) [in Russian].
12. M. Yu. Dvoesherstov, S. G. Petrov, V. I. Cherednik, *et al.*, Zh. Tekh. Fiz. **72** (8), 103 (2002) [Tech. Phys. **47**, 474 (2002)].
13. T. Thorvalsson, *Proc. IEEE Ultrason. Symp*. (1989), pp. 820–826.
14. Yu. Pisarevsky, P. Senushencov, B. Mill, *et al.*, *Proc. IEEE International Freq. Control Symp*. (1998), pp. 742–747.
15. G. Kovacs, M. Anhorn, H. Engan, *et al.*, *Proc. IEEE Ultrason. Symp*. (1990), pp. 435–438.

Translated by A. Svechnikov

Acoustical Physics, Vol. 51, No. 4, 2005, pp. 477–478. Translated from Akusticheskiĭ Zhurnal, Vol. 51, No. 4, 2005, pp. 558–559.

DISCUSSION

On the Noise Immunity of a Combined Hydroacoustic Receiver

M. D. Smaryshev

Morfizpribor Central Research Institute, Chkalovskiĭ pr. 46, St. Petersburg, 197376 Russia

e-mail: mfp@mail.wplus.net

Received December 22, 2003

The authors of [1] study the gain (usually called the noise immunity factor in the Russian literature on acoustics) of a combined receiver that consists of a three-component pickup for the particle velocity and a sound pressure detector. The paper states that, in the case of multiplicative processing of signals obtained from the pressure detector and the particle velocity pickup, the noise immunity factor tends to infinity in an isotropic noise field, while, in an actual field of ambient sea noise, it reaches (15–30) dB. These conclusions seem to be questionable.

When the signals of particle velocity pickups oriented along the *X*, *Y*, and *Z* axes are subjected to an additive summation with some real coefficients a_x, a_y, and a_z, the non normalized directivity pattern of the three-component pickup of particle velocity has the form

$$R(\theta, \varphi) = a_x R_x(\theta, \varphi) + a_y R_y(\theta, \varphi) + a_z R_z(\theta)$$
$$= a_x \sin\theta\cos\varphi + a_y \sin\theta\sin\varphi + a_z \cos\theta.$$

Without loss of generality, one can assume that $a_x^2 + a_y^2 + a_z^2 = 1$. Then, as is known, the expression on the right-hand side of the above equation represents the cosine of the angle θ' between two directions, one of which (the current one) is determined by the angles θ, φ while the other has the direction numbers equal to a_x, a_y, and a_z; i.e., the latter direction is determined by the angles θ_0, φ_0 satisfying the relations $\sin\theta_0\cos\varphi_0 = a_x$, $\sin\theta_0\sin\varphi_0 = a_y$, and $\cos\theta_0 = a_z$, which yield $\varphi_0 = \arctan(a_y/a_x)$ and $\theta_0 = \arcsin(a_x^2/a_y^2)^{0.5}$. In other words, the directivity pattern of the three-component particle velocity pickup is described by the function $\cos\theta'$ and has a maximum in the direction θ_0, φ_0. In the particular case of $a_x = a_y = a_z$, the angles are $\varphi_0 = 45°$ and $\theta_0 = 55°$ and the symmetry axis of the directivity pattern makes identical angles approximately equal to 55° with the *X*, *Y*, and *Z* axes.

Thus, the directivity pattern of a three-component particle velocity pickup differs from the directivity pattern of a one-component pickup in only its orientation in space. Therefore, the noise immunity of a combined receiver does not depend on the number of its component particle velocity pickups if the direction of the maximum of its directivity pattern coincides with the direction of the signal arrival. The noise immunity factor of a combined receiver consisting of one particle velocity pickup and one pressure sensor has been comprehensively studied (not only for the case of multiplicative processing) in [2–4] and other publications. The results of these studies showed that, in the operation of combined receivers, both single and in arrays, in both isotropic and anisotropic noise fields, in a free medium or in the presence of baffles, the use of multiplicative processing for the output signals of the pressure and particle velocity channels in most cases leads to a decrease in the noise immunity factor. For example, as stated in [1], a single multiplicative combined receiver consisting of a pressure detector and a particle velocity pickup and operating in an isotropic noise field has a noise immunity factor equal to 2.4 (instead of infinity), whereas, in the case of an additive scheme of data processing, this factor is equal to 3.

The authors of [1] proceed from the fact that the directivity pattern of a three-component particle velocity pickup is written in the form

$$R(\theta, \varphi) = R_x^2(\theta, \varphi) + R_y^2(\theta, \varphi) + R_z^2(\theta)$$
$$= \sin^2\theta\cos^2\varphi + \sin^2\theta\sin^2\varphi + \cos^2\theta = 1;$$

i.e., it is omnidirectional.

To obtain such a directivity pattern, the output signals of the particle velocity pickups should presumably be subjected to a certain processing, for example, to a quadratic detection. In this case, the authors of [1] should not estimate the noise immunity by using the formula from [2] (a detailed derivation of this formula is given in [4]). This formula determines the threshold ratio at the output of a multiplicative detector only in the case of multiplication of normal random processes with zero means. Precisely the inappropriate use of this formula in the case under discussion has led to the conclusion that the noise immunity factor of a combined receiver operating in an isotropic noise field can be infinitely large. The same formula was used by the authors of [1] to obtain the expressions for processing the experimental data.

1063-7710/05/5104-0477$26.00

In the context of the above comments, the results reported in [1] (both theoretical results and experimental ones processed on their basis) cannot be used to evaluate the noise immunity and efficiency of the detection modes of hydroacoustic systems.

REFERENCES

1. V. A. Shchurov and A. V. Shchurov, Akust. Zh. **48**, 110 (2002) [Acoust. Phys. **48**, 98 (2002)].
2. M. D. Smaryshev and E. L. Shenderov, Akust. Zh. **31**, 502 (1985) [Sov. Phys. Acoust. **31**, 296 (1985)].
3. A. V. Pesotskiĭ and M. D. Smaryshev, Akust. Zh. **35**, 495 (1989) [Sov. Phys. Acoust. **35**, 289 (1989)].
4. E. L. Shenderov, in *Hydroacoustics* (St. Petersburg, 2002), No. 3, p. 24 [in Russian].

Translated by E. Golyamina

Acoustical Physics, Vol. 51, No. 4, 2005, p. 479. Translated from Akusticheskiĭ Zhurnal, Vol. 51, No. 4, 2005, pp. 560–561.

DISCUSSION

Reply to the Letter Written by Smaryshev

V. A. Shchurov

Il'ichev Pacific Institute of Oceanology, Far-East Division, Russian Academy of Sciences, ul. Baltiĭskaya 43, Vladivostok, 690041 Russia

e-mail: shchurov@poi.dvo.ru

Received February 16, 2004

The problem of noise immunity of a single combined receiver has been being discussed since the 1960s. The literature devoted to this subject is quite voluminous. In [1–4], one can find a variety of references concerning this issue. In our paper [1], unlike preceding papers, we presented an estimate of the noise immunity of a combined receiver on the basis of results obtained from a field experiment in a deep open ocean. We also performed a theoretical analysis of the mechanism governing the formation of the signal-to-noise ratio for energy density and orthogonal components of energy flux in a partially coherent field of dynamic noise. Two cases were considered for partially coherent dynamic noise: with a prevailing diffusive noise component and with a prevailing coherent noise component.

In [1], we described a four-component combined receiver consisting of a scalar omnidirectional pressure detector and a three-component vector receiver. Smaryshev, in his letter, analyzes the nonnormalized directivity pattern of a three-component particle velocity receiver: $R(\theta, \varphi) = a_x \sin\theta\cos\varphi + a_y \sin\theta\sin\varphi + a_z \cos\theta$. Since, in the case under consideration, the characteristic $R(\theta, \varphi)$ is nonnormalized, the coefficients a_x, a_y, and a_z have a physical meaning: they represent the sensitivities of the x, y, and z channels with the corresponding physical dimension. Then, what does the relation $a_x^2 + a_y^2 + a_z^2 = 1$ presented in Smaryshev's letter mean? In experimental underwater acoustics, the relation proposed by Smaryshev is never used and has no actual physical meaning. The cardioid pattern of combined receivers had been successfully used for years in actual underwater systems [2]. In [1], we presented the normalized characteristic of a four-component combined receiver in the form $R(\theta, \varphi) = R_x^2(\theta, \varphi) + R_y^2(\theta, \varphi) + R_z^2(\theta) = 1$. This expression suggests that the sensitivity characteristic of a four-component combined receiver is a sphere. However, this characteristic of sensitivity has nothing to do with the multiplicative data processing performed by us in [1], which was not taken into account by Smaryshev.

It is unclear which of the results of our study [1] has caused the following comment by Smaryshev: "…the noise immunity factor in an isotropic noise field… reaches (15–30) dB in the actual field of ambient sea noise. These conclusions seem to be questionable." Here, it is necessary to note that we considered the situation not "in an isotropic noise field" (as Smaryshev writes) but in a diffusive field. These cases essentially differ from each other from the physical point of view. Besides, we wrote not "(15–30) dB" but "(15–16) dB" in a diffusive field in the horizontal plane and up to 30 dB in the case of the compensation of opposing energy fluxes in the vertical plane [1, 4]. We would like to see a more specific criticism, namely, which part of [1] represents incorrect studies (i.e., is "questionable"): the processing of the field-experiment data or the theoretical calculation of the combined receiver gain? If Smaryshev's conclusions are only based on the inappropriate use of formula (3) in [1], these conclusions are wrong in the case under discussion, because the signals from the channels of the combined receiver were not subjected to "quadratic detection" but, as was indicated in [1], the multiplicative processing was applied to Gaussian random processes with zero means, which agrees well with [3]. In closing, it should be noted that the approach represented in [1] has been successfully used for years in solving practical problems of underwater acoustics (see, e.g., [2]) despite the fact that many theoretical acousticians in Russia consider it to have no potential.

REFERENCES

1. V. A. Shchurov and A. V. Shchurov, Akust. Zh. **48**, 110 (2002) [Acoust. Phys. **48**, 98 (2002)].
2. G. L. D'Spain, W. S. Hodgkiss, G. L. Edmonds, *et al.*, in *Proceedings of Mastering the Oceans Through Technology (Oceans'92)* (Newport, Rhode Island, 1992), p. 346.
3. M. D. Smaryshev and E. L. Shenderov, Akust. Zh. **31**, 502 (1985) [Sov. Phys. Acoust. **31**, 296 (1985)].
4. V. A. Shchurov, *Vector Acoustics of the Ocean* (Dal'nauka, Vladivostok, 2003) [in Russian].

Translated by E. Golyamina

1063-7710/05/5104-0479$26.00

Acoustical Physics, Vol. 51, No. 4, 2005, pp. 480–481. Translated from Akusticheskiĭ Zhurnal, Vol. 51, No. 4, 2005, pp. 562–563.

CHRONICLE

In Memory of L.M. Brekhovskikh (May 6, 1917–January 15, 2005)

On January 15, 2005, Academician Leonid Maksimovich Brekhovskikh—an outstanding Russian scientist, the founder of ocean acoustics as a new field of research in oceanology, and Counselor of the Presidium of the Russian Academy of Sciences—passed away at the age of 87.

Brekhovskikh was born on May 6, 1917, in Strunkino (a village near Arkhangel'sk) to a peasant family. There, he spent his first school years, and his eight-year school education was completed in Krasnoural'sk in 1934. To continue his education, Brekhovskikh entered Perm State University, from which he graduated with honors in 1939, and then became a postgraduate student of the Lebedev Physical Institute of the Academy of Sciences of the USSR. In October 1941, Brekhovskikh received his candidate degree for a work entitled *Theory of X-Ray Scattering in Crystals.*

The talent of the young scientist became evident during World War II, when he worked with a research group headed by Corresponding Member of the Academy of Sciences of the USSR N.N. Andreev on the development of acoustic minesweepers. For this purpose, one would apply the empirical trial-and-error method to form an appropriate acoustic imitator. However, Brekhovskikh decided to carry out a comprehensive analysis of the problem. He calculated the oscillations of plates forming the skin of a ship. The calculations allowed him to choose the sort of plates and the type of their fastening and excitation, so that, finally, he developed the first minesweeper imitating the noise of an actual vessel. Within four months after the beginning of the project, the first working imitator model was presented to the navy, and the device was soon successfully tested in action.

The late 1940s and the early 1950s were the period of Brekhovskikh's best work in theoretical science. In particular, he proposed a method for solving the problem of wave scattering by rough surfaces whose characteristic roughness scale was large compared to the sound (or electromagnetic) wavelength, which was called the "tangential plane approximation." This problem could not be solved for almost 50 years after it was first formulated by Rayleigh. Brekhovskikh's work aroused great interest and stimulated numerous publications in both Russia and abroad on the scattering of waves of different nature. In 1946, after analyzing the results of experiments carried out in the Sea of Japan by Rozenberg and Sigachev in cooperation with navy engineers, Brekhovskikh discovered the presence of the underwater sound channel. In subsequent years, he comprehensively studied this phenomenon both theoretically and in field experiments. The results of these studies were of fundamental importance for the development of underwater acoustics, including the theory of wave propagation in the ocean and various practical applications.

In 1947, Brekhovskikh received his doctoral degree for a theoretical work on the propagation of acoustic and electromagnetic waves in layered media. This work, which was presented in his doctoral dissertation under the title *Propagation of Sound and Radio Waves in Layers*, brought him a Papaleksi Award in 1948. In 1951, for the discovery of the underwater sound channel, Brekhovskikh and his colleagues received a Stalin Award of the first degree. In 1953, Brekhovskikh received the title of Professor and was elected Corresponding Member of the Academy of sciences of the USSR. In the same year, Brekhovskikh took part in organizing the Acoustics Institute of the Academy of Sciences of the USSR and became its first director (until 1962).

In the late 1950s, Brekhovskikh supervised the development of the Rubin long-range hydroacoustic system for nuclear-powered submarines. This work was carried out with the participation of leading scientists from the Acoustics Institute and the best engineers from

1063-7710/05/5104-0480$26.00

the Leningrad Research Institute-3 (today, the Morfizpribor Central Research Institute). For the first time, with the use of the underwater sound channel properties and wide-aperture arrays, the range of hydroacoustic systems could be increased by an order of magnitude. For this work, Brekhovskikh together with the leading researchers and engineers from other organizations received a Lenin Prize in 1970.

Brekhovskikh invited many gifted young physicists and engineers to work at the Laboratory of Acoustic Studies of the Ocean, which was organized at the Acoustics Institute. These scientists formed the basis of his scientific school: N.S. Ageeva, I.B. Andreeva, O.P. Galkin, Yu.Yu. Zhitkovskiĭ, B.F. Kur'yanov, I.E. Mikhal'tsev, A.V. Furduev, S.D. Chuprov, R.F. Shvachko, and others. Together with the young scientists in the laboratory, Brekhovskikh carried out many expeditions on the unique research vessels of the Acoustics Institute, *Sergeĭ Vavilov* and *Petr Lebedev*, in different regions of the ocean. The expeditions allowed Brekhovskikh to test his theoretical results in practice. Some of the researchers from the Laboratory of Acoustic Studies of the Ocean became coauthors of the well-known monograph *Ocean Acoustics*, for which they received a State Award in 1976.

Brekhovskikh also was widely known for his many-sided scientific, pedagogical, and organizational activities. In 1963–1969, he represented Soviet acousticians at the International Acoustical Commission. In 1964–1967, he was a member of the Bureau of the International Geophysical Association in Physical Oceanology. Over many years, he chaired the Oceanographic Commission (later, the Scientific Council on the Ocean) at the Presidium of the Academy of Sciences of the USSR. From 1966 to 1969, he chaired the Scientific Council on Acoustics of the Academy of Sciences of the USSR. In 1968, he was elected Full Member of the Academy of Sciences of the USSR, and, in 1969, he became Academician-Secretary of the Division of Oceanology, Atmospheric Physics, and Geography. He headed this division until 1991. In 1970, Brekhovskikh supervised the Poligon-70 hydrophysical experiment carried out in the Atlantic Ocean. This experiment resulted in one of the most significant discoveries made in the Earth sciences in the 20th century, namely, the discovery of oceanic synoptic vortices, which contain more than 90% of the kinetic energy of oceanic waters. This discovery profoundly changed the understanding of the dynamics of waters in the ocean.

Over twenty years, starting in 1975, Brekhovskikh chaired the Department of Hydrospace at the Moscow Institute of Science and Technology. Many well-known Russian acousticians working in Russia and abroad were educated at this department. In 1977, Brekhovskikh was elected Member of the Polish Academy of Sciences, and, in 1978, he was awarded a Rayleigh Gold Medal of the Institute of Acoustics of Great Britain (the most distinguished international award for acousticians) for the discovery of the underwater sound channel. In 1986, he received the Karpinsky Prize—an international prize established to mark scientific achievements in the fields especially important for the future of mankind. In 1991, Brekhovskikh was elected Foreign Member of the National Academy of Sciences of the United States. In 1999, he received the title of Honored Member of the Acoustical Society of America "for his pioneering works on the propagation and scattering of waves." He also became the first Honored Member of the Russian Acoustical Society.

In 1980, Brekhovskikh organized the Department of Ocean Acoustics at the Oceanology Institute of the Academy of Sciences of the USSR and became head of this department. He moved there with a small group of his students and colleagues from the Acoustics Institute. Thus, Brekhovskikh established one more research center for the study of sound propagation in the ocean. Brekhovskikh's Workshop in Ocean Acoustics is a widely known regular event, and the proceedings of the Workshop are fairly popular among acousticians. The "acoustic" research vessels of the Academy of sciences of the USSR, *Akademik Sergeĭ Vavilov* and *Akademik Ioffe*, were constructed under Brekhovskikh's supervision. Brekhovskikh took active part in the expeditions carried out on these vessels as well.

Brekhovskikh's services to Russian science were highly appraised by the government: he received the Lenin Prize and the USSR State Award, was given the title of Hero of Socialist Labor, and was awarded the Order of Lenin (three times), the Order of the Red Banner of Labor, and the Order for the Services to the Country of the third degree.

Leonid Maksimovich Brekhovskikh will remain in the memory of his students and colleagues as a prominent theoretical scientist and a tactful supervisor and teacher. The books written by Brekhovskikh alone or together with his colleagues (Yu.P. Lysanov, V.V. Goncharov, and O.A. Godin) and, especially, his popular monograph *Waves in Layered Media* have become handbooks for several generations of specialists in hydroacoustics. For Brekhovskikh, the best reward was his numerous works and the sincere love and shining memory that will last in the hearts of those who knew him. The life of Academician L.M. Brekhovskikh is a bright example of utter devotion to his country and to the ideas of honor, goodness, and justice.

Translated by E. Golyamina

Acoustical Physics, Vol. 51, No. 4, 2005, pp. 482–483. Translated from Akusticheskiĭ Zhurnal, Vol. 51, No. 4, 2005, pp. 564–565.

CHRONICLE

In Memory of A.M. Dykhne (October 27, 1933–January 6, 2005)

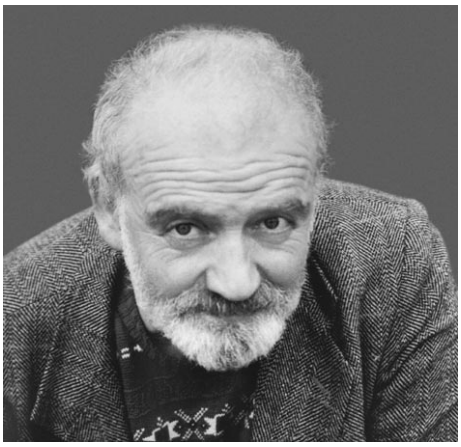

Academician Aleksandr Mikhaĭlovich Dykhne—director of the Center of Theoretical Physics and Computational Mathematics of the State Research Center Troitsk Institute for Innovation and Thermonuclear Research—died unexpectedly on January 6, 2005.

Dykhne was born on October 27, 1933, in Moscow. He was educated at the Kiev Polytechnical Institute and began his career as an engineer at integrated iron and steel works in Siberia. After the establishment of the Siberian Division of the Academy of Sciences of the USSR, Dykhne changed his work place to the Institute of Radio Physics and Electronics organized in Novosibirsk by Yu.B. Rumer, who immediately understood the potential of the young metallurgical engineer as a talented theoretical physicist.

Dykhne simultaneously worked in several fields of research: electrodynamics (the theory of horn antennas), statistical physics (the Ising–Onsager two-dimensional dipole lattice), and quantum mechanics (adiabatic transitions). In connection with the development of magnetic traps for controlled thermonuclear synthesis, Dykhne calculated the change in the adiabatic invariant of a charged particle in such a trap. The solution to the problem of transitions in a two-level system under an adiabatic perturbation is known as the Landau–Dykhne formula. L.D. Landau, a reviewer of the Dykhne's candidate dissertation, appreciated the talent of the author. The degree of candidate of science was received by Dykhne in 1960.

In 1962, Dykhne returned to Moscow and began working at the Kurchatov Institute of Atomic Energy. In the following years, he worked in such fields of science as quantum mechanics, plasma physics, solid state physics, astrophysics, biophysics, laser physics, and laser technologies.

Dykhne is the author of more than 150 papers, two books, one discovery, and a number of inventions covered by Russian and foreign patents. In 1987, Dykhne was elected corresponding member and, in 1992, full member of the Russian Academy of Sciences.

Russian acoustics owes much to Dykhne for his scientific achievements and for his organizational activities in science. He was an active member of the Scientific Council on Acoustics of the Russian Academy of Sciences. In 1992–2001, he chaired the Expert Council in Physics of the Supreme Certification Commission. In 1994–2000, Dykhne chaired the Expert Council of the Russian Foundation for Basic Research, and, beginning in 2000, he was a member of the Bureau of the Council of the Russian Foundation for Basic Research. Simultaneously, he worked as a member of the Bureau of the Division of Physical Sciences of the Russian Academy of Sciences. Working in all these organizations during years that were difficult for Russian science, Dykhne actively supported basic research in acoustics; he called special attention to the burning problems of this field of science and promoted additional financial support for research.

Dykhne published several remarkable works in acoustics, which were characterized by fundamentally new ideas and elegant theoretical representations. He proposed the method of excitation of large-amplitude surface elastic waves by a moving laser beam and predicted the effect of the group resonance that allowed a selective excitation of these waves. Dykhne suggested the use of the noise correlation functions of higher orders to extract information on the internal structure of bodies. One of this most important achievements was the discovery of "self-dual" inhomogeneous media and new physical phenomena in such media. Exact expressions were found for the conductivity of thin microinhomogeneous films of the metal–dielectric type, the parameters of composites and polycrystalline media were calculated, and the theory of the fractional Hall effect and wave scattering by a rough surface was developed. Similar results were obtained in acoustics and in the theory of elasticity of inhomogeneous media. Strong fluctuations caused by the presence of broadband resonances in "Dykhne media" were observed experimentally, as well as the strong scattering of waves and the flicker noise.

1063-7710/05/5104-0482$26.00

The methods developed by Dykhne in solid state physics were applied to molecular biology. On their basis, the theory of "melting" of a DNA molecule was developed, and the specificity of the thermodynamics of ring biopolymers was studied. The results of the long-term studies of biological problems have found application in such an important area as medicine design, the appearance of which is largely due to the efforts by Dykhne.

Dykhne developed a hydrodynamic model of the resonant radiation transfer in gases. The dominant role of smooth trajectories in the gamma-radiation transfer in heterogeneous media, which followed from this model, served as the key idea in analyzing the radioactive radiation flows from the Chernobyl "sarcophagus." A related problem was the detection of a set of instabilities of waves of self-sustained melting under the effect of residual heat of radioactive sources, which was called the "Chinese syndrome."

Although Dykhne was a theoretical physicist, he generated numerous ideas that were realized experimentally. His great experience and unique intuition allowed him to create new technologies, materials, and instruments and to discover new physical effects.

Dykhne took active part in international cooperation. He headed the Expert Committee of the program "Fundamental Science and Higher Education," which was organized by the Ministry of Education of Russia and the Civil Research and Development Foundation of America with the aim to establish modern centers of scientific education in Russia. He supervised a research project that was included in the international cooperation program "Russian Academy of Sciences–Department of Energy of the USA," which was aimed at improving the safety of radioactive burials in different countries, especially, in Russia.

Dykhne received a USSR State Award and other awards from the government, including the one for the participation in the liquidation of the consequences of the Chernobyl disaster.

Dykhne, being a gifted person, could fascinate other people with interesting problems and stimulate creative ideas. He was a tactful person with a good sense of humor, but also a man of principle and a strong personality. Helping other people in difficult situations and showing courage in surviving the difficulties in his own life, he won the respect of a great number of people.

The world has lost a brilliant scientist and a wonderful person. Dykhne has left many students, successors, and friends who were fond of his keen mind and original ideas.

The memory of Aleksandr Mikhaĭlovich Dykhne will remain with his friends, colleagues, and all those who knew him.

Translated by E. Golyamina

Acoustical Physics, Vol. 51, No. 4, 2005, pp. 484–485. Translated from Akusticheskiĭ Zhurnal, Vol. 51, No. 4, 2005, pp. 566–567.

CHRONICLE

In Memory of V.I. Zaborov (March 16, 1927–August 30, 2004)

Vladimir Isaakovich Zaborov—Professor, Doctor of Engineering, a well-known specialist in constructional and architectural acoustics, the author of more than 250 publications, which include 11 monographs and 26 papers published in the *Akusticheskiĭ zhurnal* (the *Acoustical Physics*)—has passed away.

Zaborov graduated from the Moscow Institute of Constructional Engineering (including its post-graduate department) in 1949. His first place of work was the Central Research Institute of Industrial Structures (Moscow), where he studied the problems of structure mechanics and prepared a thesis devoted to calculating the strength and stability of composite arches. In 1952, he received the degree of Candidate of Science. In 1955, Zaborov moved to the Urals. There, he investigated topical problems of the sound insulation of buildings and structures and, later on, other problems of constructional and industrial acoustics.

Zaborov's first experimental and theoretical studies of sound insulation of buildings were concerned with the development of methods for calculating sound transmission through multilayer protecting walls, vibration excitation in multilayer structures under an impact and a subsequent sound radiation by these structures, and other problems of sound insulation in buildings. He carried out calculations to determine the sound insulation properties of two-layer structures and also those of three-layer structures with point constraints, with air-filled gaps, and with porous and elastic interlayers. He calculated the sound insulation under an impact noise for slabs with an elastic coating and for three-layer structures with different constrains. He also calculated the sound insulation in buildings with allowance made for indirect sound transmission. In 1962, Zaborov published his monograph *Theory of Sound Insulation by Protecting Structures*, which was mainly based on the results he himself had obtained. In the same year, he received the degree of Doctor of Science. The contribution made by Zaborov to solving the problems of sound insulation is very large. His name is related to the transformation of particular problems of sound insulation in buildings into a large independent field of science with a wide scope of practical applications. The basic concepts of this field of science were formulated by Zaborov in the aforementioned monograph, in its modified and extended second edition (Stroiizdat, Moscow, 1969), in the books *Sound Insulation in Large-Panel Buildings* (Stroiizdat, Moscow, 1964) and *Noise Suppression by Sound Insulation* (Stroiizdat, Moscow, 1973), in the handbook *Noise Control in Industry* (Mashinostroenie, Moscow, 1985), and in *A Handbook of Noise and Vibration Control in Private and Public Buildings* (Budivel'nik, Kiev, 1989), etc. Zaborov worked in the field of sound insulation all his life and made a substantial contribution to the development of acoustic design of sound insulation in buildings and structures in Russia.

In 1972–1979, while working at the All-Union Research Institute of Ferrous Metals (Chelyabinsk), Zaborov organized a large and efficient working team of specialists in industrial noise and vibration control. Many of the results obtained within this period of time were included in his book *Noise and Vibration Control in Ferrous Metallurgy* (Metallurgiya, Moscow, 1976).

In 1981–1988, Zaborov headed the Noise and Vibration Department of the Institute of Construction and Architecture of the State Construction Committee of the BSSR. At that time, he worked at solving the topical problem of protecting buildings from noise and vibration produced by shallow subways. He studied the excitation and propagation of vibrations from the subway and developed methods for calculating these vibrations and reducing them in buildings. He also studied the vibration excitation in the subway tunnel structures, the transfer of vibration from the tunnel to the environ-

1063-7710/05/5104-0484$26.00

ment, the transmission of longitudinal and transverse waves through obstacles in an elastic medium (plates or water-filled gaps), the interaction of elastic waves with buildings, and the vibrations of multilayer floors with a sound-insulating layer.

Zaborov was also well known for his organizational activities in science. He had many students who became scientists under his supervision. More than twenty of his students have become candidates of science. He brilliantly organized and conducted two All-Union Acoustical conferences in Chelyabinsk (in 1966 and 1980). He was an active member of many scientific councils and conferences and gave many talks and lectures for specialists in acoustics, engineers, and students.

With his death, we have lost a wonderful person, an excellent scientist and engineer, a teacher, and a dear friend. The memory of Vladimir Isaakovich Zaborov will remain forever in our hearts.

Translated by E. Golyamina

Acoustical Physics, Vol. 51, No. 4, 2005, pp. 486–487. Translated from Akusticheskiĭ Zhurnal, Vol. 51, No. 4, 2005, pp. 568–569.

CHRONICLE

In Memory of V.A. Robsman (March 18, 1937–January 9, 2005)

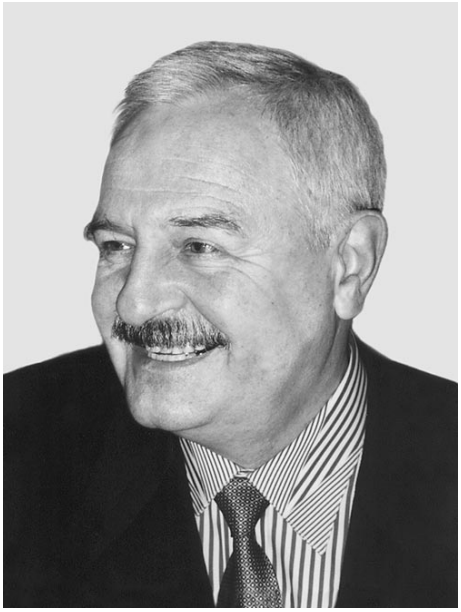

Vadim Aleksandrovich Robsman—Doctor of Physics and Mathematics, principal researcher of the Central Research Institute of Transport Engineering, Honored Builder, and Honored Transport Builder of the Russian Federation—passed away on January 9, 2005.

Robsman was born on March 18, 1937 in Moscow. In 1959, he graduated from the Building Faculty of the Moscow Institute of Transport Engineers. Then, he worked at the Ministry of Transport Communications and at the Vilyuĭ Hydro. In 1970, Robsman moved to Moscow to work at the Faculty of Geography of Moscow State University. There, he was deeply involved in the fundamental sciences: mathematics, physics, and geology. He was one of the first to master computer methods in science [1]. He also took part in expeditions to the Far East. An important role in the formation of Robsman's scientific interests was played by Academician R.V. Khokhlov, Rector of Moscow State University, who attracted Robsman's attention to the problems of acoustics and physics of nonlinear waves. In 1981, Robsman began working at the Central Research Institute of Transport Engineering, which remained his place of work until the end of his life. Although his main occupation was solving applied problems, he retained an interest in the fundamental problems of solid-state physics [2, 3], fracture mechanics [4, 5], nonlinear dynamics, and acoustics.

Robsman worked on the construction of the Sevan–Arpa tunnel in Armenia just before the catastrophic earthquake in Spitak. He took active part in the elimination of the consequences of the earthquake. He proposed several methods of acoustic nondestructive testing of the load-carrying structures of damaged buildings with the aim to determine which of the buildings could be reconstructed and which of them should be demolished. By combining active sounding of beams and floors by acoustic signals and shock pulses with recording the spectra of acoustic emissions under quasi-static loads, Robsman observed nonlinear distortions of wave spectra. He understood that the formation of isolated cracks, their growth, collective behavior (interaction), and subsequent coalescence are the origin of increasing nonlinear distortions. When the external force action on a structure was increased, the nonlinear effects became more pronounced.

On the basis of full-scale testing, Robsman developed empirical criteria for the relation between the nonlinear distortions of spectra and the loss of strength in a structure [6, 7]. Later, thanks to close cooperation with the Department of Acoustics of Moscow State University, the effects observed by Robsman were given a more elaborate theoretical explanation on the basis of the ideas and results of nonlinear acoustics [8–13].

In the last fifteen years, the methods of nonlinear nondestructive testing were put to practice by Robsman and his colleagues in transportation, the power industry, and civil engineering. Nondestructive testing was carried out for thirty bridges, several tens of highway overpasses, more than twenty thermal electric power stations, and many tunnels and subways. The work carried out in zones of seismic hazard made it possible to restore tens of structures damaged by earthquakes and to provide for the seismic safety of residential areas and power stations. In Moscow, nondestructive testing was used to monitor different stages of construction of the third transport ring, as well as in the restoration of some ancient buildings.

Robsman took part in the liquidation of the consequences of the Chernobyl accident, where he received a high radiation dose. Though he was seriously ill during the last five years of his life, he continued working. In these years, Robsman not only worked on the problems of the modern construction industry but also obtained some fundamental scientific results. He proposed a new nonlinear equation with a fourth-order derivative that describes intense waves in a scattering

1063-7710/05/5104-0486$26.00

medium [14]. This equation is of fundamental physical importance and continues the series of the well-known Burgers (second order) and Korteweg–de Vries (third order) equations. The equation allows for exact solutions, which were obtained in [14]. Although these results were published only recently, references to the new model as the "Robsman equation" have already appeared in the literature.

In a publication that appeared one month before his death [15], Robsman solved the problem of nonlinear waves in a hysteretic medium. The formulation of the problem is directly related to the nondestructive testing of piles used in the construction of the third transport ring of Moscow. In solving this applied problem, Robsman generalized the well-known Mandel'shtam–Leontovich theory to the case of relaxation of the nonlinear "internal parameter." In addition, he obtained several important physical results and a family of new nonlinear equations with a set of exact solutions.

All those who worked and communicated with Vadim Aleksandrovich Robsman will forever remember this wonderful and kind man.

LIST OF THE MAIN PUBLICATIONS BY V.A. ROBSMAN IN ACOUSTICS OF THE SOLID STATE, GEOACOUSTICS, AND NONDESTRUCTIVE TESTING

1. V. A. Robsman, *Problems of Mathematical Modeling of Geosystems*, Vestn. Mosk. Univ., Ser. 5: Geogr., No. 6, 72 (1972).
2. V. A. Robsman and M. Sh. Shikhsaidov, *Acoustic Emission and the Photoplastic Memory Effect in the Deformation of Zinc Sulfide and Zinc Selenide Crystals*, Fiz. Tverd. Tela (Leningrad) **30** (8), 2437 (1988).
3. V. A. Robsman and M. Sh. Shikhsaidov, *Effect of Ultrasonic Pulses on the Plastic Properties of II–IV Semiconductor Compounds*, Fiz. Tverd. Tela (Leningrad) **30** (11), 3329 (1988).
4. M. V. Kas'yan, G. N. Nikogosyan, and V. A. Robsman, *Changes in the Spectra of Emission Signals with the Development of Cracks and with the Fracture of Rock*, Dokl. Akad. Nauk SSSR, Ser. Geofiz., No. 3 (1989).
5. V. A. Robsman and V. V. Braun, *Methods and Results of Automated Fatigue Tests of Concrete*, Beton i Zhelezobeton (1990).
6. A. V. Kashko and V. A. Robsman, *Methods of Full-Scale Measurements and Evaluation of the Structure Damage after the Spitak Earthquake*, in *Measuring and Testing Means for Ensuring the Seismic Stability of Structures* (Yerevan, 1990).
7. V. A. Robsman and V. É. Stepanyan, *Instrumental Diagnostics of Seismic Stability of Structures in Seismoactive Areas*, in *Problems of Engineering Geology and Engineering Seismicity of Towns and Urban Areas* (Institute of the Lithosphere, Russian Academy of Sciences, Moscow, 1990), pp. 82–84.
8. V. A. Robsman, *Nonlinear Transformation of Noise Spectra in Nondestructive Testing of Concrete Structures*, Akust. Zh. **37** (5), 1038 (1991) [Sov. Phys. Acoust. **37**, 541 (1991)].
9. V. A. Robsman, *Transformation of Acoustic Spectra in Inhomogeneous Solid Media under Nonlinear Deformation*, Akust. Zh. **38** (1), 129 (1992) [Sov. Phys. Acoust. **38**, 66 (1992)].
10. V. A. Robsman, *Accumulation and Chaotic Development of Nonlinear Acoustic Processes in the Dynamic Fracture of Geological Structures*, Akust. Zh. **39** (2), 333 (1993) [Acoust. Phys. **39**, 176 (1993)].
11. V. V. Krylov, P. S. Landa, and V. A. Robsman, *A Model of the Development of Acoustic Emission as the Chaotization of Transient Processes in Coupled Nonlinear Oscillators*, Akust. Zh. **39** (1), 108 (1993) [Acoust. Phys. **39**, 55 (1993)].
12. P. S. Landa, G. I. Firsov, and V. A. Robsman, *A Model of Crack Dynamics and Acoustic Emission as a System of Coupled Nonlinear Oscillators*, J. Tech. Phys. **37** (3–4), 513 (1996).
13. V. A. Robsman and O. V. Rudenko, *A New Method for Nonlinear Nondestructive Testing of Developing Defects Inside Inhomogeneous Solids*, J. Acoust. Soc. Am. **105** (2), 1015 (1999).
14. O. V. Rudenko and V. A. Robsman, *Nonlinear Wave Equation in a Scattering Medium*, Dokl. Akad. Nauk, Ser, Fiz. **384** (6), 434 (2002) [Doklady Physics **47** (6), 443 (2002)].
15. O. V. Rudenko and V. A. Robsman, *Nonlinear Processes in Media with an Acoustic Hysteresis and the Problems of Dynamic Interaction between Piles and the Earth Foundation*, Akust. Zh. **50** (6), 825 (2004) [Acoust. Phys. **50,** 725 (2004)].

Translated by E. Golyamina

Acoustical Physics, Vol. 51, No. 4, 2005, pp. 488–491. Translated from Akusticheskiĭ Zhurnal, Vol. 51, No. 4, 2005, pp. 570–573.

INFORMATION

"Magnetoacoustics and Acoustoelectronics," Session of the Scientific Council on Acoustics of the Russian Academy of Sciences

A topical session of the Scientific Council on Acoustics of the Russian Academy of Sciences, "Magnetoacoustics and Acoustoelectronics," was held at Syktyvkar State University on June 22–26, 2004. Researchers from the Physics Faculty of Syktyvkar State University, Syktyvkar Forestry Institute, and Kirov Forestry Engineering Academy, St. Petersburg, as well as specialists from research centers in Moscow, St. Petersburg, Ul'yanovsk, Chelyabinsk, and Brest took part in the session.

An introductory speech was made by the Cochairman of the organizing committee of the session, the Head of the laboratory of the Institute of Radio Engineering and Electronics, Russian Academy of Sciences, Professor V.G. Shavrov. He noted that the first papers in acoustoelectronics (G. Weinreich, Yu.V. Gulyaev, V.I. Pustovoĭt, V.L. Gurevich, and others) and magnetoacoustics (E.A. Turov, Yu.P. Irkhin, Ch. Kittel, A.I. Akhiezer, V.G. Bar'yakhtar, S.V. Peletminskiĭ and others) were published about 50 years ago. Today, these fields of research remain topical, because the fundamental results of studying these problems are of great importance for applications in devices used for data processing and communication. He stressed the fact that such a session was being held in the Komi Republic for the second time. The first session was organized in 1993. Since that time, research in magnetoacoustics and acoustoelectronics has progressed a great deal and young researchers actively working in this field have appeared. The guests were also greeted by the Rector of Syktyvkar State University, Chairman of the Local Organizing Committee, Professor V.N. Zadorozhnyĭ and Head of the Department of Radio Physics and Electronics, Professor L.N. Kotov. Zadorozhnyĭ noted that the session will enhance basic research in physics in the Komi Republic and wished successful work to all participants. Then, 13 papers were presented at several sections of the session.

Section A: Acoustomagnetic Phenomena in Condensed Media

A paper by V.G. Shavrov (coauthors: V.D. Buchel'nikov, V.V. Koledov, Yu.A. Kuzavko, and T.O. Khudaverdyan from the Institute of Radio Engineering and Electronics of the Russian Academy of Sciences, Chelyabinsk State University, and Brest State Technological University), "Effect of Ultrasound on the Structural Transition and the Shape Memory Effect in a Ferromagnet," presented the results of research into the acoustic properties of NiMnFeGa polycrystals, where anomalies of the Young modulus and ultrasonic attenuation near the magnetic, structural, and modulation transitions were detected. It was demonstrated experimentally that ultrasound can cause austenite–martensite and martensite–austenite structural transformations at constant temperature. The nonthermal mechanism of the ultrasonic effect on the structural transition was proved using a pulsed technique. It was shown that the effect of ultrasound on the structural transition differs from the effects of constant pressure and magnetic field. For example, a magnetic field shifts the temperature loop of hysteresis to the higher temperature range and constant pressure smears and shifts it to the right, whereas ultrasound makes the hysteresis loop narrower.

A paper by V.D. Buchel'nikov (coauthors: N.K. Dan'shin, L.T. Tsymbal, and V.G. Shavrov from Chelyabinsk State University, the Donetsk Physicotechnical Institute of the National Academy of Sciences of Ukraine, and the Institute of Radio Engineering and Electronics of the Russian Academy of Sciences), "Magnetoelastic Interactions in Rare-Earth Orthoferrites in the Phase Transition Region," was devoted to a review of experimental and theoretical studies of the magnetoacoustics of rare-earth orthoferrites in the region of orientation phase transitions. The temperature and field dependences of the frequencies of soft magnetoresonance modes and of the velocity and attenuation of sound in the vicinities of different orientation phase transitions were presented. The dependences were obtained by the methods of microwave and ultrasonic spectroscopy. It was found that the contributions of precession and longitudinal oscillations of magnetization intensity to the dynamic properties always coexist and are additive, while their ratio depends on both the external parameters and the ratio of the temperatures of spontaneous reorientation and ordering of the corresponding spin subsystem. The origin of the energy gaps in the spectrum of spin waves and the change in the dispersion law at the points of orientation phase transitions was discussed. It was demonstrated that the observed values of energy gaps and the behavior of sound velocities result from the interaction of all indicated subsystems of orthoferrites.

1063-7710/05/5104-0488$26.00

In the paper by N.S. Shevyakhov (coauthors: S.N. Maryshev and V.G. Shavrov from the Ul'yanovsk Branch of the Institute of Radio Engineering and Electronics and the Institute of Radio Engineering and Electronics of the Russian Academy of Sciences), "Modes of Shear Magnetoelastic Waves Propagating in a Ferromagnetic Cylinder in a Circulation Manner," a solution to the problem of the propagation of magnetoelastic waves in a ferromagnetic cylinder was given. The magnetostatics conditions and the periodic boundary conditions for magnetization and elastic displacements were taken as the boundary conditions. The solution to the equations of magnetoelasticity was selected in the form of the product of a harmonic function of time and cylindrical functions of coordinates. The nonreciprocity of the propagation of waves with different polarizations, the frequency dispersion of the azimuth wave number with respect to the wave frequency, and a high-frequency ferromagnetic resonance for the modes of inverse propagation were revealed. The nonreciprocity of the mode propagation manifests itself more strongly away from the magnetoacoustic resonance and is most pronouced for the lowest mode. The presence of a demarcation frequency for the lowest mode of direct propagation was revealed, and its dependence on the cylinder radius was investigated for the case of a moderate magnetoelastic coupling.

The paper by V.S. Vlasov (coauthors: F.F. Asadullin, L.N. Kotov, D.E. Tsurikov, and V.G. Shavrov from Syktyvkar State University, the Syktyvkar Forestry Institute, and the Institute of Radio Engineering and Electronics of the Russian Academy of Sciences), "Dynamics of Interaction of Elastic Vibrations with the Magnetic Subsystem in the Ferromagnetic Resonance Region in Particles and Films," analyzed the numerical solution to the system of magnetoelasticity equations in a plane ferrite particle and a ferrite film under the condition of nonlinear magnetoacoustic resonance for different values of the magnetic dissipation parameter. The rise of a nonuniform distribution of energy between the elastic and magnetic subsystems under the resonance conditions was revealed. The presence of three relaxation regions for magnetization oscillations was observed under magnetoacoustic resonance conditions in the presence of an alternating field at certain values of the magnetic dissipation parameter. The relaxation nonlinearity becomes significant only at the end of the relaxation time interval. The interval of the values of the magnetic dissipation parameter was determined, within which the nonlinear relaxation and magnetization damping, as well as the largest growth of elastic vibrations, are observed.

The paper by L.S. Nosov (coauthors: V.S. Vlasov, L.N. Kotov, and V.G. Shavrov from Syktyvkar State University and the Institute of Radio Engineering and Electronics of the Russian Academy of Sciences), "Behavior of an Elastic Subsystem under the Magnetization Reorientation in a Single-Domain Particle," was devoted to the simulation of the dynamics of the elastic and magnetic subsystems in a cubic ferrite particle under the effect of magnetization reorientation by a strong alternating magnetic field. A numerical solution to the simultaneous equations of motion of the magnetization vector in Gilbert's form and the equation for the elastic subsystem of a small magnetic particle was obtained in the approximation of a uniform precession of the magnetization vector. It was demonstrated that, when the frequencies of the acoustic and ferromagnetic resonances differ widely, the elastic subsystem does not affect the reorientation conditions. If these frequencies are of the same order of magnitude, the elastic subsystem decelerates the reorientation and represents an additional channel of energy loss.

Yu.A. Kuzavko (coauthors: M.M. Karpuk, D.A. Kostyuk, and V.G. Shavrov from Brest State Technological University and the Institute of Radio Engineering and Electronics of the Russian Academy of Sciences) presented the paper "Characteristic Features of Reflection and Refraction of Acoustic Waves at the Boundary with a Magnetically Ordered Crystal in Its Phase Transition Region." He considered a semi-infinite antiferromagnetic crystal with an anisotropy of the easy-plane type near the orientation phase transition in a magnetic field applied in the basal plane. When the free surface of the crystal is loaded with a fluid and, then, with a nonmagnetic dielectric, the number of critical angles for a transverse wave increases and reaches a value of three. In this case, accompanying surface oscillations occur, which may deteriorate in the vicinity of the phase transition, i.e., begin to radiate into the volume. Analogous effects are discussed for a ferromagnetic crystal of the Geissler alloy, Ni_2MnGa, with a shape memory, for which a one-order-stronger as compared to hematite acoustic anisotropy is observed in the region of the premartensite and martensite phase transitions.

The paper by S.N. Karpachev (coauthors: K.V. Kopytin and D.E. Khasanov from Moscow State University) "Propagation and Transformation of Different Types of Magnetoelastic Waves in a Manganese Zinc Spinel Crystal" presented experimental data on the propagation of bulk and surface magnetoelastic waves in a Mn–Zn spinel sample. It was demonstrated experimentally that, in external magnetic fields corresponding to the magnetoacoustic resonance region, the maximum efficiency of the surface magnetoelastic wave generation is observed when the waves are excited by a meander. Anomalies appear in the case of the elimination of the magnetic component of bulk magnetoelastic waves by the meander and in the opposite case, when bulk magnetoelastic waves are excited by the meander and the signal is eliminated by a bulk wave transducer.

The paper by L.N. Kotov (coauthors: F.F. Asadullin, A.M. Ulyashev, and V.G. Shavrov from Syktyvkar State University, the Syktyvkar Forestry Institute, and the Institute of Radio Engineering and Electronics of the Russian Academy of Sciences), "Characteristic Features of Damping of Ultrasonic waves in the Region

of the Magnetic Phase Transition in Manganese Zinc Spinel," reported on new results of the studies of ultrasonic wave damping near the point of inversion of the first anisotropy constant in manganese zinc spinel crystals, which were grown by different methods. Different damping in these samples was explained taking into account the internal fields and the variations of the parameters of magnetization relaxation. It was associated with the macroscopic disorder of the crystals and different ordering of the ferrous and ferric iron ions in the lattice. A strong damping at very low frequencies (in the frequency range of several megahertz) was revealed in the region of spin reorientation in manganese zinc spinel, which was caused by the magnetoelastic interaction in this region.

Section B: Acoustoelectronic Phenomena in Condensed Media

The paper by L.A. Kulakova (coauthors: A.V. Lyutetskiĭ, N.A. Pikhtin, I.S. Tarasov, and E.Z. Yakhkind from the Ioffe Physicotechnical Institute, Russian Academy of Sciences, St. Petersburg), "Study of the Effect of Alternating Strain on the Electronic and Optical Properties of Heterolasers," discussed the results of the first studies of acoustoelectronic and acoustooptic effects in InGaAsP/InP laser heterostructures. A new principle of the periodic frequency tuning of the diode laser radiation by the action of an alternating elastic strain on the active region of laser heterostructures was reported. The first data on the effect of the strain action of bulk and surface ultrasonic waves on the spectral parameters of laser radiation were obtained. To implement the action of elastic strain on the optical generation mode, excitation of both bulk and surface sound waves was performed in heterostructures in the frequency range of 5–10 MHz. It was demonstrated that the introduction of ultrasound into a heterostructure sample leads to the modulation of the generation frequency with a period equal to the period of the sound wave. It was found that, in the structures studied, the effect of sound on the band structure of the active region is the determining factor.

The paper by L.N. Kotov (coauthors: I.V. Piir, A.M. Ulyashev, and F.F. Asadullin from Syktyvkar State University and the Syktyvkar Forestry Institute), "Acoustic Properties of Solid Solutions of Complex Bismuth Niobates with a High-Temperature Conductivity," is devoted to studies of the acoustic properties (the velocity and damping of ultrasonic waves at frequencies of 2.5–10 MHz) of solid solutions of complex bismuth niobates $Bi_2MgCu_xNb_2O_9$ (x = 0.25, 0.5, and 0.75), $Bi_2Zn_{0.8}Fe_{0.2}Nb_2O_9$, and $Bi_5Nb_{0.1}Cr_{0.9}O_9$ in the temperature interval of 290–620 K. It was demonstrated that the ultrasonic damping coefficient increases for all samples as the temperature grows, which is connected with the increase in the conductivity of the samples and with the interaction of the ultrasonic wave with charge carriers. It was found that the high-temperature velocity value strongly depends of the concentration of transition metals. The presence of several high-temperature jumps of sound velocity was revealed. The jumps are related to the existence of metastable states of the crystal structure and to the presence of relatively weakly interacting solid phases in the samples under study.

F.F. Asadullin (coauthor: L.N. Kotov, the Syktyvkar Forestry Institute and Syktyvkar State University) presented the paper "Excitation of Piezoelectric Oscillations in Particle Ensembles." He considered the conditions for the resonance excitation of acoustoelectric oscillations of particles (with a particle size of 50–150 μm) by a pulse of electric field at frequencies of 10–50 MHz. The effect of the interaction of oscillating particles on the relaxation time of elastic and electric oscillations was demonstrated. The origin of coherent responses of piezoelectric particles was discussed. Formulas for the amplitude of acoustoelectric particle oscillations were given and compared with experimental data for piezoelectric powders of different materials.

Section C: Critical and Nonlinear Phenomena in the Physical Acoustics of Solids

The paper by Yu.A. Kuzavko (Brest State Technological University), "Propagation of Bulk and Surface Acoustic Waves at the Boundary with a Dissipative Medium," considered the case of an oblique reflection of a longitudinal acoustic wave from the boundary between a liquid and a dissipative medium, in which a strong absorption of ultrasonic oscillations is observed. At the critical angle of incidence, when the reflected signal begins to be observable, its amplitude is determined by the dissipative loss parameter. At other angles of incidence of the longitudinal wave, the effect of its maximum conversion into a transverse wave occurs at the boundary of a solid with a dissipative medium. This transverse wave is sensitive to the shear viscosity of the reflecting medium. In the case of the incidence of a transverse wave at an angle higher than critical, accompanying surface oscillations are generated, while the wave itself only slightly penetrates into the medium. At the boundary between a solid and a dissipative medium, the dissipative factor favors the presence of surface waves with polarization parallel to the boundary plane.

Yu.N. Belyaev (Syktyvkar State University) presented the paper "The Characteristic Matrix for the Dynamics of Elastic Properties of Layered Periodic Structures." He determined the interference coefficients of reflection and refraction of elastic waves in layered periodic media. The methods of the characteristic matrices of the fourth to sixth orders were used to determine the coefficients. In the case of the critical phenomena in layered periodic structures, the coefficients were calculated using higher orders of the indicated characteristic matrices.

Section D: Application of Acoustic Oscillations and Waves in Various Devices

The paper by S.G. Alekseev (coauthors: I.M. Kotelyanskiĭ and G.D. Mansfel'd from the Institute of Radio Engineering and Electronics, Russian Academy of Sciences), "Microwave Resonators and Filters Using Bulk Acoustic Waves," characterized the modern state-of-the-art and the prospects for the development of acoustoelectronic elements using bulk acoustic waves in the microwave range. The presentation was based on original results obtained at the Institute of Radio Engineering and Electronics in the design of microwave resonators and filters and also sensors for some physical quantities on the basis of microwave resonators. Special attention was given to the achievements of the Institute of Radio Engineering and Electronics in developing the metrics of new promising acoustic materials for the microwave range and the design of thin piezoelectric and metal films to be used in elements intended for the microwave range.

The session was concluded by a round table discussion of topical problems of magnetoacoustics and acoustoelectronics. The general opinion was expressed that it is necessary to develop acoustic research into new nanomaterials, composite thin films, and layered structures. It also is necessary to pay more attention to the nonlinear aspects of the physical acoustics of solids.

L. N. Kotov

Translated by M. Lyamshev

Acoustical Physics, Vol. 51, No. 4, 2005, pp. 492–493. Translated from Akusticheskiĭ Zhurnal, Vol. 51, No. 4, 2005, pp. 574–575.

INFORMATION

Review of the Book *Baffling of Hydroacoustic Transducers* by V.E. Glazanov and A.V. Mikhaĭlov (Élmor, St. Petersburg, 2004)

The book is devoted to the basic problems of the theory and practical design of acoustic baffles for modern hydroacoustic transducers and arrays. Since the appearance of the monograph *Baffling of Hydroacoustic Arrays* (by V.E. Glazanov, Sudostroenie, Leningrad, 1986 (in Russian)), which was the only book on acoustic baffles in the Russian literature at that time, the authors, well-known specialists in this area of engineering, have carried out many theoretical and experimental studies of both baffles themselves and characteristics of baffled transducers. The newly published book is mainly concerned with the methods of calculating the baffle elements and the acoustic characteristics of individual transducers and to the comparison of calculations with experiments. The theoretical consideration is not limited to the derivation of the final expressions for calculation. The mathematical methods used for their derivation give an insight into the principles of operation of the devices in question and allow researchers and engineers to master the mathematical description of the physical problems of baffle design. The book consists of five parts and contains 22 sections and two appendices. The authors provided a comprehensive description of the basic problems of baffling according to the current status of this field of research.

Part I, entitled *Baffling Properties of Plane Layered Systems* (Sections 1–4), presents the formulas for calculating single-layer, two-layer, and multilayer systems serving as the basic elements in designing acoustic baffles. Using an array consisting of bar transducers as an example, the authors estimate the effect of a plane baffle on the back lobe of the array directivity pattern.

Part II is entitled *Acoustic and Elastic Parameters of a Medium with Cylindrical Ducts* (Sections 5–8). This part is devoted to a comprehensive study of the statistical and dynamic properties of a rubber medium with cylindrical ducts (under small and large deformations). Layers of such a medium are widely used in hydroacoustics for making sound-insulating and sound-absorbing coatings and baffles. (This kind of medium was first described by Tyutekin in the paper *Elastic Wave Propagation in a Medium with Cylindrical Ducts*, Akust. Zh. **2**, 291 (1956) [Acoust. Phys. **2**, 307 (1956)].) An approximate theory that allows one to determine the acoustic and elastic parameters of such media with sufficient accuracy is developed. The calculated frequency characteristics of the reflection and transmission coefficients of baffles made of rubber with cylindrical ducts are found to agree well with experimental data.

In Part III, entitled *An Acoustic Baffle for a Broadband Hydroacoustic Array* (Sections 9–13), a method of designing an acoustic baffle for a receiving hydroacoustic array is proposed and justified. A sound reflector consisting of a metal plate combined with a compliant layer of rubber with cylindrical ducts is studied. Such baffles are optimum ones from the point of view of acoustic and weight–size characteristics and are used in practice in modern broadband arrays. Results of experimental studies of baffle elements under different hydrostatic pressures are presented. These results agree well with the calculated characteristics of the reflection and transmission coefficients. The sensitivity of a receiver positioned near the baffle under consideration is determined by both calculation and experimental measurement.

Part IV, *Baffling of Cylindrical Transducers* (Sections 14–18), describes the effect of baffles on the parameters of cylindrical transducers. The authors proceed from the possibility of obtaining simplified expressions that are suitable for engineering calculations to determine the acoustic characteristics of baffled transducers with actual properties of the baffles. In addition to the physically justified statement of the problem, the validity criterion for the derived expressions is the coincidence of the results of calculations with experimental data. An approximate method is proposed for determining the field produced by a cylindrical transducer of finite height with allowance for the radiation from the ends of its inner volume filled with an elastic medium with an arbitrary Poisson ratio. This problem is solved without taking into account the interaction of the ends of the inner cavity and the outer surface of the transducer, where the latter is considered as an opaque cylinder in perfectly rigid semi-infinite baffles. The sound pressure generated along the radius by a transducer that has a foam-plastic inner baffle or is filled with water is calculated. For the wave generated by the cylinder, the problem of its diffraction by a nonclosed array of perfectly compliant cylindrical scatterers surrounding the cylinder is solved, and the results are used to calculate the pressure and the radiation resistance of the cylinder for arbitrary baffling angles and sound insulation of the array. The calculated direc-

1063-7710/05/5104-0492$26.00

tivity patterns agree well with the measured ones. The problem of radiation from a cylinder positioned near a plane baffle with a given input impedance is solved. The possibility to design side baffles for cylindrical transducers on the basis of resonant-type baffling plates is considered. A theory for calculating the acoustic and strength parameters of baffling plates is developed. (It should be noted that oscillatory systems of this kind were studied by Grinchenko and Vovk in their monograph *Wave Problems of Sound Scattering by Elastic Shells*, Naukova Dumka, Kiev, 1986).

Part V, *Application of the Multipole Method in Calculating the Acoustic Characteristics of Cylindrical Transducers* (Sections 19–22), describes the methods for calculating some unconventional types of cylindrical transducers and baffles for them.

For each of the issues considered in the book, exhaustive information is given, which provides the possibility for designing baffles and baffling schemes for transducers according to the modern engineering level.

The book contains ample graphical material that gives better insight into the essence of the problems under consideration. This book is definitely useful for engineers and researchers involved in the development of hydroacoustic transducers and arrays, as well as in other problems concerned with sound insulation in water, and also for university students and postgraduates specializing in acoustics.

In closing, it should be noted that the appearance of this book after a long absence of Russian publications in applied acoustics is an important event, which should be welcomed by the scientific community.

V.V. Tyutekin

Translated by E. Golyamina

Acoustical Physics, Vol. 51, No. 4, 2005, p. 494. Translated from Akusticheskiĭ Zhurnal, Vol. 51, No. 4, 2005, p. 576.

INFORMATION

Shirshov Oceanology Institute of the Russian Academy of Sciences and the Russian Acoustical Society invite specialists to the XI Brekhovskikh's Workshop on Ocean Acoustics and the XVII Session of the Russian Acoustical Society dedicated to the memory of Academician L.M. Brekhovskikh

ORGANIZING COMMITTEE:

B. Kuperman
N. A. Dubrovsky
V. A. Akulichev
S. S. Lappo
A. G. Luchinin
B. F. Kur'yanov
O. A. Godin
Yu. A. Chepurin
E. V. Yudina
V. G. Selivanov

PROGRAM GROUP:

R. F. Shvachko (Chair)
A. L. Virovlyanskiĭ
V. V. Goncharov
V. S. Gostev
E. A. Kopyl
Yu. P. Lysanov
A. I. Malekhanov

The program of the Workshop includes lectures, oral presentations, and poster presentations.

Scope:

- sound propagation in the ocean
- acoustic tomography
- ambient noise of the ocean
- scattering and reflection of sound
- signal processing
- acoustic methods and means for ocean studies
- oceanological characteristics important for underwater acoustics
- ecological factors in solving acoustic problems.

The Workshop and the XVII Session of the Russian Acoustical Society will be held May 23–26, 2006 in the Large Conference Hall of the Shirshov Oceanology Institute, Russian Academy of Sciences, in Moscow (Nakhimovskiĭ pr. 36).

November 1, 2005, is the deadline for submitting abstracts of papers. An abstract should contain no more than 200 words. The authors should indicate the point of the scope to which their paper belongs.

The list of papers accepted for presentation will be announced by the Organizing Committee before **December 1, 2005.**

Full versions of the accepted papers should be submitted before **February 1, 2006.**

Mailing address:

Organizing Committee of the Workshop on Ocean Acoustics, Shirshov Oceanology Institute, Russian Academy of Sciences, Nakhimovskiĭ pr. 36, Moscow, 117851 Russia

Tel.: (095) 129-1936, (095) 126-9835

Fax: (095) 124-5983

e-mail: acoustics@ocean.ru

The best way to submit the abstracts is by e-mail in the form of Word files.

Instructions for formatting the papers, as well as information on the event as a whole, news, and current status, can be found on that Internet at http://rav.sio.rssi.ru/school-11.html

The Organizing Committee would appreciate your sharing information on the XI Workshop on Ocean Acoustics and the XVII Session of the Russian Acoustical Society with your colleagues.

1063-7710/05/5104-0494$26.00